

Imaging the Chilean continental margin using seismic wide-angle data

vorgelegt von

Daniel Chalbaud A.

Berlin, 2010

DISSERTATION

zur Erlangung des Grades eines
Doktors der Naturwissenschaften
bei dem Fachbereich Geowissenschaften
der Freien Universität Berlin

Tag der mündlichen Prüfung: 19.05.2010.

- | | |
|----------------------|---------------------------------|
| 1. Gutachter: | Prof. Dr. Serge Shapiro. |
| 2. Gutachter: | Prof. Dr. Rainer Kind. |

Erklärung

Hiermit versichere ich, dass ich die vorliegende Arbeit selbständig verfasst und keine anderen als die angegebenen Hilfsmittel benutzt habe. Die Stellen der Arbeit, die anderen Werken wörtlich oder inhaltlich entnommen sind, wurden durch entsprechende Angaben der Quellen kenntlich gemacht.

Diese Arbeit hat in gleicher oder ähnlicher Form noch keiner Prüfungsbehörde vorgelegen.

To my Mother

Abstract

Wide-angle experiments represent one of the most common methods to study deep structures of the lithosphere in different tectonic settings. The principal benefit of these methods is the recording of strong amplitude signals reflected at larger incidence angles, originating not only from first order discontinuities, but also from higher discontinuities located in zones with small velocity contrast.

Since 1993, in the frame of the Collaborative Research Center (SFB 267) "Deformation Processes in the Andes", several active and passive seismic projects have been conducted along the Chilean continental margin with the aim to understand the subduction orogeny of the Andes and related surface processes. Between 19°S and 26°S the CINCA-95 project combined off-onshore seismic measurements including wide-angle and near-vertical-reflection (NVR) data to investigate the evolution and structure of the erosive convergent margin. In southern Chile, between 36°S and 40°S, active seismic experiments during the SPOC-2001 project were carried out to compile data of the seismogenic plate interface and to study the geometry of the accretive convergent margin. In both projects the wide-angle experiments were performed using marine, amphibious as well as onshore layouts, covering a total area that extends from west of the trench to the recent volcanic arcs.

The Kirchhoff prestack depth migration (KPSDM) is a robust algorithm that has provided successful results in the imaging of the Chilean convergent margin. Until now, only KPSDM has been applied to near-vertical-reflection (NVR) data on the region. We present the application of KPSDM to the CINCA and SPOC wide-angle datasets, with the aim to obtain new images of the seismogenic coupling zone in northern and southern Chile.

In order to reduce the generation of artifacts during the migration process, the seismic data were pre-processed using a flow designed to attenuate the background noise originated by heterogeneities in the subsurface and the reverberations generated by the air-gun source. The velocity models used for migration were derived from interpretation and inversion of the most prominent arrivals interpreted on the record sections.

The KPSDM of the CINCA wide-angle data imaged major features below the forearc region of the erosive continental margin in northern Chile. The migration results show the oceanic Moho as a strong dipping reflector at 25-32 km depth. The crystalline upper crust is imaged by a series of horizontal reflectors visualized in the amphibious and onshore data between 10-20 km depth, which reveals layering in a region composed mainly by remnants of the Paleozoic continental crust and the volcanic and granitoid rocks of the ancient Jurassic magmatic arc. Additionally, an east dipping reflector occurring above of the low velocity zone has been interpreted as the top of the subduction channel. A possible location of the continental Moho or downward continuation of the subduction channel below the Coastal Cordillera is indicated by a sharp east dipping reflector observed at 47-55 km depth in the migrated section of the onshore data.

Fresnel Volume Migration (FVM), a novel extension of KPSDM, was applied to the data in northern Chile providing successful results with an improved resolution and signal to noise ratio. Reflection Image Spectroscopy (RIS) was applied by imaging the data in three narrow frequency bands in order to characterize the medium in terms of scattering concentration. Additional structural details were revealed and the occurrence of those imaged in the full frequency section was confirmed. Also, the prestack depth migration of narrower offset ranges provided results that support the structures imaged in the full offset section.

In southern Chile the oceanic Moho has been imaged from the trench area at 13-14 km depth down to 42-49 km depth under the Coastal Cordillera. The migration of the amphibious data images structures in the upper continental crust beneath the offshore forearc. The reflectors observed on the migrated section may be associated to changes in the acoustic impedance caused by the intercalation of the basally accreted rocks of the Western Series, characterizing the upper continental plate as strongly segmented.

The KPSDM results are compared with results of other geophysical methods applied in the region including gravimetry, magnetotellurics, hypocentre locations, heat-flow density and temperature distribution, seismic tomography, V_p/V_s ratios in order to describe the observed structures from a tectonic and geological point of view. Further, two geological models are proposed for the off-onshore forearc area of the erosive and accretive convergent margins, based on the results of previous investigations and those obtained in this study.

In summary, the prestack depth migrated sections derived in the present study provide a first insight into the structural architecture of the Chilean seismogenic coupling zone which has not been imaged before.

Zusammenfassung

Weitwinkel-Experimente stellen eine der häufigsten Methoden dar, um Tiefenstrukturen der Lithosphäre in verschiedenen tektonischen Umgebungen zu studieren. Der Hauptvorteil dieser Methode ist die Erfassung starker Amplituden, die unter großen Einfallswinkeln reflektiert wurden, resultierend nicht nur aus den Diskontinuitäten erster Ordnung, sondern auch aus wichtigen Diskontinuitäten in Regionen mit geringem Geschwindigkeitskontrast.

Im Rahmen des Sonderforschungsbereichs (SFB 267) "Deformation in den Anden" wurden seit 1993 mehrere aktive und passive seismische Projekte entlang des chilenischen Kontinentalrandes durchgeführt mit dem Ziel, die Gebirgsbildung der Anden und ihre Oberflächen-Prozesse zu verstehen. Zwischen 19°S und 26°S kombiniert das CINCA-95-Projekt *Off-* bzw. *Onshore* seismische Messungen inklusive Weitwinkel- und Steilwinkelreflexions-Daten (NVR), um die Entwicklung und Struktur des erosiven konvergenten Kontinentalrandes zu untersuchen. Im südlichen Chile wurden zwischen 36 °S und 40 °S aktive seismische Experimente während des SPOC-2001-Projektes durchgeführt, um Daten aus der Schnittstelle seismogener Platten zusammenzustellen und um die Geometrie des akretionären konvergenten Kontinentalrandes zu untersuchen. In beiden Projekten wurden marine, amphibische und Land Meßanordnungen verwendet, welche eine Fläche abdecken, die sich vom Westen des Trenches bis zu den modernen vulkanischen Bögen erstreckt.

Kirchhoff-Pre-Stack-Tiefen-Migration (KPSDM) ist ein robuster Algorithmus, mit dem erfolgreiche Ergebnisse bei der Abbildung des chilenischen konvergenten Kontinentalrandes erzielt wurden. Bis jetzt ist die Methode nur auf die Steilwinkelreflexionsdaten (NVR) in der Region angewandt worden. Wir wenden die KPSDM auf die Cinca- und SPOC-Weitwinkel-Datensätze an mit dem Ziel, neue Bilder von den seismogenen Kopplungszonen im nördlichen und südlichen Chile zu erhalten.

Um die Erzeugung von Artefakten während der Migration zu verringern, wurden die seismischen Daten preprozessiert, um Stürsignale aufgrund von Heterogenitäten im Untergrund sowie die Reverberation der airgunsschüsse abzuschwächen. Die für die Migration verwendeten Geschwindigkeits-Modelle, wurden aus der Inversion der Ankunftszeiten der markantesten Ereignisse abgeleitet.

Die KPSDM der CINCA-Weitwinkel-Daten bildete die wichtigsten Strukturen unterhalb der *Forearc* Region des erosiven Kontinentalrandes im Norden Chiles ab. Die Migrations-Ergebnisse zeigen die ozeanische Moho als starken und geneigten Reflektor in 25-32 km Tiefe. Die kristalline Oberkruste ist durch eine Reihe von horizontalen Reflektoren in den amphibischen und *Onshore*-Daten zwischen 10-20 km Tiefe abgebildet. Die Interpretation dieses Ergebnisses ist, daß die Obere Kruste aus einer Schichtung der paläozoischen Gesteine und vulkanischer Gesteine und Granitoide des alten jurassischen magmatischen Bogens besteht. Ein zusätzlich auftretender, nach Osten geneigter Reflektor oberhalb der

Zone niedriger Geschwindigkeiten (LVZ) kann als die Oberkante des Subduktionskanals interpretiert werden. Ein stark nach Osten geneigter Reflektor bei 47-55 km Tiefe in der Migrationssektion der *Onshore* Daten bildet möglicherweise die Lage der kontinentalen Moho oder die Fortsetzung des Subduktionskanals unter die Küsten-Kordillere ab.

Die Anwendung der Fresnel Volume Migration (FVM), eine Erweiterung der KPSDM, auf die Daten aus dem südlichen Chile produziert erfolgreiche Ergebnisse, die eine bessere Auflösung und ein höheres Signal-Rausch-Verhältnis zeigen. Bei der so genannten Reflection Image Spectroscopy (RIS) wurde die Daten in drei schmale Frequenzbänder unterteilt. Diese wurden dann separat tiefenmigriert, um das Medium hinsichtlich der Konzentration der Streuer zu charakterisieren. Es wurden zusätzliche strukturelle Details ermittelt und die Reflexionen, die schon im gesamten Frequenzbereich auftraten, wurden bestätigt. Außerdem bestätigte die Pre-Stack Tiefen-Migration schmaler Offset Bereiche die Abbildung der Strukturen in der gesamten Offset-Sektion.

In Süd-Chile wurde die ozeanische Moho vom Tiefseeegraben bei 13-14 km Tiefe bis hin zu 42-49 km Tiefe unter die Küsten-Kordillere abgebildet. Die Migration der amphibischen Daten bildete Strukturen in der oberen Kontinentalkruste unterhalb des *Offshore-Forearcs* ab. Die bei der migrierten Sektion beobachteten Reflektoren können mit den Änderungen der akustischen Impedanz assoziiert werden, die durch die Schichtung der Gesteine der Western Series verursacht sind, die die obere Kontinentalplatte als stark segmentiert charakterisieren.

Die KPSDM Ergebnisse werden mit Ergebnissen anderer in der Region angewandter geophysikalischer Methoden wie Gravimetrie, Magnetotellurik, Erdbebenlokalisierung, Wärmeflußdichte und Temperaturverteilung, seismische Tomographie und V_p / V_s Verhältnis verglichen, um die beobachteten Strukturen aus dem tektonischen oder geologischen Blickwinkel zu beschreiben. Desweiteren werden zwei geologische Modelle für das Off- und Onshore Forearc-Gebiet des erosiven und akretionären Kontinentalrandes vorgeschlagen. Diese Modelle basieren auf Ergebnissen früherer Untersuchungen und Ergebnissen dieser Arbeit.

Zusammenfassend läßt sich sagen, daß die Pre-Stack tiefenmigriertesektionen, die in der gegenwärtigen Arbeit abgeleitet wurden, eine erste Einsicht in die strukturelle Architektur der chilenischen seismogenen Kopplungszone liefern, die bisher noch nicht abgebildet wurde.

Table of Contents

1	Introduction.....	1
2	Geological setting.....	5
2.1	The Central Andes.....	5
2.2	The Southern-Central Andes.....	10
2.3	Accretionary and erosive margins.....	12
3	Previous active seismic experiments in northern and southern Chilean Andes.....	15
3.1	Imaging in the Central Andes.....	15
3.2	Imaging in southern Chile.....	22
4	The Seismogenic coupling zone.....	25
4.1	Characteristics of coupling zones.....	25
5	Fundamentals in seismic wide-angle data.....	29
5.1	Development of wide-angle investigations for exploration of the Lithosphere	29
5.2	Characteristics of the wide-angle data.....	30
5.3	Typical wide-angle arrivals and some basic interpretation parameters.....	31
5.4	Wide-angle Migration.....	33
5.5	Energy partitioning at wide-angle incidence.....	34
6	Seismic Migration.....	37
6.1	Kirchhoff prestack depth migration.....	39
6.2	Vertical resolution.....	43
6.3	Fresnel zone and horizontal resolution.....	45
6.4	Fresnel Volume Migration.....	47
6.4.1	Fundamentals of Fresnel Volume Migration.....	48
6.4.2	Validity of approximations.....	50

7	The wide-angle dataset.....	53
7.1	The CINCA wide-angle dataset.....	53
7.2	The SPOC wide-angle dataset.....	56
7.3	Data and phase correlations.....	58
7.3.1	Seismic phases of CINCA wide-angle data.....	58
7.3.2	Seismic phases of SPOC wide-angle data.....	60
7.4	Seismic Data Processing.....	62
7.5	Modeling and velocity models.....	65
7.5.1	Velocity models in Northern Chile.....	65
7.5.2	Velocity models in Southern Chile.....	68
7.6	Kirchhoff prestack depth migration of CINCA wide-angle data.....	69
8	Results of wide-angle imaging using Kirchhoff prestack depth migration.....	73
8.1	Wide-angle imaging in northern Chile.....	75
8.1.1	Lines 201/202 at 21°S.....	75
8.1.2	Lines 301/302 at 22°S.....	79
8.1.3	Lines 401/402 at 23.25°S.....	82
8.1.4	Fresnel Volume Migration.....	85
8.1.5	Offset Analysis and RIS.....	87
8.1.6	Onshore data.....	93
8.2	Wide-angle imaging in southern Chile.....	95
8.2.1	Line SO161-038-amphibious profile.....	97
8.2.2	OBS/OBH profile.....	97
8.2.3	Onshore data.....	97
9	Interpretation.....	101
9.1	Erosive margin in northern Chile.....	101
9.1.1	Integration with other geophysical methods.....	106
9.2	Accretive margin in southern Chile.....	116
9.2.1	Integration with other geophysical methods.....	119
9.3	Summary: filling the gap.....	129

10	Summary and overview.....	135
	10.1 Erosive margin in northern Chile.....	136
	10.2 The accretive margin in southern Chile.....	137
	10.3 Geological cross section of the forearc.....	138
11	References.....	145
12	Acknowledgments.....	157

Figures

1.1	Compilation of KPSDM results at 21°S (after Buske et al. 2002). Left: the CRS image of CINCA near vertical reflection data. Middle: the Antofagasta aftershocks as derived by (Patzig et al. 2003). Right: the depth migrated image of the ANCORP profile.....	2
2.1	The main morphotectonic units in North Chile (modified after Scheuber et al. 1994) and CINCA wide-angle profiles.....	6
2.2	Convergence rate and convergence obliqueness between the Farallon/Nazca plate and the South American plate since the early Cretaceous. Major deformational regimes are also depicted after Scheuber et al. 1994).....	8
2.3	The main morphotectonic units in South Chile (after Melnick and Echtler, 2006) and the SPOC wide-angle profiles.....	11
2.4	Location of the erosive and accretive margin along the Chilean subduction zone. Thickness of the trench fill and convergence rates are denoted in yellow (from Lohrmann et al. 2006).....	13
3.1	Cross section at 21°15'S as derived by ray tracing methods (Wigger et al. 1994). Lines denote zones proven by ray vertices, indicating reliable parts of the model. Average P-wave velocity values are shown in km/s.....	16
3.2	Horizon migration results for the CINCA lines 201/202 at 21°S (Patzwahl, 1999). a) Starting velocity: 5.7 km /s and gradient: 0.025 (1/s); b) Starting velocity: 6 km/s and gradient: 0.035 (1/s). Red thick lines are the horizons picked from the CDP stacked section. Black thick lines are the migrated horizons.....	17
3.3	KPSDM sections of the CINCA-NVR profiles at 21°S (top) and 23.25°S (bottom) (Sick, 2005).....	19
3.4	KPSDM section of the ANCORP-NVR profile at 21°S (Yoon, 2005).....	20
3.5	KPSDM section of the PRECORP profile at 22.5°S (Yoon, 2005).....	21
3.6	KPSDM section of the TIPTEQ profile at 38.2 °S (Gross et al. 2007).....	23
4.1	Thermal and composition updip and downdip limits of the seismogenic coupling zone. Modified from Oleskevich et al. (1999).....	28
5.1	Common seismic phases recorded in wide-angle data experiments. The critical distance X_c defines the maximum amplitude zone on the record section. The distance X_d is an useful parameter to estimate crustal thickness. Modified from Giese et al. (1976).....	33

5.2	Reflection and transmission coefficients versus incidence angle for a downgoing SH-wave incident on the Moho. Modified from Shearer (2006).....	34
5.3	Relation between velocity contrasts and amplitude values for wide-angle data (after Meissner, 1967).....	35
5.4	Schematic velocity model with gradient zone and first order discontinuity at the Moho, theoretical traveltimes and amplitude curves of PmP arrivals. After Giese et al. (1976).....	36
6.1	2D Migration of one shot with wave equation based methods (after Simon, 1993). The wavefield is downward from the surface ($z=0$) until the diffraction point location at $z=z_0$ where the diffraction hyperbola collapses into one point.....	38
6.2	Kinematics of Kirchhoff prestack depth migration. After Simon et al. (1996).....	40
6.3	KPSDM and velocity errors. Top: migration with correct velocity values; middle: submigration; bottom: overmigration.....	41
6.4	Migration of an horizontal reflector without (left) and with (right) random noise.....	42
6.5	Migration and spatial aliasing. Using sparse trace sampling cause the introduction of aliased energy yielding artifacts that distort the migrated image.....	42
6.6	The tuning effect. Dependence of the resolution on the shape of the wavelet and frequency content. Modified from Brown (1991).....	44
6.7	Concept of Fresnel zone. Lower frequencies define broader Fresnel zones on the reflector. Modified from Brown (1991).....	45
6.8	Fresnel zone and migration. Migration causes a focusing effect on the seismic data by reducing the Fresnel zone. Modified from Lindsey (1989).....	47
6.9	Fresnel Volume Migration scheme from Buske et al. (2009).....	48
6.10	FVM validity of approximations. a): case of symmetric source and receiver locations and vanishing velocity contrast; b): case of dipping reflector and vanishing velocity contrast; c): case of symmetric source and receiver and non-vanishing velocity contrast. Modified from Buske et al. (2009).....	51
7.1	Location map of the CINCA wide-angle profiles.....	54
7.2	Location map of the SPOC wide-angle profiles.....	57
7.3	CINCA Lines 201/202 at 21°S. Receiver gather of station 2 with interpreted phases. Vertical axis is time reduced with 6 km/s.....	59

7.4	Shot gather of the onshore seismic profile at 21°S with interpreted phases. Vertical axis is time reduced with 6 km/s.....	59
7.5	SPOC Line SO161-038. Receiver gather of station 1 with interpreted phases. Vertical axis is time reduced with 8 km/s.....	60
7.6	SPOC Line SO161-038. Receiver gather of the OBS/OBH data with interpreted phases. Vertical axis is time reduced with 8 km/s.....	61
7.7	Shot gather of the onshore seismic profile at 38.2°S with interpreted phases. Vertical axis is time reduced with 6 km/s.....	61
7.8	Receiver gather of Line 201/202 at 21°S before (top) and after (bottom) application of the processing flow. Interpreted phases and typical noise are indicated.....	62
7.9	Processing flow.....	63
7.10	Spectral analysis of the interpreted phases of the CINCA wide-angle data. The dominant frequency of the whole dataset ranges between 6-8 Hz.....	64
7.11	Effects of the reverberations on the seismic record (modified after Shearer, 2006). The source-time function $s(t)$ produced by an airgun contains a series of bubble pulses yielded by pressure reverberation withing the water. When $s(t)$ is convolved with reflectivity series $r(t)$, a complex time series $w(t)$ is produced, in which the closely spaced reflectors are not easy to identify.....	64
7.12	Receiver gather before (left) and after (right) predictive deconvolution. Reverberations are attenuated and the interpretation of seismic phases becomes easier.....	65
7.13	CINCA Velocity model Lines 201/202 at 21°S as derived from iterative travelttime modeling. P-wave velocities are shown in km/s.....	67
7.14	CINCA Velocity model Lines 301/302 at 22.2°S as derived from iterative travelttime modeling. P-wave velocities are shown in km/s.....	67
7.15	CINCA Velocity model Lines 401/402 at 23.5°S as derived from iterative travelttime modeling. P-wave velocities are shown in km/s.....	68
7.16	SPOC Velocity model Line SO161-038 at 38.2°S as derived from iterative travelttime modeling. P-wave velocity values are shown in km/s.....	69
7.17	Computation of diffraction surfaces. First arrivals travelttime are calculated at the node of each cell for every source and receiver location. The summation of traveltimes for every receiver and the corresponding source satisfy the imaging condition $t_1 = t_s + t_R$	70
7.18	Wide-angle migration volume for Lines 201/202 at 21°S. The migration is performed from topography in a volume of 400 km in x-direction, 50 km in y-direction and 80 km in z-direction.....	72

8.1	Synthesis of wide-angle imaging in northern Chile. The results comprise the KPSDM of the amphibious and onshore data.....	74
8.2	CINCA Lines 201/202. KPSDM of the complete wavefield. Top: stacking according to the absolute value of the traces. Bottom: stacking by phase-consistent summation.....	76
8.3	CINCA Lines 201/202. KPSDM of the reflected wavefield stacked according to the absolute value of the traces. Refracted arrivals coming from the upper crust and uppermost mantle as well as S waves are removed before migration.....	77
8.4	CINCA Lines 201/202. KPSDM of PcP and PmP arrivals. Stacking by phase-consistent summation.....	78
8.5	CINCA Lines 301/302. KPSDM of the complete wavefield. Stacking according to the absolute value of the traces.....	80
8.6	CINCA Lines 301/302. KPSDM of PcP (top) and PmP (bottom) phases. Stacking according to the absolute value of the traces.....	81
8.7	CINCA Lines 401/402. KPSDM of the complete wavefield. Stacking by phase-consistent summation.....	83
8.8	CINCA Lines 401/402. KPSDM of PcP and PmP arrivals. Stacking by phase-consistent summation.....	84
8.9	KPSDM section at 21°S (top) and its counterpart FVM section (bottom). Stacking by phase-consistent summation.....	86
8.10	Offset analysis. The dataset was separated in three offsets ranges: near, intermediate and far offsets. Imaging of the near (top) and intermediate (bottom) offsets led to visualize major features in the continental crust as well as the oceanic Moho. Stacking according to the absolute value of the traces.....	88
8.11	Offset analysis at narrower offset ranges. Near offsets clearly image structures in the upper continental crust while the farthest offsets contribute with the imaging of the deeper features including the oceanic Moho. Stacking according to the absolute value of the traces.....	89
8.12	Reflection Image Spectroscopy (RIS) of the CINCA wide-angle data at 21°S. The dataset was band pass filtered in three frequency bands and each band was migrated separately. Stacking according to the absolute value of the traces.....	92
8.13	KPSDM of the CINCA onshore data at 21°S. Stacking by phase-consistent summation.....	94
8.14	Synthesis of imaging in southern Chile. The results comprise KPSDM of OBH/OBS data, amphibious and onshore data.....	96

8.15	SPOC Line SO161-038. KPSDM of the amphibious data stacked by phase-consistent summation. Refracted arrivals coming from the upper continental crust and uppermost mantle were removed before migration.....	98
8.16	SPOC Line SO161-038. KPSDM of OBS/OBH data stacked by phase-consistent summation. The migration involved crustal and PmP arrivals only.....	99
8.17	SPOC Line SO161-038. KPSDM of the onshore data stacked by phase-consistent summation.....	100
9.1	Free air and Bouguer anomaly map of North Chile (after Schmidt and Goetze, 2006).....	106
9.2	Overlay of the CINCA wide-angle KPSDM images with gravity results of Prezzi et al. (2009). Density values in Mg/m ³ are indicated. Top: KPSDM of onshore data; Bottom: KPSDM of the amphibious data.....	108
9.3	Overlay of CINCA wide-angle KPSDM images with magnetotelluric results at 21°S. Top: KPSDM of the onshore data; Bottom: KPSDM of the amphibious data.....	110
9.4	Overlay of CINCA wide-angle KPSDM results at 21° with isotherms (Springer, 1999) and hypocentre locations at ~19°30'S (Farías et al. 2005).....	113
9.5	Overlay of wide-angle KPSDM image at 23.25°S with Vp/Vs section (top) and seismic tomography (bottom) from Husen et al. (1999). Full color areas denote good resolution while fair resolution is shown in faded colors. The white star marks the hypocentre determination of the Antofagasta earthquake by NEIC.....	115
9.6	Free-air and Bouguer anomaly map of southern Chile (after Krawczyk et al. 2006).....	119
9.7	Overlay of SPOC wide-angle KPSDM images at 38.2°S with gravity results of Tašárová (2007). Top: KPSDM of amphibious data; bottom: KPSDM of onshore data. Density values are in Mg/m ³ indicated.....	121
9.8	Overlay of SPOC wide-angle KPSDM images with magnetotelluric results at 38.2°S from (Kapinos pers. comm., 2009). Top: KPSDM of onshore data; bottom: KPSDM of amphibious data.....	123
9.9	Overlay of SPOC wide-angle KPSDM images with hypocentre location and tomographic velocity model of (Haberland et al., 2009). Top: KPSDM of the amphibious data; bottom: KPSDM of the onshore data. Black star indicates the hypocentre of the 1960 earthquake (Engdahl and Villaseñor, 2002).....	125
9.10	Overlay of SPOC wide-angle KPSDM images and Vp/Vs section of (Haberland et al., 2006). Top: KPSDM of the onshore data; bottom: KPSDM of the amphibious data. Black star indicates location of the 1960 earthquake (Engdahl and Villaseñor, 2002).....	126

9.11	Overlay of SPOC wide-angle KPSDM results at 38.2° with isotherms (Kellner, 2007) and hypocentre locations (Haberland et al., 2009).....	128
9.12	Combination of KPSDM results at 21°S (modified after Buske et al. 2002 and Sick et al. 2006).....	131
9.13	Combination of KPSDM results at 38.2°S (modified after Krawczyk et al. 2006).....	133
10.1	Geological cross section of the forearc region in northern Chile as derived from migration of seismic data.....	140
10.2	Geological cross section of the forearc in southern Chile as derived from migration of seismic data.....	143

Tables

6.1	Threshold for vertical resolution of different seismic data recorded for crustal studies in northern Chile.....	44
6.2	Estimated radius of the Fresnel zone (R) for the CINCA wide-angle data. The radius (in km) was calculated at different depth levels using the lower and upper limits of the frequency content, the average crustal velocity and the velocity at the oceanic crust-mantle boundary.....	46
7.1	Summary of the acquisition parameters of the CINCA wide-angle profiles.....	55
7.2	Summary of the acquisition parameters of the SPOC wide-angle profiles included in this study.....	57
8.1	Frequency bands used for RIS analysis.....	90

1 Introduction

Wide-angle seismic data have been used to study the lithospheric structure of continents, oceans and their margins for more than 50 years. Provided its ability to record large amplitude signals beyond the critical angle, the wide-angle or wide-aperture experiments have been the most common method to determine the velocity structure of the crust and uppermost mantle. Crustal velocity models have been constructed worldwide by means forward and inversion techniques using first arrival information derived from wide-angle experiments. Nevertheless, due to the low pass filter effect of the ground, the frequency content of the wavefield recorded at larger offsets tends to be narrow. Thus the resolution power of wide-angle data is lower in comparison to the near vertical reflection data, whose broader frequency bandwidth including low and high frequencies are normally acquired to produce detailed structural images of the subsurface. Despite this “disadvantage” wide-angle experiments are largely carried out to study offshore-onshore transition zones using amphibious layouts, where marine air-gun shots are recorded in receiver stations deployed onshore. Onshore and offshore near vertical reflection data is acquired along profiles normally starting at the coast, leading to low coverage data below this area. The wide-angle amphibious layout allows the recording of information beneath the coast, allowing the possibility to produce a complete image of the subduction zone from the trench axis down to several kilometers depth.

Since January 1993, in the frame of the Collaborative Research Center (SFB 267) “Deformation Processes in the Andes”, several active and passive seismic projects have been conducted along the Chilean continental margin with the aim to understand the subduction orogeny of the Andes and related surface processes. The CINCA project was carried out in 1995 to study the structure and composition of the oceanic and continental crust in the area of the erosive convergence zone between 19°S and 26°S (Hinz et al. 1995). The scientific program included the recording of near vertical reflection data along three offshore profiles, the recording of amphibious data using the air-gun shots fired along the marine profiles as seismic source, and the acquisition of onshore data using chemical explosions as seismic energy. Data from the last two layouts were used for the construction of velocity cross sections using ray tracing/forward modeling methods (Patzwahl, 1999).

In 1996 the ANCORP project was carried out with the goal to image the subduction zone from the coast area toward the east along a 400 km long integrated seismic reflection/refraction profile across the Central Andes at 21°S.

Imaging methods, in particular Kirchhoff prestack depth migration (KPSDM) was applied to the near vertical reflection dataset of the CINCA and ANCORP projects in order to produce high resolution images of the erosive continental margin at 21°S (Buske et al. 2002). Kirchhoff prestack depth migration is considered the state-of-the-art approach to image

structures in complex geological settings provided its ability to accommodate irregular trace spacings and because it is a straightforward technique to implement (Audebert et al. 1997). The prestack depth migrated section of the CINCA near vertical reflection data shows the ocean floor dominated by horst-and-graben-like structures whose presence increase laterally toward the trench area (Sick et al. 2006). Also, several eastward dipping parallel active fault systems are visible above the subducted Nazca plate. East of the trench the subducted Nazca plate can be observed down to about 12-15 km depth .

On the other hand, the prestack migrated section of the ANCORP data shows a double reflection zone between 40-60 km depth, indicating the subducting Nazca plate. The downgoing slab is observed down to approximately 80-90 km depth, where it becomes less reflective maybe due to the complex structure of the reflector with depth and the influence of heterogeneities of the media on the seismic signal (e.g. the Quebrada-Blanca Bright Spot) (Yoon, 2005).

By combining the previous imaging results, the Nazca plate can be traced from the trench area down to 80-90 km depth. Information from hypocentre location derived from passive seismic studies of the CINCA project at 23°S completed the geometry of the oceanic slab in the offshore-onshore transition zone (Fig. 1.1). Similarly, in southern Chile, the subducting Nazca plate has been imaged through prestack depth migration applied to offshore near vertical reflection data of the SPOC project (Yoon, 2005) and the near vertical reflection data of the TIPTEQ profile (Gross et al. 2007). In this area, hypocentre location also completes the geometry of the downgoing plate in the transition zone.

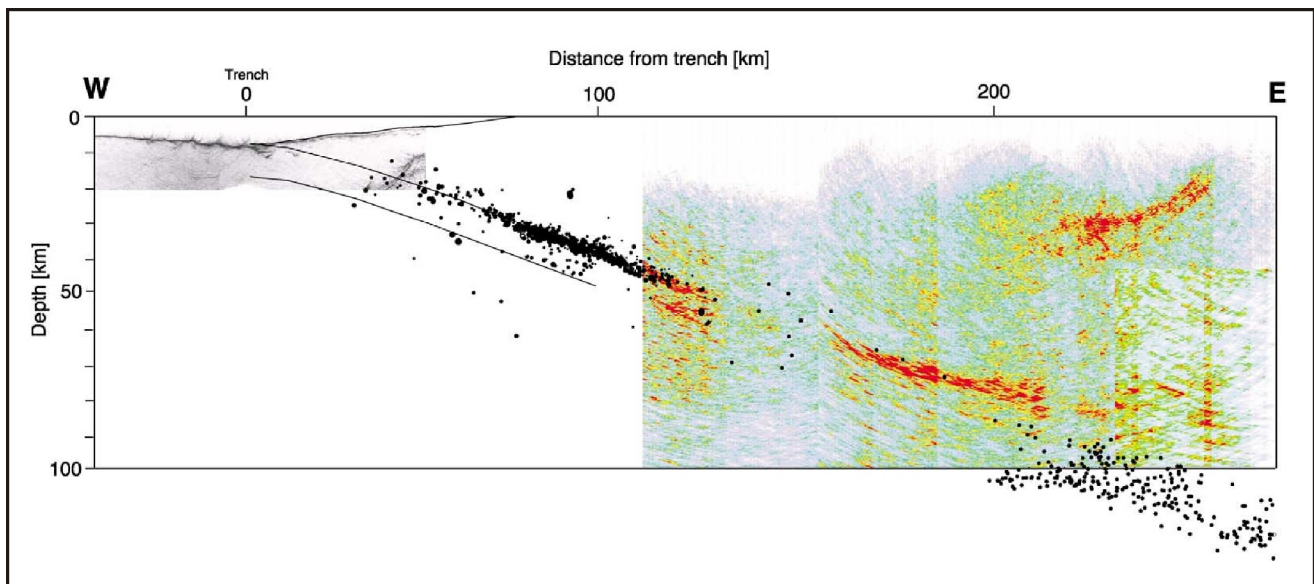


Figure 1.1: Compilation of KPSDM results at 21°S (after Buske et al. 2002). Left: the CRS image of CINCA near vertical reflection data. Middle: the Antofagasta aftershocks as derived by (Patzig et al. 2003). Right: the depth migrated image of the ANCORP profile.

The principal objective of the present thesis is to apply Kirchhoff prestack depth migration to the wide-angle dataset of the CINCA and SPOC projects in order to improve the understanding of the plate interaction in the seismogenic coupling zone and provide images of the offshore-onshore transition zone that have not been imaged before.

Further, Fresnel Volume Migration, a novel extension of Kirchhoff prestack depth migration was applied. In this approach the migration operator is restricted in a physically frequency dependent way to the region around the reflection point, leading to the attenuation of migration artifacts and the enhancement of image quality (Buske et al. 2009).

Additional analyses are also done to extract structural details of the recorded wavefield. These include the migration in narrow offset ranges in order to image structures at different depth levels. The so called Reflection Image Spectroscopy (RIS), based on the frequency dependence of scattering due to heterogeneities and its influence on the reflection image (Yoon et al. 2009) was also applied. The images show that the scattering produces phase changes and amplitude loss in a certain frequency band whereas its effects appears to be less severe in another band.

In Chapter 2 the geology and tectonic setting of the study area are summarized as well as the description of the types of convergent margins along the Chilean subduction zone. Chapter 3 presents a summary of the previous reflection/refraction seismic investigations in northern and southern Chile. In Chapter 4 an overview of the concept of the seismogenic coupling zone is given. Chapter 5 summarizes fundamentals about wide-angle seismic and the characteristics of the wavefield when it is recorded at critical angles. Fundamental theory about Kirchhoff prestack depth migration and Fresnel Volume Migration is introduced in Chapter 6. Chapter 7 comprises the description of the CINCA wide-angle data and the interpreted seismic phases. Also, in this chapter the processing flow applied to the data is schematically described as well as the Kirchhoff prestack depth migration approach applied in this study. The imaging results are presented in Chapter 8 and their interpretation and comparison with other geophysical methods are given in Chapter 9. To conclude, the summary and two geological cross sections derived from the seismic data in North and South Chile are presented in Chapter 10.

2 Geological setting

The Andes, as a part of the eastern Pacific convergence system, are located at the convergence zone between the oceanic Nazca plate and the South American plate, representing the largest active subduction controlled orogen on Earth with a length of about 7500 km extending across the continent from Colombia to southern Argentina.

2.1 The Central Andes

Between 16° to 28°S, the Central Andes form an about 800 km wide mountain belt between the Peru-Chile Trench in the west and the Chaco and Amazonia Basin in the east, developing mountain ranges with longitudinal segmentation with differences in topography, magmatism and geological evolution. In the Paleozoic started the interaction between the oceanic and continental plates in western Gondwana followed by two major orogenic cycles: the Paleozoic Preandean cycle and the post-Triassic Andean cycle (Giese et al. 1999) characterized by changes in the magmatic front positions and related tectonic processes.

During the Andean cycle, specifically since the Jurassic, the magmatic arc migrated eastward by about 200 km until its present location in the Western Cordillera (Scheuber et al. 1994). Thus, the modern forearc represents a region comprising areas characterized during long periods of the Mesozoic by backarc and then by arc settings.

The crustal structure of the Central Andes at the present results from the combination of different mechanisms including magmatic addition, crustal shortening, rigid and ductile deformation and thermal uplift in combination with shortening (Schmitz et al. 1999 and references therein). Specifically in the magmatic arc areas, the subduction obliqueness is the key for stress field variations and deformational regimes (e.g., orogen-normal shortening or extension and orogen-parallel strike-slip combined with plutonism and volcanism) occurring in the upper plate (Scheuber and Reutter, 1992).

Five geomorphological units and arc systems have been identified from the coast to the Puna Plateau comprising the forearc, magmatic arc and backarc regions (Reutter et al. 1988; Scheuber et al. 1994). Fig. 2.1 depicts the location of these units in the North of Chile.

Oceanic crust and the offshore forearc

The topography of the oceanic crust is characterized by horst and graben structures trending about 8° diagonal to the trench axis and also cut by a northwest-southeast diagonal trend parallel to magnetic anomalies (Hinz et al. 1995) of closely spaced fractures probably representing the original structure of the oceanic crust. Close to the trench this trend appears on horst and disappears in the next graben, covered probably by pelagic sediments (von Huene et al. 1999).

Miocene sediments cover the steep continental slope over a basement unit composed of Jurassic igneous rocks and Paleozoic metamorphics. von Huene et al. (1999) studied the bathymetry off Antofagasta and described the tectonic features of the northern Chile trench. They discussed these features from the upper slope, through the middle slope and ending in the trench axis, revealing the erosive character of the subduction zone in the region. The upper slope shows dip angles about 4° close to the coast and steepens seaward to 12° down to 3500-4000 m depth. It is characterized by canyons crossed locally by extensional faults and composed of relatively coherent crust. The middle slope is formed by series of segmented terraces 3-6 km deep which break the seaward descend of the upper slope with wide areas of gentle dip. Characterized by mass of debris, the lower slope presents the subducting horst and graben structures of the lower plate. Finally, in the trench area debris and thin continental sediments cover the topography of some grabens which have sufficient space to accommodate subduction of all the slope debris without building an accretionary prism.

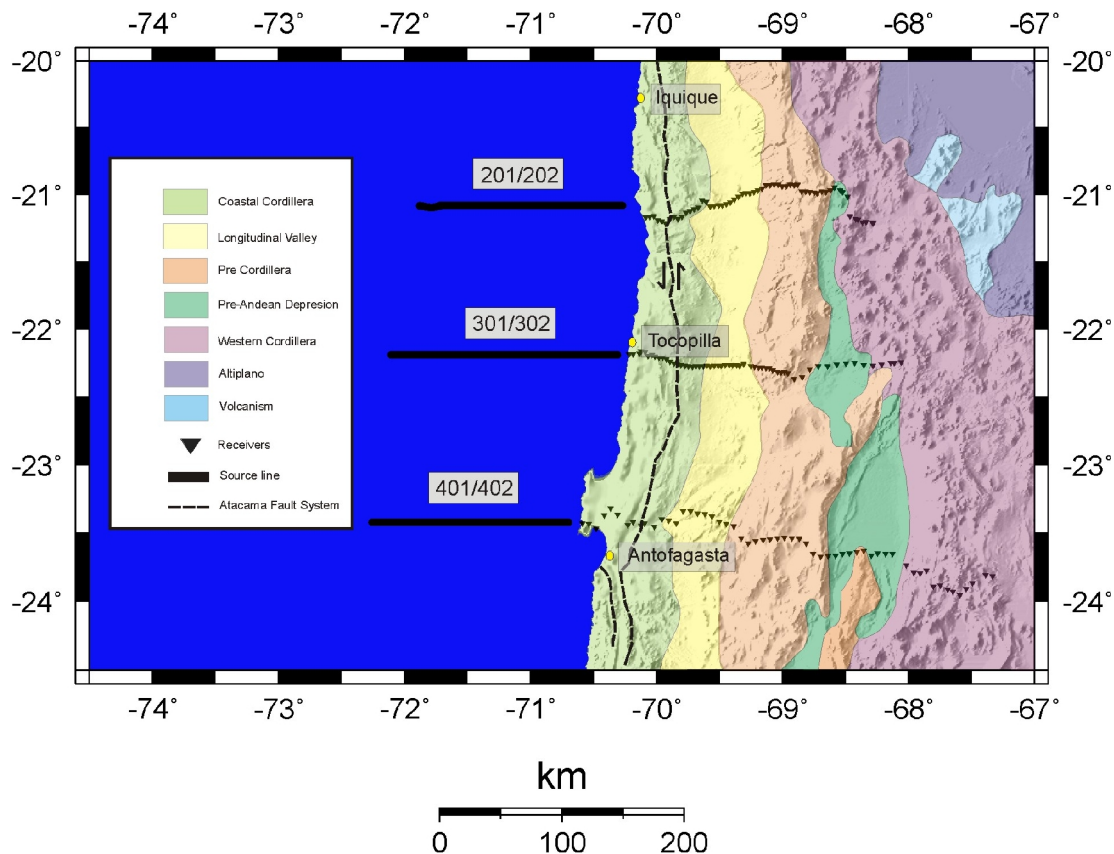


Figure 2.1: The main morphotectonic units in North Chile (modified after Scheuber et al. 1994) and CINCA wide-angle profiles.

Onshore forearc

The forearc comprises three morphological units that represent ancient magmatic arcs: the Coastal Cordillera, the Longitudinal Valley and the Precordillera. The Coastal Cordillera is an N-S oriented mountain range parallel to the coast that was the centre of the volcanic activity during the Jurassic-early Cretaceous. It is composed of lavas, plutons and andesitic to dacitic subvolcanic stocks and dykes with elevations around 2000 m (Scheuber et al. 1994) which started to erupt in a shallow marine basin that was subsiding since the Late Triassic and overlap Paleozoic sedimentary rocks, indicating a basement with continental characteristics.

Normal orogen extension and strikes-slip movements parallel to the arc as a product of an oblique subduction at angles between 45° - 90° (Scheuber and Reutter, 1992) at high convergence rates and or high degree of plate coupling define the main tectonic activity during this period. The Atacama Fault System, an orogen parallel sinistral strike-slip fault that has been traced over more than 1000 km (in the range of 20° S- 30° S) is considered the most important structural feature of the Coastal Cordillera formed as a result of the oblique convergence.

The magmatic activity during the Jurassic-earlier Cretaceous was also subject to orogen-normal extension indicated by:

- the presence of mafic to felsic dykes parallel to the orogen dipping at high angles between 60° - 90° .
- mantle-derived plutonic rocks (gabbros and granodiorities) without continental crust material contamination indicating crustal thinning and that the original continental crust has been replaced by this mantle material.
- the assumption of crustal subsidence to explain the non existence of high mountain ranges in spite of the great production of volcanic material.

The Longitudinal Valley, a depression with mean elevations of 1000 m, is part of the magmatic arc characterized by Paleozoic-early Cretaceous sediments and volcanic rocks intruded by mid-Cretaceous plutonics. The centre of magmatic activity was emplaced eastward under extensional tectonic regimes within the subsiding basin in the back-arc of the Jurassic-early Cretaceous arc (Scheuber and Reutter, 1992). Strong orogen-normal shortening led to intense folding during the last stage of the magmatic arc. This change in tectonic regime was the product of changes in plate configuration in the South east Pacific during the Late Cretaceous (110-70 Ma) when the Aluk-South America convergence (very high angle of sinistral convergence obliqueness) changed to the Farallon-South America convergence (smaller convergence obliqueness and dextral).

Fig. 2.2 depicts the convergence rate (cm/a) and convergence obliqueness between the Farallon/Nazca plate and the South American plate since the early Cretaceous (Scheuber et al. 1994 and references therein).

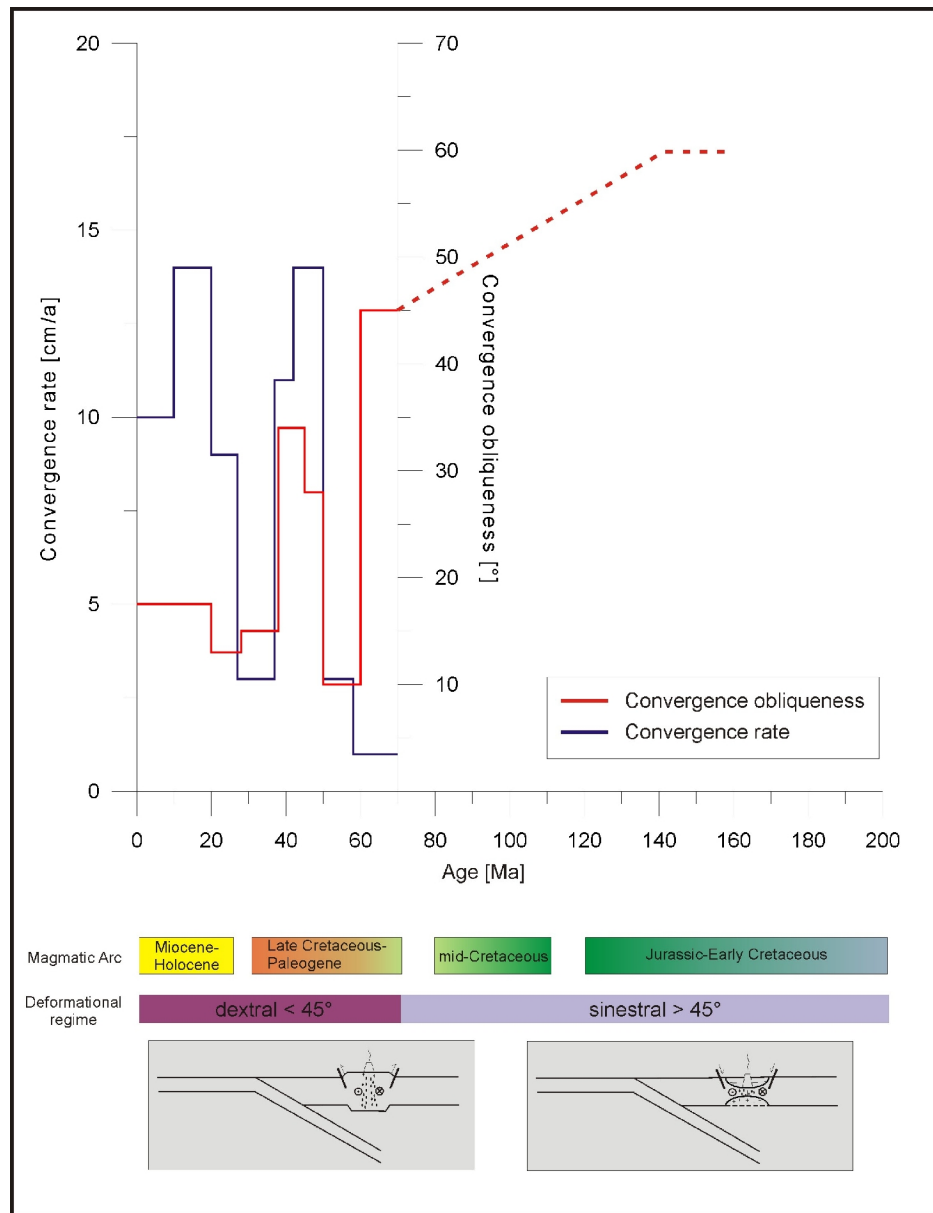


Figure 2.2: Convergence rate and convergence obliqueness between the Farallon/Nazca plate and the South American plate since the early Cretaceous. Major deformational regimes are also depicted (after Scheuber et al. 1994).

The Chilean Precordillera, whose topography is characterized by elevations between 2000-4000 m is mainly composed by sediments above plutonic and metamorphic rocks and represents the late Cretaceous-late Eocene part of the magmatic arc.

N-S striking faults originated as trench linked strike-slip faults contemporary with magmatism in the different magmatic arcs cut the forearc crust (Scheuber and Giese, 1999). These fault systems are represented by the West Fissure Fault in the Precordillera.

Magmatic arc

The modern magmatic arc is located since the Oligocene in the Western Cordillera. Characterized by transpressional structures and a volcanoes chain with more than 6000 m high, this area is composed by andesitic lavas and dacitic ignimbrites above Triassic plutonic and volcanic rocks.

Backarc

The backarc is composed of Paleozoic-Cenozoic sediments which have been suffering contractional deformation since the Oligocene, leading to the thrusting of the Andes over the Brazilian shield. In the backarc area the eastern part of the Altiplano, the Eastern Cordillera, the Interandean Zone, the Subandean belt and the Chaco are located (Scheuber and Giese, 1999). The latter forms the foreland of the Andean orogen. The Altiplano represents a 3700 m mean elevation plateau conformed by marine and lacustrine sediments uplifted during the late Cretaceous.

2.2 The Southern-Central Andes

The forearc region

The coastal ranges of the southern Andes are located over a Paleozoic basement with low metamorphism grade and deformation consisting mainly of slates, greenstones and turbiditic sequences (Herve, 1994). This complex was intruded during the Jurassic-Neogene by the North Patagonian Batholith (NPB) forming a backarc basin eastward filled with marine sediments and volcanic sequences. During the Mesozoic-Cenozoic the subduction of the oceanic plate beneath the continental plate yielded a magmatic arc developed above the Paleozoic complex.

The Liquiñe-Ofqui Fault Zone (LOFZ) is a dextral strike-slip structure with N-S trending originated as a product of oblique subduction of the Nazca Plate or from the indenter effect of the Chile ridge at the southern termination of the fault zone. The LOFZ has been active since the Eocene controlling the access of magma to upper levels in the crust. Additionally, the LOFZ which separates the forearc and magmatic arc, absorbed most of the strain developed in the edge of the margining thus the generation of a backarc fold-and-thrust belt was inhibited (Herve, 1994).

Another important tectonic feature of the Arauco-Lonquimay segment is the Lanalhue fault zone (LFZ), a NW-SE trending shear zone that defines the contact between Western and Eastern series of the accretionary complex with the late Paleozoic coastal batholith.

Based on geophysical and geological data compilation, the southern Andes between 36°-42°S have been divided into nine morphological units (Hackney et al. 2006 and references therein), which are shown in Fig. 2.3.

The coastal platform, the Coastal Cordillera and Central Valley conform the forearc region. The coastal platform presents low altitudes and consists of 20-50 km wide late Cretaceous to Quaternary marine and continental uplifted shelf deposits.

The Coastal Cordillera is a mountain range with maximum elevations about 1500 m in the Cordillera de Nahuelbuta (38°S) and an extension between 10-100 km which includes a Permo-Triassic accretionary complex and a Permo-Carboniferous magmatic arc.

The Permo-Triassic accretionary complex comprises the Western series, mainly conformed by metagraywackes, metabasites, metapelites and other oceanic rocks that show high grade metamorphism. North of 38°S, rocks of the Eastern series also compose the accretionary complex, represented by metagraywackes that underwent lower grade metamorphism and are associated to the late Paleozoic arc granitoids.

The Carbo-Permian magmatic arc represents a phase of granitoid magmatism developed along the western margin of Gondwana which forms a batholith whose composition points out

to a major recycling of continental crust by the late Paleozoic magmatism (Lucassen et al. 2004).

Further to the east, the Central Valley (also referred as Longitudinal Valley or Central Depression), extended from few kilometers up to 100 km width in the study area, comprises Pliocene and Quaternary sediments deposited on Oligocene-Miocene volcano-sedimentary basins.

The magmatic and backarc region

With elevations up to 2700 m, the Principal Cordillera comprises the southern volcanic arc that coincides with the axis of a long lived magmatic arc built since the Jurassic (Hackney et al. 2006 and references therein). In the area, Pliocene-recent volcanic complexes outcrop while southward roots of the magmatic arc are exposed due to glacial erosion and transpressional tectonics. Subduction related magmatism occurring since the Jurassic is expressed through most of the intrusions between 36°-42°S whose age were estimated as late Cretaceous-late Tertiary.

The backarc area, located east of the Principal Cordillera, is characterized by a gentle plateau-like morphology.

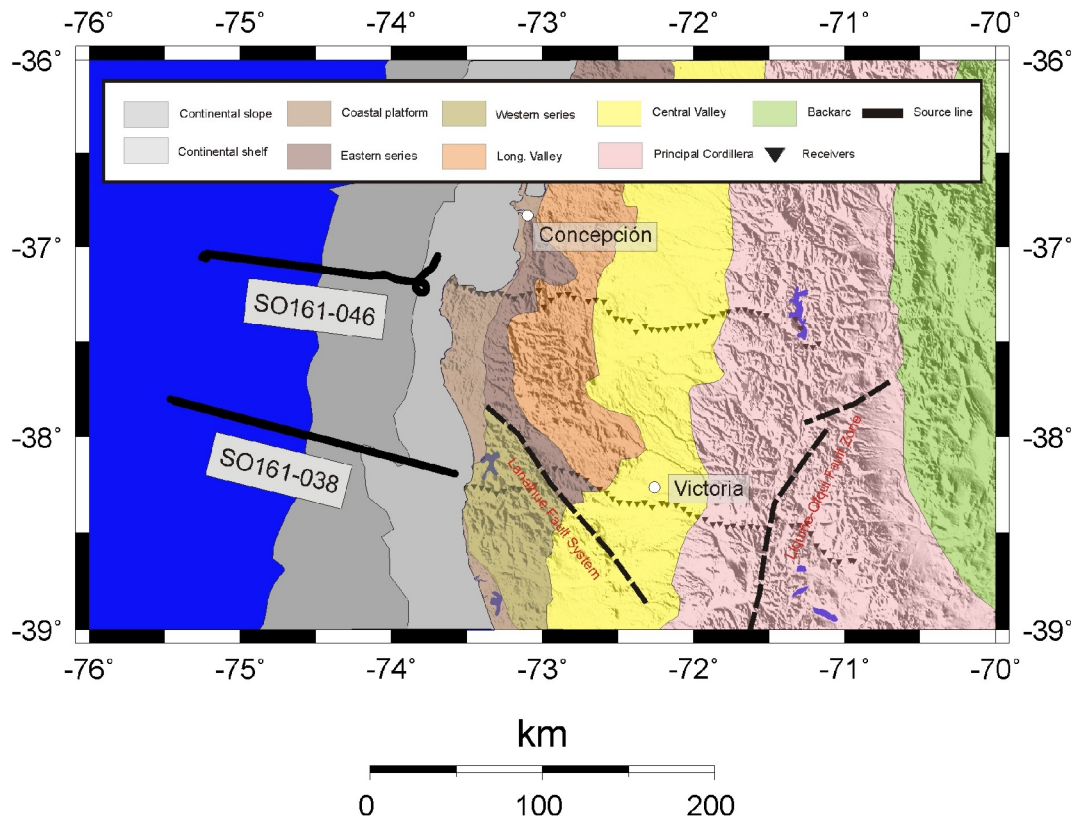


Figure 2.3: The main morphotectonic units in South Chile (after Melnick and Echtler, 2006) and the SPOC wide-angle profiles.

2.3 Accretionary and erosive margins

The forearc area in a subduction zone can be distinguished as those that grow up and widen by addition of material along the trench and those which do not. The amount of sediments being subducted represents a key factor. If the sediment supply is high enough, sediments are scrapped off the subducting slab and transferred to the upper plate forming an accretionary prism (Stern, 2002).

Accretionary forearcs build up in areas near the continents where the sediment supply is high. The dominant process in the construction of accretionary forearcs is the frontal accretion whereby the downgoing slab scrapped off sediments form an accretionary wedge or prism. The accretionary wedge comprises arcward dipping thrust-bound packets, normally high deformed, whose emplacement ages become younger toward the trench.

Underplating of material through the subduction channels is a process associated with subduction zones with high sedimentation rates which leads to the formation of thickener forearcs and the formation of basins between the accretionary wedge and the magmatic arc. On the other hand, erosive or nonaccretionary forearcs are characterized to have poorly developed forearc basins and build up in areas where the sediment supply is low. In the erosive forearcs the accretionary wedge is missing what leads to outcrop the igneous continental crust. The dominant process in the formation of erosive forearcs is the material remotion through subducting or tectonic erosion. Here, two processes are involved: a) basal accretion, in which upper crust material is scrapped off and b) frontal erosion, in which upper crust material is slumped into the trench. Basal accretion is carried through the scrapping off the base of the forearc by roughened seafloor consisting of horst-and-graben structures as a product of slab bending between the forearc bulge and the trench. Frontal erosion is inferred from disrupted topography at the base of the inner trench wall (Stern, 2002).

Along the Chilean subduction zone the above mentioned forearc types have been recognized (Fig. 2.4). In our study area, in particular, the forearc between 21°-24°S is considered as erosive whereas between 36°-39°S is cataloged as accretive.

Two main factors control the tectonic processes and evolution of the arc/forearc in the more than 3500 km long Chilean continental margin (Ranero et al. 2006): variations in the sediment supply and the topographic features of the subducting slab. The first is related to the climate variations from the arid Atacama region in the north to glacial conditions in the south. Erosion in the forearc and arc regions is controlled by climatic conditions, what influence at the same time the amount of sediments carried to the trench. In the north of Chile where the precipitation rates are low, small amounts of eroded material are deposited in forearc basins. Additionally, few rivers flow in the area and the trench axis lacks of turbidites. This is not the case for South-Central Chile, where the precipitation rates are higher and many rivers run across the forearc and arc areas, supplying great amounts of sediments to the trench. The second factor controlling the tectonic processes in the Chilean margin involves features on the Nazca plate that influence the tectonics in the collision area with the continent and

divide the trench axis into several segments where the thickness of the trench sediments varies. In northern Chile, the Juan Fernandez Ridge represents a seamount chain that collided with the Chile margin in the late Oligocene and moved southwards to the present collision zone between 32°-33°S. South of 40°S, the Chile Rise is an active spreading center trending NW that collides the continent at 46°S at low angle and represents the limit between the Nazca plate to the north and the Antarctic plate to the south.

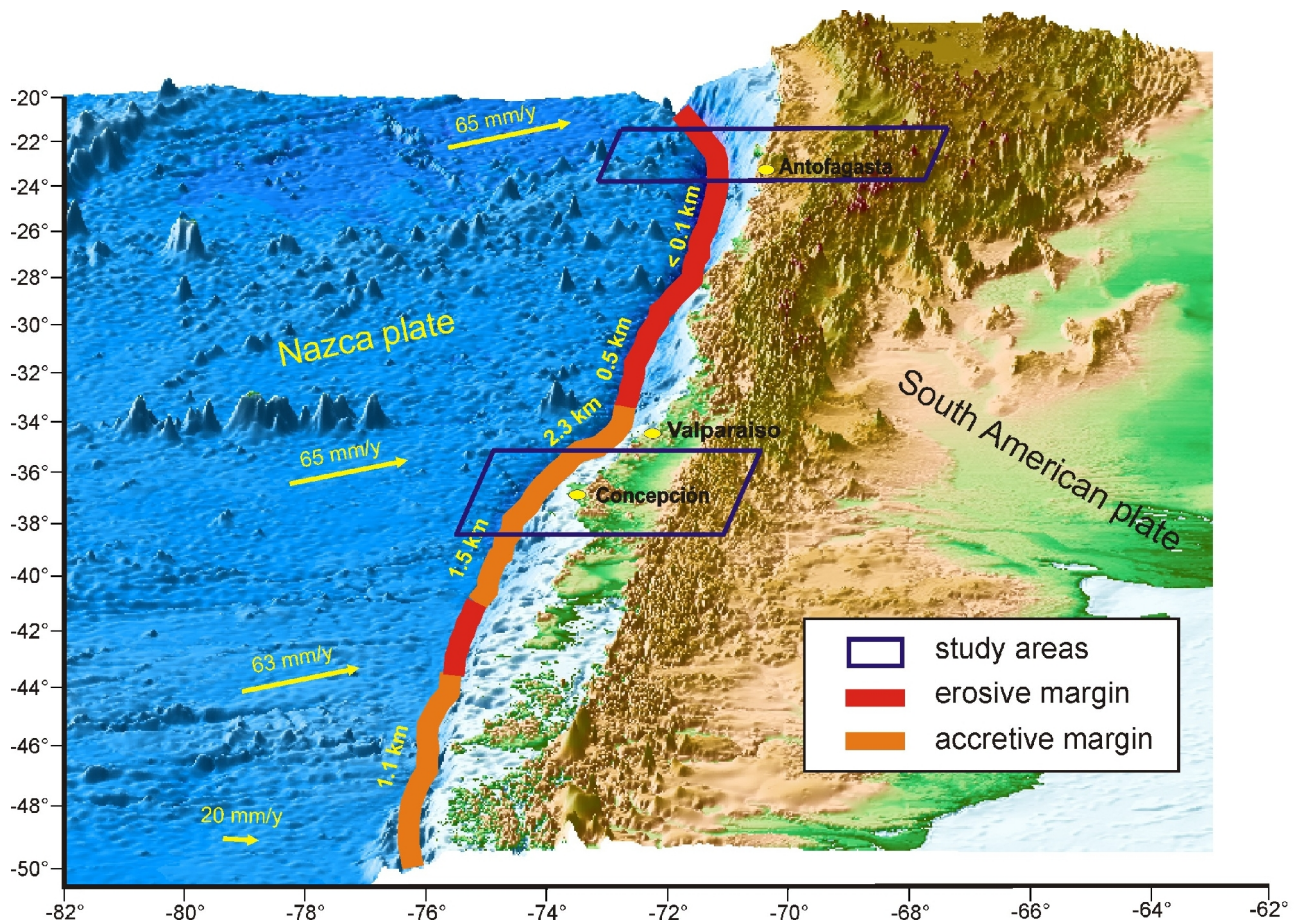


Figure 2.4: Location of the erosive and accretive margin along the Chilean subduction zone. Thickness of the trench fill and convergence rates are denoted in yellow (from Lohrmann et al. 2006).

Seismic offshore investigations in the northern and southern Chilean margin resolved details about the ocean bottom topography, the sedimentary cover, trench geometry and the structure of the oceanic plate and continental slope (Sick et al. 2006).

In the area between 21°-24°S the seafloor is characterized by horst-and graben structures on both sides of the lacking in sediments trench axis. Also, reflections parallel to the subduction

plane are imaged up to 5 km above the slab at the lower continental slope. These structures correlate with escarpments at the ocean bottom suggesting eastward underthrusting of material forming the frontal prism. Material slumped from the middle slope and upper plate toward the trench conforms the frontal prism (Lohrmann et al. 2006). A low angle detachment occurring at 7 km depth in the middle slope comprises several normal faults that are tilted, indicating the gravitational mass flux that supply sediments to the frontal prism.

The geometry of the erosive forearcs in northern Chile have been recognized by von Huene and Ranero (2003) to be strongly influenced by the morphology of the incoming plate. Horst-and-graben structures and seamounts enable frontal erosion and indicate strong coupling between the oceanic and continental plates. Also, basal tectonic erosion takes place beneath the coast and the frontally and basally eroded material is dragged down through the subduction channel. The subducted material and those covering the graben structures contains considerable amounts of fluid that may migrated into the plate interface.

Between 36°-39°S the scenario is very different. In contrast to the northern forearc, the morphology of the seafloor is very smooth. The trench is filled with ~3 km thick Quaternary terrigenous sediment that reflect periodicity and the oceanic crust shows a thin cover of pelagic sediments (<200 m). The upper part of the incoming sediments is frontally accreted to the tip of the upper plate while the lower part is being subducted (up to 70%) (Lohrmann et al. 2006).

3 Previous active seismic experiments in northern and southern Chilean Andes

3.1 Imaging in the Central Andes

Wide-angle/refraction experiments

Lithospheric studies in the Andes started in the 50's and 60's led by the Carnegie Group during the "International Geophysical Year" using the copper mine blasts in Toquepala and Chuquicamata as energy source to study the crustal structure of the Central Andes (Tatel and Tuve, 1958). These were the first wide-angle experiments reported in the area. The estimated crustal thickness was 56 km below the Precordillera and 70 km beneath the Bolivian Altiplano with an average P-wave velocity of 6.6 km/s.

During the period 1982-1984 the Berlin Research Group "Mobility of Active Continental Margins" carried out wide-angle seismic measurements in the north of Chile and south of Bolivia (Wigger, 1986, 1988). They reported a discontinuity interpreted as a Jurassic Paleo-Moho at 30 km depth and crustal thickness of 40 km approximately below the Precordillera.

In 1987 and 1989 deep refraction profiles over the main morphostructural units from the coast to the Andean foreland were acquired with the aim to study the crustal structure of the region (Wigger et al. 1994). More than 7000 km of seismic lines were recorded using the blast of the Chuquicamata copper mine as well as off-onshore chemical explosions. The results are compiled in the W-E section at 21°15'S shown in Fig. 3.1. Three main crustal types were interpreted along the profile based on the average velocity values: in the forearc region the crust was characterized as rigid; between the Western Cordillera and the Altiplano the crust was considered as ductile while in the Eastern Cordillera-El Chaco range was again interpreted as rigid.

In the forearc region, the east dipping 20 km thick upper crust presents high velocities of 7.2-7.4 km/s and was interpreted as the former Jurassic arc and backarc crust of the continental margin. The lower crust, estimated to be in the range of 20-30 km depth and characterized by alternation of high and low velocities, is considered a mixture of continental and mantle material. Some tectonic processes were proposed to explain the origin of the lower crust and its reduction of P-wave velocity: 1) the serpentinization of the uppermost mantle by the introduction of water from the subducting oceanic slab. 2) the assumption that the Jurassic arc was built upon a continental crust with the forearc located further west to the actual position. Considering the 300 km distance between the trench and the magmatic arc at the present, this interpretation proposes the consumption of the old forearc by tectonic erosion. 3) magmatic addition and 4) a combination of processes. Finally, the oceanic Moho was

estimated at 40 km depth approximately below the Coastal Cordillera.

The structure below the arc region and the Altiplano is characterized by the reduction of the average velocity and the distribution of low velocity zones that suggest zones of partial melting or magma chambers. The crust-mantle boundary was estimated at 70 km depth below the western Altiplano. After correlating the LVZ and zones of high conductivity, the upper crust (40 km thick) is related to the Jurassic continental crust and the lower part to the actual Cenozoic lower crust (Wigger et al. 1994).

The continental crust in the backarc region is folded and overthrust in its foreland. Some discontinuities between 25-30 km depth define the base of the lower continental crust which were previously located further west. The total crustal thickness reduces from 70 km under the Altiplano to 40 km at the Andean foreland.

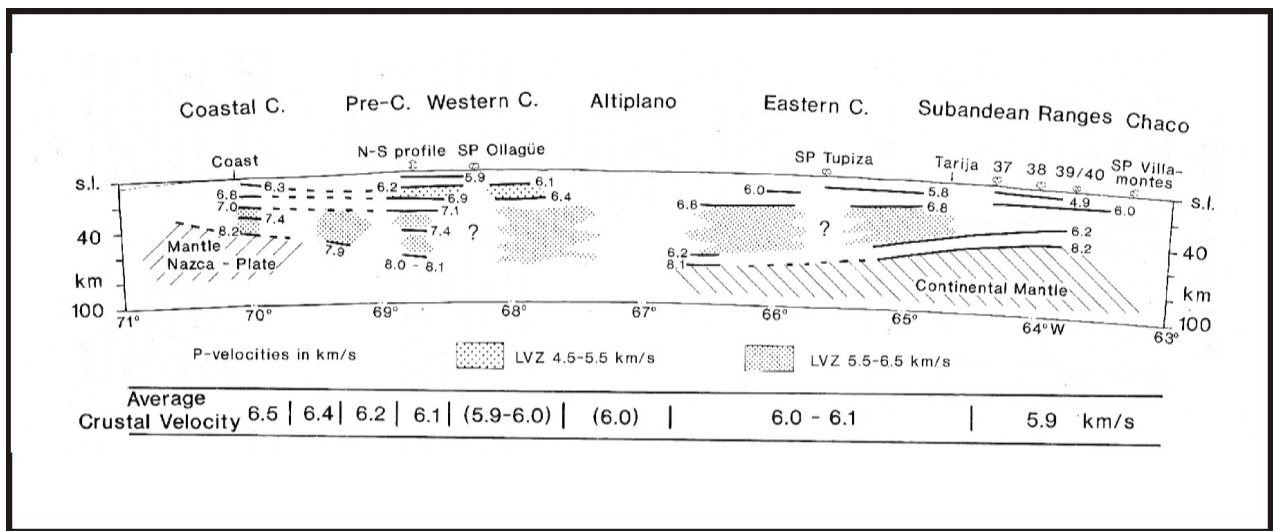


Figure 3.1: Cross section at 21°15'S as derived by ray tracing methods (Wigger et al. 1994). Lines denote zones proven by ray vertices, indicating reliable parts of the model. Average P-wave velocity values are shown in km/s.

In the frame of the Collaborative Research Center (SFB 267) seismic experiments have been performed with the objective to image the plate convergence in the Chilean subduction zone, and to get an insight of the geometry of the seismogenic plate interface, the mode of mass transfer and the internal structure of the Wadati-Benioff-Zone (WBZ).

The PISCO project was carried out in 1994 along two N-S profiles at 68°W and 69°W (Lessel, 1997; Schmitz et al. 1999). In the derived crustal structure models the upper-lower continental crust limit is defined by an east dipping boundary at about 20 km depth. The crust-mantle boundary was estimated at approximately 65-70 km depth below the Precordillera.

In 1996 the ANCORP project was performed along a profile at 21°S including near-vertical and wide-angle observations (ANCORP Working Group, 2003). From the latter a 360 km

long (from the coast to the Bolivian Altiplano) P-wave velocity model was derived. Under the Longitudinal Valley and above the oceanic crust a geophysical Moho was modeled at 55 km depth indicating the transition from the lower continental crust to an hydrated mantle wedge. The oceanic Moho was estimated at about 55-60 km depth below the Coastal Cordillera. Further east, beneath the Western Cordillera, a LVZ (5.0-5.5 km/s) is observed in the range of 15-20 km depth, while below the Altiplano Plateau observed lower P-wave values were modeled as thick sedimentary structures. In general, the average P-wave values decrease in W-E direction.

Horizon migration of the CINCA wide-angle data.

Patzwahl (1999) applied a simple migration approach based on the horizon migration described by Yilmaz (2001). A wide-angle CDP stacked section was generated using a stacking velocity of 7 km/s. From this section horizons at different depths were extracted and converted to depth using a standard velocity value of 3 km/s. P-wave velocity values derived from ray tracing/forward modeling were not used in the migration approach. Instead, two parameters were used: the starting velocity and the velocity gradient. Several tests were conducted until results that best fit the velocity model were produced. Fig 3.2 shows the horizon migration of the CINCA wide-angle data for different starting velocity and velocity gradient values. Here, the gray lines denote the horizons as extracted from the stacked section and converted to depth, and the black lines mark their migrated counterparts.

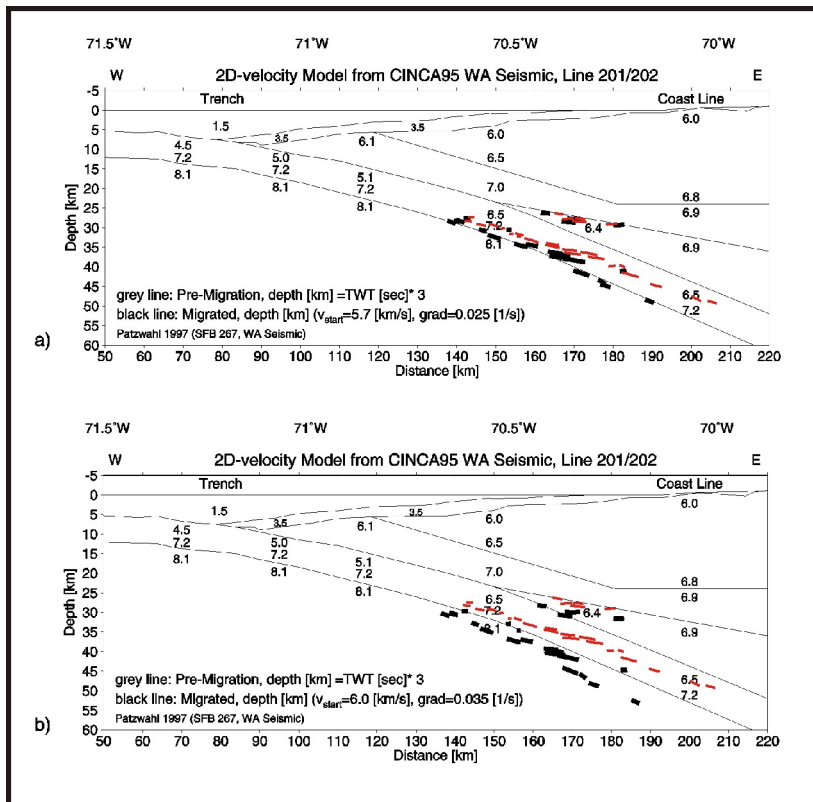


Figure 3.2: Horizon migration results for the CINCA lines 201/202 at 21°S (Patzwahl, 1999). a) Starting velocity: 5.7 km/s and gradient: 0.025 (1/s); b) Starting velocity: 6 km/s and gradient: 0.035 (1/s). Red thick lines are the horizons picked from the CDP stacked section. Black thick lines are the migrated horizons.

Imaging of near vertical reflection data-offshore/onshore

In the framework of the CINCA and ANCORP projects near-vertical reflection (NVR) data was also recorded. Sick (2005) presents the results of the application of Kirchhoff prestack depth migration to two offshore profiles at 21°S (profile SO104-07) and 23.25°S (profile SO104-13) acquired within the CINCA project and shown in Fig. 3.3. In the upper section corresponding to the profile at 21°S the following features can be identified:

- a) The trench is clearly imaged at 74 km distance.
- b) West of the trench, at 25 km distance, starts a horst-and-graben-like system prolonged to the trench area.
- c) East of the trench the subducted Nazca plate can be observed down to about 12 km depth.
- d) A subducted horst-and-graben-like structure is shown at 82 km distance and 8.5 km depth.
- e) Further west, in the range of 80-95 km distance, an eastward dipping parallel fault system can be observed.

Similar structures can be visualized in the profile SO104-13 at 23.25°S (Fig. 3.3):

- a) The trench is imaged at 68 km distance.
- b) Compared to the northern section, the horst-and-graben-like system starting at 10 km distance is more pronounced, with horst flanks up to 1000 m high.
- c) The oceanic Moho is visualized at 12-15 km depth west of the trench in the range of 40-55 km distance.
- d) The subducted Nazca plate can be traced up to 15 km depth east of the trench.
- e) Subducted horst-like structures are also visible east of the trench at 9-10 km depth.
- f) East of the trench, a series of parallel reflectors is visible down to about 10 km depth. These reflectors parallel to the subducted slab are interpreted as active thrusts operating at lower rates and define the upper part of the subduction channel where sedimentary material coming from different levels of the continental slope is being underthrust (Sick et al. 2006).

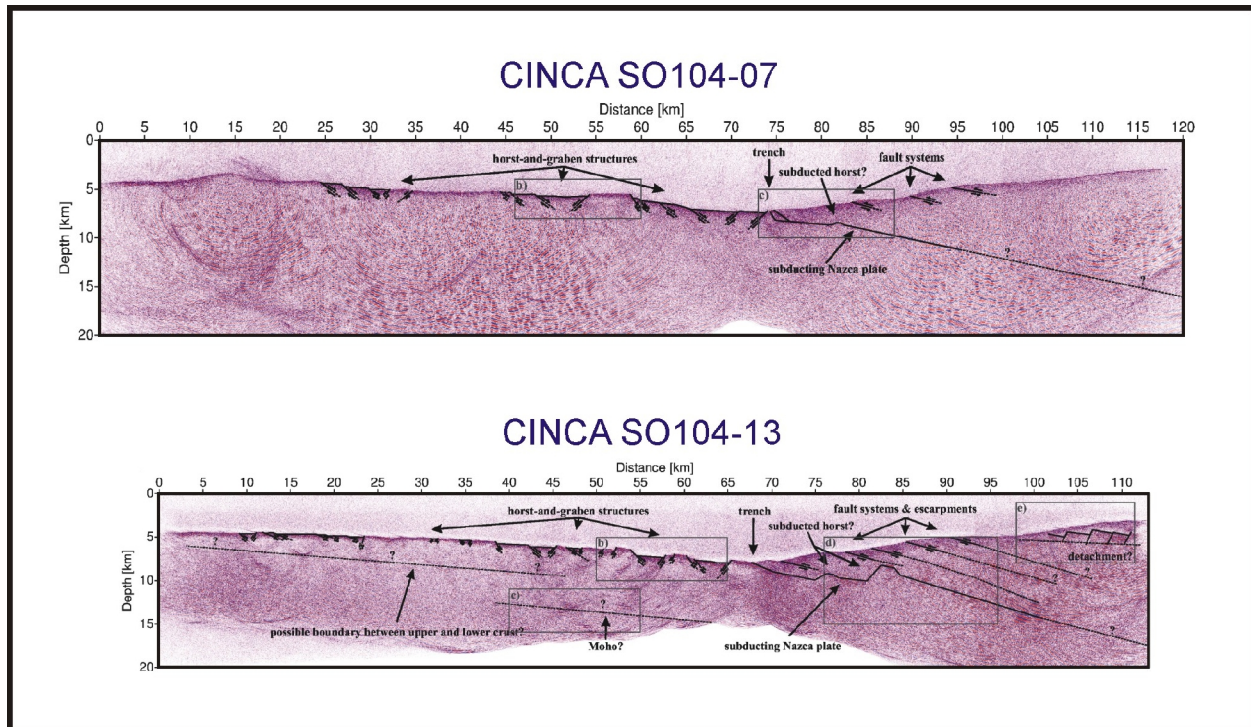


Figure 3.3: KPSDM sections of the CINCA-NVR profiles at 21°S (top) and 23.25°S (bottom) (Sick, 2005)

Kirchhoff prestack depth migration was also applied to the onshore NVR data recorded within the ANCORP and PRECORP projects with the aim to obtain images from deep crustal structures and the subducting Nazca plate.

In the ANCORP section shown in Fig. 3.4 (Yoon, 2005) two parallel east dipping strong reflectors appear under the Coastal Cordillera. The upper one starting at 40 km depth was interpreted as the Nazca reflector and can be traced down to 80-90 km depth approximately where it becomes weaker and unclear maybe due to the complex structure of the reflector with depth and the influence of the heterogeneities of the media on the seismic signal. On the other hand, the second reflector starting at 50 km depth interpreted as the lower boundary of the subducting oceanic crust, can not be observed down to 80 km depth as clear as the upper reflector. Hypocenters of local earthquakes are plotted on to the section (ANCORP Working Group, 1999; Patzig, 2000). Below 80 km depth an offset of 10 km approximately exists between the Nazca reflector and the hypocenters whose top seems to be aligned along some weak reflectors segment. If the Nazca reflector defines the upper boundary of the oceanic slab, these weak reflectors possibly mark the lower boundary of the oceanic crust (Buske et al. 2002), meaning that the subducting plate is 7-8 km thick.

These results are in agreement with the crustal models derived from the CINCA wide-angle data (Patzwahl, 1999). At 115-160 km distance along the section appears the Quebrada Blanca Bright Spot (QBBS), a west-dipping reflector that has also a northward dipping component as determined from the 3D analysis of the migrated section.

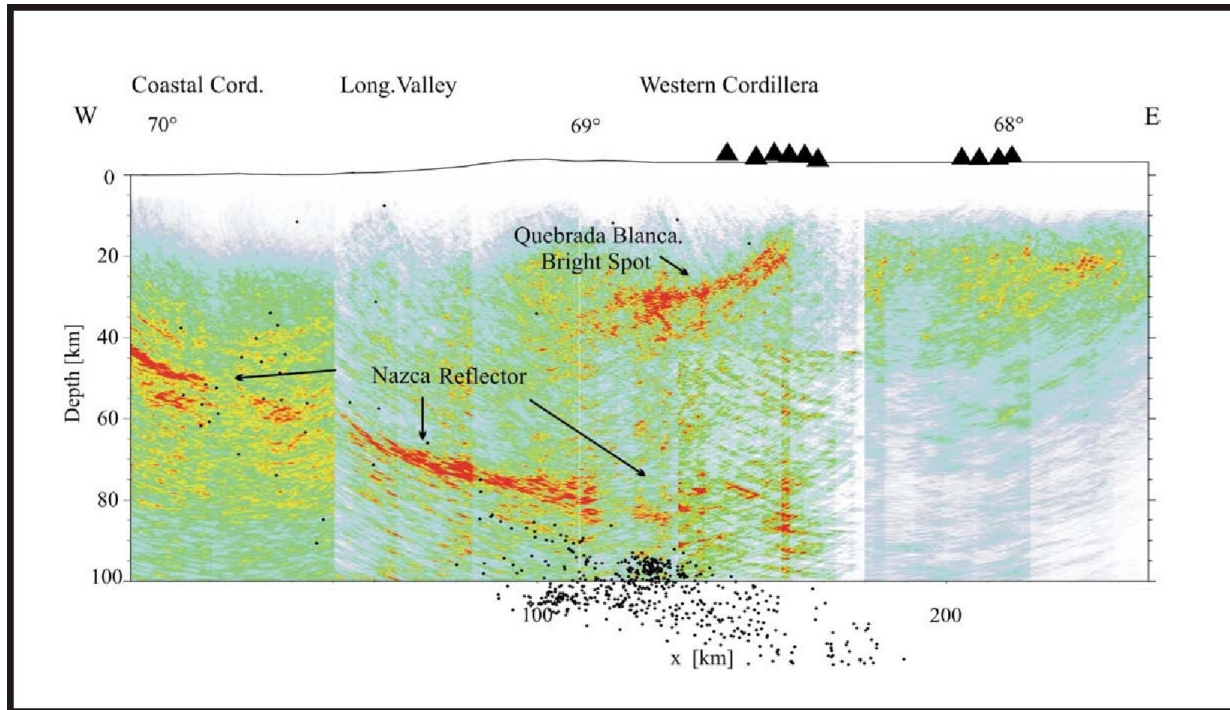


Figure 3.4: KPSDM section of the ANCORP-NVR profile at 21°S (Yoon, 2005).

In the migrated section of the PRECORP data (Fig. 3.5) the upper boundary of the oceanic plate is associated to a reflector segment located at 65 km depth and 50-60 km distance. Due to the short profile length the reflector can only be observed along the section in the range of 95-125 km where it is visible at 80-85 km depth. The Calama Bright Spot (CBS) is also visible at 15-25 km depth but it is not clear whether its lateral extension is real because of the limited recording geometry (Yoon, 2005).

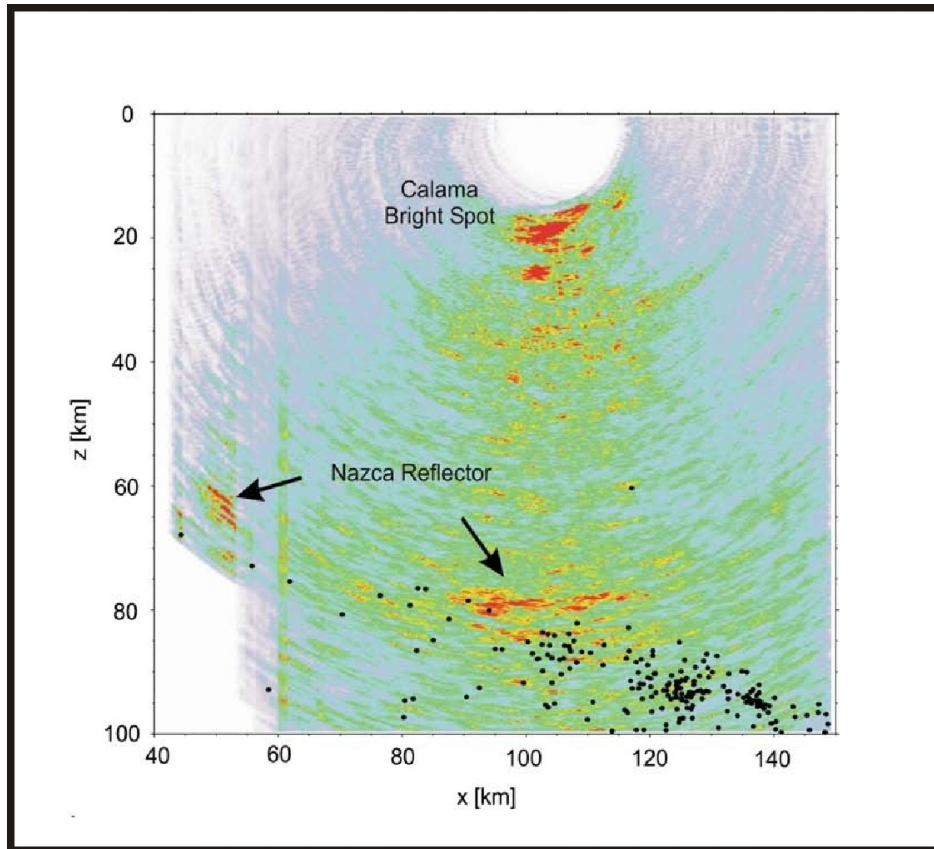


Figure 3.5: KPSDM section of the PRECORP profile at 22.5°S (Yoon, 2005).

3.2 Imaging in southern Chile

Wide-angle experiments in southern Chile

Within the ISSA and SPOC projects the most recent wide-angle measurements were performed. The ISSA project was carried out at 39°S along a 320 km long profile consisting of 65 stations with an average spacing of 4-5 km. Five chemical explosions were used as an energy source, one located in the Main Cordillera and four in the Pacific Ocean (Lüth et al. 2003).

The 2D P-wave velocity derived from ray tracing/forward modeling shows the upper-lower crust limit at 15 km depth under the Coastal Cordillera and 10 km depth beneath the magmatic arc. The average velocity increases eastward from 6.1 to 6.4 km/s. The lower crust characterized by P-wave velocities larger than 6.5 km/s thickens from 10 to 20 km from the forearc to arc region. Below the Coastal Cordillera the oceanic Moho was estimated at 55 km depth. A wedge shaped structure with P-wave velocities in the range of 6.9-7.2 km/s occurs between the lower continental crust and the subducting slab. In spite of the fact that the upper boundary of this layer is not directly represented by a determined arrival in the data, this inversion zone can be attributed to the continental mantle in its eastern part, but this consideration can not be taken in the western part because the P-wave velocity appears to be lower than typical for mantle material.

Imaging of near vertical reflection data-offshore/onshore

With the aim to provide high resolution subsurface images of the trench with sedimentary fill, the shelf slope and the shallow water area, migration methods (pre-poststack as well time and depth) were applied to the offshore reflection data recorded along three profiles in the framework of the SPOC project. The data was acquired offshore by a 3000 m long streamer with 132 channel separated 50 m (Rauch, 2004). The final images show the terrigenous sediments in the trench area affected by folding and faulting. In two of the three processed lines a significant periodicity of the reflections can be observed. These effect can be related to the distance from the sediment source. Due to the northward dipping of the sea floor the terrigenous sediments are transported through the canyons and deposited in the trench by turbidites. In the case of the lines showing periodicity, the sediments are transported along short distances from the source (Bio-Bio and Imperial/Tolten fans) whereas the line missing periodicity, the sediments travel distances larger than 100 km.

Within the TIPTEQ project a 95.5 km long NVR profile was recorded with the goal to study and identify structural properties in the seismogenic coupling zone of the Central Andes at 38.2°S (Gross et al. 2007). Explosive shots were fired every 1.5 km along the profile and the signals were recorded by three component receivers deployed every 100 metres.

Imaging methods were applied to the data including Kirchhoff prestack depth migration and poststack time migration. Fig. 3.6 shows the KPSDM final section. Below the coast an east

dipping reflector occurs at 25 km depth which can be traced down to 50 km depth below the Central Valley after a non reflective zone between 30-50 km along the profile. The bottom of this reflectivity zone is interpreted as the upper boundary of the subduction channel. Predominantly horizontal structures can be seen in the range 50-90 km distance. The origin of the sharp reflector located at depths of 42-45 km is attributed dehydration processes. A clear continental crust-mantle boundary has not been observed in the data. The reflective region between 60-90 km distance shows horizontal structures that can be associated to the continental Moho. The highest position at 25 km depth would coincide with receiver function investigations carried out at 39°S (Yuan, 2006).

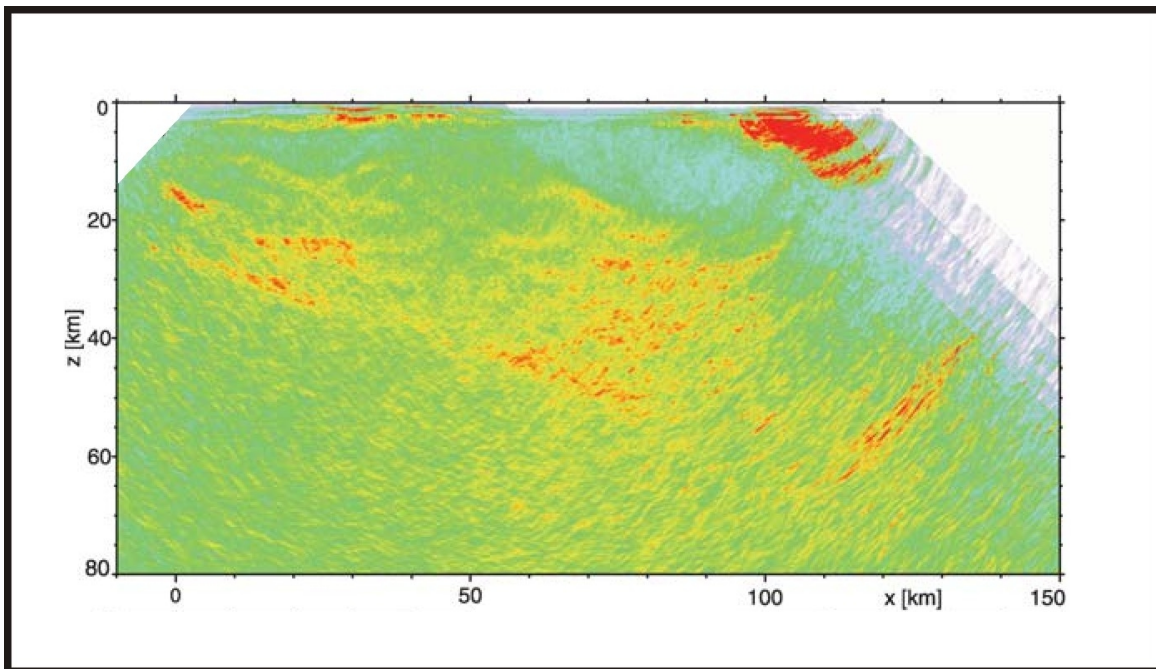


Figure 3.6: KPSDM section of the TIPTEQ profile at 38.2 °S (Gross et al. 2007).

4 The Seismogenic coupling zone

Subduction zones and continental-continental collision zones are the two types of convergent boundaries, the first ones represent around 90% of the world's convergent boundaries at zones of oceanic-oceanic or continental-continental convergence (Lay and Wallace, 1995). The convergence mechanism consists in the underthrusting of the one plate beneath another. The subducting plate is colder and more dense than the surrounding media in the asthenosphere and this effect forces it to descend. How a subducting plate descends is a process that depends on the age of the subduction zone, the age of the lithosphere and the convergence rate.

In a subduction zone three types of seismic activity occurs: a) the interaction between the converging plates, b) the internal deformation of the overriding plate and c) the internal deformation within the descending slab. In the first type, interplate seismicity is the result of the large interaction zone with frictional sliding between the two plates. The internal deformation of the overriding plate is related to back-arc extension or upper-plate compression. Finally, the subducted plate is internally deformed due to the interaction with the surrounding upper mantle.

The coupling zone is the interface between the overriding continental and subducting oceanic plate where large earthquakes ($M > 7$) are generated. It is characterized by a dipping, relatively narrow (100-200 km wide) and shallow (< 50 km depth) zone that produces earthquakes via stick-slip sliding (Dixon and Moore, 2007, and references therein). The term stick-slip is associated to the stress and strain accumulation during interseismic periods released in a catastrophic manner.

4.1 Characteristics of coupling zones

Mechanism

Coupling zones are characterized to show unstable frictional slip, meaning that slip acceleration takes place when the frictional strength decreases as a product of a slip velocity increase. On the other hand, aseismic regions along the plate interface, located normally shallower or deeper than the coupling zones, are though be dominated by stable frictional slip i.e., the frictional strength increases as slip velocity increases (Dixon and Moore, 2007, and references therein). Therefore, great earthquakes are more likely to occur along the seismic portion than the aseismic portion of the plate interface.

Seismic coupling and its variations

It has been shown that the earthquake magnitude increases with fault rupture area. Hence, earthquake magnitudes $M \sim 9$ have seismic ruptures covering areas about 100 km downdip and 1000 km along strikes, like the Valdivia 1960 or Sumatra 2004 earthquakes, while the seismic behavior of smaller events (magnitudes $M \sim 7$) occur in small patches with few tens of kilometers across.

The term seismic coupling usually refers to the fraction of the plate convergence rate at a subduction zone that is accommodated in thrust events. Another definition implies the fraction of relative convergence motion that is placed seismically over a defined downdip fault width (also known as seismic efficiency). The rest of the plate convergence is accommodated by aseismic motion, i.e., aseismic transient slip or slow slip events. It is important to mention that part of the plate convergence can be also accommodated by crustal shortening in the backarc or forearc regions.

Three factors have been proposed to be responsible for the variation in seismic coupling (Dixon and Moore, 2007, and references therein): the seismogenic fault area, the stress state and the frictional conditions.

The seismogenic fault area is normally wide at subduction zones with great earthquakes while are narrow in zones where only small thrust events occur. In both cases, within the downdip width, the thrust is complete or partially coupled. The downdip limit of the coupled zone has been defined from passive seismic data analysis as the maximum depth at which the greatest events occur, so that the maximum magnitude decreases with decreasing downdip width.

The stress regime also has influence on the variations in the downdip location of the seismic coupling zone. It has been proposed that small maximum earthquake magnitudes are associated mainly to island arcs, where extension is the dominant stress regime. Since the fact that forearc crust in island arcs is thin, large earthquakes can occur at shallower levels. In the case of continental subduction, where the dominant stress regime is compressional, the largest earthquakes occur at deeper levels because the large thickness of the continental crust.

The force required for rupture or frictional state cause also variations in the seismic coupling. Great and infrequent earthquakes in subduction zones are though to occur in margins where the incoming plates have smooth surface or where there are accretionary prisms. The sediments from the accretionary prism may smooth the plane interface so that stress concentrations are minimal and strain can build up to large ruptures ($M > 9$). This is not the case for convergence margins with rough subducting plate interfaces. Here, the irregularities caused by seamounts and fracture zones yield low stress concentration that lead to smaller and frequent thrust events ($M < 8$).

Updip and downdip limits

The updip and downdip limits of the coupling zone have been constrained by structural and thermal analysis as well as by the localization of great earthquakes and aftershock series. Their location define the transitions between velocity weakening (seismic) and velocity strengthening (stable sliding).

Byrne et al. (1988) proposed the contact zone between the thrust and the accretionary prism as the updip limit of the rupture zone. Provided the aseismic behavior of this tens of kilometers wide zone, the seismogenic coupling zone should start landward of the thrust contact with the backstop or overriding continental crust of the forearc region. The accreted sediments are generally unconsolidated and might have little strength to support elastic strain buildup. Nevertheless, great earthquakes have occurred at or near the base of large accretionary prisms in continental subduction zones (Cascadia and Alaska).

The intersection of the subduction thrust and the hydrated forearc Moho has been defined by some authors as the downdip limit of the seismogenic zone (Ruff and Tichelaar, 1996; Oleskevich et al. 1999). Below this intersection, the forearc mantle rocks are serpentinitized and due to the weak layered structure of the serpentinite a seismic behavior is unlikely generated. Additionally, amounts of talc from dehydration (rise of silica-rich fluids) of the subducting oceanic crust are also thought to produce an aseismic behavior in this region provided its weak layered mineral structure (Dixon and Moore, 2007, and references therein).

Dehydration of stable sliding clays is a temperature control mechanism that has been proposed to define the updip limit of the coupling zone (Oleskevich et al. 1999). Stable sliding smectite and other sort of clays are usually found in accretion prisms and their presence along the plate interface may be linked to shearing process in the thrust fault itself. Due to the increase of temperature with depth smectite clays dehydrate to illite and chlorite which may have velocity weakening behavior. The temperature at which this transformation take places is in the range of 100°-150°C (Fig. 4.1).

From temperature models analysis, Oleskevich et al. (1999) suggested that the downdip limit of the coupling zone is controlled at 350°-450°C. Laboratory analyses in crustal rocks have shown that above 450°C a rapid increase in instantaneous shear stress exists, whereas at higher temperatures there is plastic flow meaning a change from brittle to ductile behavior (Fig. 4.1).

5 Fundamentals in seismic wide-angle data

Since the 60's wide-angle seismic methods have been the key to fill the gap between near vertical reflection (NVR) and refraction measurements, in particular for deep crustal investigations. Nevertheless, its low resolution power (compared to NVR data) makes this method a complementary tool in Lithosphere exploration projects. The main advantage of the wide-angle measurements is that many discontinuities in the upper and lower crust are nearly first order interfaces which generate considerable reflection coefficients in the region around the critical angle.

5.1 Development of wide-angle investigations for exploration of the Lithosphere

The first deep seismic sounding was carried out by G.A. Gamburtsev in 1948 in the Caucasus. These studies were extended to northern Tien-Shan, western Turkmenia and the Pamir-Alai area (Kosminskaya, 1971). The main object of these projects was to record first arrivals coming from the Moho (previously observed in earthquake seismology) by using profile lengths up to 400 km. At that time, segmented profiles were used leading to a poor resolution due to the incompleteness of the data that constraint its full evaluation.

During the middle of the 50's the acquisition schemes were improved by using continuous profiling in regions with different tectonic features. According to Kosminskaya (1971) a new stage of development started with a marine version of deep seismic profiling in the old Soviet Union to be used in the study of continental margins, oceanic deeps and island arcs.

At present, the development in acquisition systems have enabled the recording of long geometries in 2D and 3D deep seismic surveys. The most common ways to record wide-angle data in marine and transition domains are:

- Airgun shots recorded at seismometers deployed on the sea-floor.
- Airgun shots recorded at seismometers deployed on the sea-floor.
- Airgun shots recorded at longer hydrophon streamers.
- The use of two vessels sailing at long offsets.

Onland, the acquisition of wide-angle data to image the deep lithosphere has been improved by the use of multicomponent receivers and the use of Vibroseis® as an alternative seismic source.

5.2 Characteristics of the wide-angle data

The product of seismic velocities and densities as well as the incidence angle determine the reflection and refraction coefficients. The velocity values in the subsurface generally increase with depth and critical refractions at diverse angles can be generated. Aki and Richards (2002) classified the reflection coefficients in two groups: the precritical regime where the reflection angles are smaller than the critical angle and the postcritical regime in which large reflections are produced at larger angles than the critical angle.

The acquisition geometry is perhaps the most relevant difference between NVR and wide-angle methods. The acquisition parameters not only define the recording logistic but also the wavefield recorded, the methods applied to image the structures in the subsurface and the meaning and resolution of the final image (Levander et al. 2007). The maximum offset between source S and receiver R positions with respect to the target depth z_{max} is a simple relation used to distinguish the way the waves propagate through the subsurface in both acquisition methods. In NVR measurements, the final images are defined by reflections or back-scattered wavefields where the waves travel longer vertical than horizontal distances. The relation that describes this phenomenon produced in the precritical regime is:

$$\max((S-R)/z_{max}) \leq 1 \quad (5.1)$$

On the other hand, in wide-angle experiments, the wavefield travels longer horizontal than vertical distances and the wavefield propagation takes place in the postcritical regime:

$$\max((S-R)/z_{max}) > 1 \quad (5.2)$$

The typical recorded wavefield includes first arrival refractions and large amplitude-postcritical reflections. In fact, one of the benefits of recording data at large offsets is that the amplitudes of wide-angle reflections increase toward the critical angle, meaning that at large offsets (large incidence angles) reflections have larger amplitudes than short offsets reflections (small incidence angles). If wide-angle reflections are the first arrival, the absence of earlier signal generated noise means that the signal to noise ratio of these reflections is larger than the near offset reflection coming from the same interface which arrives after shallower reflections.

Construction of velocity models is another benefit of wide-angle data. The seismic velocity control that can be obtained from large offset arrivals is better than that derived from short offset hyperbolic move-out, providing an effective imaging of deep arrivals from crustal or mantle structures. Wavefields traveling long distances carry more information about the velocity distribution than those propagating shorter distances. That means that incorporating information from other seismic phases, like refracted waves and head waves, can be very beneficial in constraining the velocity model. The inclusion of refracted waves supply information about the velocity gradient from the near surface to their maximum penetration depth.

Concerning the reflected events, at longer offsets they show clearer hyperbolic move-out, which enables the picking of these phases with confidence on the record section.

In media where the velocity increases with depth, the first arriving energy at any offset is always a primary event. In the case of marine deep profiling, the contamination of the wide-angle record sections with multiples coming from the sea surface and the sea-floor is reduced because these kind of events have lower moveout velocity, arriving considerably later at the receivers (Fliedner and White, 2003).

Another basic distinction between NVR and wide-angle methods is the frequency content of the recorded wavefield that defines the resolution of the structural images. Typical frequency bands for NVR data includes frequency ranges between 8-60 Hz while wide-angle methods produce signals with lower frequency ranges, normally between 1-20 Hz (Levander et al. 2007). Due to the absorption of high frequencies along the longer trajectories and the convergence of arrivals in time with offset, the resolution power of wide-angle data is not comparable to the resolution power of NVR data. This difference in frequencies makes the NVR method the most convenient approach to produce high resolution structural images of the subsurface, while wide-angle measurements have been used to locate the most prominent structures and to build lower resolution velocity models.

5.3 Typical wide-angle arrivals and some basic interpretation parameters

Due to the above mentioned inherent characteristics of the wide-angle measurements, the interpretation and correlation of wave trains on recorded sections is more difficult compared to those performed in NVR sections. The curvature of the travel time curves influenced by the velocity gradient (dv/dz) plays an important role in the interpretation of the recorded signals. There are two cases: positive and negative velocity gradients (Giese et al. 1976).

Within the case of positive velocity gradient, other possibilities can also be considered:

- $dv/dz=0$. This is the case of constant velocity layers. Reflections arise from the top and bottom of the layer and the head waves are generated at the top of the layer. A constant velocity layer is characterized by a linear travelttime curve.
- $0 < dv/dz < \infty$. In this case the layer has an arbitrary velocity gradient. Rays penetrate within the layer except in the case where the same velocity interval is already present in overlying layers. Every depth interval has one ray. In the case of arbitrary positive velocity layer for refractions, the typical travelttime curves present convex and concave curvature with respect to the distance axis. Weak velocity gradients produce travelttime curves with convex curvature, while in the case of strong velocity contrast retrograde or reversed travelttime curves with concave curvature are generated.
- $dv/dz=\infty$. In this case we are in the presence of a discontinuity. Since the same depth is related with different velocity intervals, more than one ray is reaching the same depth, therefore the resulting travel time curve contains different points

associated with the same depth. Typical traveltimes curves for reflections in a infinite velocity gradient medium are those with concave curvature.

On the other hand, negative velocity gradients or inversion zones cause lacking of information in traveltimes curves since no refracted rays can penetrate. Therefore, no information from this velocity area is available on the record sections.

In most of deep seismic exploration studies at least three main wave groups are generally correlated, whose position and move out depend on the velocity distribution in the subsurface. These wave groups are (Fig. 5.1):

- Refraction waves coming from the upper crust. Known as the Pg phase, this wave group characterized by linear move out represents the observable first arrival up to 100 km distance.
- Reflection on the crust-mantle boundary called PmP. They are the essence of the wide-angle experiments since from those the continental or oceanic crustal thickness is estimated.
- The Pn group, which represent refracted waves from the uppermost mantle, are the signals recorded at the longest offsets.

The critical point x_c is defined as the distance in a record section where the reflection time equals the refracted time and it is also characterized by a maximum of amplitude. Thus the critical point represent the region where the propagating wavefield reach the critical angle. Beyond the critical point, the hyperbolic move-out of the reflections is clearly distinguished from the linear move-out of the head waves corresponding to the same boundary.

The relationship between x_c and the depth z can be used for crustal thickness estimation in a homogeneous crust through the following expression (Giese et al. 1976):

$$z = (x_c/2) * ctg(i) \quad (5.3)$$

where $\sin(i) = v_0/v_1$; v_0 is the crustal velocity and v_1 is the uppermost mantle velocity.

The intersection between the Pn and Pg traveltimes curves x_d is another useful basic parameter to estimate, in a first approximation, the crustal thickness. Provided that Pg phases are not observable beyond 100 km distance, it is difficult to define the intersection between the two refracted phases. In some cases is better to use the average crustal velocity (6 km/s) as a mean Pg curve. For a homogeneous crust with velocity v_0 and an uppermost mantle with constant velocity v_1 , the following expression describes the linear relationship between the cross-over distance x_d and the crustal thickness z :

$$z = (x_d/2) * \sqrt{((v_1 - v_0)/(v_1 + v_0))} \quad (5.4)$$

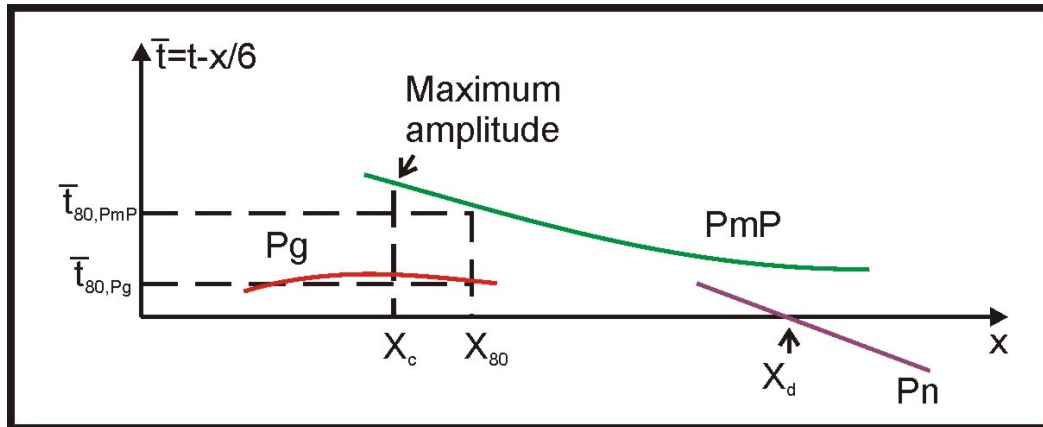


Figure 5.1: Common seismic phases recorded in wide-angle data experiments. The critical distance X_c defines the maximum amplitude zone on the record section and represent an useful parameter to estimate crustal thickness. Modified from Giese et al. (1976)

5.4 Wide-angle Migration

In spite of its low resolution, imaging methods have been applied to wide-angle data to produce images of the deep lithosphere in different tectonic settings or to combine them with those obtained by migration of NVR data (e.g. Mueller et al. 2001; Fliedner and White, 2003).

Different wave equation based algorithms have been used, including Kirchhoff approach (Milkereit, 1987; Holbrook, et al. 1992, Lafond and Levander, 1995; Simon et al. 1996; Van Avendonk, 2004, Fujie et al. 2006), finite difference methods (Thornton and Zhou, 2008) and frequency-wavenumber algorithms (Lizarralde and Holbrook, 1997).

From the characteristics mentioned above, migration of wide-angle data leads to high amplitude images not affected by arrivals from the overlying section as in the case of near offset data at same depth, owing to the fact that the arrivals at larger offsets are strong near the critical angle and the slower arrivals from shallower regions arrive later in the seismic traces.

The most significant benefit of wide-angle migration is that apart from the primary modelled phases other wavelength-scale structures are imaged from individual arrivals that have not been interpreted, picked and modelled in velocity model construction. However, the resolution of wide-angle migrated sections is lower due to the absorption effect and amplitude loss affecting the wavefield during its propagation along longer horizontal and vertical trajectories typical in long offsets experiments.

Particularly, prestack depth migration is a suitable tool to image wide-angle data because of its versatility to accommodate non-hyperbolic moveout effects corresponding to reflected energy that propagates in complex velocity media along wavepaths (Colombo, 2005).

5.5 Energy partitioning at wide-angle incidence

Amplitudes of the vertical ground motion are larger in the critical angle region than in the near vertical region, including amplitudes coming from deeper boundaries with small velocity contrasts (Meissner, 1967).

Zoeppritz' equations describe the amplitude of the reflected and refracted waves at a plane interface for an incident P-wave. The energy partitioning can be analysed as a function of the angle of incidence for determined values of parameters: incident P, SH, SV wave, P wave velocity ratio, density ratio and S wave velocity (Sheriff and Geldart, 1995).

Reflection and transmissions coefficients versus ray angle for a downgoing SH-wave incident on the Moho were studied by Shearer (2006).

Here, the Moho interface is represented by a velocity transition zone from 3.9 km/s to 4.49 km/s. The results are plotted in Fig. 5.2.

In the near vertical incidence region ($\theta=0$) the transmitted and reflected SH-waves show amplitude values as expected by the impedance change. At low angles ($\theta < 30^\circ$) the transmitted and reflected amplitude values change slightly and are still similar to those in the near vertical incidence region. At larger angles the ray incidence becomes more horizontal and the amplitude for transmitted waves increases while the reflected amplitude is approximately zero. At $\theta=49^\circ$, the transmitted amplitude is one and reflected amplitude is zero. Even though the waves propagate through a zone with significant changes in acoustic impedance, reflected waves are generated at this angle.

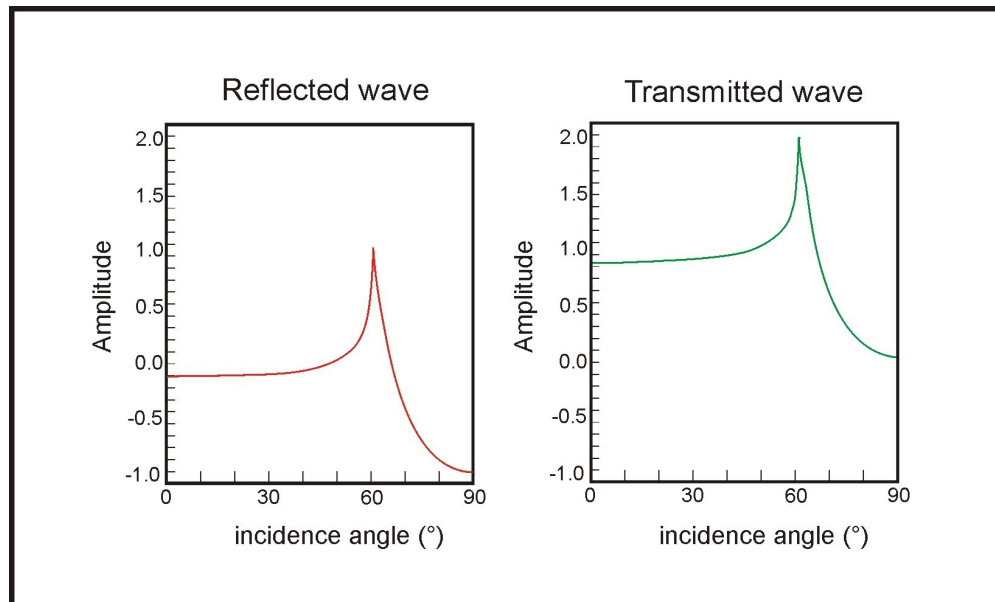


Figure 5.2: Reflection and transmission coefficients versus incidence angle for a downgoing SH-wave incident on the Moho. Modified from Shearer (2006).

5.5 Energy partitioning at wide-angle incidence

At larger angles than 49° the orientation of the transmitted wave becomes more horizontal and the amplitude continues to increase. Rays with near horizontal orientation contribute less to the vertical energy flux compared to the near vertical rays of the same amplitude. For this reason, the amplitude of the near vertical rays must increase in order to balance the energy flux.

The amplitude of the reflected wave increases as θ increases. At the critical angle ($\theta=60^\circ$) the transmitted wave is horizontal and both, transmitted and reflected waves, reach their peak amplitude values. Such a buildup in reflection strength in region of the critical angle is called wide-angle reflection.

This fundamental theory has been used since many years in deep seismic exploration to define the major features of the lithosphere. The recording of data using very long offsets makes it possible to map reflectors that can not be followed at short offsets.

The amplitude ratio of the vertical ground motion of the incident energy in the critical region and the energy incidence in the near vertical region $q = w(i_c)/w(i_v)$ was studied by Meissner (1967) using first order and higher order interfaces.

As the velocity contrast between the two interfaces decreases, the ratio increases (Fig. 5.3). In the case of the occurrence of gradient zones over (model 2) and below (model 3) the first order interface, high amplitude overcritically reflected and refracted waves are produced. In the case of smaller velocity contrast (models 4, 4a and 4b) the reflection coefficient for near vertical incidence is very small and depends on the thickness of the transition zone and wavelength. In the wide-angle region events with much stronger amplitude as the first order interface are recorded.

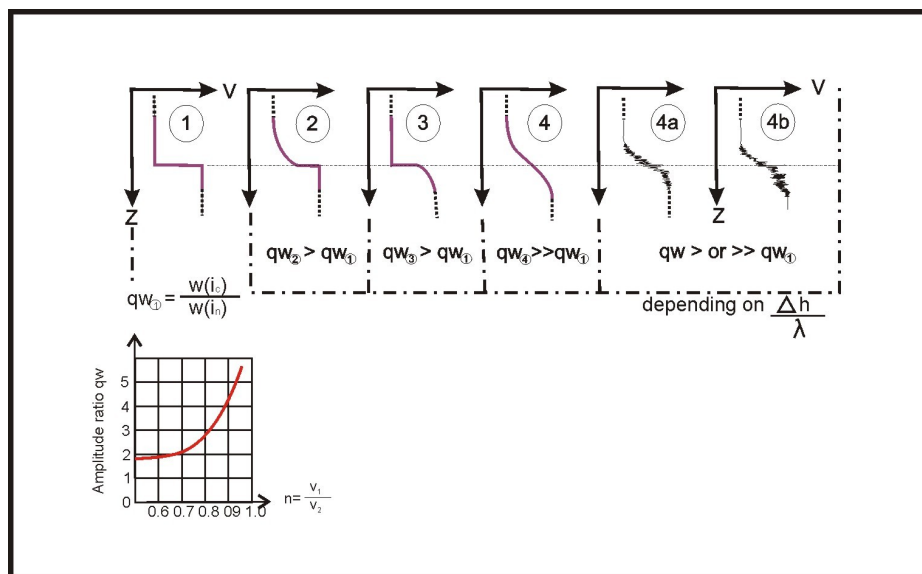


Figure 5.3: Relation between velocity contrasts and amplitude values for wide-angle data. After Meissner (1967).

Giese et al. (1976) show amplitude curves of PmP waves from deep seismic experiments in continental zones. The crust has been modeled with a low velocity gradient and the Moho is represented as a first order discontinuity. The derived amplitude curve shows two maxima (Fig. 5.4), the first one close to the region of the critical point (i_c) at 120 km distance and the second one (i_t) at 210 km distance around the region where the head wave begins, indicating the existence of arrivals coming from the uppermost mantle.

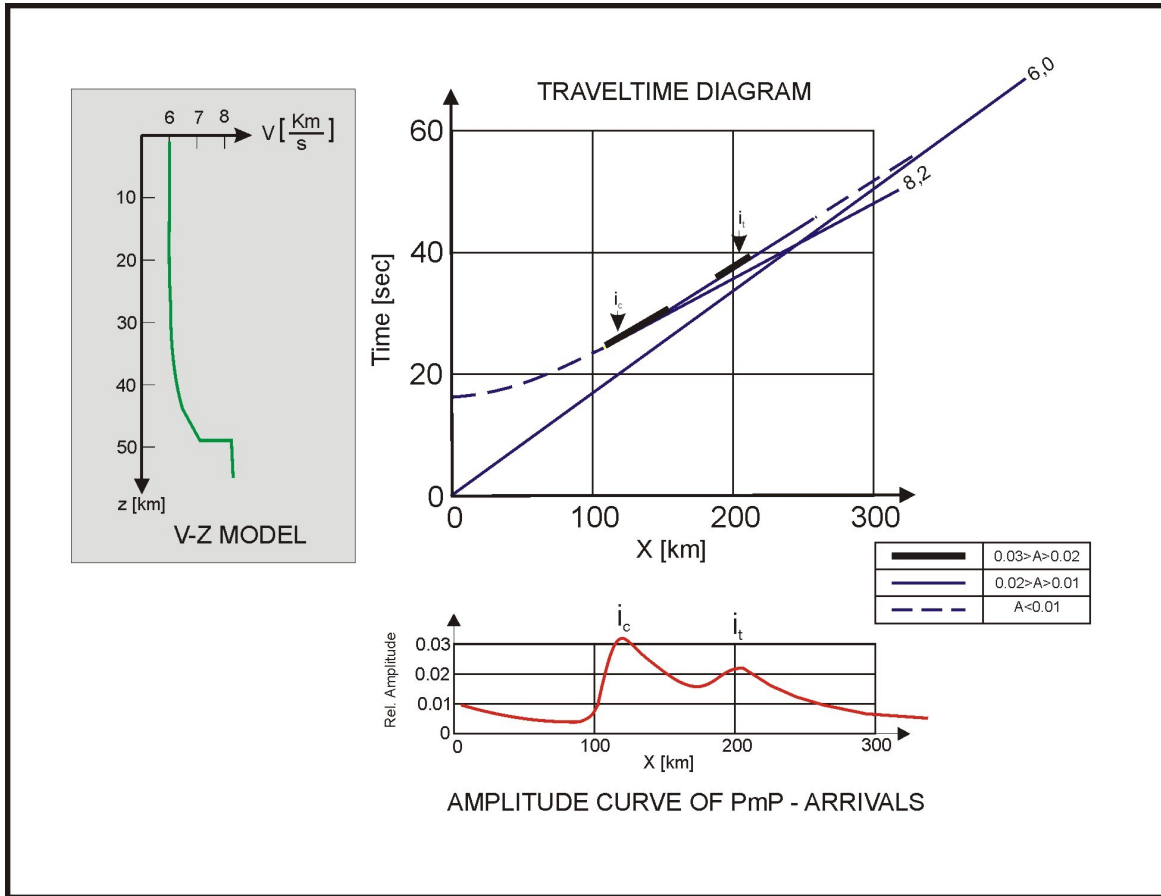


Figure 5.4: Schematic velocity model with gradient zone and first order discontinuity at the Moho, theoretical traveltimes and amplitude curves of PmP arrivals. After Giese et al. (1976).

6 Seismic Migration

The main goal of recording seismic data is to produce an accurate and reliable image of the geological structures in the subsurface. During the recording of seismic data the wave propagation from the source point to reflectors and back to the surface causes undesirable effects on the record sections, some of these effects are removed by seismic migration.

Seismic migration is a wave-equation-based approach that reconstructs geometrically and quantitatively the reflectivity distribution in the subsurface by relocating events to their true spatial position and by collapsing energy from diffractions back to their scattering points. The traveltimes in a record section give information about the position and shape of the recorded events while amplitudes provide the quantitative information about their reflection properties. In summary, seismic migration focuses the data and yields a correct image of the subsurface.

The data space represented by the recorded data sorted in shot, receiver or common offset gather has a relationship with the image space defined by the wave equation, thus seismic migration represents an adequate methodology to perform the inversion.

Migration methods are grouped in kinematic and wave-equation-based approaches. The main difference is that the latter takes into account the amplitude information of the wavefield during the migration process.

The fundamental element of these methods is the acoustic wave equation:

$$\frac{\partial^2 U}{\partial x^2} + \frac{\partial^2 U}{\partial y^2} + \frac{\partial^2 U}{\partial z^2} = \frac{1}{v^2} \frac{\partial^2 U}{\partial t^2} \quad (6.1)$$

The recorded wavefield $U(x, y, z=0, t)$ is considered as boundary value of the wavefield $U(x, y, z, t)$ originating from a reflector or diffraction points in the subsurface.

Between the most commonly used wave-equation-based migration schemes are: Kirchhoff migration (Schneider, 1978), Finite Difference methods (Claerbout and Doherty, 1972) and migration in the frequency-wavenumber domain (Gazdag, 1978; Stolt, 1978).

Wave equation migration methods consist of two main steps:

1. Downward continuation of the wavefield or wavefield extrapolation.
2. Imaging.

The extrapolation process represents the solution of the wave equation where the wavefield is calculated at any position and time from the knowledge of the wavefield at previous positions and times.

The imaging process consist in the determination of the position and time at which the extrapolated wavefield is required. Here, the wavefield propagating from a source point at the surface $z=z_0$ is computed in the diffraction point P at depth $z=z_1$. The point P contains the value of the wavefield at depth $z=z_1$, meaning that the wavefield will be imaged at point P. If the wavefield value is non zero, the point P is considered a reflector and a new wave will propagate upwards. The traveltme from the source to the diffraction point P is called imaging time t_I , which is a function of the selected subsurface points and depends on the velocity distribution and the wave type (Fig. 6.1). The total wavefield values yield the migrated section $M(x, z)=U(x, z, t_I(x, y, z))$.

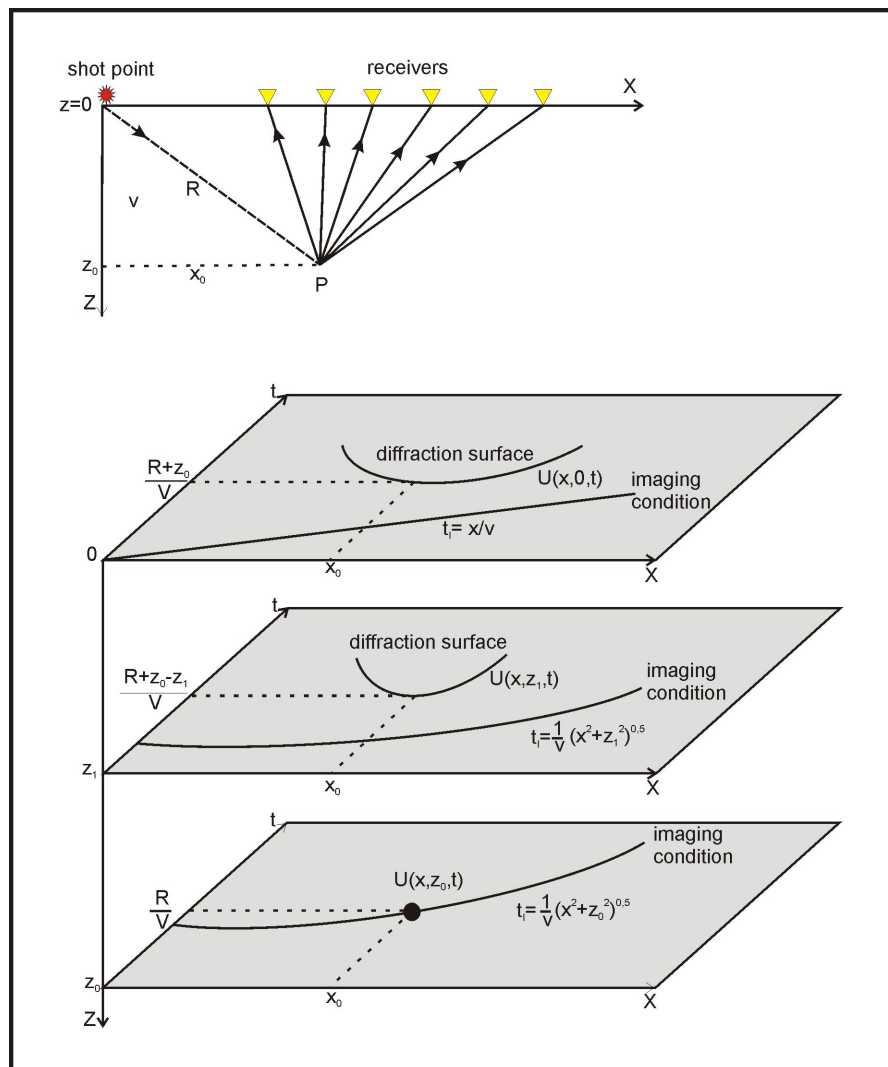


Figure 6.1: 2D Migration of one shot gather with wave equation based methods (after Simon, 1993). The wavefield is downward extrapolated from the surface ($z=0$) until the diffraction point location at $z=z_0$ where the diffraction hyperbola collapses into one point.

The wave-equation-based migration approach can be applied in the pre or post stack domain. In the case of prestack migration, the imaging condition is $t_I = R/v$ where R is the distance between the source and the diffraction point P and v is the velocity. For poststack migration the scheme is applied in a CMP sorted section, simulating zero offset recording. In this case the imaging condition equals zero.

6.1 Kirchhoff prestack depth migration

Kirchhoff migration is based on Green's function theory and on an integral solution of the wave equation (Biondi, 2007). The general form is given by the following integral expression (Schleicher et al. 1993):

$$I(p) = \frac{-1}{(2\pi)} \iint_A w(p, \xi) \frac{\partial U}{\partial t}(\xi, t_I) d\xi \quad (6.2)$$

where $I(p)$ denotes the image space at any subsurface point $p(x, y, z)$ and is equal to the integral over the aperture A (the ensemble of source-receiver locations) of the weighted time derivative of the wavefield $U(\xi, t_I)$ recorded on the surface evaluated along diffraction trajectories $t_I = t_s + t_r$.

Diffraction curves

The time t_I represents the diffraction curves or Green's functions along which the energy is summed, and forms the basis of Kirchhoff migration. Here, t_s is the travelttime from the source point to the image point $I(p)$ and t_r is the travelttime from the latter to receiver at the surface.

The diffraction curves are functions of the velocity structure and the location of the image point $I(p)$. All energy associated with the diffraction at a subsurface point can be observed along them. Kirchhoff migration uses the time distance information provided by the diffraction curves, and the migrated image is derived as superposition of all contributing amplitudes along them, interfering constructively at the imaging point and interfering destructively at all other locations (Milkereit, 1987).

For homogeneous velocity the diffraction curves are represented by hyperboloids whereas for variable velocity medium their shape is more complicated and numerical computation is required. The latter represents a major disadvantage of the Kirchhoff migration applied to complex seismic velocity structures (Audebert et al. 1997) because it introduces approximations in the representation and calculation of Green's functions that define the Kirchhoff migration integral. Several methods exist for computing diffraction surfaces through a complex velocity medium, which solve the eikonal equation, a high frequency approximation of the wave equation (Biondi, 2007). Most numerical methods are either ray tracing (Červený and Pšenčík, 1983), which solve the eikonal equation along its characteristics or finite difference methods (Vidale, 1990; Podvin and Lecomte, 1991).

Weighted functions

The weighted functions $w(p, \xi)$ in the migration integral compensate for the loss of amplitudes before summation, including the spherical divergence correction and obliquity factor. The first accounts for the loss of amplitudes as the wavefield travels away from the source or scatterer point, resulting in a decrease of amplitude as traveltime or distance from the source increases. The second corrects for the angle at which each event arrives at the receivers. When the energy arrives at the surface, the receivers near the image point record a greater amplitude than those receivers located further away. The obliquity factor is given by the cosine of the angle between the direction of propagation and the vertical axis (Yilmaz, 2001)

The wave shaping factor

This factor restores amplitudes and phases that are distorted when constructive and/or destructive interference occurs as the seismic wave propagates. In 2D Kirchhoff migration, the wave shaping factor is a filter designed with 45° constant phase spectrum and an amplitude spectrum proportional to the square root of the seismic data frequency. In 3D Kirchhoff migration, the filter is designed with 90° constant phase spectrum and an amplitude spectrum proportional to the frequency of the seismic data (Yilmaz, 2001).

Kinematically, Kirchhoff migration is carried out by distributing the amplitude value of a sample at time t of an unmigrated trace to all points of its corresponding isochrone in a regular image space grid, that is, the surface where a reflection of diffraction might produce the sample at time t , and by superimposing all isochrones for all samples of all traces in the record section. This process is shown in Fig. 6.2.

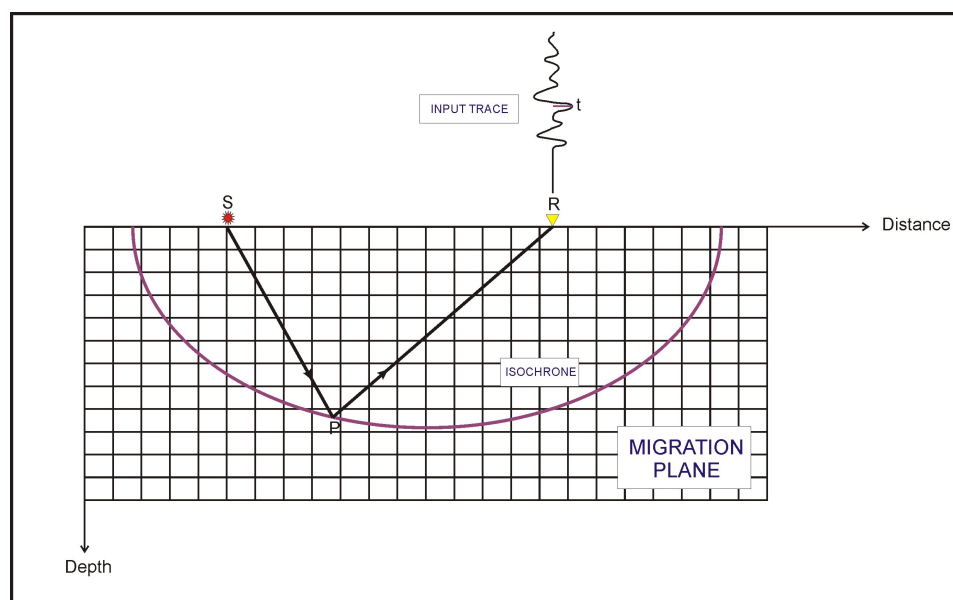


Figure 6.2: Kinematics of Kirchhoff prestack depth migration. After Simon et al. (1996)

A high fold and good signal-to-noise ratio are not the most important conditions to produce a reliable image of the subsurface by using migration methods. Some other factors that can impact the frequency content and quality of the migrated data must be taken into account.

Velocity errors

The accuracy of the velocity is an impacting parameter to collapse diffractions and relocate dipping events to their true position. The use of low migration velocity results in an incomplete collapse of diffractions and dipping events are only partially repositioned to their real location. On the other hand, if the velocity used is too high, diffraction hyperbolas are overmigrated, yielding migration artifacts like inverted hyperbolas or smiles. The effects of using too low and too high velocities in Kirchhoff migration are shown in Fig. 6.3. The upper subfigure illustrates nine diffractor points migrated with the correct velocity. The middle and lower subfigures are the same nine diffractors but migrated with lower and higher velocities respectively.

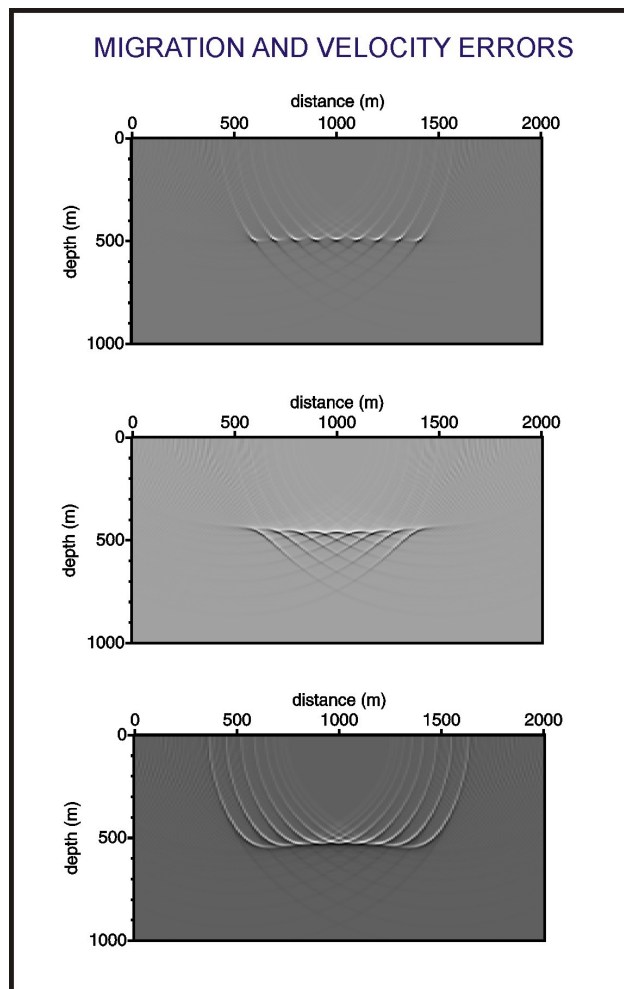


Figure 6.3: Migration and velocity errors. Top: migration with correct velocity values; middle: submigration; bottom: overmigration.

Migration and random noise

The migration of record sections contaminated with strong random noise may produce severe adverse effects in the migrated section if they are not processed properly. These effects can include smearing of amplitude and the appearance of smiles as the product of the migration of sparsely distributed amplitude spikes in the input section. Fig. 6.4 shows the migration of an horizontal event with and without ambient noise.

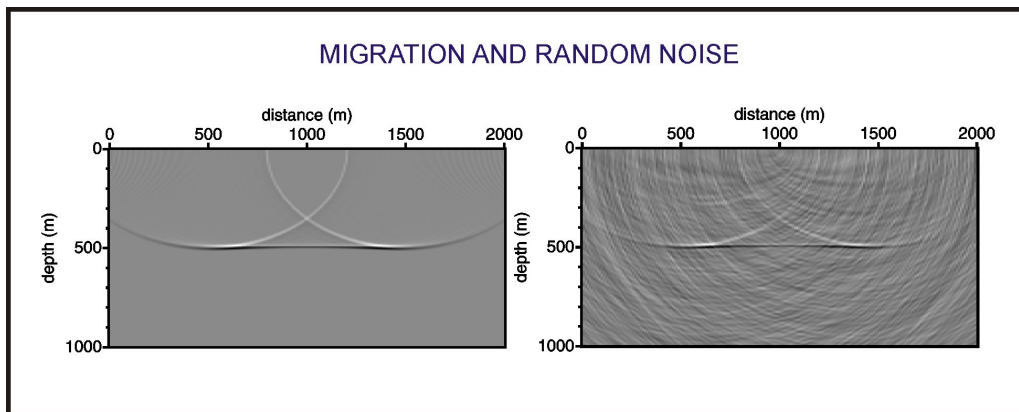


Figure 6.4: Migration of an horizontal reflector without (left) and with (right) random noise.

Migration and spatial aliasing

Using a sparse trace spacing results in the introduction of aliased energy that can reduce the quality of the migrated section. If the aliased energy is not removed, migration will move the spatially aliased frequencies in the wrong direction and produce dispersive noise (Yilmaz, 2001). The example in Fig. 6.5 depicts the migration of data using a convenient (left) and too large trace spacing (right). Although the event seems to be migrated at the right position, not all the input energy is collapsed, resulting in residual inverted hyperbolas that distort the final image.

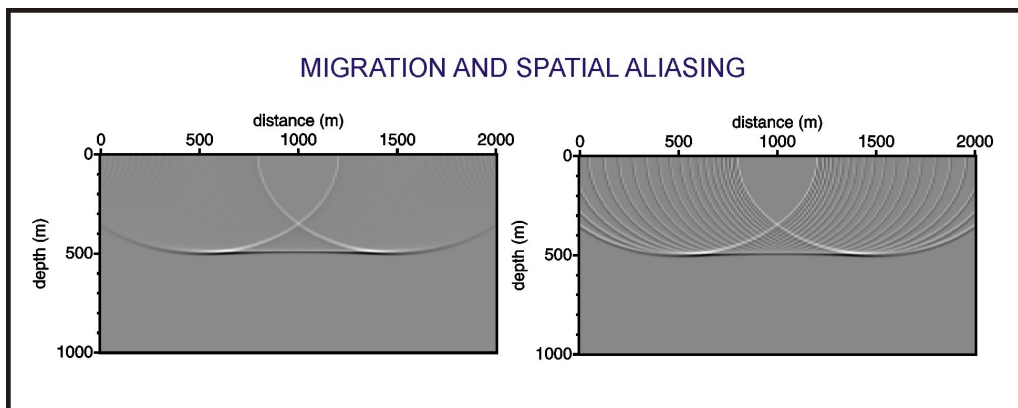


Figure 6.5: Migration and spatial aliasing. Using sparse trace sampling cause the introduction of aliased energy, yielding artifacts which in turn distorts the migrated image.

6.2 Vertical resolution

The minimum distance (in time or space) needed to separate two interfaces so that they form separated reflectors is the base of the vertical resolution problem.

Different thresholds for vertical resolution have been proposed by several authors. Jenkins and White (1957) defined the separable limit when two reflectors are separated by half a wavelength, where the dominant wavelength of seismic waves is given by the relation between the velocity and the dominant frequency:

$$\lambda = v/f \quad (6.3)$$

On the other hand, the threshold defined by Widess (1973) as the quarter of the dominant wavelength is the most accepted in the literature even though it can be considered subjective and dependent of the noise level in the data (Yilmaz, 2001). For a bed thickness on the order of a seismic wavelength or larger, there is little or no interference between the wavelets from the top and bottom of the bed and each is recorded without alterations. For thinner layers these wavelets interfere constructively and destructively. In the case of wavelets with opposite polarity, the amplitude of the composite wavelet reaches a maximum for a bed thickness of one quarter wavelength and this called the tuning thickness. For layers thinner than this threshold, the shape of the composite wavelet does not change but its amplitude decreases. The layer thickness where the tuning phenomena occurs depends on the shape of the wavelet and its frequency content (see Fig. 6.6).

The dominant frequency of a seismic section depends on the physical properties of the subsurface, the pre-processing flow applied and the recording parameters. The earth behaves as a low-pass filter as a wavefield propagates through it so that the high frequency signal is attenuated by the physical properties of the subsurface. For this reason some efforts must be done in seismic acquisition (adequate sampling rate, antialias filtering, type of seismic source) and processing (deconvolution, filters) in order to preserve the high frequency signals as much as possible.

The wide-angle data is characterized by its lower resolution power compared to the NVR data. The long horizontal and vertical distances covered by the wavefield at larger propagation angles have a strong influence on the frequency content of the recorded wavefield.

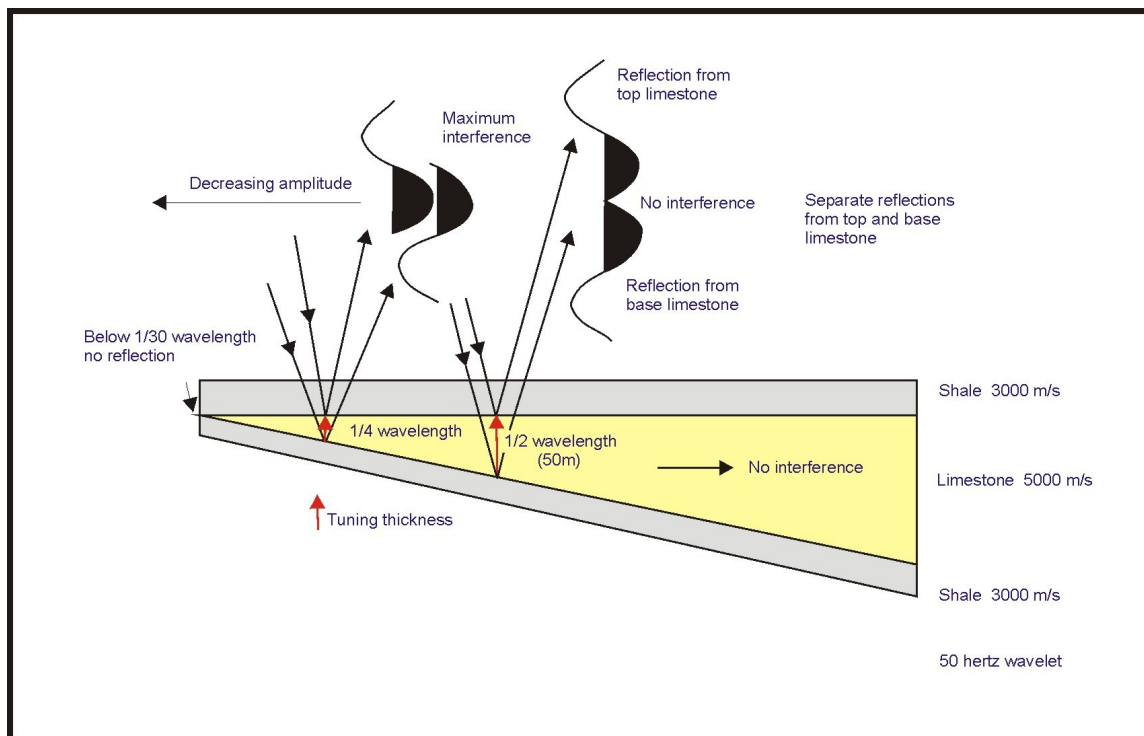


Figure 6.6: The tuning effect. Dependence of the resolution on the shape of the wavelet and frequency content. Modified from Brown (1991).

Using the one-quarter-wavelength criteria, Table 8.1 shows the minimum size features that can be resolved with the typical frequency content recorded in crustal studies for wide-angle and NVR data. The data corresponds to CINCA (offshore-NVR and wide-angle data) and ANCORP projects at 21°S in northern Chile. The frequency content preserved after pre-processing is: (5-64 Hz) for CINCA-NVR (Sick, 2005), (3-12 Hz) for CINCA wide-angle data and (5-20 Hz) for ANCORP-NVR data (Yoon, 2005). The minimum wavelength was calculated using the lower and upper limits of the frequency bandwidth.

Velocity (m/s)	$\lambda/4$ (m)	CINCA-NVR (5-64 Hz)	$\lambda/4$ (m)	CINCA-WA (3-12 Hz)	$\lambda/4$ (m)	ANCORP (5-20 Hz)
6000	300	23,4	500	125	300	75
6500	325	25,3	541,6	135,4	325	81,2
7200	360	28,1	600	150	360	90

Table 6.1: Threshold for vertical resolution of different seismic data recorded for crustal studies in northern Chile.

6.3 Fresnel zone and horizontal resolution

The concept of the Fresnel zone plays an important role in the determination of the spatial/lateral resolution power for unmigrated seismic data although other factors as signal-to-noise ratio and trace spacing can considerably affect the ability to separate events in horizontal direction. Wave theory establishes that events on a seismic trace are originating due to a reflection process on a finite area of the reflector that increases in size with depth. This area is known as the Fresnel zone and represents the region around the geometrically predicted reflection point where only constructive interference occurs (Okoye and Uren, 2000).

Sheriff and Geldart (1995) describe the Fresnel zone as the area on the reflector from which reflected energy arriving constructively at the receiver has phases differing by no more than a half wavelength. In the case of zero offset data in a homogeneous velocity model (Fig. 6.7), the first Fresnel zone is circular and positioned perpendicular under the source-receiver location while the Fresnel zones of higher order are annular rings with larger radius. Hence, the radius of the first Fresnel zone can be expressed as:

$$R_1 = \sqrt{\lambda * z_0 / 2} = (V / 2) \sqrt{t / v} \quad (6.4)$$

where R_1 is the radius of the first Fresnel zone, z_0 is the reflector depth perpendicular to the source-receiver location, t is the arrival time, V is the average velocity and v the frequency.

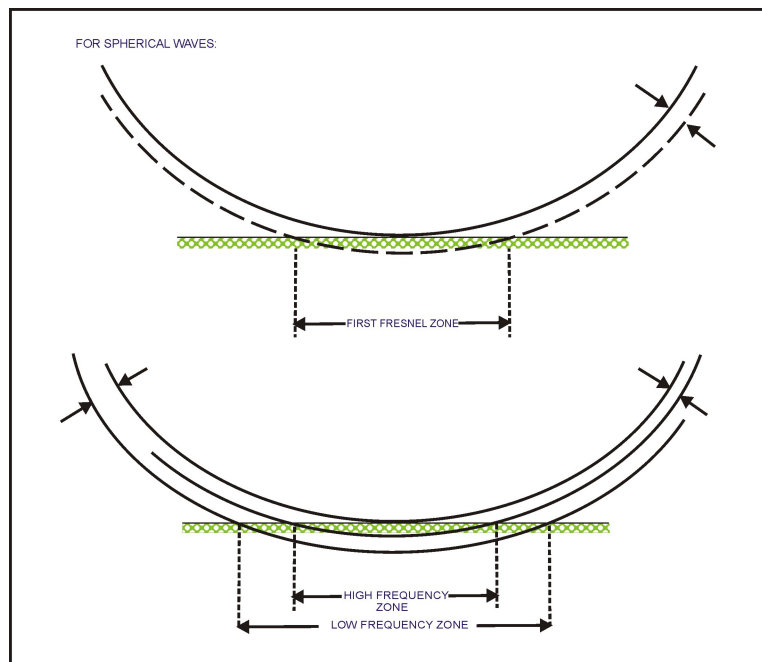


Figure 6.7: Concept of Fresnel zone. Lower frequencies define broader Fresnel zones on the reflector. Modified from Brown (1991).

Migration leads to the improvement of the lateral resolution of seismic data since it repositions reflections out of the place because of dip, collapses diffractions patterns and focuses energy spread over the Fresnel zone (Brown, 1991). Migration causes a focusing effect on the seismic data by reducing the Fresnel zone (Fig. 6.8) to an ellipse perpendicular to the line for 2D migration and to a circle by 3D migration (Lindsey, 1989).

In the case of CINCA wide-angle data the useful frequency content is in the range of 3-12 Hz with a dominant frequency at 6-8 Hz. Using 6.5 km/s as the average crustal velocity and 7.2 km/s the velocity at the oceanic crust-mantle boundary, the theoretical radius of the Fresnel zone can be estimated at different depth levels (see Table 8.2).

Depth (km)	V = 6.5 km/s	
	R (3Hz)	R (12Hz)
10	3,29	1,64
20	4,65	2,32
30	5,7	2,85
40	6,58	3,92
	V = 7.2 km/s	
30	6	3
40	6,92	3,46

Table 6.2: Estimated radius of the Fresnel zone (R) for the CINCA wide-angle data. The radius (in km) was calculated at different depth levels using the lower and upper limits of the frequency content, the average crustal velocity and the velocity at the oceanic crust-mantle boundary.

In conclusion, seismic wide-angle data is capable to resolve large structural features of the continental and oceanic crust and uppermost mantle while structural details and smaller geological features can be resolved by using NVR data. Nevertheless, it will be shown in the following sections, that despite its lower resolution power, seismic wide-angle data is capable to image the most prominent structural features of the seismogenic coupling zone in northern and southern Chile.

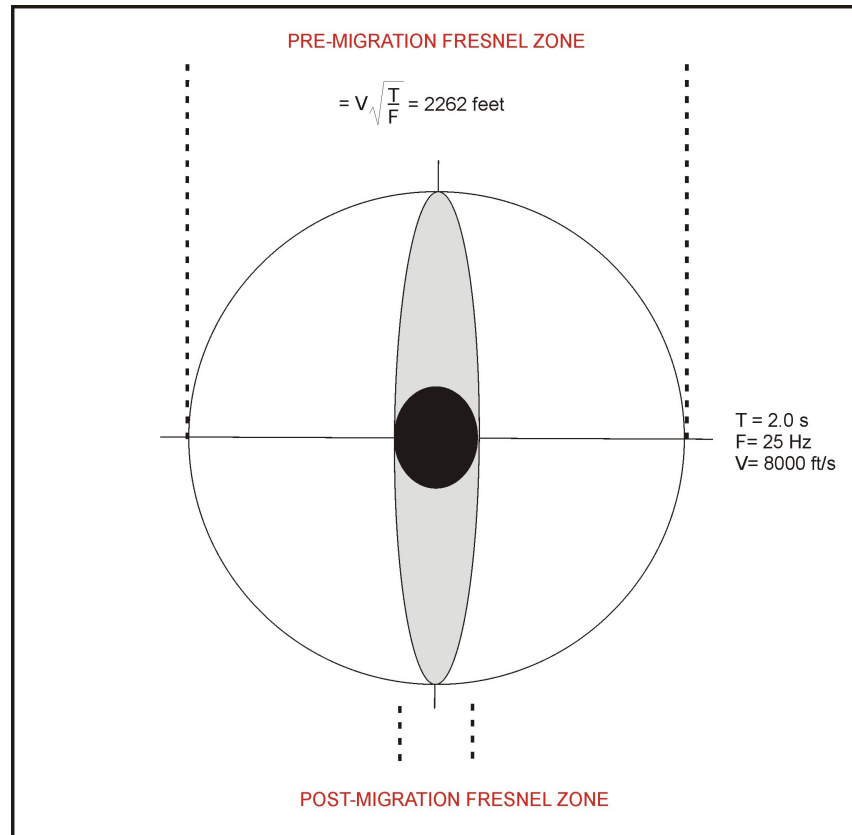


Figure 6.8: Fresnel zone and migration. Migration causes a focusing effect on the seismic data by reducing the Fresnel zone. Modified from Lindsey (1989).

6.4 Fresnel Volume Migration

When seismic data is recorded with limited aperture, strong artifacts can be produced after migration due to an incomplete summation of energy. Similarly, imaging of sparsely sampled data with low fold (spatial coverage) leads to images with migration noise because of the poor constructive interference of the back propagated wavefield. In these cases the restriction of the migration operator to the region around the reflection point is very convenient to reduce spatial ambiguities and to avoid the summation of undesired energy during the migration process.

6.4.1 Fundamentals of Fresnel Volume Migration

Fresnel Volume migration (FVM), an extension of standard Kirchhoff prestack depth migration has been implemented for multicomponent data (Lüth et al. 2005) and for single component data (Buske et al. 2009).

FVM has been shown to be a very efficient approach in the imaging of structures not only for limited aperture experiments carried out ahead of a tunnel (Lüth et al. 2005) but also for deep seismic exploration (Sick, 2005).

It is based on the fact that the migration operator is restricted, in a physically frequency-dependent way, to the Fresnel volume of the specular reflected raypath, meaning that the imaging condition is limited to the region that physically contributes in the reflection process, leading to the correct imaging of the reflected energy by reducing migration artifacts and eliminating spatial ambiguities (Fig. 6.9).

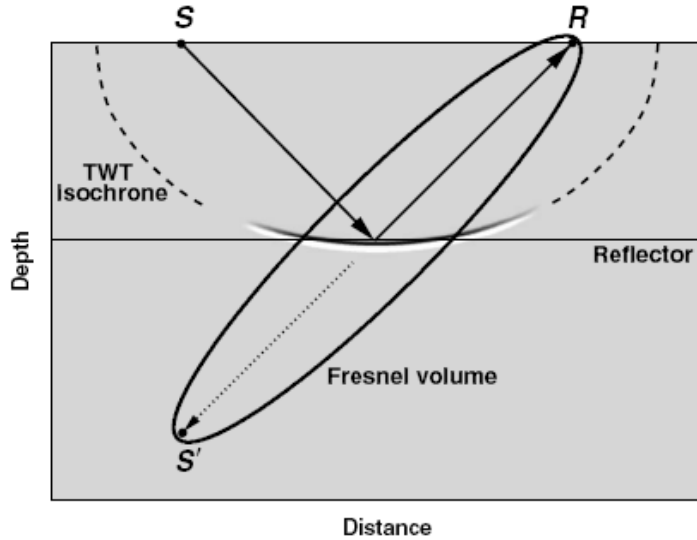


Figure 6.9: Fresnel Volume Migration scheme from Buske et al. (2009).

The formula for the Fresnel volume migration described by Buske et al. (2009) is:

$$V(m) = \iint_A F_c(m, x, t_s + t_r) W(m, x) \dot{u}(x, t_s + t_r) dx \quad (6.5)$$

Here, $V(m)$ represents the migrated image, $m=(x, y, z)$ is the point in the subsurface where the imaged is built as a weighted summation along the diffraction curves, $t_s + t_r = t_s(x_S, m) + t_r(m, x_R)$ denotes the imaging condition i.e. the sum of the traveltime from source and receiver to the imaging point. The vector x contains the location of receivers and sources defining the migration aperture A . The time derivative of the input wavefield needed to recover the source pulse is represented by \dot{u} . The function W is added for the treatment of the amplitudes during the summation process. Finally, F_c is the Fresnel criterion which is described below.

The migrated image $V(m)$ is the result of smearing the wavefield u along the corresponding two way traveltime isochrones and the constructive interference of the latter along the reflectors.

The FVM approach is performed for every time sample of all the traces in the record section in three main steps:

1) Estimation of the emergent angle at the receiver location. The emergent angle at the receiver is calculated through slowness analysis of neighboring traces by using a cross-correlation procedure (Haslinger, 1994). The procedure considers a data sample A at a time t from a trace with a distance X from the source, called the reference trace. A time window, called the reference window, with length dt approximately equal to the dominant wavelength must be defined and centered around t . Inside this reference window the cross-correlation between the reference trace and each segment of n adjacent traces is computed. The time shifts which are associated with the maxima of cross-correlation functions plotted against the trace distances, are the input for a linear square regression analysis that defines the local horizontal slowness vector according to the relation:

$$P_x(x, t) = \delta_t / \delta_x \quad (6.6)$$

The vertical and horizontal slowness component are related to each other by the following expression, which includes the near velocity value V_0 :

$$P_z(x, t) = \sqrt{(1/V_0 * V_0) - p_x * p_x} \quad (6.7)$$

The temporal and spatial extension of the window is estimated by using the dominant wavelength. The number of traces n and the number of samples m are defined by the following expressions:

$$n = \lambda / \delta_x ; \quad m = 1 / F_{dom} * \delta_t \quad (6.8)$$

2) Ray tracing into the subsurface. Using the estimated emergent angle as starting direction, a ray is projected until the time t_o is reached. This ray passes the actual reflection point and continues to the point S' which represents, in a homogeneous model without velocity gradients, the actual source point S mirrored at the reflector. The traveltime of this ray equals the traveltime of the ray path SMR (Fig. 6.9).

3) Fresnel volume estimation. Based on a similar version of Fresnel-Volume-Ray-Tracing (Cerveny and Soares, 1992) the Fresnel volume is calculated at every point of the ray traced until time t_o based on the following expression where T corresponds to the dominant period of an element of the wavefield, r_0 denotes the last point of the ray at time t_o and $\Pi_{13}(r)$ represents the ray propagator matrix (see Lüth et al. 2005):

$$r_F(r) \approx \sqrt{\frac{T}{\Pi_{13}^{-1}(r) - (\Pi_{13}(r) - \Pi_{13}(r_0))^{-1}}} \quad (6.9)$$

4) Energy smearing along the migration operator. The Fresnel volume calculated before establishes the Fresnel criterion F_c acting like an additional weighting factor. Here, the smeared energy is weighted so that inside the Fresnel volume the weighting factor equals one and outside it is linearly tapered to zero with increasing distance from the Fresnel volume. The following expression describes the Fresnel criterion F_c , where d represents the distance between the image point under consideration and its nearest point on the corresponding traced ray until t_o , and r_F is the size of the Fresnel radius at this nearest point on the ray:

$$F_c = \begin{cases} 1 & \text{if } d \leq r_F \\ 1 - \frac{(d - r_F)}{d} & \text{if } r_F < d < 2r_F \\ 0 & \text{if } d \geq 2r_F \end{cases} \quad (6.10)$$

By applying the Fresnel criterion the smearing process is restricted to the region around the reflection point and the migration artifacts created by smearing amplitudes away from the reflection it are suppressed, leading to higher resolution images.

6.4.2 Validity of approximations

Buske et al. (2009) describe the validity of the FVM approximations based on the velocity contrast between layers (Fig. 6.10). The region around the reflection point is defined by the Fresnel volume of the direct ray, which is the one starting at the receiver and projected into the subsurface until the time t_o is reached at the source point S' (Fig. 6.10a).

The reflected Fresnel volume describes the region around the reflected ray between source and receiver that contributes to the wavefield recorded at the receiver R. Thus the Fresnel volume of the direct ray is used as an approximation of the Fresnel zone defined by the reflected ray on the reflector.

In the case of vanishing velocity contrast, the intersection between the Fresnel volume of the direct and reflected ray defines the true Fresnel zone on the reflector (Fig. 6.10a).

In the case of dipping reflectors, represented by differences in travel distances from source and receiver to the reflector, both Fresnel volumes define also the same Fresnel zone on the reflector in the case of vanishing velocity contrast (Fig. 6.10b).

On the other hand, for decreasing and increasing velocity, the Fresnel zone defined by the intersection of the above mentioned rays changes. For decreasing velocity in the lower layer, the Fresnel volume represented by the direct ray is smaller and the Fresnel zone on the

reflector is slightly underestimated. On the contrary for increasing velocity in the lower layer, the Fresnel volume defined by the direct ray is greater and the Fresnel zone on the reflector is then overestimated (Fig. 6.10c).

Nevertheless, in both cases the position of the reflected ray does not depend on velocity contrast and the center of the estimated Fresnel zone on the reflector is still correct. Even more since the migration operator is tapered at the boundary of the Fresnel volume defined by the direct ray, the minor under/overestimation of the Fresnel zone does not cause any significant effects on the migrated section.

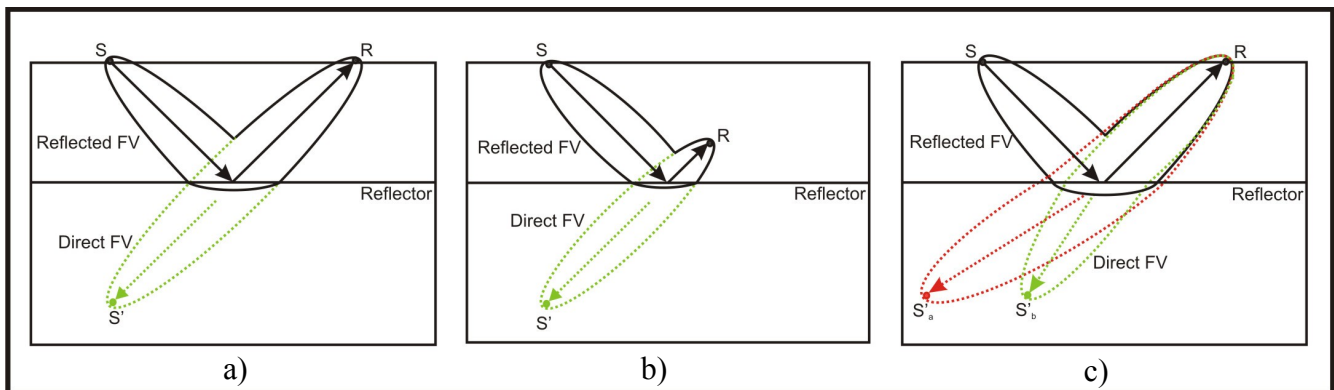


Figure 6.10: FVM validity of approximations. a): case of symmetric source and receiver locations and vanishing velocity contrast; b): case of dipping reflector and vanishing velocity contrast; c): case of symmetric source and receiver and non-vanishing velocity contrast. Modified from Buske et al. (2009).

7 The wide-angle dataset

7.1 The CINCA wide-angle dataset

CINCA-95 (Crustal Investigations Off- and Onshore Nazca/Central Andes) was a successful multidisciplinary research program carried out by German and Chilean institutions in order to investigate the structure and evolution of the subduction zone in Northern Chile between 19°S and 26°S. Different geophysical/geological methods including active (near vertical reflection and wide-angle/refraction seismic measurements) and passive seismic, gravity, magnetic, bathymetric, sediment echography and geological sampling were applied with the aim to study (Hinz et al. 1995):

- the composition and geometry of the subducting Nazca plate and the overlying South American plate in the area of convergence zone and further depths.
- the tectonic mechanism in the development of the convergent continental margin focused on erosional and/or accretionary processes.
- the regional seismicity, stress and geothermal fields.

The CINCA wide-angle data was recorded in an amphibious configuration i.e. the air gun pulses fired along three west-east profiles at 21°S, 22.2°S and 23.25 °S were recorded by station arrays deployed on land (Fig 7.1). Such a configuration leads to record signals originating from shallow levels of the coupling zone in the forearc area.

Airgun Pulses

The seismic sources were two linear arrays of 20 airguns divided in six groups with a total volume of 51.2 litres. The total length of the source array was 19.6 m, operating at 7 m depth and 135 bar pressure (Hinz et al. 1995). The shot interval was 1 pulse/minute with a distance of around 160 m.

Receiver Stations

Portable Digital Acquisition Systems (PDAS) with 3C seismometers of 1Hz natural frequency and analogue systems with 1C seismometers and 2 Hz natural frequency were deployed on land to record the airgun pulses (Patzwahl, 1998). The distance between stations was approximately 3.5 km. The data was recorded using a sample interval of 10 ms and total record length of 50 s.

The airgun lines were identified as follows: Lines 201/202 at 21°S, Lines 301/302 at 22.2 °S and Lines 301/302 at 23.25 °S. The survey was performed according to the following

procedure: each airgun line was fired first eastward, then the receivers were moved to the east one half of the original receiver distance and the recording was completed westward.

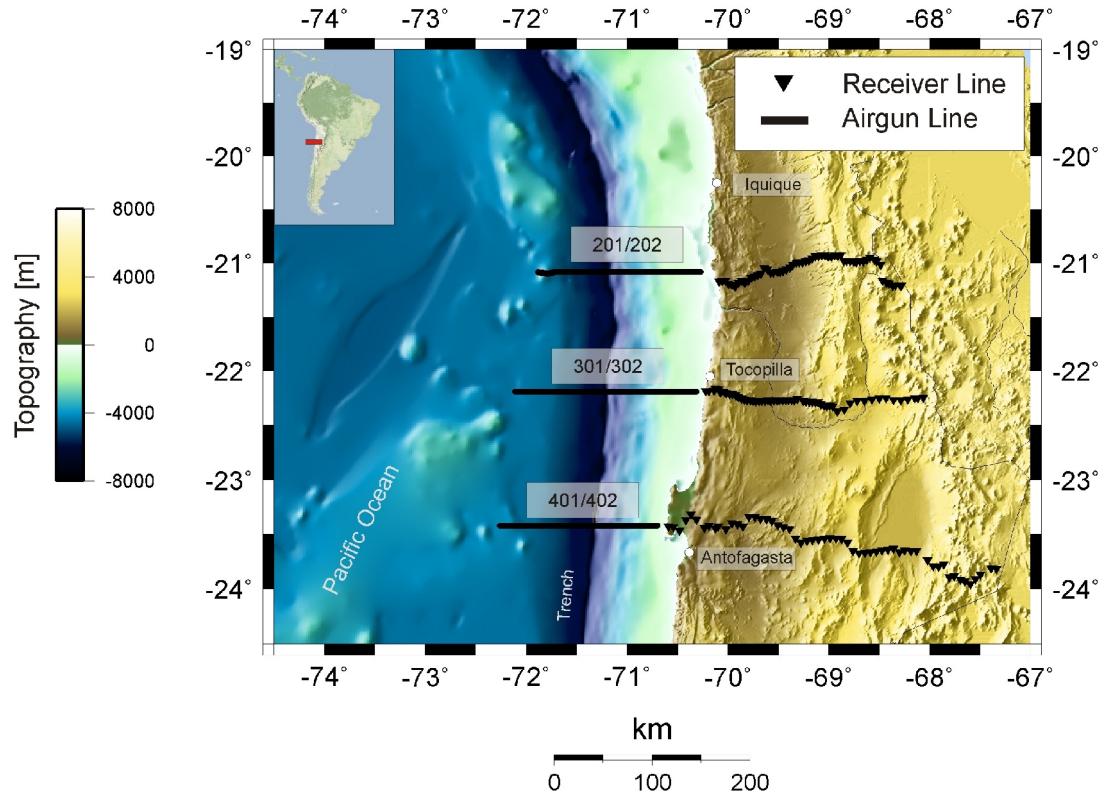


Figure 7.1: Location map of the CINCA wide-angle profiles.

Table 7.1 summarizes the parameters for each amphibious acquisition line. For more details about the multidisciplinary data collection of CINCA project see Hinz et al. (1995).

Lines	201	202
Length of source line (km)	138.5	122.3
Number of shots	880	856
Shot interval (m)	160	160
Length of receiver line (km)	179.8	184.2
Number of receiver	28	29
Minimum offset (km)	27.4	37.8
Maximum offset (km)	344.6	357.2
Sample rate (ms)	10	10

Lines	301	302
Length of source line (km)	184.7	130.5
Number of shots	1147	824
Shot interval (m)	160	160
Length of receiver line (km)	217	219.1
Number of receiver	29	29
Minimum offset (km)	12.9	13
Maximum offset (km)	412	362.6
Sample rate (ms)	10	10

Lines	401	402
Length of source line (km)	133.1	98.7
Number of shots	824	634
Shot interval (m)	160	160
Length of receiver line (km)	329.1	329.4
Number of receiver	29	29
Minimum offset (km)	15.7	16.2
Maximum offset (km)	498.8	443.6
Sample rate (ms)	10	10

Table. 7.1: Summary of the acquisition parameters of the CINCA wide-angle profiles.

7.2 The SPOC wide-angle dataset

The SPOC project (**S**ubduction **P**rocesses **O**ff **C**hile) was conducted in 2001 in South-Central Chile between 28°S-44°S with the general aim of defining the processes and constraints that control the formation of the Chilean continental margin (Reichert et al. 2002). Similar to CINCA, during the SPOC project different geophysical methods were applied including active seismic (multichannel and wide-angle/refraction measurements) off- and onshore, passive seismic, gravity, magnetics, high resolution bathymetry and echonographic methods. The recording of this dataset was focused specifically on the following subjects (Reichert et al. 2002):

- Determination of structure, composition and age of the oceanic crust and its sedimentary cover.
- Study of the thermal state of the oceanic crust.
- Definition of the subduction angle and obliquity.
- Study of the subduction front, the subduction interface, the structure of the slope and forearc basin.
- Distribution of gas hydrate in the slope area.
- Comparison with previous studies of the Chilean active margin (CINCA and CONDOR).

The airgun shots from R/V SONNE were recorded at 50 receivers deployed onland along four west-east profiles at 36°15'S, 37°17'S, 38°2'S and 38°45'S (Fig. 7.2), shaping a similar amphibious configuration as in CINCA project to cover the area of the seismogenic coupling zone close to the coast.

Airgun Pulses

The source signals were produced every 50 m by two tuned linear arrays consisting of 20 airguns (type VLF Prakla-Seismos) in 6 groups with a total volume of 51.2 litres. The total length of the source array was 19.6 m, operating at 7 m depth and 13.5 MPa pressure (Reichert et al. 2002).

Receiver Stations

50 portable acquisition systems equipped with 3C seismometers type MARK L-4C and 1 Hz natural frequency were deployed every 2.5-4.5 km along four profiles. The data was recorded with 10 ms sample interval. The OBS were 4C systems, meaning that they are equipped with one hydrophone for the registration of pressure and 3C seismometers to measure compressional and shear waves on the ocean bottom.

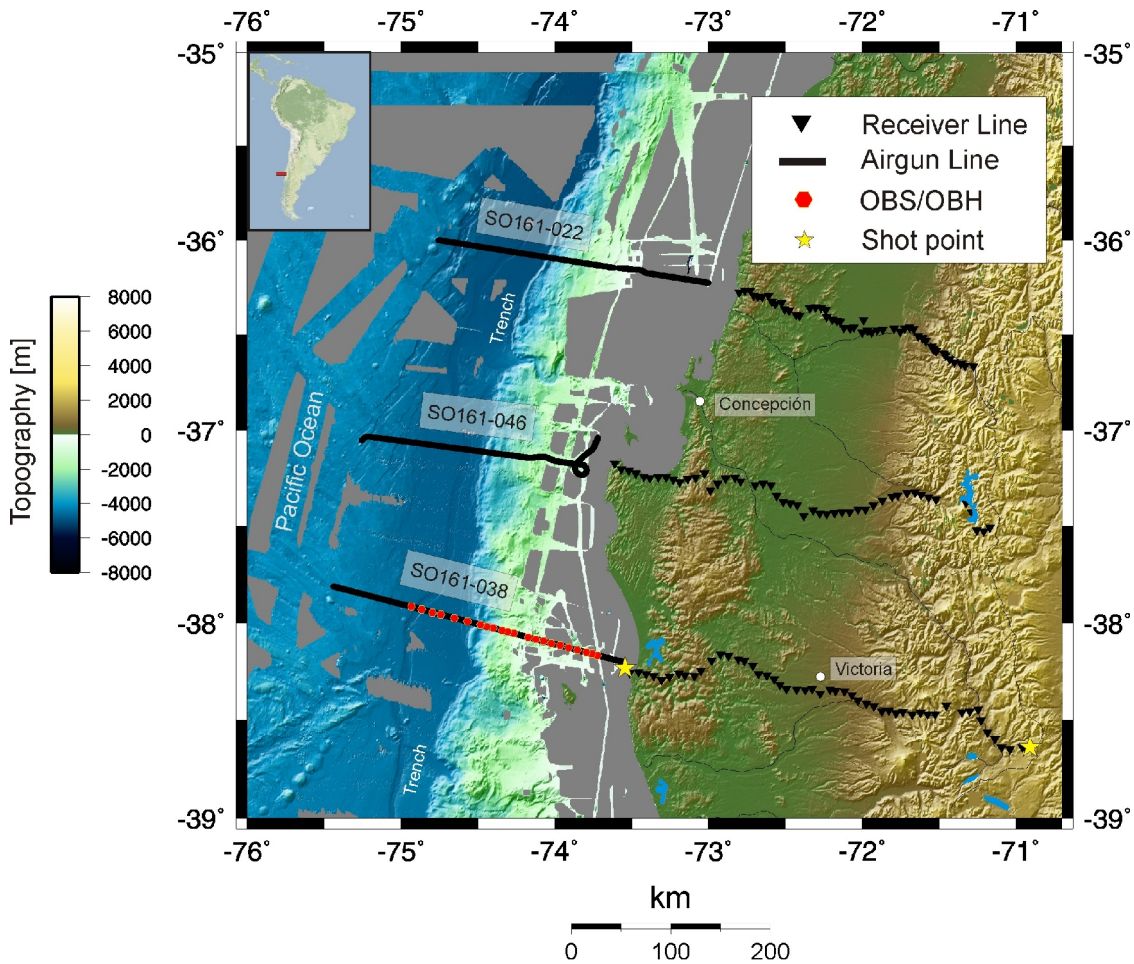


Figure 7.2: Location map of the SPOC wide-angle profiles.

Table 7.2 summarizes the acquisition parameters of the SPOC wide-angle profiles included in this study: the amphibious profile SO161-038 and the OBH/OBS profile.

Lines	SO161-038	OBH/OBS
Length of source line (km)	189.8	171.3
Number of shots	3598	1109
Shot interval (m)	50	50
Length of receiver line (km)	228.5	110
Number of receiver	51	22
Minimum offset (km)	17.9	0.47
Maximum offset (km)	365.7	149.5
Sample rate (ms)	10	0

Table 7.2: Summary of the acquisition parameters of the SPOC wide-angle profiles included in this study.

7.3 Data and phase correlations

Four main phases were interpreted on the wide-angle record sections of CINCA and SPOC projects:

- Pg: refracted waves emerging from the upper continental crust.
- PcP: reflected phases from intracrustal structures.
- PmP: reflections from the oceanic crust-mantle boundary.
- Pn: refracted waves traveling through the uppermost mantle.

7.3.1 Seismic phases of CINCA wide-angle data

The Pg phase is the first arrival on the amphibious data traveling distances of about 100 km for receivers located in the coast area, and until 120 km for receivers placed far off the coast. On the record sections, the Pg arrival shows an apparent velocity close to 6.0 km/s and arrives at positive reduced traveltimes, indicating the occurrence of low velocity material under the receiver line (Fig. 7.3).

Intracrustal reflections were observed close to the Pg phase on most of record sections along the whole profile. They form the second arrival in the distance range of 20-130 km. At near offsets, PcP phases are clearly separated from refraction phases and show slightly higher velocities than 6.0 km/s.

The reflection on the oceanic Moho was observed at offsets between 50-130 km. This phase is asymptotic to the Pn, meaning that the correlated phase corresponds to reflections on the oceanic crust-mantle boundary. From the record sections it is evident that the oceanic Moho is dipping to the east, due to the fact that the distance at which the PmP is observed increases eastward. The Pn phase constitutes the first arrival at longer offsets (75-170 km) on the record sections. Its apparent velocity value was estimated to be in the range of 8.7-9.5 km/s (Patzwahl, 1998).

On the onshore data, the Pg phase was correlated up to 200 km offsets with velocities close to 6.0 km/s (Fig. 7.4). Asymptotic to Pg, a PcP phase was interpreted in the land shot of Caleta-Patillos at 21°S. This phase covers an offset range between 100-200 km. Reflections on the oceanic Moho were also correlated as the second main arrival at offsets larger than 150 km. Pn phases were only interpreted as the first arrival on the section corresponding to the Isla Santa Maria shot at 23.25°S. For more details about the phase correlations on the airgun and onshore data see Patzwahl et al. (1998) and Patzwahl (1999).

7.3 Data and phase correlations

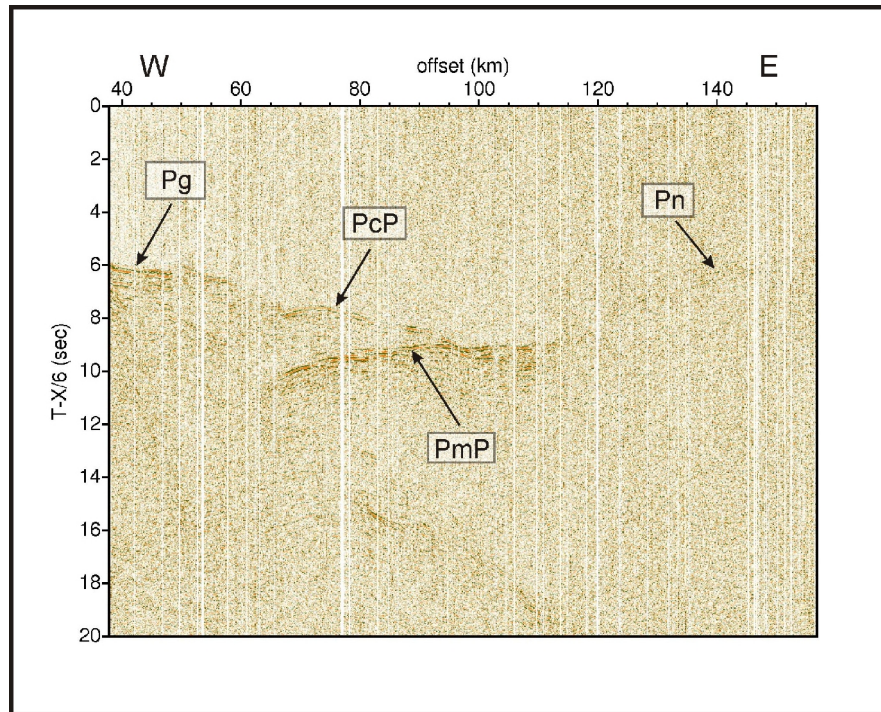


Figure 7.3: CINCA Lines 201/202 at 21°S. Receiver gather of station 2 with interpreted phases. Vertical axis is time reduced with 6 km/s.

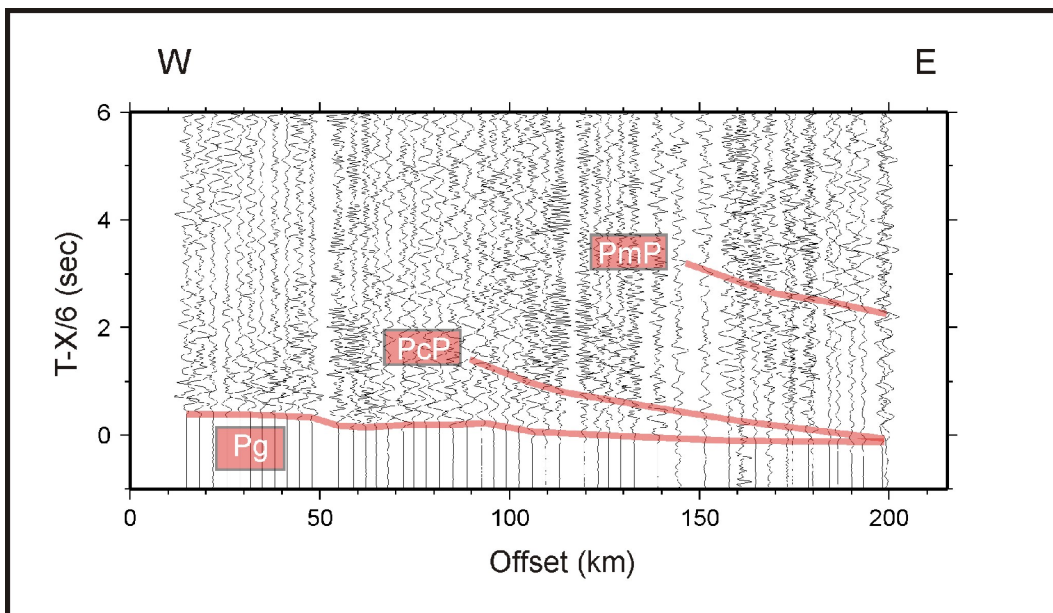


Figure 7.4: Shot gather of the onshore seismic profile at 21°S with interpreted phases. Vertical axis is time reduced with 6 km/s.

7.3.2 Seismic phases of SPOC wide-angle data

Refractions from the upper continental crust are clearly recognized up to 120 km source-receiver distance. Their linear moveout suggests an apparent velocity close to 6.0 km/s which slightly increases toward the east. Intracrustal reflections PcP can be observed on the record sections at offsets between 35-135 km. Near the coast the PcP phase occurs immediately after the Pg phase, while eastward it clearly arrives later and at farther offsets. Similar to the CINCA data, the PmP phase arrives at longer distances for stations eastward, suggesting that the oceanic Moho dips in the same direction. The Pn phase is not observed in all the record sections, but represents the first arrival for offsets larger than 150 km (Fig. 7.5).

On the OBS/OBH dataset, Pg, PcP and PmP phases were correlated on the stations located east of the trench, while on record sections corresponding to stations placed west of the trench, two phases (L2 and L3) were interpreted as diving waves of the layer 2 and layer 3 of the oceanic crust. West of the trench PmP phases and refractions from the uppermost mantle were also correlated (Fig. 7.6).

On the onshore data the Pg phase is the first arrival for offsets up to 20 km. In the range of 100-150 km distance, upper and lower crustal refractions are the first arrivals with average apparent velocity of 6.4 km/s. Between 30-90 km offset, two intracrustal reflections appear as first arrivals. After 1 second reduced traveltime, the PmP phase is observed between 110-180 km offset. No Pn phase was recognized on this section (Fig. 7.7). Details about phase correlation and modeling can be found in Krawczyk et al. (2006).

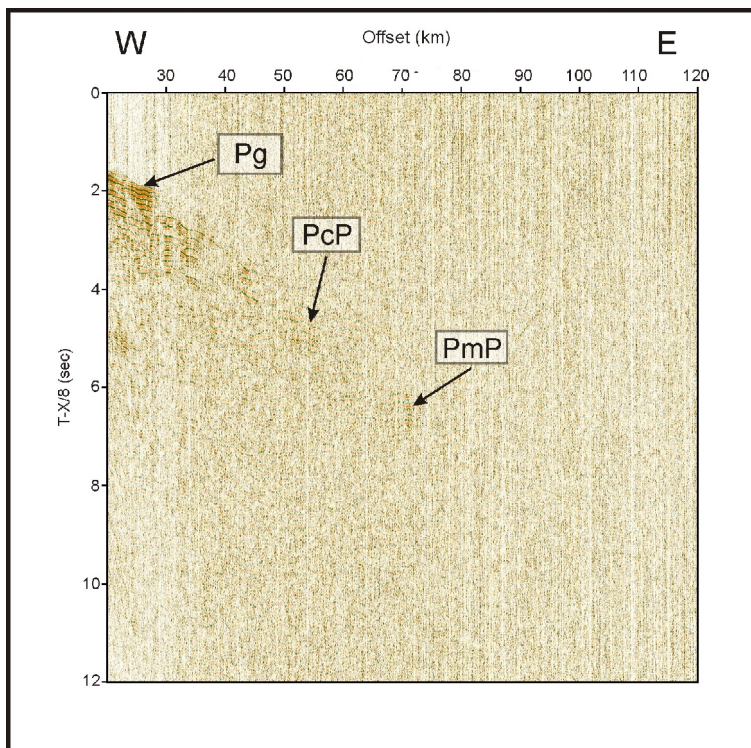


Figure 7.5: SPOC Line SO161-038. Receiver gather of station 1 with interpreted phases. Vertical axis is time reduced with 8 km/s.

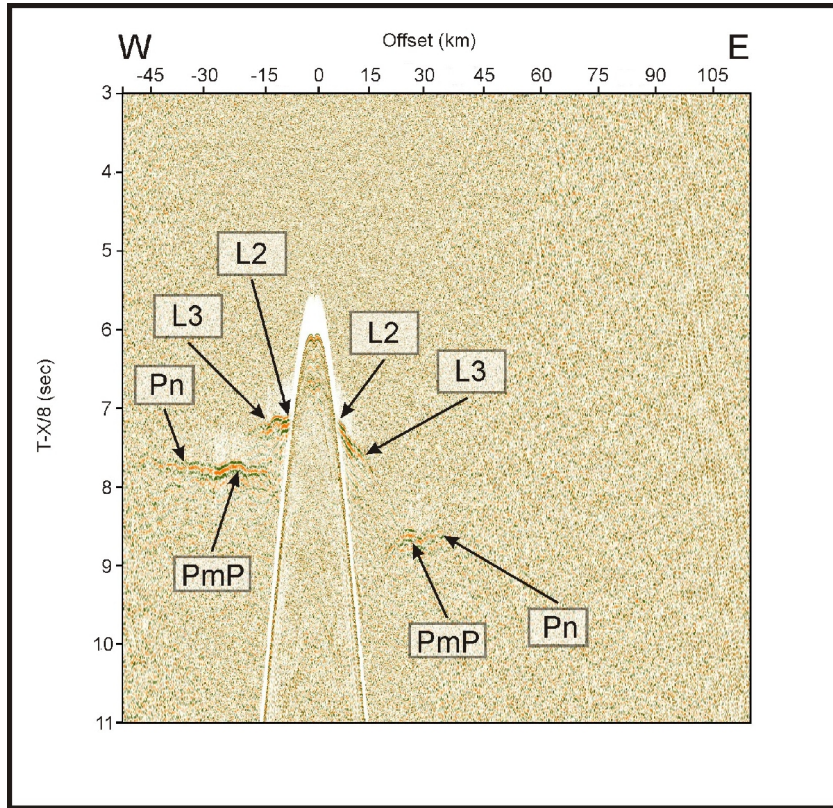


Figure 7.6: SPOC Line SO161-038. Receiver gather of the OBS/OBH data with interpreted phases. Vertical axis is time reduced with 8 km/s.

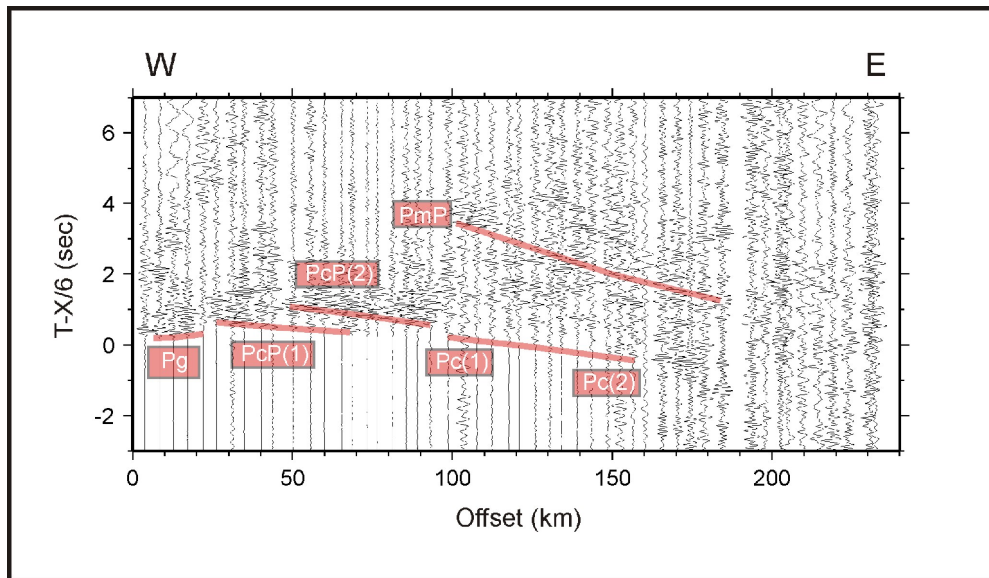


Figure 7.7: Shot gather of the onshore seismic profile at 38.2°S with interpreted phases. Vertical axis is time reduced with 6 km/s.

7.4 Seismic Data Processing

Wide-angle marine data is usually contaminated with coherent and random noise, masking reflections and useful signals. The unwanted signal must be eliminated or attenuated in order to avoid artifacts during the migration process. In the case of the CINCA wide-angle data the signal-to-noise ratio of the raw data is very low. The severe background noise generated by the heterogeneities in the subsurface and reverberations represent the most prominent noise features. In addition, refracted S arrivals coming from the uppermost crust are present at short offsets in some of the recording sections. Fig. 7.8 shows an example of one receiver gather of the CINCA Line 201/202 before and after the application of the processing flow. Interpreted phases and typical noise are indicated.

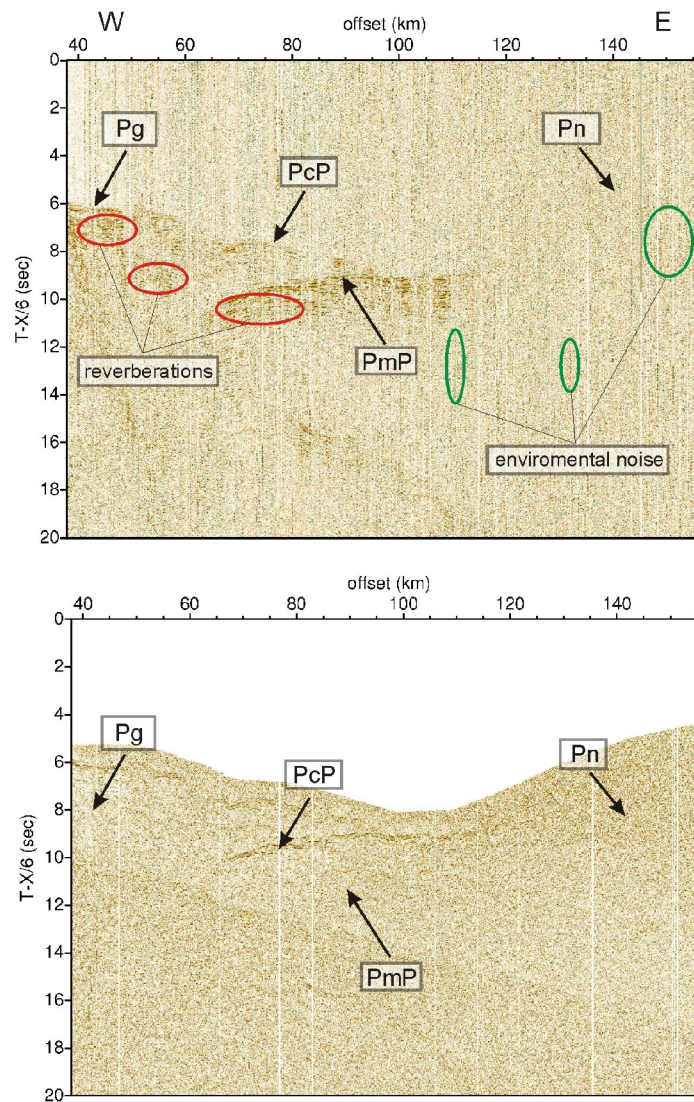


Figure 7.8: Receiver gather of Line 201/202 at 21°S before (top) and after (bottom) application of the processing flow. Interpreted phases and typical noise are indicated.

Before migration, standard pre-processing tools were applied with the seismic data processing software ProMax® in order to remove unwanted signals and to improve the signal-to-noise ratio. Fig. 7.9 shows the processing flow applied to the CINCA and SPOC wide-angle dataset. Every step of the processing flow is described in detail in the following.

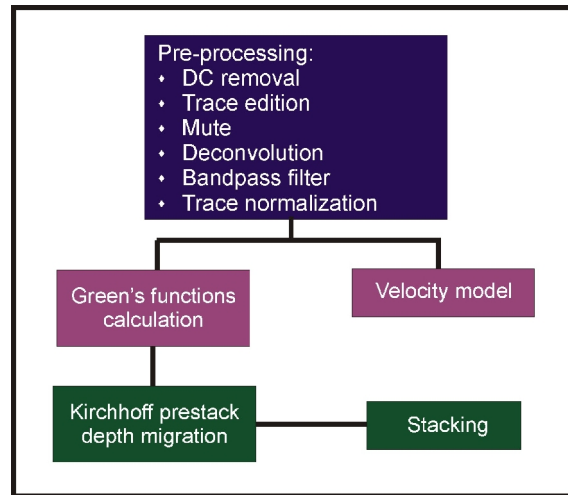


Figure 7.9: Processing flow.

1) DC removal. To correct for the instrument amplifier drift, the mean amplitude value of each trace is calculated and then subtracted.

2) Trace editing. Spiky and null traces as well as those presenting strong ambient noise were removed.

3) Muting. A top mute was applied to the data to eliminate the noisy signal before the first arrivals.

4) Spectral analysis. In order to define the dominant frequency, the useful frequency band and the low and high cut for a bandpass filter, an spectral analysis was performed. The dominant frequency ranges between 6-8 Hz while the mean useful frequency range is 3-12 Hz. Some recording section have narrower or larger useful frequency band. Fig. 7.10 illustrates the amplitude spectrum of the interpreted seismic phases in the CINCA data.

5) Predictive deconvolution. Deconvolution is a process that improves the temporal resolution of seismic data not only by compressing the basic seismic wavelet but also by removing unwanted signal like multiples and reverberations (Yilmaz, 2001) and it has been applied in several wide-angle experiments as an useful aid in seismic phases identification (Gohl and Smithson, 1993; Lizarralde and Holbrook, 1997; Kopp et al. 2000; Thornton and Zhou, 2008). The airgun shots produce bubble pulses or pressure reverberations within the water that oscillate for several cycles and affect the recorded data by creating a ringy source function (Shearer, 2006). This source function when convolved with the reflectivity series will be reproduced for each reflector (Fig. 7.11). The reverberations produced by the collapse of

the source bubble were successfully removed in the CINCA wide-angle dataset applying the Wiener-Levinson predictive deconvolution. An operator of 50 ms length with a predictive distance of 1000 ms provided the best results in compressing the wavelet, leading to an easier identification of the most prominent arrivals (Fig. 7.12).

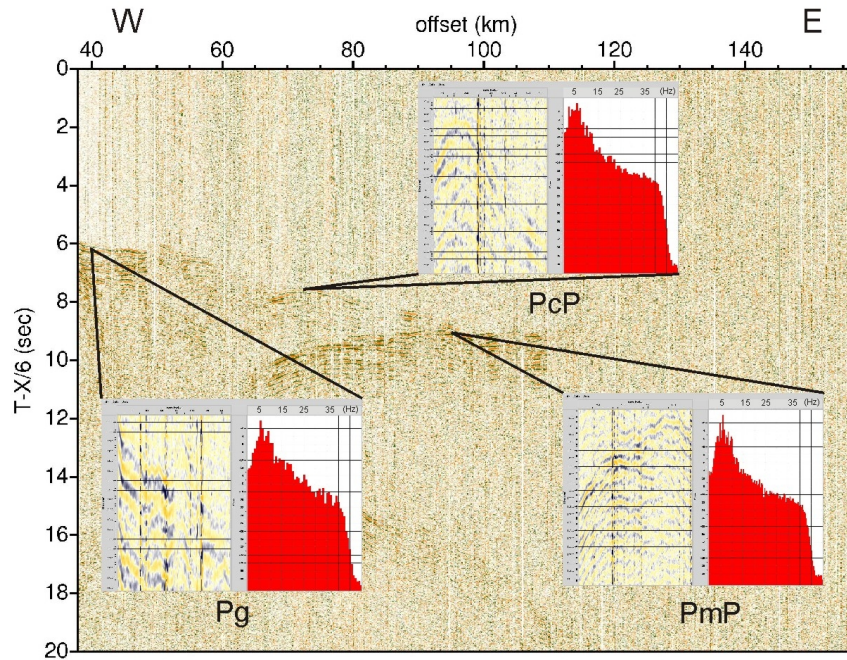


Figure 7.10: Spectral analysis of the interpreted phases of the CINCA wide-angle data. The dominant frequency of the whole dataset ranges between 6-8 Hz.

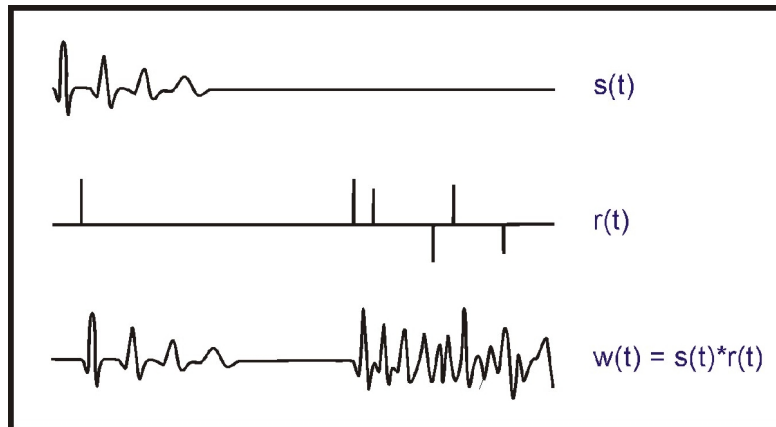


Figure 7.11: Effects of the reverberations on the seismic record (modified after Shearer, 2006). The source-time function $s(t)$ produced by an airgun contains a series of bubble pulses yielded by pressure reverberation within the water. When $s(t)$ is convolved with reflectivity series $r(t)$, a complex time series $w(t)$ is produced, in which the closely spaced reflectors are not easy to identify.

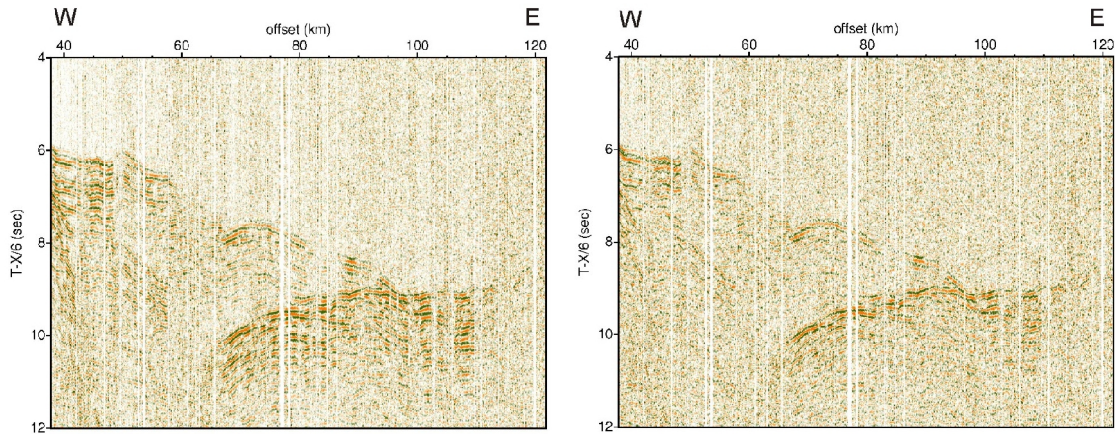


Figure 7.12: Receiver gather before (left) and after (right) predictive deconvolution. Reverberations are attenuated and the interpretation of seismic phases becomes easier.

6) Bandpass filtering. The goal of the bandpass filtering is to preserve a certain bandwidth with no modification and to suppress the remaining part of the spectrum (Yilmaz, 2001). To attenuate frequency bands with low signal-to-noise ratio and according to the results of the spectral analysis, every trace was filtered in the frequency domain using a zero phase Ormsby bandpass filter with the corner frequency values (2-3-12-14) Hz for the CINCA data and (3-4-14-16) Hz for the SPOC data.

7) Trace normalization. Before migration every trace is normalized according to its maximum amplitude value.

8) AGC. A 1000 ms window gain was applied only for display purposes.

7.5 Modeling and velocity models

7.5.1 Velocity models in Northern Chile

The velocity models used for KPSDM from the North of Chile were derived by Patzwahl (1998) using the interpreted traveltimes of the airgun data and chemical explosions data. The velocity value of the upper crust of the overriding South American plate and the low velocity material over the crystalline crust east to the trench were obtained by modelling of the Pg phase. The geometry of intracrustal reflectors has been modelled by using the intracrustal phase “b” whereas the depth of the crust-mantle boundary and uppermost mantle velocities were obtained from PmP and Pn traveltimes information.

Error estimates for the models were reported in Patzwahl (1999). The maximum absolute difference between the observed and modelled traveltimes is about 0.12 sec for the Pg phases, 0.13 sec for intracrustal reflections, 0.22 sec for PmP arrivals and 0.23 sec for Pn phases. These time differences lead to over/under estimation of boundary depths and their corresponding velocities. For the modelled intracrustal boundary the error in depth was calculated to ± 3 km, while for the oceanic Moho an increased error about $\pm 3-5$ km was reported. Details of error estimation, phase correlation and interpretation of the wide-angle data from the air gun profiles are summarized in Patzwahl et al. (1999), Table 3.

Lines 201/202 at 21°S

The upper crust was modelled with an average velocity range from 6.2 km/s offshore increasing to 6.42 km/s near the coast line and decreasing to 6.3 km/s and 6.0 km/s at 100 and 150 km from the coast line respectively. By using the interpreted phase “b” the dipping eastward intracrustal reflector between 6 and 20 km depth was modelled. Also, these intracrustal reflections were the base to model the upper-lower crust boundary at 25 km depth and 150-190 km offset. The Nazca plate was modelled as an about 7 km thick dipping layer with a dip angle of 10° near the trench to 23° at 100 km from the trench. The depth of 48-55 km of the crust-mantle boundary between 220-250 km offset was derived from onshore wide-angle data (Fig. 7.13).

Lines 301/302 at 22.2°S

The P velocity values for the upper crust have been modelled with 6.5 km/s near the coast line, increasing eastward up to 6.7 km/s at 100 km from the coast. Near the trench, the subducting slab has a dip angle of 10°, increasing to 25° close to the coast. The crust-mantle boundary has been modelled with a dip angle of 5° between 250-300 km distance at 50-55 km depth. From the modelling of intracrustal reflections, a 14° dipping eastward layer between 160-220 km from the trench up to 30 km depth was derived (Fig. 7.14).

Lines 401/402 at 23.25°S

The average velocity of the crust at 200 km distance is 6.6 km/s, decreasing eastward to 6.5 km/s at 300 km and 6.2 km/s at 400 km distance. An eastward dipping intracrustal reflector at 12 km depth and up to 100 km from the trench was modelled from the observed phase “b”. With a dip angle of 9° close to the trench and 21° near the coast, the subducting oceanic crust is modelled reaching a depth of 37 km at 75 km east of the trench. From onshore wide-angle measurements, the base of the crust extends from 250 km to 440 km distance at 43-64 km depth (Fig. 7.15).

7.5 Modeling and velocity models

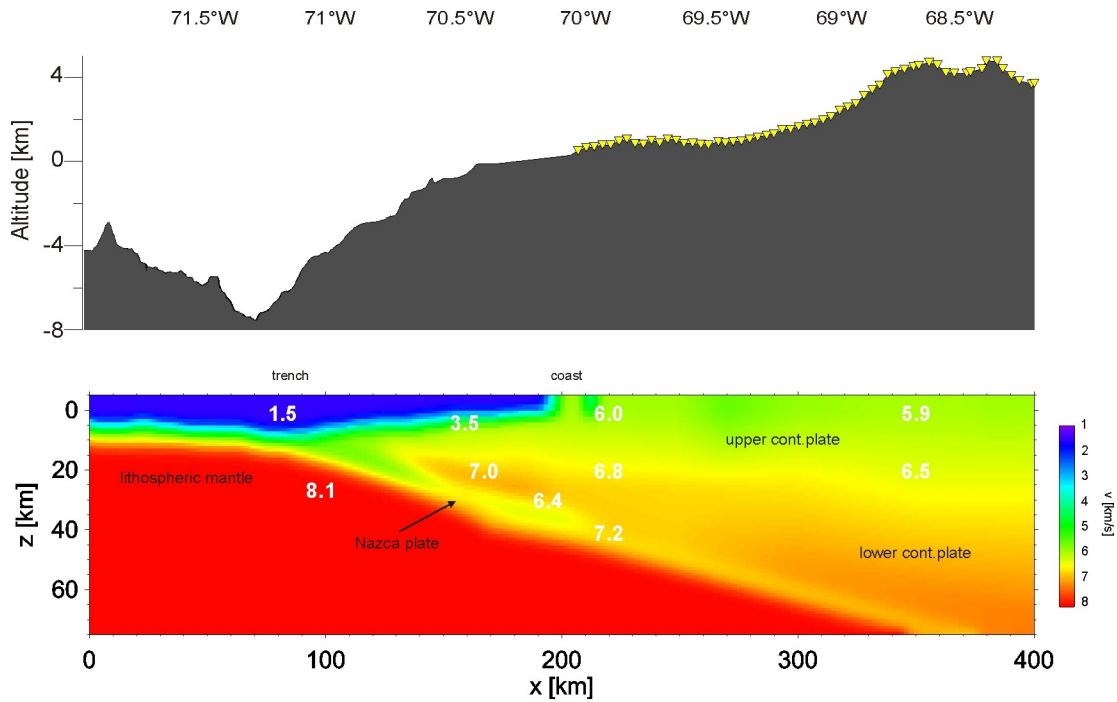


Figure 7.13: CINCA Velocity model Lines 201/202 at 21°S as derived from iterative travelttime modeling (Patzwahl, 1999). P-wave velocities are shown in km/s.

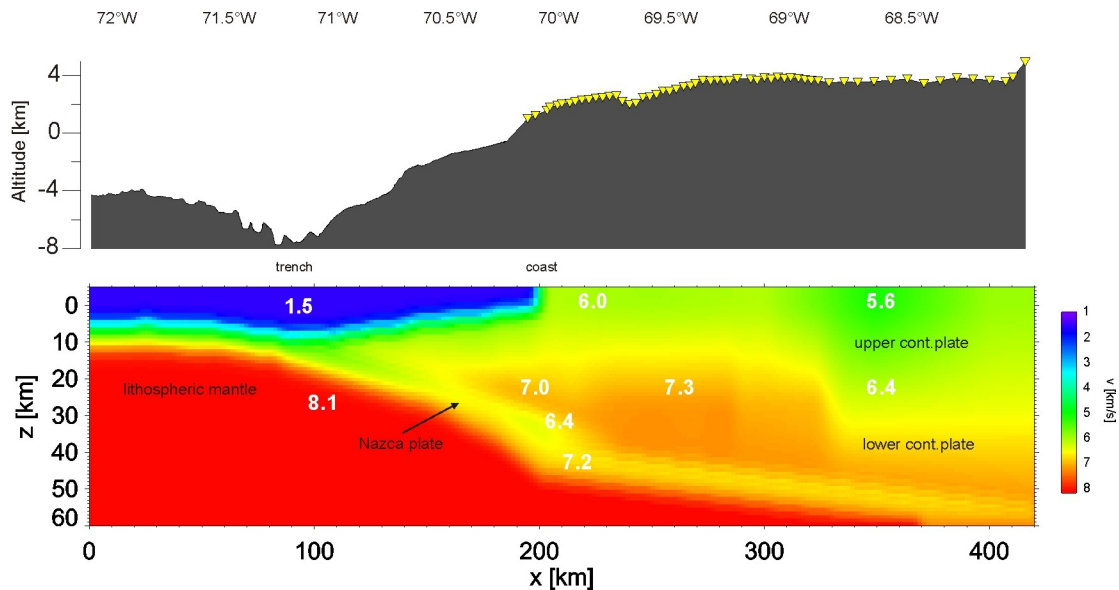


Figure 7.14: CINCA Velocity model Lines 301/302 at 22.2°S as derived from iterative travelttime modeling (Patzwahl, 1999). P-wave velocities are shown in km/s.

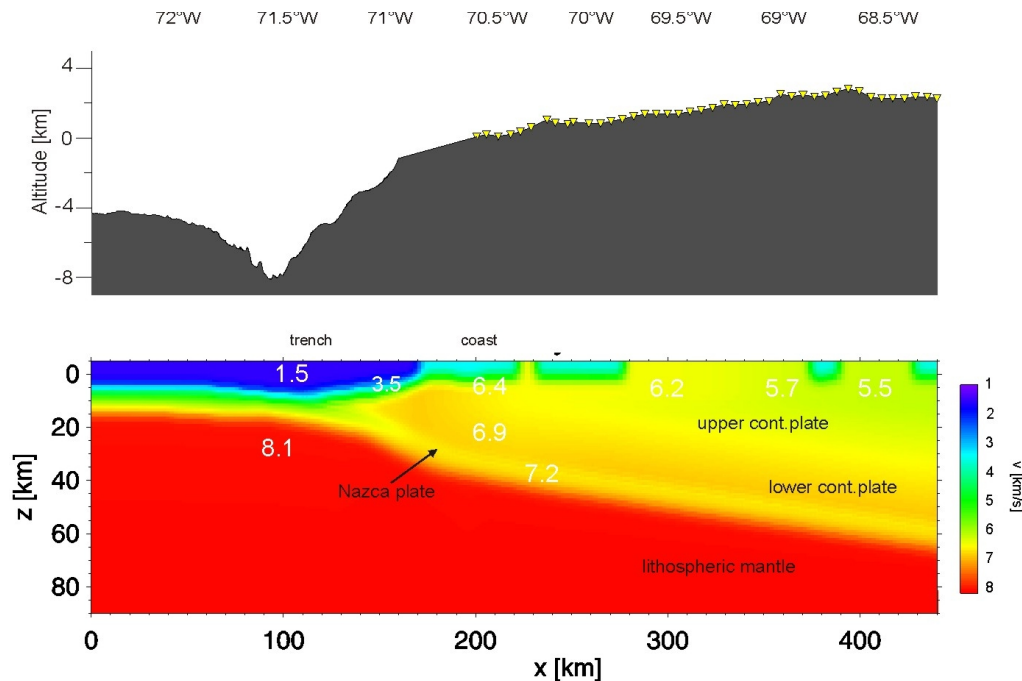


Figure 7.15: CINCA Velocity model Lines 401/402 at 23.5°S as derived from iterative travelttime modeling (Patzwahl, 1999). P-wave velocities are shown in km/s.

7.5.2 Velocity models in Southern Chile

Refracted arrivals from the upper crust, reflections on the oceanic crust-mantle boundary and refracted phases coming from the uppermost mantle were used to construct the velocity models for the SPOC profiles (Lüth et al. 2004).

Line S0161-038

The oceanic crust with 6-7 km thickness and the uppermost mantle represent the westernmost part of the model (Fig. 7.16). Between the trench area and the coast line the accretionary wedge, conformed by heterogeneous and poor consolidated sediments, has been modeled with P-wave velocities lower than 3.5 km/s. Farther inland the onshore Chilean margin was divided in three layers. The uppermost layer characterized by typical P-wave velocity values (5.9-6.1 km/s) has a thickness of about 10 km. The second layer presents higher P-wave velocity values (6.2-6.5 km/s) with an increasing thickness from the coast about 6 km until the Main Cordillera where it reaches a maximum of 10 km. Finally, the lower continental crust is modeled with P-wave velocities of up to 7 km/s. Clear arrivals from the continental Moho were not observed (Lüth et al. 2004). The Nazca plate has been modeled with a dip angle of about 18° below the coastline reaching depths of approximately 45 km. Below the oceanic slab, the uppermost mantle shows P-wave velocities of about 8.0-8.1 km/s. The offshore part of the model was constructed from the interpreted phases on the

7.6 Kirchhoff prestack depth migration of CINCA wide-angle data

OBS/OBH data being diving waves from oceanic crust layers, the reflection from the oceanic Moho and the refracted wave from the upper oceanic mantle the most prominent arrivals (Lüth et al. 2004).

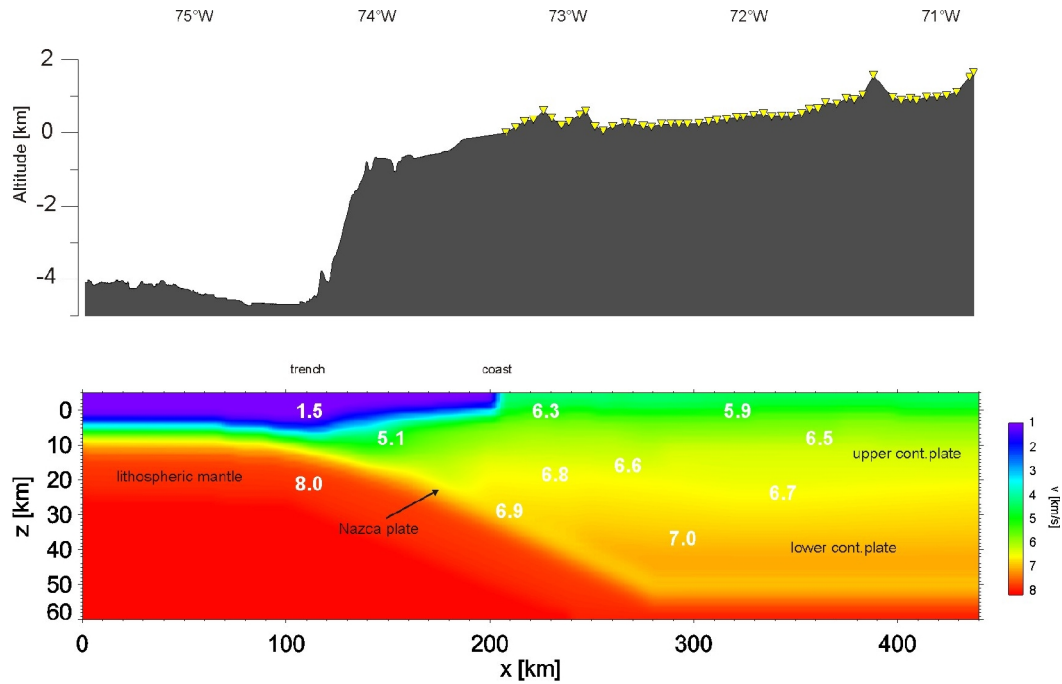


Figure 7.16: SPOC Velocity model Line SO161-038 at 38.2°S as derived from iterative travelt ime modeling (Lueth et al. 2004). P-wave velocity values are shown in km/s.

7.6 Kirchhoff prestack depth migration of CINCA wide-angle data

The data processing flow was introduced in section 7.4. The first part consisted in the application of pre-processing algorithms to attenuate unwanted signals and enhance the signal-to-noise ratio. Here, the flow continue with the application of the KPDM approach, including the preparation of the velocity models and computation of diffraction surfaces along which the amplitude summation takes place.

Velocity models

The 2D velocity models derived by Patzwahl (1998) were discretized on a sparsely sampled grid with cells of 1km x 1km and finally smoothed to avoid steep structures with strong velocity contrast. These average velocity values are the base for the travelt ime calculations described in the following. Finally, the velocity models were extended to 3D assuming no variations in N-S direction.

Diffraction surfaces or Green functions calculations

As prestack depth migration is performed in a variable velocity medium, the diffraction surfaces along which the amplitudes are summed must be computed numerically. Here, the method of Podvin and Lecomte (1991) is applied, consisting of a finite difference solution of the eikonal equation. The method computes multiple arrivals from different propagation modes including body waves, diffractions and head waves and uses the Fermat's criterion to retain the first arrival without considering amplitude information.

The velocity model is divided into cells of constant values and then the first arrival traveltimes are computed at the nodes of each cell from every source point and receiver locations (Fig. 7.17). The sum of the traveltimes of one shot location t_S and its corresponding receivers t_R defines the diffraction curve t_I for the migration process.

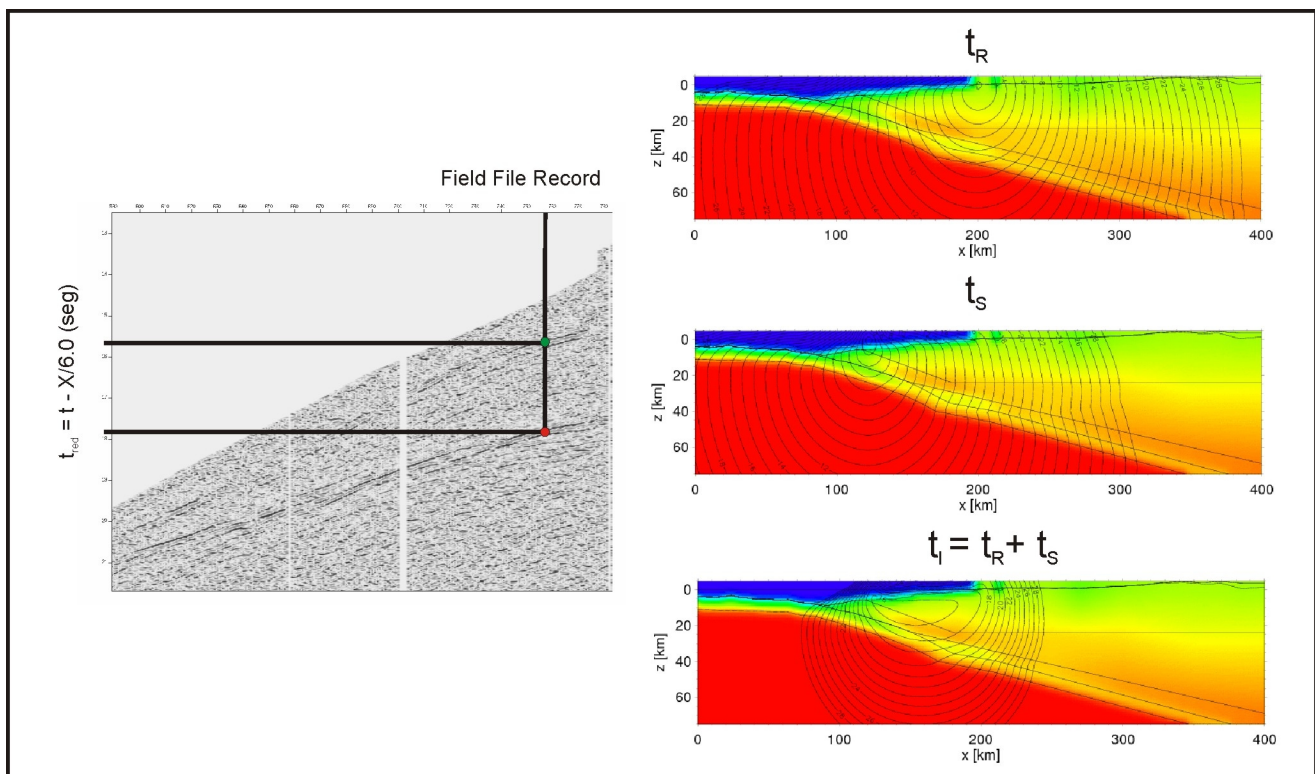


Figure 7.17: Computation of diffraction surfaces. First arrivals traveltimes are calculated at the node of each cell for every source and receiver location. The summation of traveltimes for every receiver and the corresponding source satisfy the imaging condition

$$t_I = t_S + t_R$$

7.6 Kirchhoff prestack depth migration of CINCA wide-angle data

Audebert et al. (1997) suggest that imaging assuming a single arrival from each source point may lead to inaccuracies in Kirchhoff migration results, provided that first arrivals do not supply meaningful contribution to the reflection process in complex media compared to the later maximum amplitude arrival times.

In crystalline media like deep continental settings, blurred reflectivity is produced by scattering and diffraction instead of reflections from first order discontinuities, and because the first arrivals carry significant energy their use can be justified here (Buske, 1999).

Prestack depth migration approach

Migration is performed from topography in a 3D gridded volume containing the real position of sources and receivers according to the method of Buske (1999). Fig. 7.18 shows the migration volume of lines 201/202 at 21°S, consisting of 11 slices 5 km apart (y-axis), and dimensions of 400 km length (x-axis) and 80 km depth (z-axis). Receiver gathers and traveltimes tables are the input for the summation process.

Every gather is migrated separately using the phase information of the each trace and then a migrated volume is constructed by stacking the nearest slices to the recording line. The final migrated volume of the recording line is generated by summing the migrated volumes of the individual gathers.

The stacking is done by calculating the absolute value, trace envelope summation or by phase-consistent summation of every trace. The stacking of the absolute value is an effective method to avoid destructive summation of less coherent features (Buske, 1999), while the stacking of the trace envelope yields sections with lower resolution, but which are robust against possible velocity inaccuracies (Bleibinhaus et al. 2003).

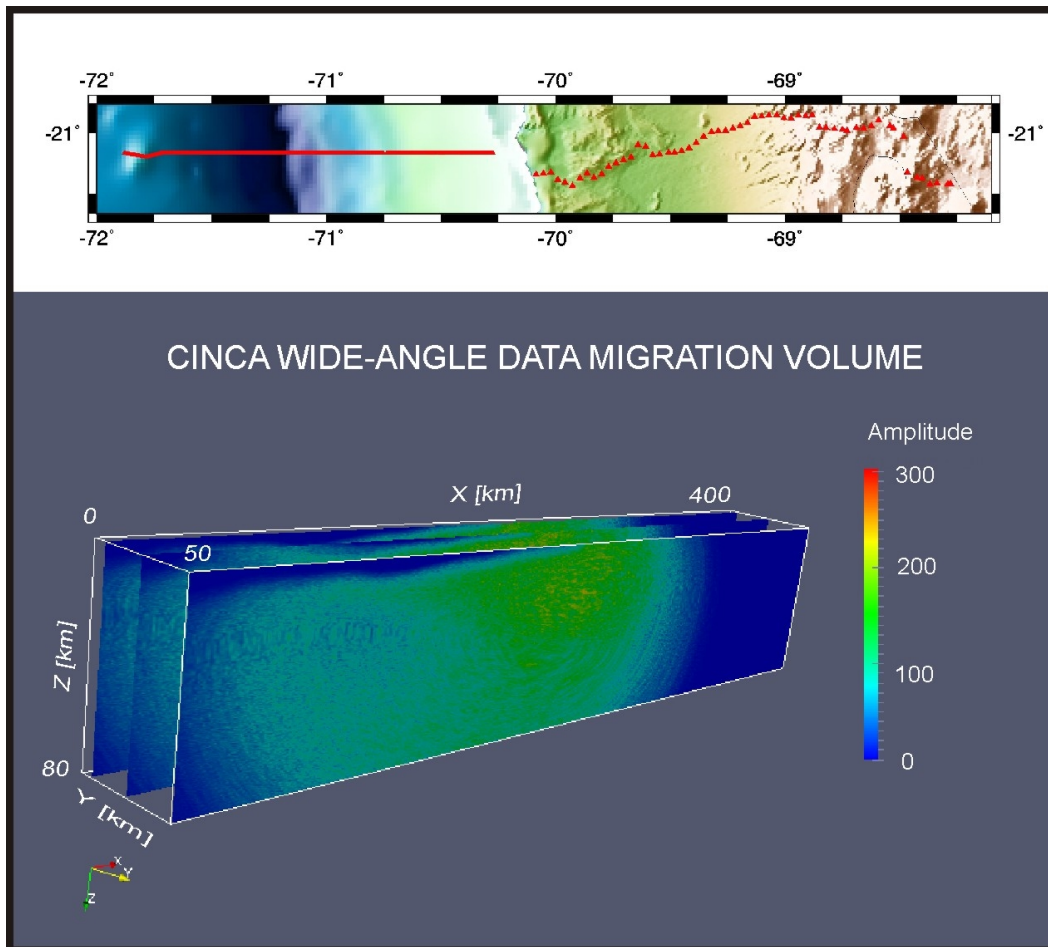


Figure 7.18: Wide-angle migration volume for Lines 201/202 at 21°S. The migration is performed from topography in a volume of 400 km in x-direction, 50 km in y-direction and 80 km in z-direction.

8 Results of wide-angle imaging using Kirchhoff prestack depth migration

The migration of the CINCA and SPOC wide-angle data has been performed taking into account different parts of the recorded wavefield e.g. the migration of the complete recorded section, migration of the reflective wavefield (refracted arrivals not considered) and migration considering only intracrustal reflectors and/or reflections from the Moho. This strategy allows to differentiate between “real” migrated reflectors and migration artifacts that could be interpreted as “real” structures. In Chapter 9 the interpretation of the structures observed in the migrated sections is given as well as their comparison with the results of other geophysical methods.

For the CINCA data further analyses were carried out including depth migration in different offset ranges and the application of the Reflection Image Spectroscopy (RIS), an approach based on the frequency dependence of the scattering due to heterogeneities in the medium. In order to provide a geological and structural meaning of the migrated energy, the velocity model boundaries are plotted on to the migrated sections.

Fig. 8.1 shows the CINCA wide-angle profiles and their corresponding prestack depth migrated sections, which are described in the following.

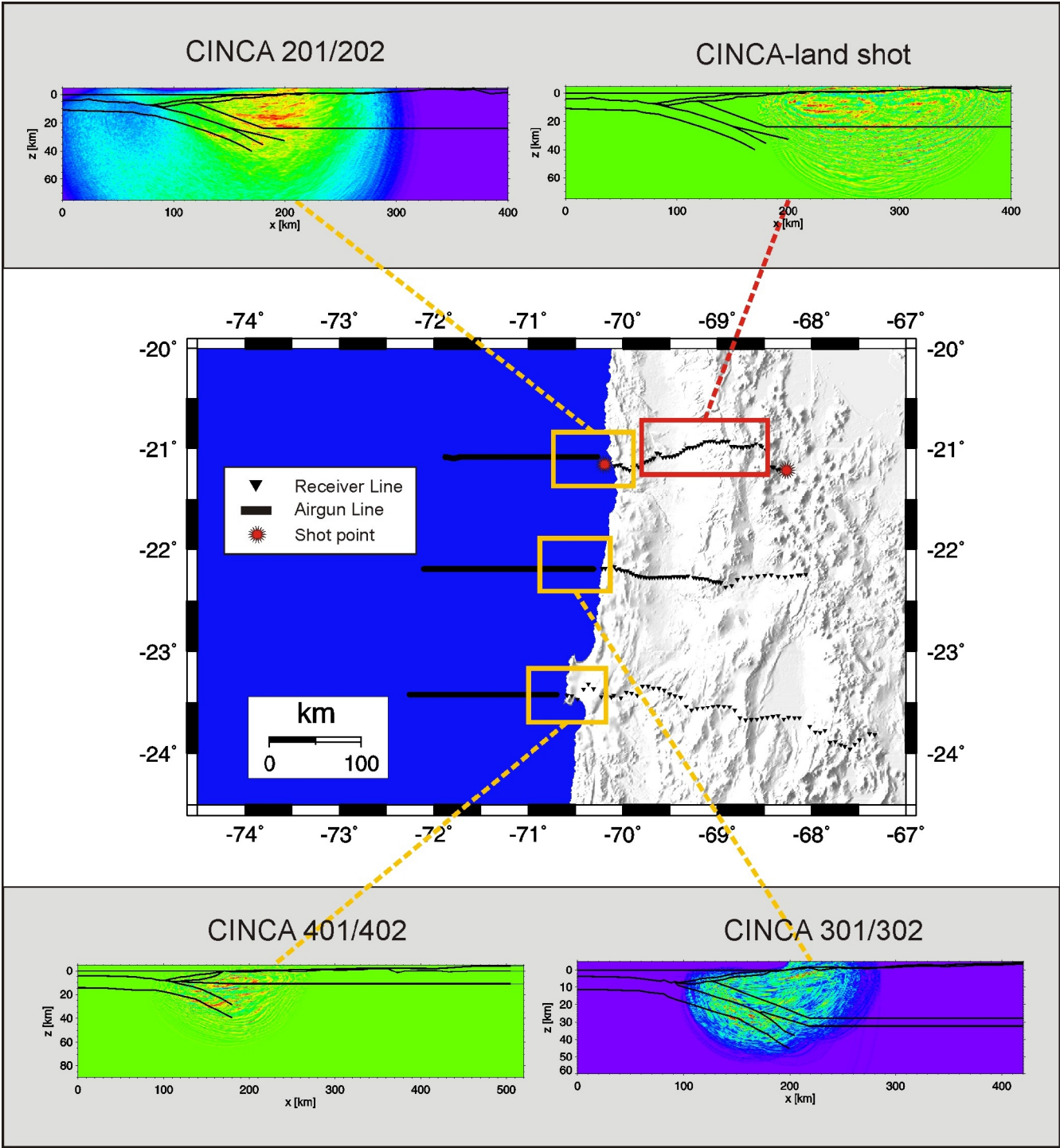


Figure 8.1 Synthesis of wide-angle imaging in northern Chile. The results comprise the KPSDM of the amphibious and onshore data.

8.1 Wide-angle imaging in northern Chile

8.1.1 Lines 201/202 at 21°S

Migration of the complete wavefield

The complete recorded wavefield, including Pg, Pn and Sg arrivals, was migrated. Fig. 8.2 shows the results corresponding to lines 201/202 stacked according to the absolute value of the traces and by phase-consistent stacking. In general, the signal-to-noise ratio of these sections is very low, making it difficult to recover “real” migrated reflections. Artifacts probably generated by refracted arrivals and background noise appear all over the sections, in particular those dipping NW between 120-230 km distance at shallow depths. A group of high amplitude reflectors between 15-25 km depth and 80-130 km distance are aligned over and below the crust-mantle velocity boundary and can be associated to structures of the bottom of the oceanic crust. Intracrustal reflectors can not be visualized because of dominant migration artifacts. Possible upper mantle reflectors can be also identified between 25-40 km depth and 80-140 km distance.

Migration of the reflective wavefield

In this case the refracted arrivals from the upper crust and uppermost mantle were removed, considering for migration only the reflective part of the wavefield. The migrated section shown in Fig. 8.3 contains less artifacts and some structures are better visualized than the in the migrated section of the complete wavefield. East dipping intracrustal reflectors are imaged between 145-180 km distance at 14-24 km depth. Strong horizontal reflectivity is visible in the upper crust between 155-215 km distance and at depths of 10-20 km. Likewise, a strong horizontal reflector can be observed in the region of the upper-lower crust boundary at 25 km approximately between 180-210 km distance. Parallel to the slab weak reflectors are visible on the top of the LVZ between 160-188 km distance at 24-28 km depth. Energy coming from the bottom of the oceanic plate and uppermost mantle is imaged as high amplitude reflectors between 25-32 km depth and 125-150 km distance.

Migration of PcP and PmP arrivals

All receiver gathers were muted so that only intracrustal arrivals and reflections from the Moho were considered for migration. Apart from the usual artifacts generated by background noise, two strong reflectors can be visualized (Fig. 8.4). The first one dipping NW at 10-20 km depth and 120-150 km distance corresponds to intracrustal structures. Associated to the oceanic crust-mantle boundary, the second strong reflector occurs between 20-30 km depth and 120-150 km distance.

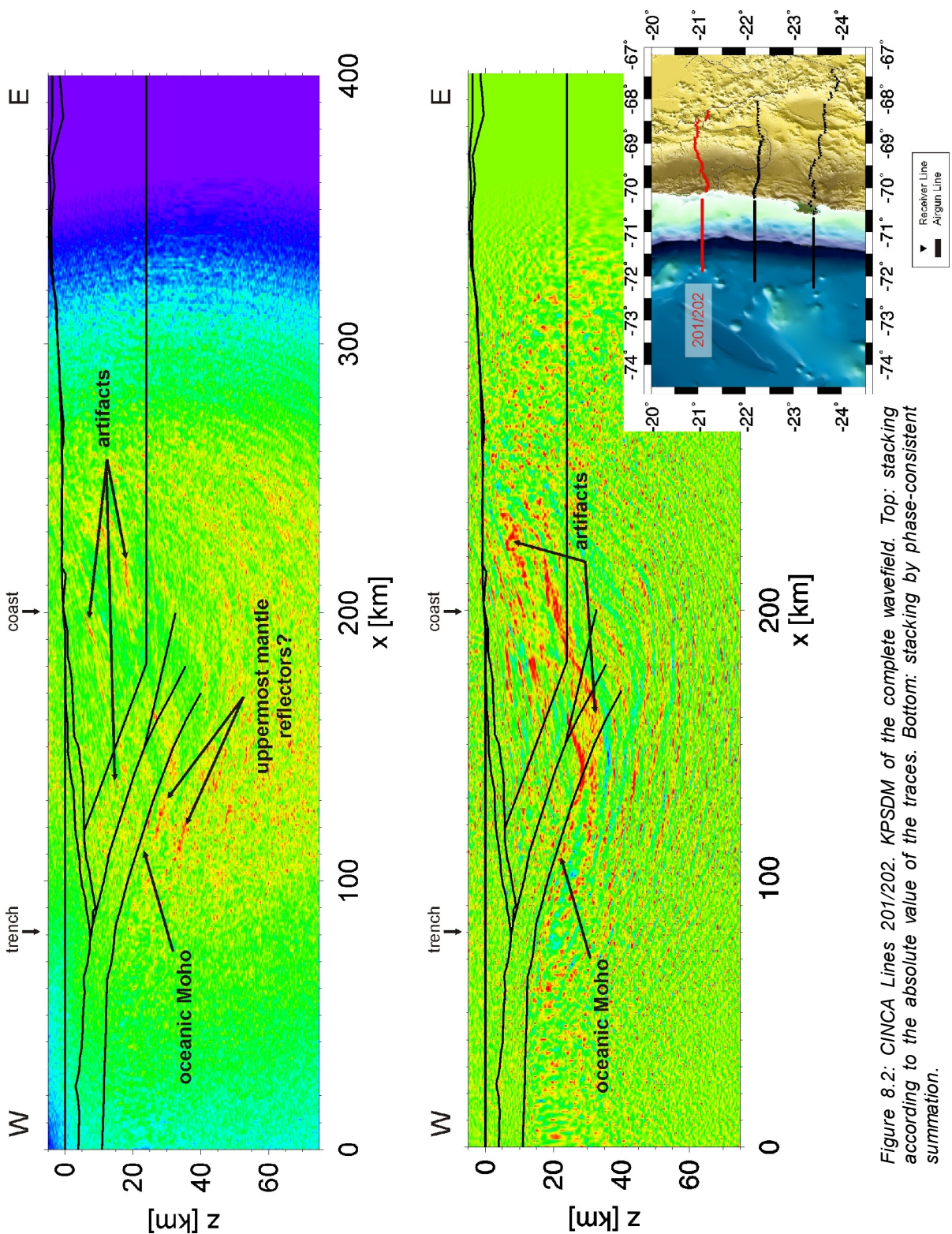


Figure 8.2: CINCA Lines 201/202. KPSDM of the complete wavefield. Top: stacking according to the absolute value of the traces. Bottom: stacking by phase-consistent summation.

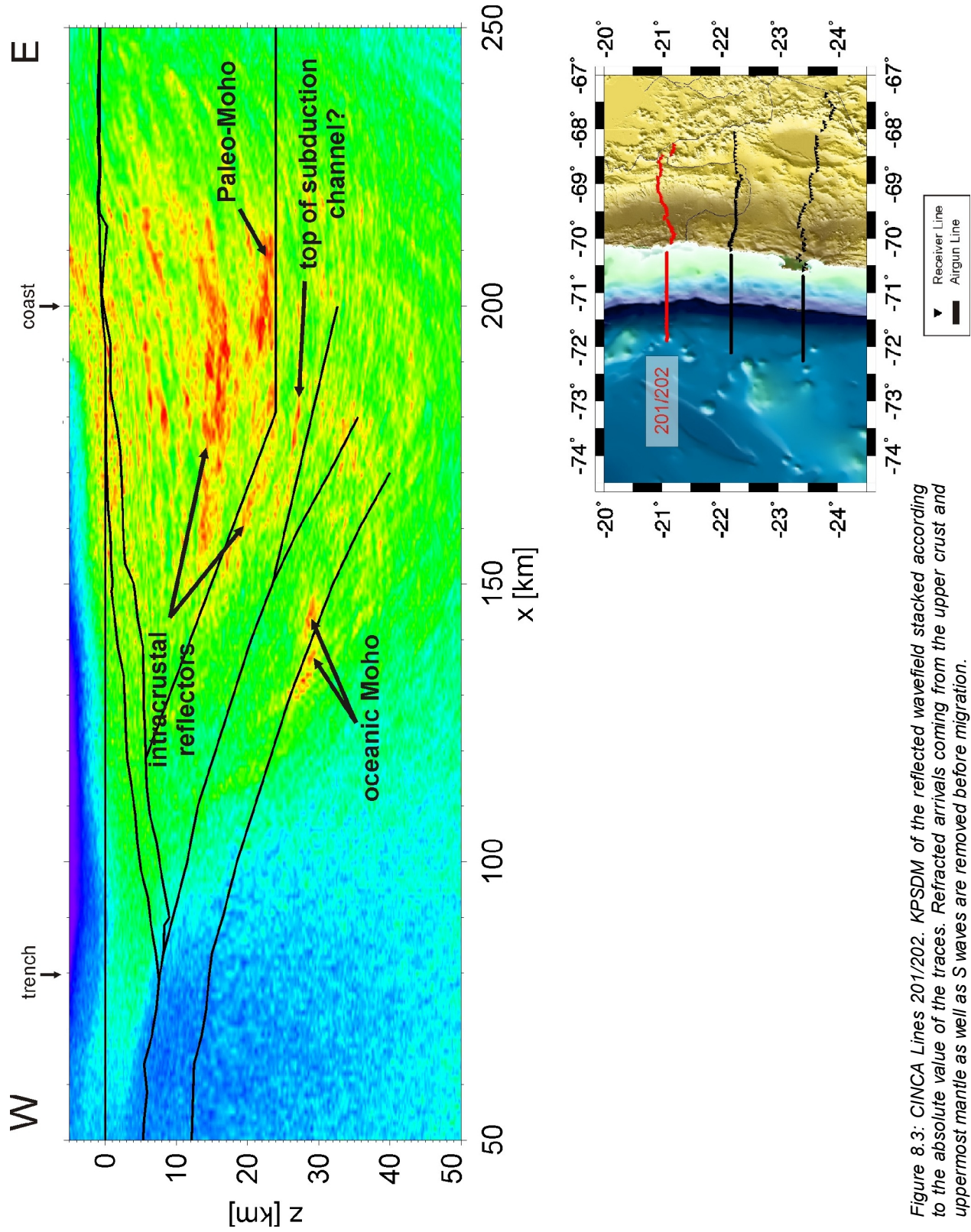


Figure 8.3: CINCA Lines 2011/202. KPSDM of the reflected wavefield stacked according to the absolute value of the traces. Refracted arrivals coming from the upper crust and uppermost mantle as well as S waves are removed before migration.

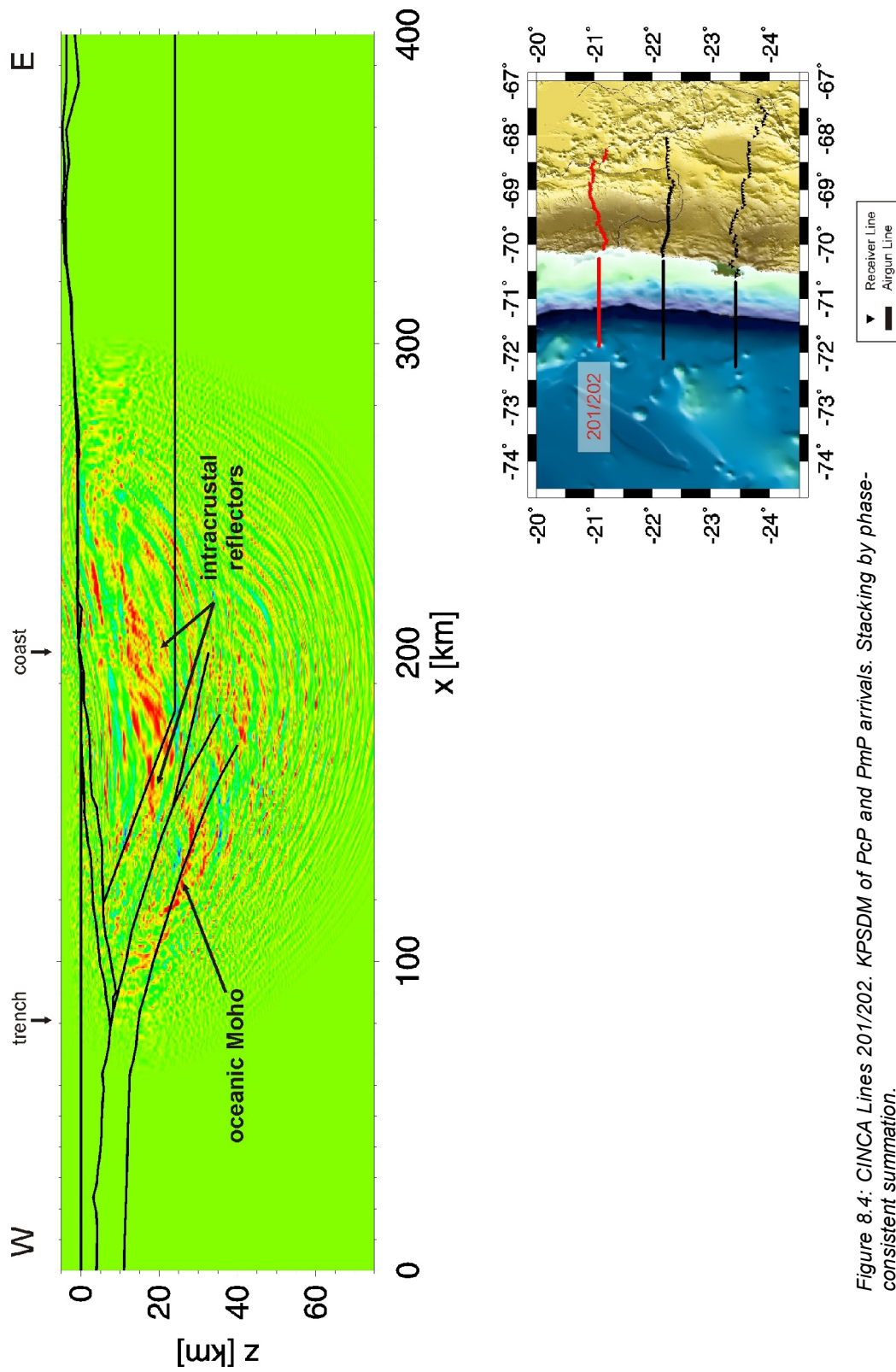


Figure 8.4: CINCA Lines 2011/202. KPSDM of PcP and PmP arrivals. Stacking by phase-consistent summation.

8.1.2 Lines 301/302 at 22°S

The Lines 301/302 show the lowest signal-to-noise ratio of the three recorded profiles. However, strong arrivals can be observed in some of the receiver gathers, in particular those located near the coast. For this reason, in this case the phases corresponding to intracrustal reflections and PmP arrivals were migrated separately.

Migration of the complete wavefield

In the migrated section considering the complete wavefield (Fig. 8.5) the oceanic crust-mantle boundary is imaged as a strong reflector at 20-25 km depth between 100-140 km distance. Additionally, east-dipping uppermost mantle reflectors are visualized under the oceanic Moho reflector, between 90-130 km distance at 22-32 km depth.

Migration of PcP and PmP arrivals

Fig. 8.6 displays the absolute value stacked sections respective to the migration of intracrustal reflections and Moho reflections. A couple of east-dipping reflectors can be visualized in Fig. 8.6 (top) above and below the velocity boundary between 150-170 km distance at 12-15 km depth representing mid-crustal structures. Some other structures can be seen as east-dipping segmented reflectors beneath the velocity boundary at 12-20 km depth.

On the other hand, the migrated section corresponding to the oceanic Moho arrivals (Fig. 8.6) reveals structures not only representing the oceanic crust-mantle boundary but also reflectors within the subducting slab.

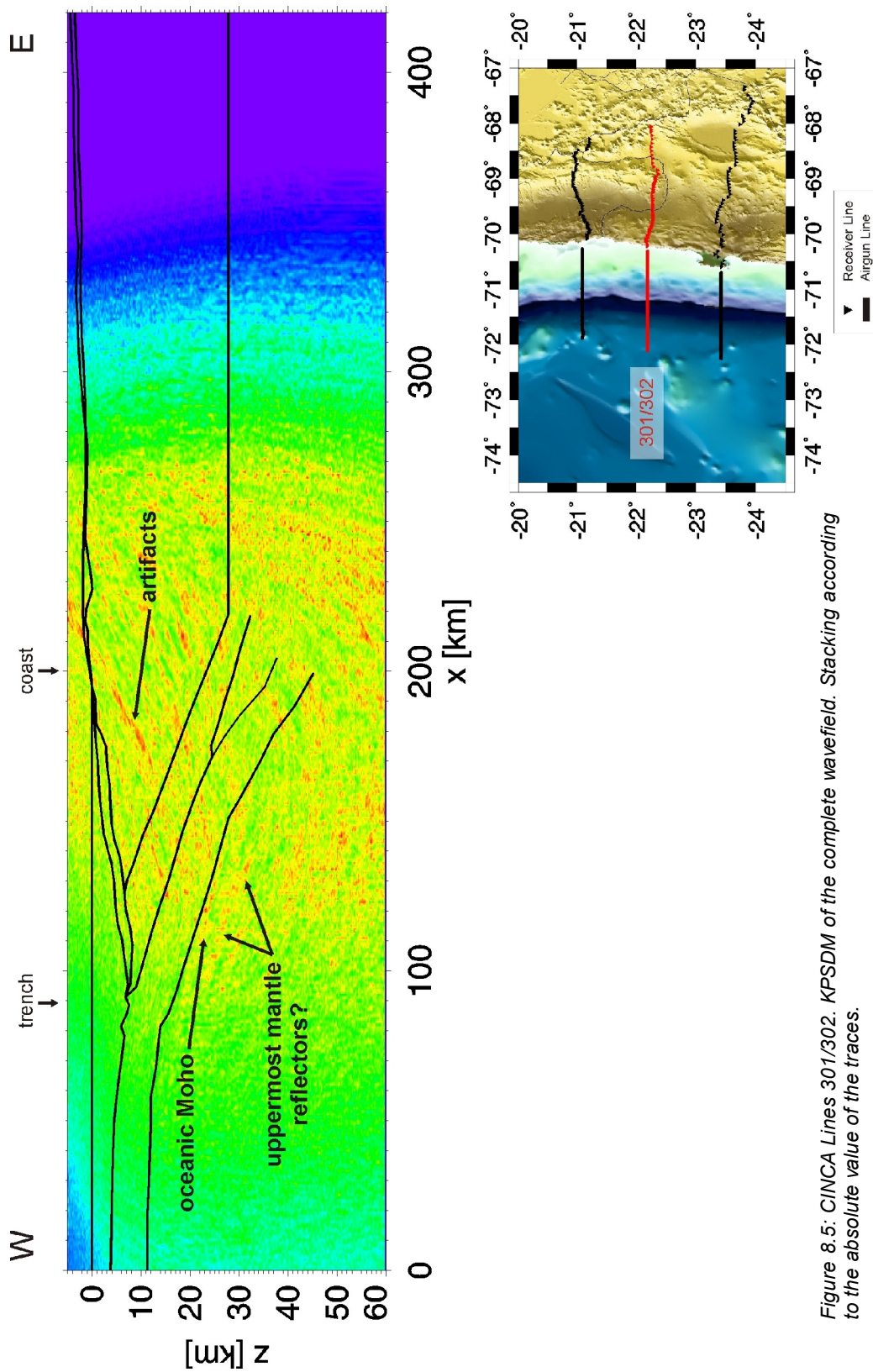


Figure 8.5: CINCA Lines 301/302. KPSDM of the complete wavefield. Stacking according to the absolute value of the traces.

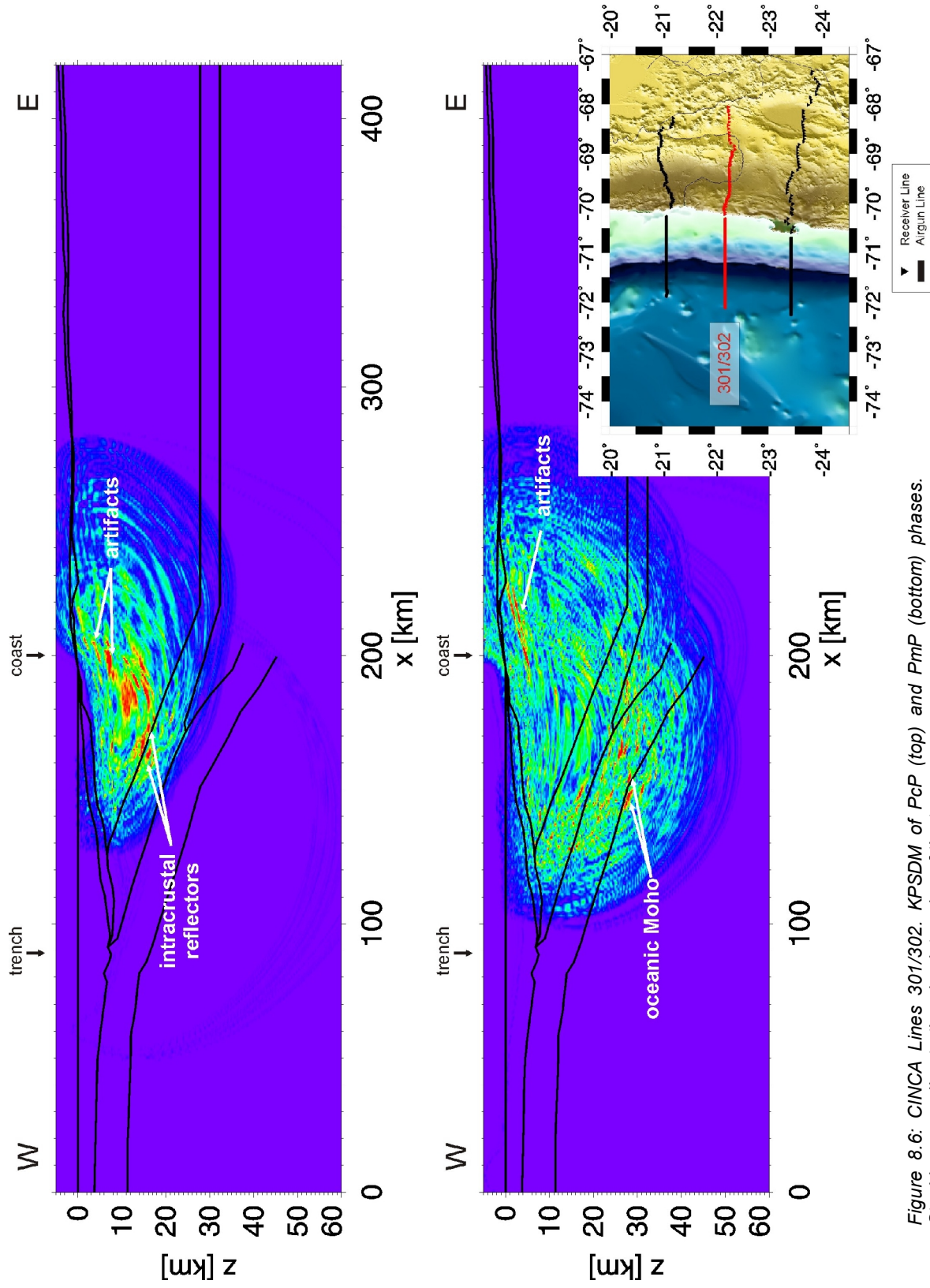


Figure 8.6: CINCA Lines 301/302. KPSDM of PcP (top) and PmP (bottom) phases. Stacking according to the absolute value of the traces.

8.1.3 Lines 401/402 at 23.25°S

The wide-angle data recorded at 23.25°S exhibit also a low signal-to-noise ratio. The background noise obscured the reflective events for the farthest receivers, so that the final migrated section comprises the contribution of the nearest receiver stations to the coast.

Migration of complete wavefield

The prestack depth migrated section of the complete wavefield is shown in Fig. 8.7. The most prominent feature is the sharp reflector representing a reflection/refraction from the oceanic Moho between 90-140 km distance at 20-25 km depth. No intracrustal reflectors were imaged due to the strong migration artifacts covering this part of the section.

Migration of PcP and PmP arrivals

The migration considering only the most prominent reflective phases is shown in Fig. 8.8. The oceanic Moho is clearly imaged at 25-30 km depth between 125-150 km along the profile. Weak uppermost mantle reflectors are also visible below the oceanic Moho. In the area below the coast, a sharp intracrustal reflector is observed between 155-190 km distance at about 10 km depth.

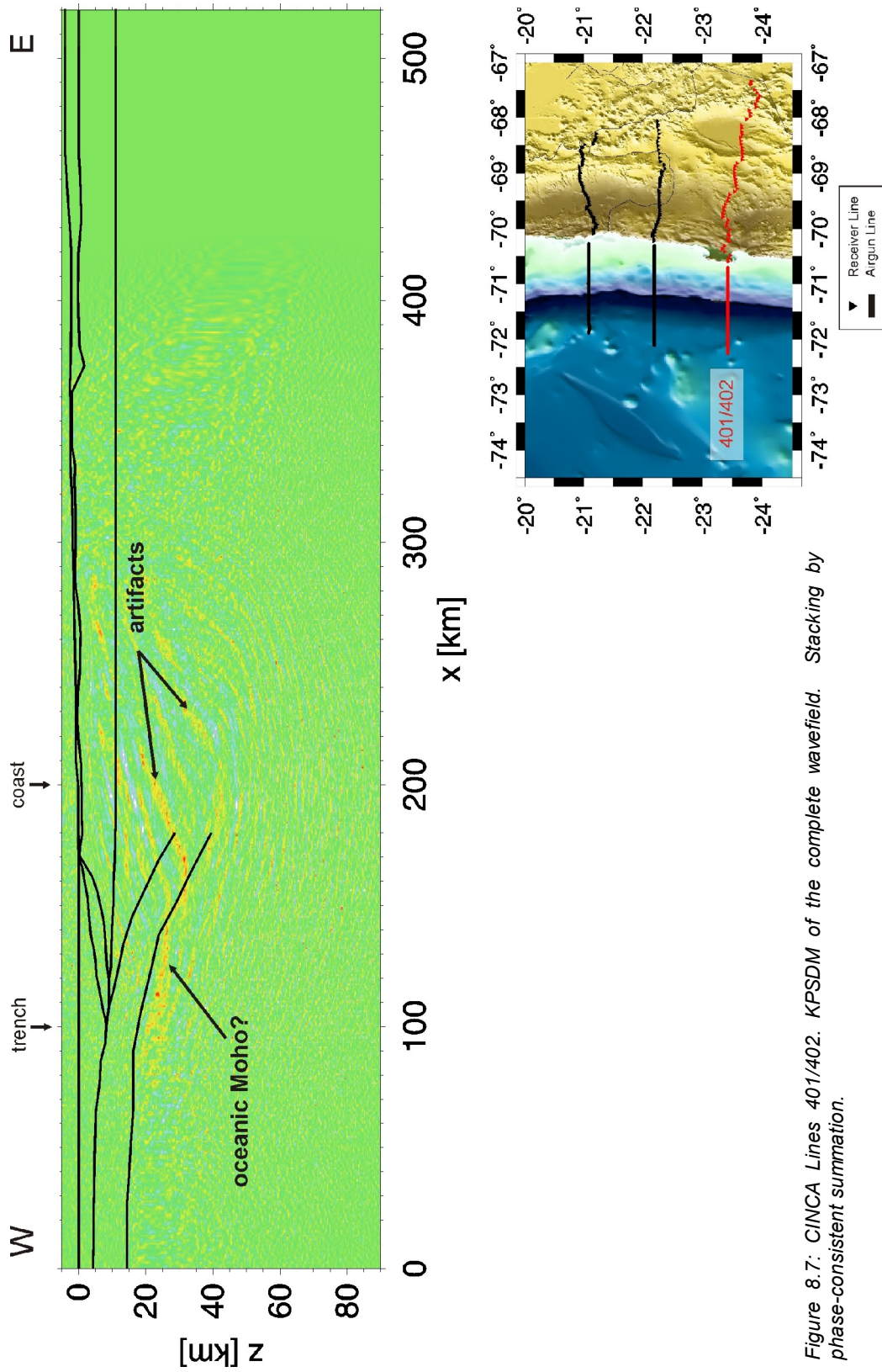


Figure 8.7: CINCA Lines 401/402. KPSDM of the complete wavefield. Stacking by phase-consistent summation.

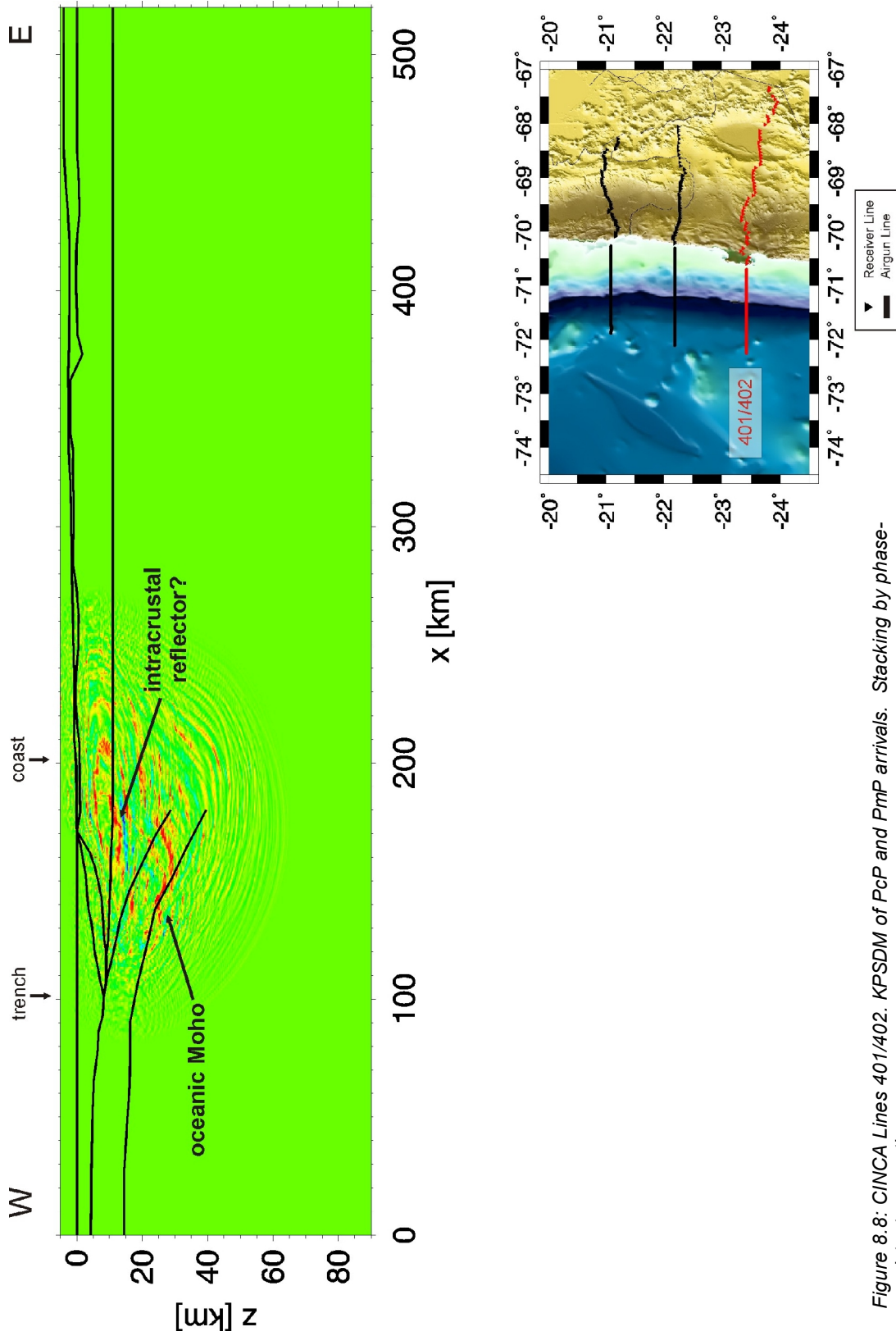


Figure 8.8: CINCA Lines 401/402. KPSDM of PcP and PmP arrivals. Stacking by phase-consistent summation.

8.1.4 Fresnel Volume Migration

FVM was applied to the data of Lines 201/202 and the results are compared with the corresponding KPSDM section in Fig. 8.9. In the upper continental crust the horizontal intracrustal reflectors above 15 km depth are more focused due to the restriction of the amplitude summation within the Fresnel Volume. The Paleo-Moho reflector is also clearly visible below the coast at around 20 km depth. The east dipping reflectors within the high velocity zone are also more focused; in the KPDM image they appear as a sharp reflector above 15 km depth whereas in the FVM section more features have been imaged at greater depths associated to structures in the internal part of the high velocity zone.

In the KPDM section the oceanic Moho is visualized as a strong reflector dominated by migration smiles and artificial events between 25-35 km depth. These migration artifacts are almost suppressed in the FVM section and the oceanic Moho is well focused between 20-25 km depth. Additionally, possible uppermost mantle structures can be observed in the FVM around 40 km depth that are not clearly visible in the KPDM section because of the effects of migration noise dominating at greater depths in the section.

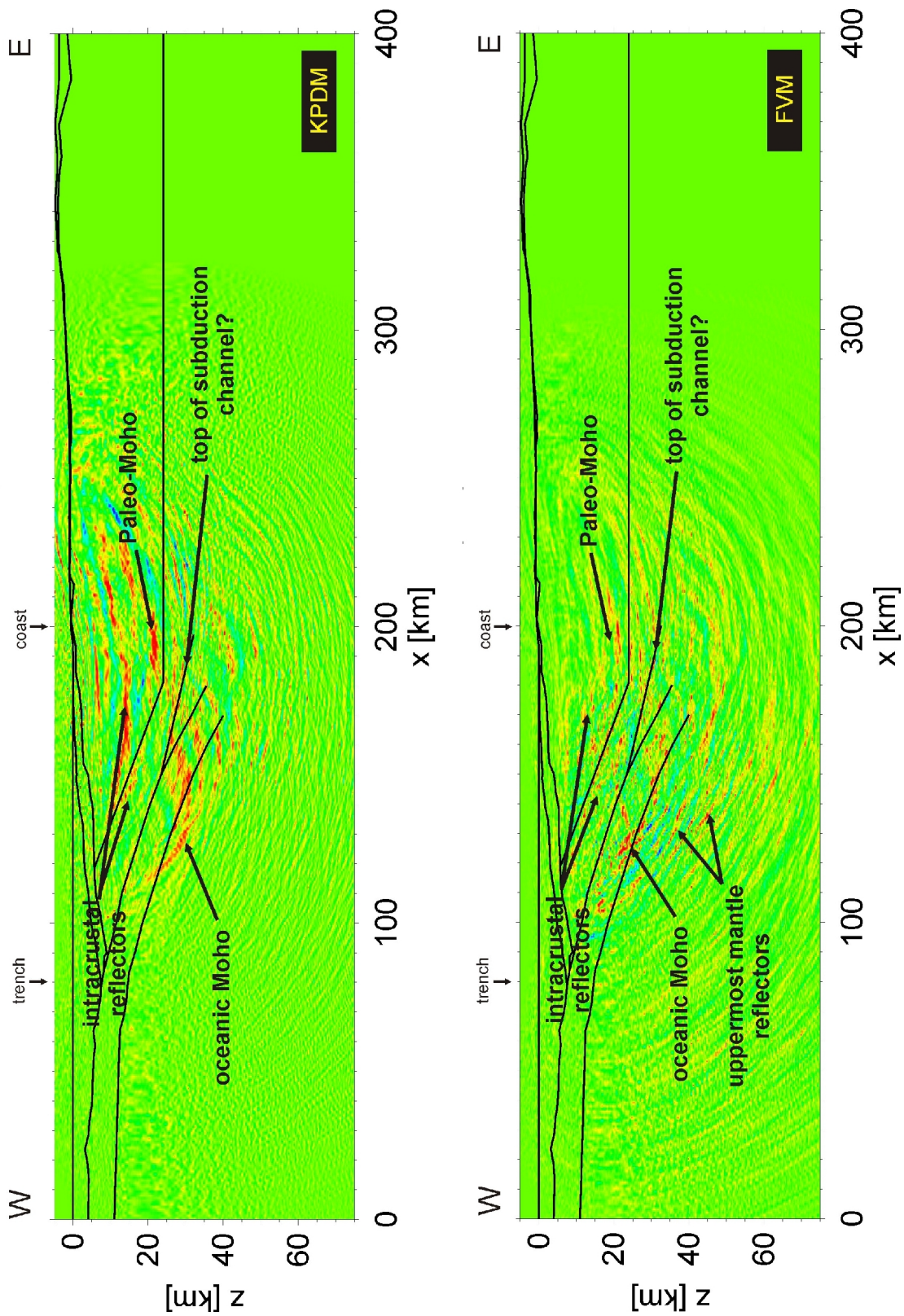


Figure 8.9: KPDM section at 21°S (top) and its counterpart FVM section (bottom). Stacking by phase-consistent summation.

8.1.5 Offset Analysis and RIS

In order to confirm the existence of the imaged structures and to obtain detailed structural features of the coupling zone two further analyses were performed. The first one consisted of the data migration for different offset ranges to examine the contribution of increasing shot-receiver distances to the imaging process. The second analysis is based on data migration in narrow frequency ranges with the aim to study the effects of velocity fluctuations and the size of heterogeneities of the propagation media. This so called Reflection Image Spectroscopy (RIS) has been successfully applied to NVR data of the ANCORP project, revealing additional features linked to fluid migration process in the subduction zone (Yoon et al. 2009). Due to the fact that the profile 201/202 contains a larger number of receiver gathers with higher signal-to-noise ratio, the analyses were restricted to this profile.

Offset Analysis

As pointed out in Chapter 7 (Table 7.1) the lines 201/202 comprise altogether an offset range from 27 to 357 km. The total range of 330 km has been divided in three equal subranges and are referred as short, intermediate and long offset range. The dataset without refraction and S wave arrivals is divided according to the offset ranges and then prestack depth migrated. The migration of the short offset range is shown in Fig. 8.10a. A stratified upper crust is visualized through the appearance of segmented subhorizontal reflectors between 170-210 km distance at 10-20 km depth. Farther west between 140-170 km distance east-dipping intracrustal reflectors can be observed at 15-25 km depth. Weak amplitude reflectors above and below the bottom of the subducting slab are also imaged.

In the migrated section corresponding to the intermediate offsets (Fig. 8.10b) deeper reflectors have been imaged. The upper crust is visualized as containing a series of subhorizontal reflectors in the distance range of 150-210 km. Between 190-220 km distance directly above the velocity boundary at 25 km depth a strong horizontal reflector is seen which is also clearly visualized in the full offset range section. Also, an east-dipping short reflector can be seen above the top of the LVZ between 150-170 km distance, possibly linked to the subduction channel. Segmented reflectors parallel to the east-dipping velocity boundary can be also recognized between 140-170 km distance. The oceanic Moho is clearly visible through short reflectors above and beneath the velocity boundary between 120-150 km distance.

Additionally, a more detailed offset analysis was done by migrating the dataset in ranges of 50 km so that four migrated sections were generated: 1) 0-50 km, 2) 50-100 km, 3) 100-150 km and 4) 150-200 km (Fig. 8.11).

The migrated section corresponding to the shortest offset range (Fig. 8.11a) shows an stratified upper continental crust with horizontal reflectors occurring west of the coast between 10-20 km depth. The section with offset range 50-100 km (Fig. 8.11b) shows again horizontal reflectors at upper crustal levels as well as weak amplitude reflectors above and below the

oceanic crust-mantle boundary at 25-30 km depth. A series of strong west-dipping reflector is imaged in the 100-150 offset migrated section (Fig. 8.11c) between 160-220 km distance at 10-15 km depth. A horizontal reflector above the upper-lower crust boundary is also visualized between 190-210 km distance. Also weak reflectors occur above the top of the LVZ between 160-180 km distance as well as east-dipping segmented reflectors in the distance range of 140-160 km at 15-20 km depth. The oceanic Moho is clearly imaged at 25 km depth between 120-140 km distance. Offset ranges larger than 150 km are poorly imaged as can be seen in Fig. 8.11d. However, some blurred reflectors can still be recognized on the oceanic crust-mantle boundary at 30 km depth and 145-155 km distance and below the east-dipping boundary at 15-20 km depth and 140-150 km distance.

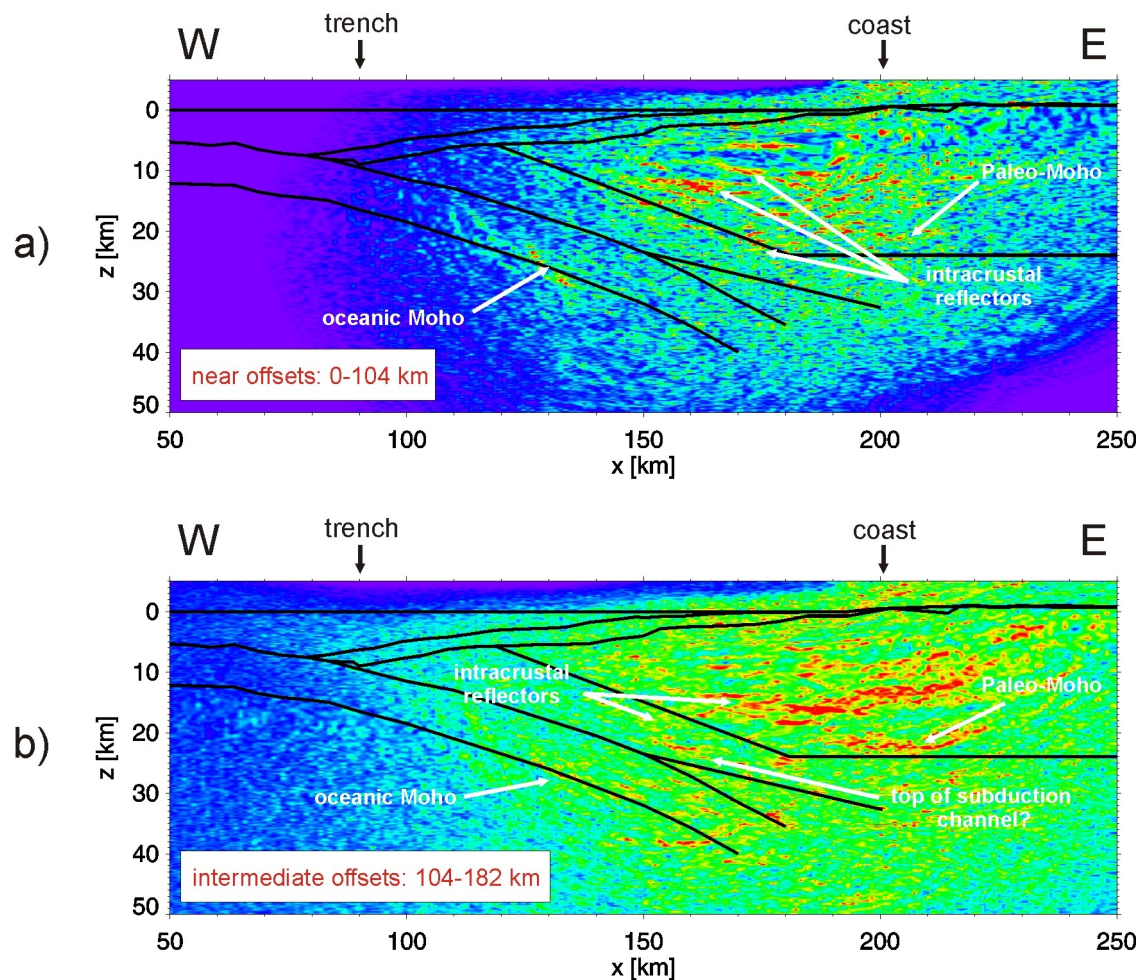


Figure 8.10: Offset analysis. The dataset was separated in three offsets ranges: near, intermediate and far offsets. Imaging of the a) near and b) intermediate offsets led to visualize major features in the continental crust as well as the oceanic Moho. Stacking according to the absolute value of the traces.

8.1 Wide-angle imaging in northern Chile

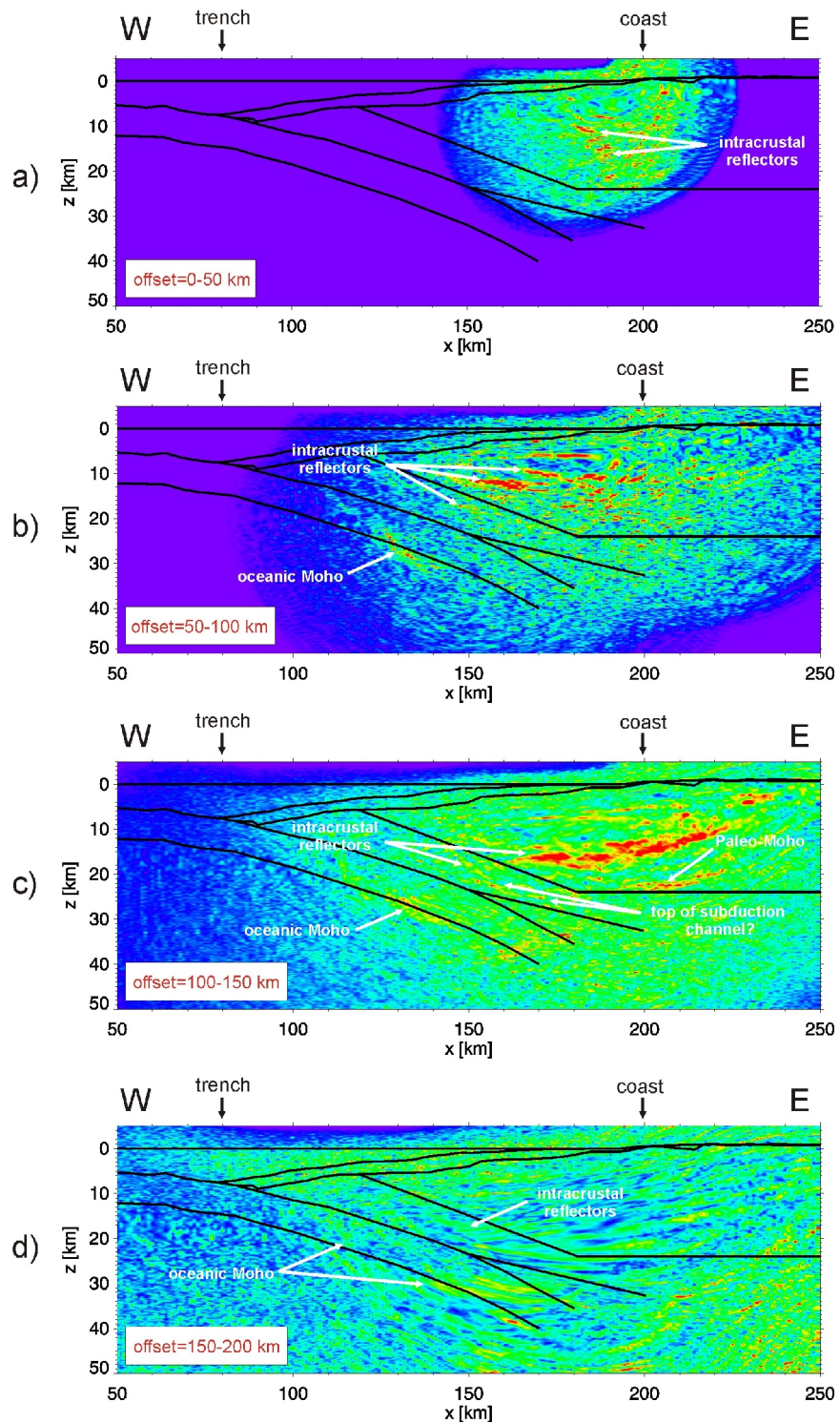


Figure 8.11: Offset analysis at narrower offset ranges. Near offsets clearly image structures in the upper continental crust while the farthest offsets contribute with the imaging of the deeper features including the oceanic Moho. Stacking according to the absolute value of the traces.

Reflection Image Spectroscopy (RIS)

When migration is performed on different frequency ranges the seismic image will be different compared to the full frequency image due to the fact that the propagation media comprises heterogeneities that produce velocity fluctuations which in turn lead to energy scattering variations. It has been shown through modeling of seismic attenuation that energy scattering variations depend on the frequency contents of the incident wave, the velocity and properties of the medium (Hong and Kennett, 2003). Also, Yoon (2005) concluded from numerical tests that the scale of heterogeneities in the overburden and velocity fluctuations strongly affect the imaging process producing amplitude loss and phase changes.

The RIS approach was applied to the lines 201/202 according to Yoon et al. (2009). The procedure consists in bandpass filtering the data by producing subsets containing narrow frequency bands after preprocessing. Afterwards, every subset is migrated separately. The frequency ranges are derived after spectral analysis and are adjusted to the useful frequency content of the data (see Chapter 7). Table. 8.1 shows the narrow frequency bands used for the analysis.

Band	Freq. Range (Hz)
bp1	3-5
bp2	5-9
bp3	9-12

Table 8.1. Frequency bands used for RIS analysis.

Fig. 8.12 displays the result of the RIS analysis for a) bp1, b) bp2 and c) bp3. The bp1 band shows the upper continental crust as composed by parallel horizontal reflectors at 150-230 km distance. Compared to the full frequency migrated section, the strong reflector located in the middle upper crust is now separated into several parallel and segmented reflectors, showing that continental crust is stratified at upper levels in the region below the coast. The reflector located directly above the upper-lower crust boundary in the full frequency section occurs now also below the boundary. Thus this structure could be extended until shallower levels of the lower crust. Beneath the east-dipping boundary small and weak amplitude reflectors are visible which can also be linked to those occurring at the top of the LVZ. The LVZ shows also some blurred and weak reflectors at shallower depths and a strong one between 180-190 km distance at 30 km depth approximately. The full frequency section shows two sharp reflectors above and below the oceanic crust-mantle boundary. The bp1 section shows a series of small and sharp reflectors at similar levels defining possible structures in the crust-upper mantle transition zone.

8.1 Wide-angle imaging in northern Chile

West of the coast, the bp2 band shows a stratified upper continental crust. A series of strong subhorizontal reflectors are visible at 15-20 km depth. Above the upper-lower continental boundary, strong reflectors can be also visualized and could be linked to the structure located in the east in the bp1 section. Strong but still blurred reflectors occur parallel to the east-dipping velocity boundary between 130-150 km distance at 15-20 km depth. A sharp reflector is clearly visible on the top of the LVZ at a similar position as in bp1 section. In the oceanic Moho zone a clear high amplitude east-dipping reflector is imaged between 110-130 km distance. Some other smaller reflectors are visualized above and below the velocity boundary.

The high frequency bp3 band images a stratified upper continental crust where the most prominent subhorizontal reflectors occur at 10, 20 and 25 km depth. Even though high frequency noise dominates the section at lower crustal levels, some reflectors are visible on the top of LVZ and below the east-dipping boundary as well. In the region of the oceanic Moho between 110-140 km distance some weak reflectors can be observed above and below the velocity boundary as well as an upper mantle reflector at 25-30 km depth.

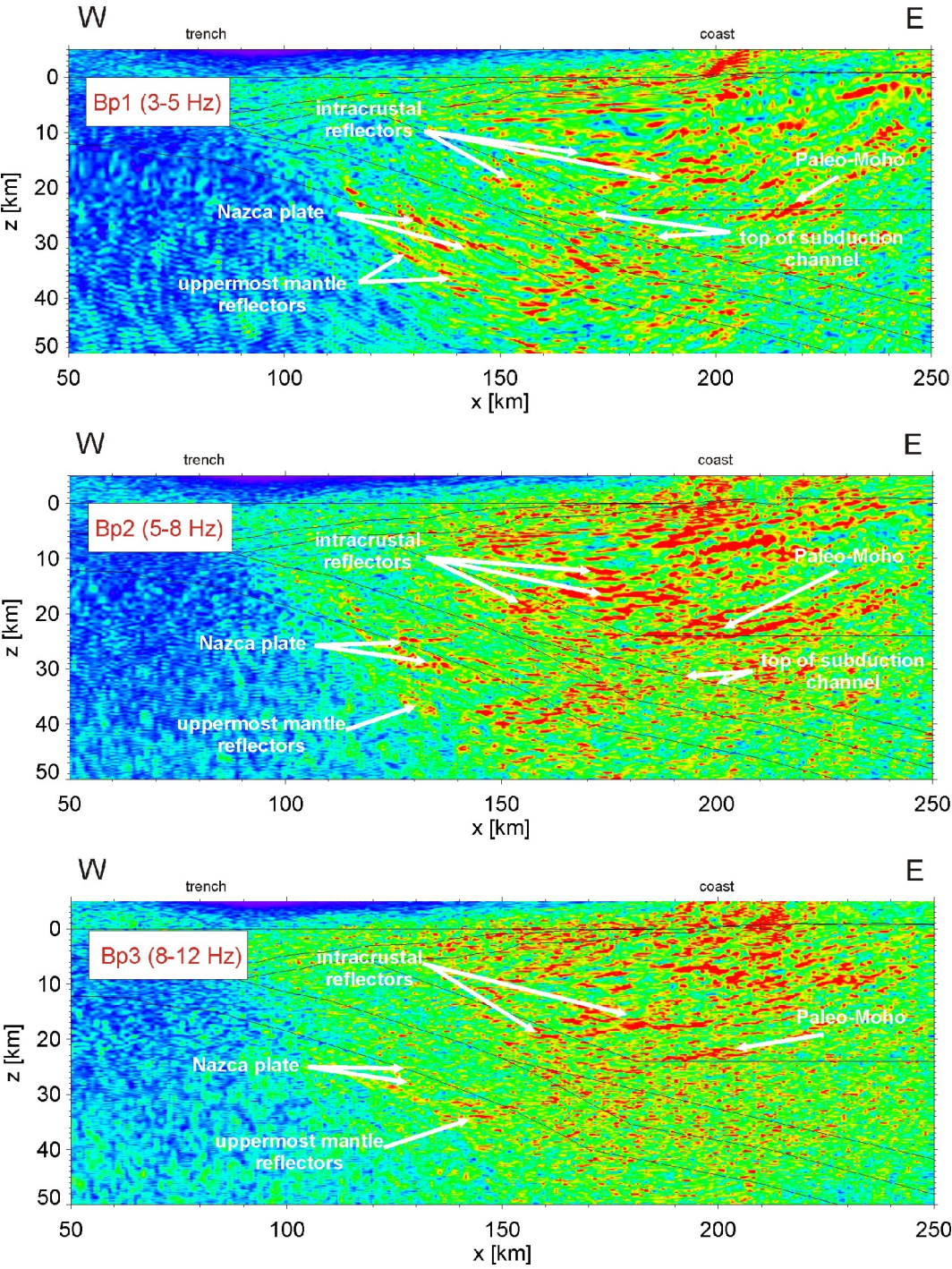


Figure 8.12: Reflection Image Spectroscopy (RIS) of the CINCA wide-angle data at 21°S. The dataset was band pass filtered in three frequency bands and each band was migrated separately. Stacking according to the absolute value of the traces.

8.1.6 Onshore data

The migration of the onshore data at 21°S reveal features in the upper and lower continental crust (Fig. 8.13). Two sharp parallel horizontal reflectors can be observed 20 km from the coast at 10-15 km depth. These structures may be correlated to the segmented horizontal reflector series visualized at shallow levels in the low frequency band of the RIS analysis (Fig. 8.12). At 25 km depth approximately, a blurred reflector is observed between 230-270 km. Further structures can be recognized up to 30 km eastern at 23 km depth. Since both reflector series are located in the vicinity of the upper-lower crust border, these structures may be associated to the strong horizontal reflector observed in the migrated section of the air-gun data (Fig. 8.3).

Strong arrivals in the distance range of 150-200 km were interpreted by Patzwahl et al. (1998) as PmP phases (see Fig. 7.4). Nevertheless, since there is a gap of about 50 km near the coast, it was not clear whether these arrivals represent the oceanic Moho or the continental Moho. The migrated section shows a sharp east dipping reflector at 47-55 km depth in the region indicated by Patzwahl et al. (1998). Comparing with the ANCORP velocity model (ANCORP Working Group, 2003), the above mentioned reflectors may be seen as the updip prolongation of the continental Moho visualized below 55 km depth at 40-80 km from the coast or to structures within the subduction channel (see Chapter 9).

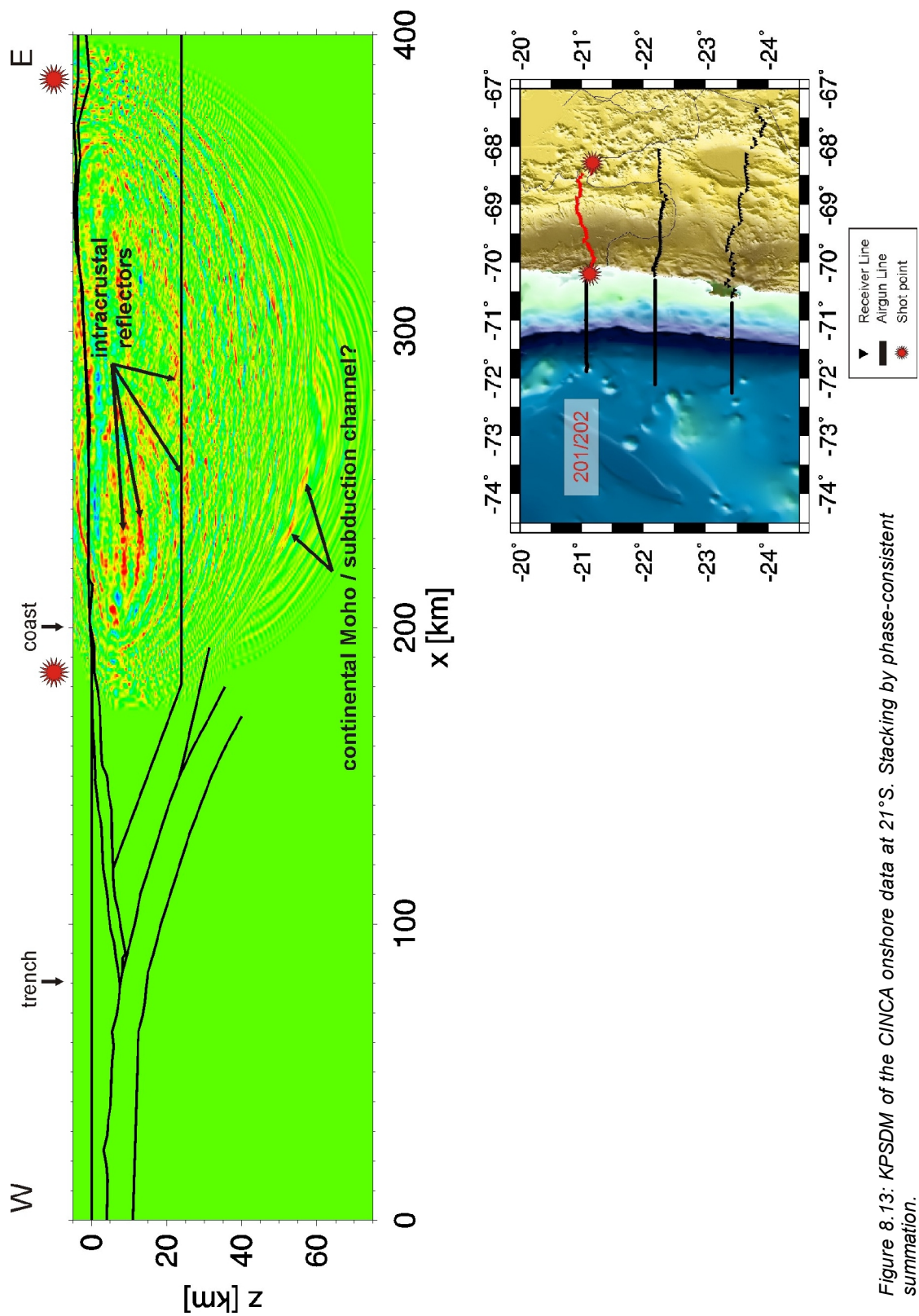


Figure 8.13: KPSDM of the CINCA onshore data at 21°S. Stacking by phase-consistent summation.

8.2 Wide-angle imaging in southern Chile

The imaging of the SPOC data involves KPDM of three different configuration of wide-angle data along the same recording profile. By combining these results, images covering offshore and onshore domains are produced, in which the oceanic Moho and reflectors observed at different continental crust levels are the most prominent structures (Fig. 8.14). The geological interpretation of the observed structures and their comparison with results from other geophysical methods is described in Chapter 9.

Following the strategy applied for the migration of the CINCA data, the SPOC wide-angle data was migrated considering the complete recorded wavefield and its reflective part separately (refracted arrivals are not included). In the following only migrated sections of the reflective wavefield are illustrated. In order to give a geological and structural meaning of the migrated energy, the velocity model boundaries are plotted on the migrated sections.

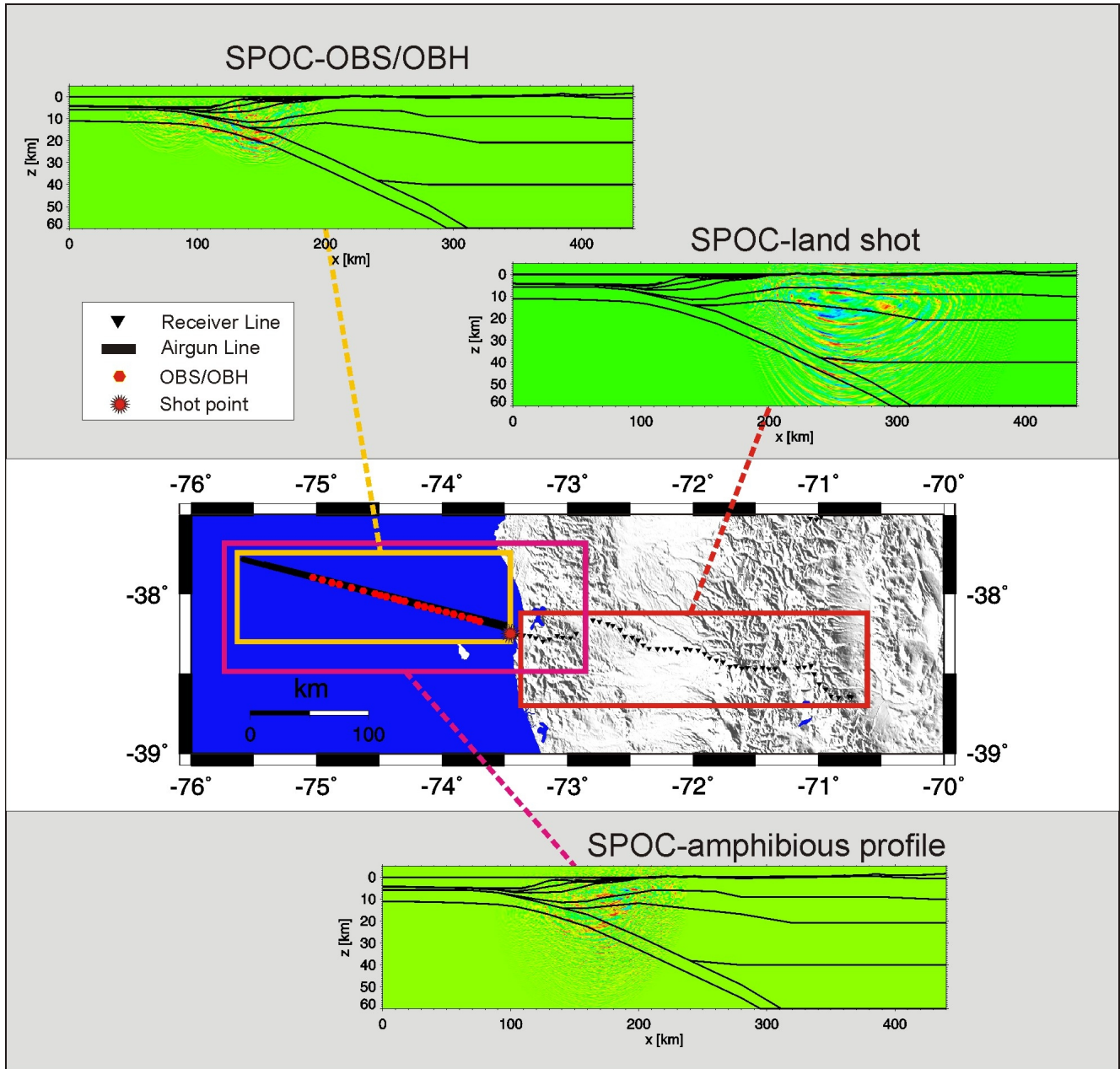


Figure 8.14: Synthesis of imaging in southern Chile. The results comprise KPSDM of OBH/OBS data, amphibious and onshore data.

8.2.1 Line SO161-038-amphibious profile

In spite of large number of receivers on this profile, only five of them recorded high quality signals. Nevertheless, some features of the continental crust as well as reflectors in the oceanic Moho zone have been clear imaged (Fig. 8.15). In the upper continental crust a strong west-dipping reflector is imaged between 160-180 km distance at 8-10 km depth. A second intracrustal reflector is observed 20 km west from the coast at 12-14 km depth. The top of the oceanic slab shows weak a reflector between 150-155 km distance while a high amplitude segmented reflector images the oceanic Moho at 16-20 km depth between 123-148 km distance. Similar to the CINCA results, some reflectors below the oceanic Moho are imaged at shallow mantle levels.

8.2.2 OBS/OBH profile

Migration of OBS and OBH data involved PmP and intracrustal reflections only. All refracted arrivals (Pg and Pn) as well as multiples were muted. The migration results are shown in the true amplitude stacked section in (Fig. 8.16). The oceanic Moho is clearly imaged westward and eastward the trench area. Parallel to the ocean crust bottom boundary weak segmented reflectors are visualized at 15-30 km west of trench. East to the trench, sharper segmented reflectors define the oceanic crust-mantle boundary between 100-150 km distance at 12-20 km depth. The top of the oceanic slab is imaged by segmented reflectors at 12 km depth and 115-140 km along the profile. In addition, segmented upper mantle reflectors are also visible west from the trench at 23-27 km depth under the strong reflector that defines the oceanic Moho between 140-150 km along the profile.

8.2.3 Onshore data

The migrated section of the chemical shot fired at the coast show strong reflectivity within the continental crust (Fig. 8.17). In the upper crust a couple of sharp reflectors occur at 9 and 13-14 km depth. The lower reflector coincides with the limit between upper and lower continental crust. Two further reflectors are visible within the lower crust. The first is located at 19-22 km depth between 235-270 km distance and the second occurs at 30-32 km depth between 240-260 km along the profile. In the boundary between the lower crust and the mantle wedge a strong reflector is visible between 245-270 km distance. Finally, following the bottom boundary of the subducted slab, a sharp reflector associated to the oceanic Moho is clearly imaged between 235-260 km distance at 42-49 km depth.

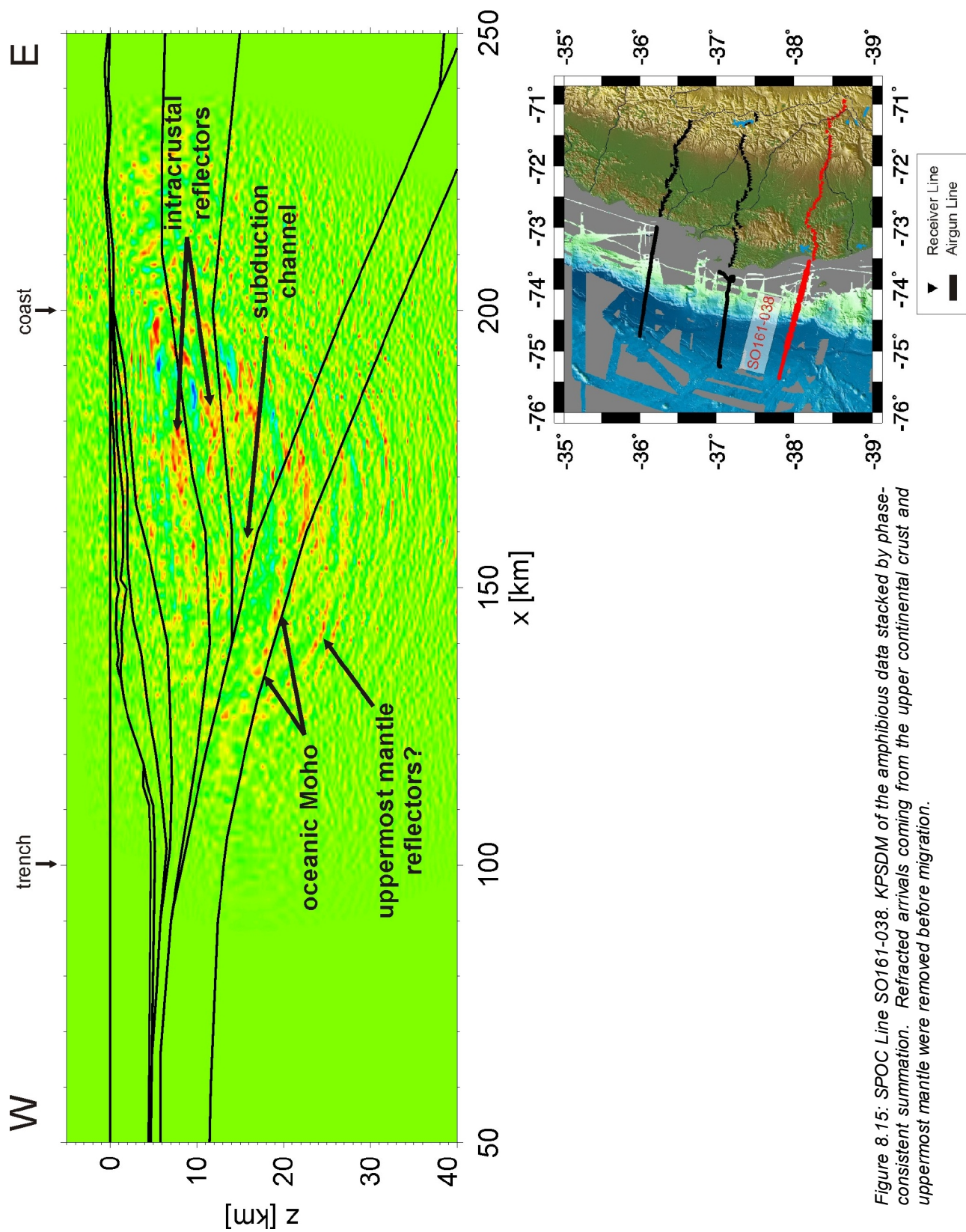


Figure 8.15: SPOC Line SO161-038. KPSDM of the amphibious data stacked by phase-consistent summation. Refracted arrivals coming from the upper continental crust and uppermost mantle were removed before migration.

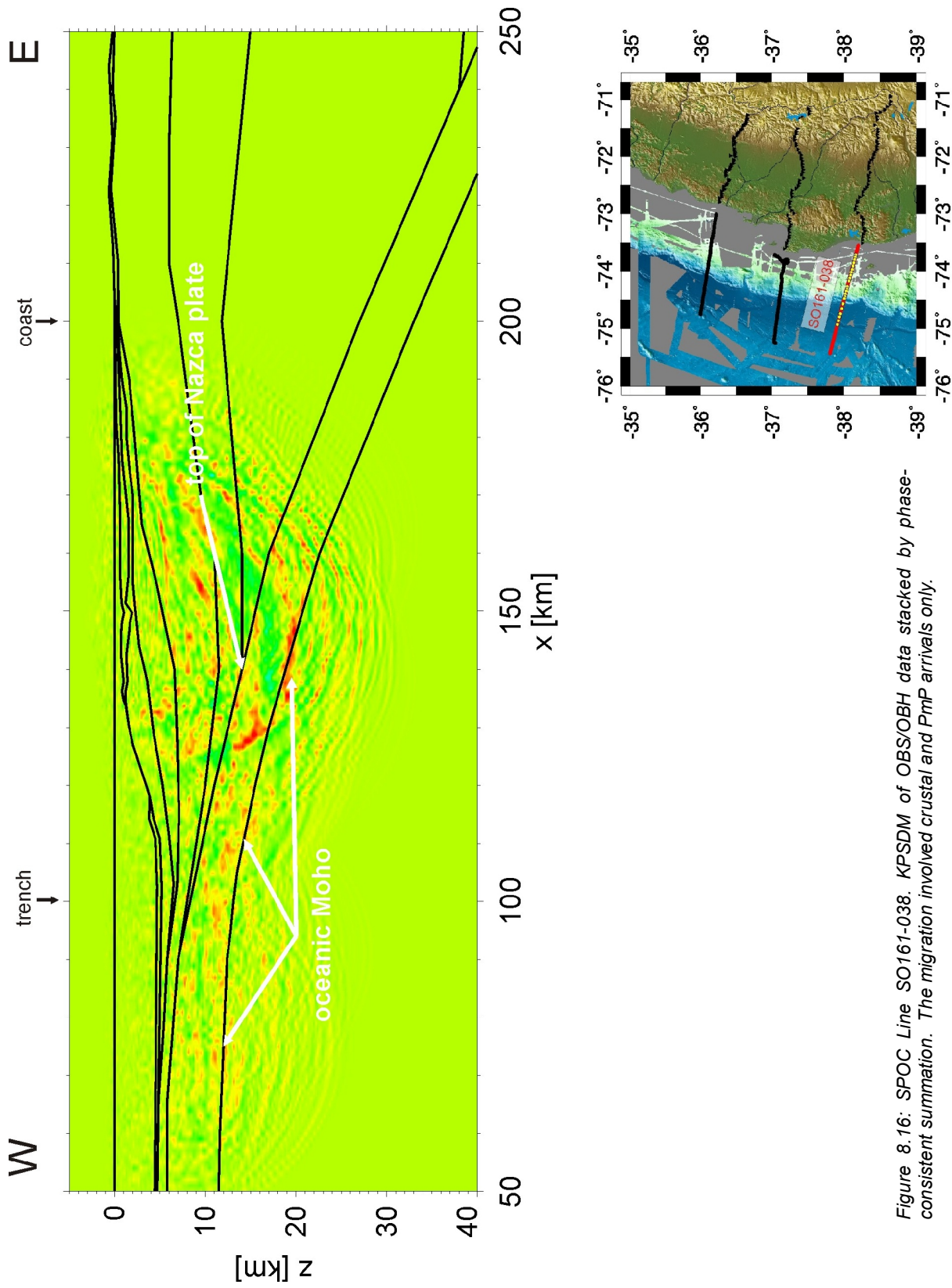


Figure 8.16: SPOC Line SO161-038. KPSDM of OBS/OBH data stacked by phase-consistent summation. The migration involved crustal and PmP arrivals only.

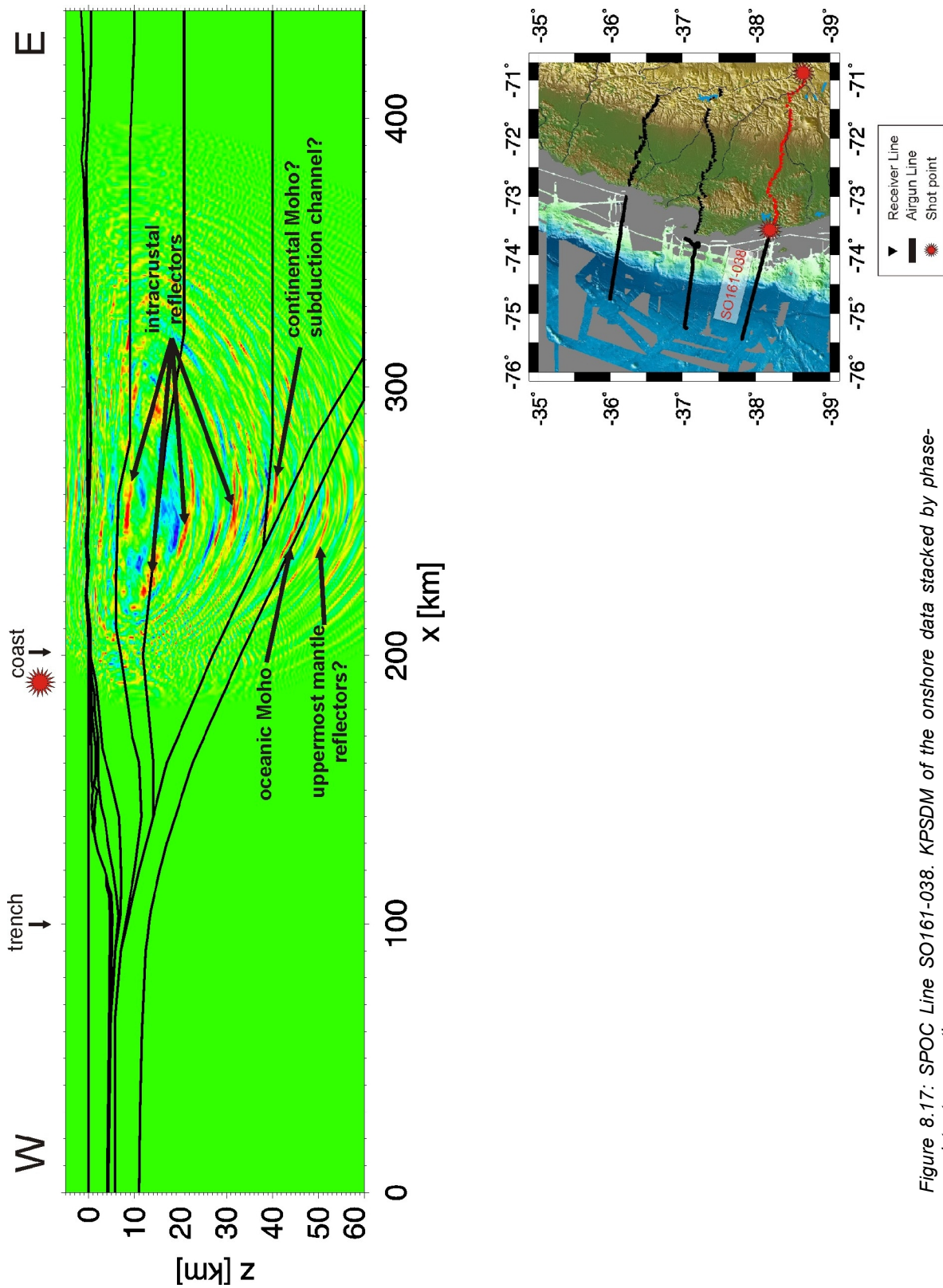


Figure 8.17: SPOC Line SO161-038. KPSDM of the onshore data stacked by phase-consistent summation.

9 Interpretation

In the previous section results of the wide-angle imaging were presented. Now the origin and meaning of the observed structures will be described from a tectonic and geological point of view by the comparison with results obtained from other geophysical experiments carried out in the study areas. These methods include gravity and magnetotelluric data, hypocentre locations, heat-flow density and temperature distribution, seismic tomography, Vp/Vs ratios and results of previous seismic refraction/reflection experiments.

The wide-angle migrated sections at 21°S (amphibious and onshore profiles) exhibit the best quality and more interpretable structures in comparison with those obtained at 22°S and 23.25°S. For this reason, these sections will be used for the comparison with gravity, magnetotelluric and heat-flow density results. Although the migrated section at 23.25°S shows lower signal-to-noise ratio and less structures are visible, this section will be compared with the passive seismic results collected in the area.

Concerning the margin in southern Chile, the interpretation is based on the events imaged in the prestack depth migrated sections of the amphibious and onshore profiles at 38.2°S.

9.1 Erosive margin in northern Chile

Continental plate and the high velocity zone

The area under the Coastal Cordillera represents a relict of the Jurassic-Early Cretaceous magmatic arc and it is characterized by high P-wave velocities of about 6.5 km/s (Wigger et al. 1994; Patzwahl, 1999). The upper continental crust in particular, is thought to be composed of volcanic flows of the La Negra Formation and Jurassic-Cretacic dioritic and granodioritic intrusions intruded into the lower crust. Roessling (1989) described such lower crust complexes outcropping south of Antofagasta in the Coastal Cordillera. From prestack depth migration of NVR data off Antofagasta the occurrence of similar rocks below the continental midslope (~8-11 km depth) as landward dipping high amplitude reflections was inferred by von Huene and Ranero (2003).

The east dipping reflectors interpreted as intracrustal structures in the wide-angle migrated section (Fig. 8.3) are located in a zone with high velocity contrast and geometry parallel to the subducting slab, representing the contact between the granitic upper continental crust (6.5 km/s) and a higher velocity layer (7.0 km/s). Laboratory measurements performed on gabbro at temperatures and pressure similar to those occurring at 20-30 km depth produce velocity values in the range of 6.7-7.1 km/s (Christensen, 1979). The origin of this contact zone has

three possible explanations (Patzwahl, 1999): a) the remnant of a Jurassic extension structure, b) underplating of the oceanic crust and c) an old continental crust-mantle boundary or Paleo-Moho.

a) The remnant of a Jurassic extension structure: During its evolution the Jurassic arc was subject to normal-orogen extension due to the high obliqueness convergence between the Aluk-South America plates producing transtensional regimes that led to the formation of sinistral strike-slip faults like the Atacama Fault System and the intrusion of mantle plutonic rocks without any continental contamination. Several graben or semi-graben structures have been formed as a result of such tectonic processes. Movements along these structures could have transported higher velocity material from deeper crustal levels on the west side of the structure against the lower velocity material at shallower crustal levels. Finally, the subduction tectonic erosion since the Jurassic brought these structures 5-10 km above the subducting oceanic plate. All these processes should have finished before the Neogene, constrained by results of analysis of offshore sediments covering the basement of the upper plate.

b) Underplating of the oceanic crust: During the mid-Late Cretaceous the plate configuration in the south east Pacific underwent changes not only in the convergence obliqueness but also in the convergence rate (see Chapter 2). These changes generated conversion from transtensional to transpressional strain regime. As a result, folding and orogen-normal shortening/extension were responsible for the deformation processes concentrated in the magmatic arc area. The high velocity values modeled by Patzwahl (1999) for this layer are similar to those found by (Mutter and Mutter, 1993) corresponding to basaltic and metabasaltic material showing P wave velocities between 6.5-7.9 km/s in the layer 3 of the oceanic crust. Therefore, the high velocity layer could be considered as oceanic crust material underplated before the Neogene. The underplating of this layer could have occurred during the Late Cretaceous when the spreading centre between the Aluk and Farallon plates migrated southward and subducted beneath the South American plate resulting in a new plate configuration (Scheuber and Reutter, 1992). New deformation regimes that influenced the subduction process arose due to the change of plate configuration, including changes in the ridge-push or slab-pull force leading to the break of the subducting slab. Because the high velocity layer is thicker than the average oceanic crust and the tectonic erosion should have also affected this layer during subduction, it is possible that the break-off/underplating process occurred more than once (Patzwahl, 1999).

c) Paleo-Moho: Wigger et al. (1994) modeled a discontinuity below the Coastal Cordillera at about 20 km depth with maximal P-wave velocities around 7.2-7.4 km/s. Below this discontinuity, a low velocity zone with P-wave velocities between 6.4-6.6 km/s have been also modeled representing the partly serpentinized Jurassic-Cretaceous mantle. Therefore, the discontinuity at about 20 km depth can be considered as an old crust-mantle boundary or Paleo-Moho (Giese et al. 1999). The east dipping reflectors in the wide-angle migrated sections can be extrapolated eastward and linked to the horizontal reflector above 25 km depth. These structures altogether could be interpreted as a Paleo-Moho as well, provided the occurrence of a LVZ about 30 km depth below the coast. The Paleo-Moho behaves as a

blurred Moho-discontinuity due to the hydration of the peridotitic mantle wedge which leads to crustal thickening under the petrologic continental crust (Giese et al. 1999). The phase boundary between serpentinite and amphibole-bearing peridotite may create a new discontinuity or boundary within deeper zones of the hydrated mantle wedge below the forearc. Considering the migration of the onshore data (Fig. 8.13), the Paleo-Moho reflector can be extrapolated up to 100 km from the coast, suggesting a similar location for the crust-mantle boundary in the area beneath the Longitudinal Valley. At 23.5°S, Schmitz et al. (1999) interpreted a high velocity layer at depths of 35-45 km under the Pre-Cordillera as the basal relicts of the Mesozoic continental Moho. In their proposed simplified cross section, this Paleo-Moho is extrapolated to the west, reaching similar depths like its counterpart at 21°S.

The subduction channel

The subduction channel is a narrow zone located below the lower continental crust and above the oceanic slab comprising material with a velocity gradient with respect to both plates and it is considered to be the part of subduction zones where tectonic mass transfer is carried out. The material conforming a subduction channel is derived from sediments deposited in the trench area, off scrapings from the base of the overriding plate by tectonic erosion or from the top of subducting slab (Cloos and Shreve, 1988). In the velocity model at 21°S (Fig. 7.13) a LVZ was modeled as a wedge overlying the top of the subducting Nazca plate which is interpreted as eroded and underplated material. The underplating leads to thickening of the continental crust and may be the origin of uplift and extensional structures in the outer forearc (Patzwahl, 1999, von Huene and Ranero, 1999). Furthermore, Wigger et al. (1994) proposed partial serpentinization caused by dewatering of the subducting slab as the process that originates the low velocities within this zone.

Recently, this LVZ has been interpreted by Lohrmann et al. (2006) as an extension of the subduction channel that begins beneath a link to the surface active thrust fault system imaged at 10 km depth approximately in the offshore CINCA NVR dataset (Sick et al. 2006) and reproduced in sandbox experiments. The material slumped trenchwards from the middle slope and upper continental plate is then transported by underthrusting to the subduction channel through these structures.

The migration of wide-angle data shows few evidences of the existence of a subduction channel in the area below the coast. In Fig. 8.3 a strong reflector imaged at 30 km from the coast and 24-28 km depth may define the top of the subduction channel. Within the subduction channel weak reflectors can be also observed like those shown in the low frequency band of the RIS analysis (Fig. 8.12) and in the migration of intermediate offset ranges (Fig. 8.10). Further, Lohrmann et al. (2006) suggest that the 3 km wide zone defined by hypocentres located by Patzig (2002) above the downgoing slab forms a portion of the subduction channel where current material movement between the continental and oceanic plate takes place. On the contrary, the ANCORP NVR data shows no evidence of subduction channel-related structures (Lohrmann et al. 2006).

Top of the subducting slab

As mentioned in Chapter 5, when the interface between two layers is modeled as a transition zone with low velocity contrast, it is possible to record strong amplitude reflections from this interface if the incidence angle is close to the critical angle. The migration of the CINCA wide-angle data does not show clear energy associated to the top of the slab, only small and weak reflectors are imaged but they might be migration artifacts instead. The velocity values assigned to the bottom of the LVZ are similar to those used to model the top of the subducting slab. Therefore a small velocity contrast between the two layers must be expected. Two possible reasons for the existence of absent reflectivity are suggested:

- 1) the velocity contrast is too small so that waves propagating in the near vertical domain do not perceive the existence of the interface.
- 2) Despite of the existence of a low velocity contrast, the incidence angle of the propagating waves must be lower than the critical angle, thus no wide-angle reflections are produced.

The upper continental crust below the forearc region

The intracrustal reflectors imaged above 20 km depth in the wide-angle migrated section (Fig. 8.3) represent the layered crystalline upper crust comprising relicts of the Paleozoic continental crust and the volcanic and granitoid rocks of the ancient Jurassic magmatic arc. The volcanics of the La Negra Formation, commonly identified as basalts to andesites, were formed as a consequence of strong changes in the kinematic of the plate convergence, leading to the subduction of the oceanic plate (Pichowiak, 1994).

The oblique plate convergence in combination with the arc parallel motion along the strike-slip faults of the Atacama Fault System yielded extension normal to the plate boundary, bringing the formation of pull-apart basins. Upper mantle decompression and the influence of the subduction fluids controlled the mantle wedge melting causing magma generation. The subduction increased the magma production leading to the formation of a ~10 km thick basalt/andesite layer and the intrusion of huge granitoid plutonic complexes into the lower crust. There is no evidence of the inclusion of the older crust material in the course of the magmatic process in the Jurassic magmatic arc. For this reason, it is accepted that the host rock was broke up and dispersed by the intruded magmatic rocks (Pichowiak, 1994).

Continental Moho

In the migrated section of the onshore data an east dipping reflector appears at 30-50 km from the coast between 47-55 km depth. It was mentioned in Chapter 8 that because of a data gap of about 50 km near the coast, it was not clear whether the arrivals interpreted by Patzwahl (1998) represent the oceanic Moho or the continental Moho. The position of the imaged reflector in the onshore data correlates well with the updip extension of the reflector element interpreted as the geophysical Moho in the ANCORP velocity model (ANCORP Working Group, 2003). Nevertheless, the migration velocities for this reflector (7.2-8.1 km/s)

differ slightly from those assigned in the ANCORP model (7.1-7.6 km/s) for the geophysical Moho.

Lüth (2000) modified the ANCORP velocity model by adding a 10-20 km thick layer with 8 km/s velocity above the oceanic crust and reproduced comparable results to the original model. However, this velocity value was ruled out because it does not correlate with the N-S velocity model constructed by Lessel (1998) for the region beneath the Pre-Cordillera.

On the other hand, because their proximity to the top of the subducted slab, these reflectors may be also interpreted as part of the subducted material being transported downwards (Wigger, 2010, pers. comm.).

9.1.1 Integration with other geophysical methods

Gravimetry

From 1993 to 1996 the MIGRA group (**M**ediciones **I**nternacionales de **G**ravedad en los **A**ndes) acquired about 3500 new gravity observations in a study area covering 900 x 1000 km between 20°-29°S and 64°-71°W in the Central Andes. The gravity dataset not only includes onshore measurements but also the recording of data along the survey lines of the CINCA offshore experiment. Maps of free air, Bouguer and isostatic-residual anomalies as well as 3D density models are presented in Goetze and Kirchner (1997) and Kirchner (1997). In their combined Bouguer and free air anomaly map shown in Fig. 9.1, two main features can be observed: a N-S positive anomaly which extends parallel the coast from 20°S down to 28°S and the regional negative anomaly (-450 mGal) in the arc region at about 22.5°S. The first one has been interpreted as the effect of the dense subducting Nazca Plate (calculated gravity effect of about 60 mGal). Further local positive anomalies observed in the forearc region are yielded by the presence of uplifted Jurassic batholiths intruded into the volcanic rocks of La Negra Formation. The regional negative anomaly is produced by low density material of the volcanic arc and crustal thickening by isostatic compensation.

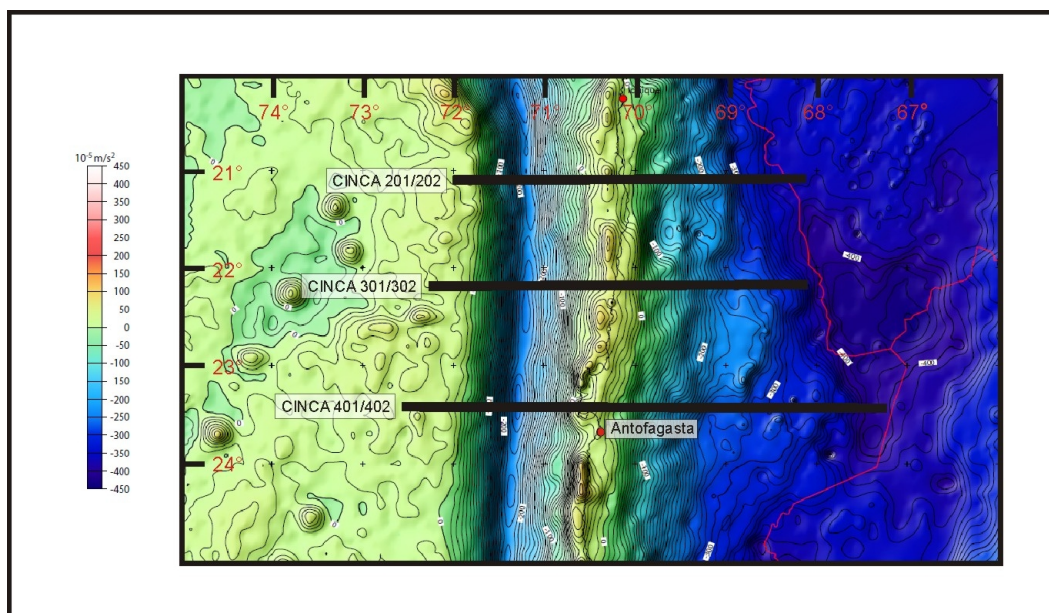


Figure 9.1: Free air and Bouguer anomaly map of North Chile (after Schmidt and Goetze, 2006).

With the aim to study the structural geometry of the lithosphere of the Central Andes, Prezzi et al. (2009) derived a 3D density model for the area between 20°-29°S and 74°-61°S through the forward modeling of the Bouguer anomaly. The model comprises 31 blocks extending to 220 km depth. The model geometry is characterized by the E-W segmentation of the continental crust in several bodies representing the main N-S striking morphotectonic units. Different geophysical and geological data were integrated to define the model geometry, including velocity models derived from wide-angle measurements (CINCA, ANCORP and PISCO projects), prestack depth migration results (ANCORP and PRECORP projects), hypocentre location, receiver function analysis, magnetotelluric experiments, thermal models and balanced structural cross sections. The density values assigned to the blocks were derived from geochemical and petrological data and pressure-temperature conditions expected for each body.

The CINCA wide-angle migrated sections at 21°S and the density section at 21.3°S (Prezzi et al. 2005) are integrated and shown in Fig. 9.2.

The intracrustal reflectors imaged at 10-15 km depth coincide with the body of 2.73 Mg/m³ that represents the uplifted Jurassic batholiths intruded into La Negra Formation. The forearc middle crust comprises bodies with densities values over 3.0 Mg/m³ obtained from the chemical composition of Jurassic basaltic andesites. Most of the intracrustal reflectors in the amphibious seismic section and the Paleo-Moho reflector coincide with these bodies which were interpreted as the lower crust of the ancient Jurassic magmatic arc. These structures conforming the upper and middle crust beneath the Coastal Cordillera are responsible for the positive anomalies (> 50 Mg/m³) shown in the residual gravity map obtained by Prezzi et al. (2009) and correspond to those observed in the maps of Bouguer anomaly.

Above the subducting slab, the lower crust has been modeled with density values around 2.9 Mg/m³ representing the serpentinized mantle peridotite beneath the Coastal Cordillera or crustal material added by tectonic erosion or magmatic addition. The density values allocated to these bodies were derived from laboratory measurements made on chlorite serpentinite wehrlites and dunites (3.5-7.5% H₂O; 29-40% serpentinite) (Prezzi et al. 2009).

The eastward dipping reflectors imaged in the amphibious migrated section corresponds to a high velocity zone as seen in Fig. 7.13. Therefore it is more likely that such structures correspond to the bodies with density over 3.0 Mg/m³ than to the serpentinized mantle body.

The oceanic crust is modeled as composed by two kilometers of sedimentary rocks (2.55 Mg/m³) and 6 km anhydrous basaltic-gabbroic rocks and hydrated basalts (2.9 Mg/m³). Due to the increase of hydrostatic pressure and dewatering processes from 40 km depth approximately, a 3.05 gr/cc model body simulates the transition from oceanic crust to eclogite in the area below the Coastal Cordillera. Finally, the lithospheric mantle (conformed by mafic and ultramafic rocks like harzburgites), where some reflectors are visualized in the amphibious migrated section (Fig. 8.3), is modeled with density values about 3.17 Mg/m³.

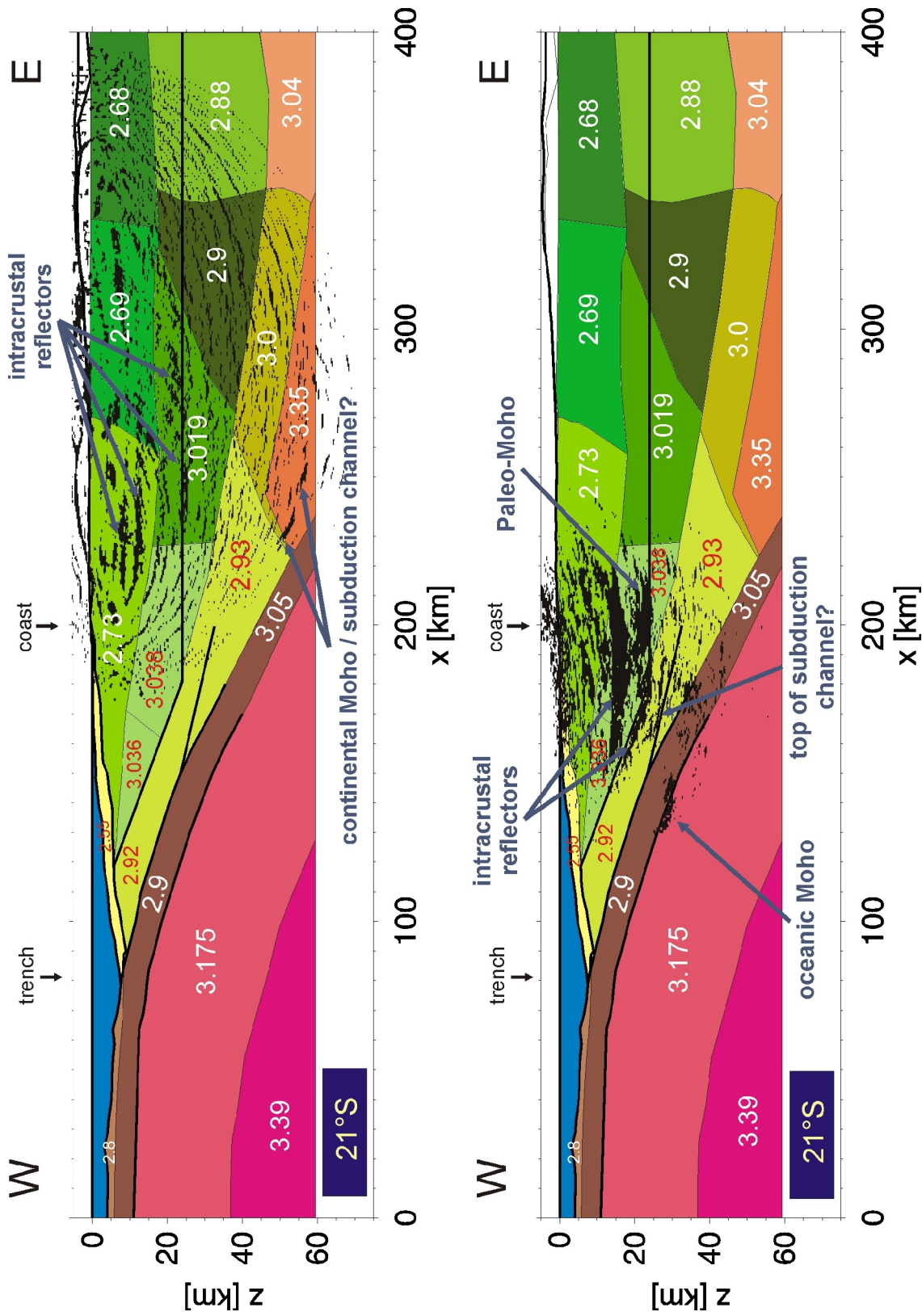


Figure 9.2: Overlay of the CINCA wide-angle KFDPM images with gravity results of Prezzi et al. (2009). Density values in Mg/m^3 are indicated. Top: KPSDM of onshore data; Bottom: KPSDM of the amphibious data.

Magnetotelluric methods

Resistivity models were derived in the area of the CINCA and ANCORP projects from inversion of magnetotelluric data (Schilling et al. 2006). Fig. 9.3 shows one of the models considering the hydrated subducting Nazca plate as a good conductor (Brasse, 2009, pers. comm.). Migration results of wide-angle data are superimposed. The area under the Coastal Cordillera represents in general a high resistivity region even though subduction processes such as dewatering could contribute to the formation of conductive structures above the downgoing plate.

A low resistivity anomaly can be observed 10 km west of the coast at 12-18 km depth approximately. Since the origin of this anomaly is still unknown, from its location in the vicinity of intracrustal structures at mid-crustal levels, a possible relationship with the occurrence of magmatic intrusions could be speculated.

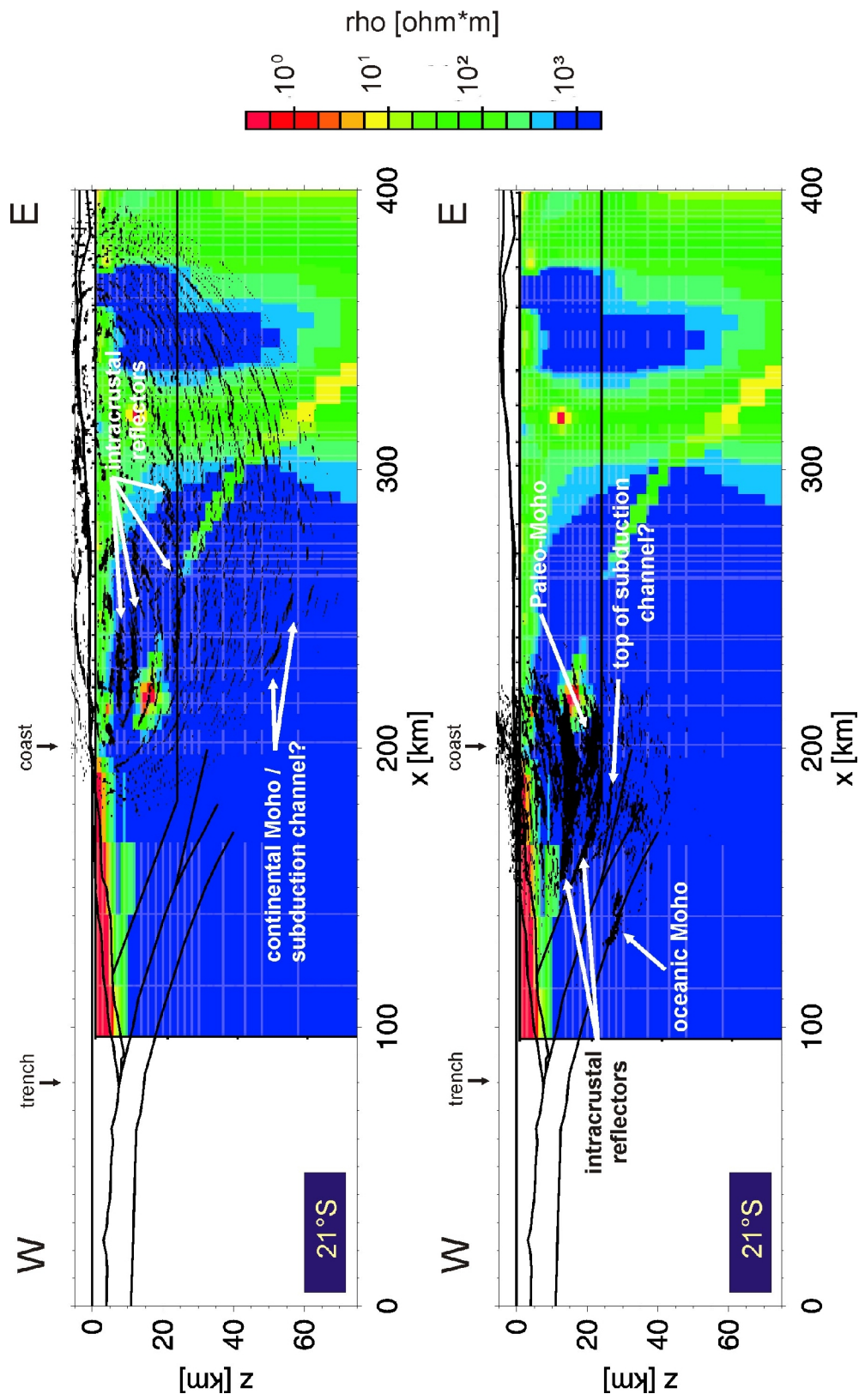


Figure 9.3: Overlay of CINCA wide-angle KPSDM images with magnetotelluric results at 21°S (Brasse, 2009, pers.comm.). Top: KPSDM of the onshore data; Bottom: KPSDM of the amphibious data.

Hypocentre locations, heat-flow density and temperature distribution

Seismicity recorded during one year by a local onshore network in the area of Antofagasta with the aim to obtain further information about the geometry and stress regime of the subduction zone between 22°-25°S revealed details concerning to characteristics of faulting along the subducting oceanic plate (Delouis et al. 1996). The seismogenic coupling zone or locked zone was defined by the location of events with clear pattern of thrust to reverse focal mechanisms in the shear zone between the two plates in the depth range of 20-50 km. The earthquakes located within this depth range define therefore the seismically coupled zone of the plate interface. Below 50 km depth, a transition from thrust to normal faulting focal mechanism takes place, probably due to changes in the mechanical behavior of the interface from unstable (seismic) to stable (aseismic) frictional slip. An accurate determination of the minimum depth of the seismogenic coupling zone was not reported in this study due to the lack of stations placed offshore.

It has been shown that the combination of distribution analysis corresponding to normal seismicity and aftershocks aims to define more accurately the extent of the seismogenic coupling zone. As part of the main objectives of the CINCA project, a seismic network was installed in the area around Antofagasta in order to study the seismicity in the region for a period of three months. Nine ocean bottom seismometers were deployed offshore and 35 stations were deployed onshore, covering an area of 340 x 210 km around the city of Antofagasta and the Mejillones Peninsula (~23.25°S).

A subset of the aftershock series of the Antofagasta event ($M_w=8.0$; July, 1995) was recorded by the CINCA seismic network and used to study the seismogenic zone in northern Chile (Husen et al. 1999, Husen et al. 2000). After the inversion of P and S arrivals, the pattern of high precision located events shows an average dip of 19-20° down to 46 km where the downdip limit of the coupling is suggested. Below 50 km, the pattern changes and the depth distribution becomes irregular, indicating the maximum depth of the coupling zone and the transition from compressional to tensional regime as proposed by (Delouis et al. 1996). The incorporation of OBH allowed good control of events located offshore leading to an accurate estimation of the minimum depth of the coupling zone. Disregarding events located within the subducting oceanic plate and considering the shallowest events, the minimum depth of the seismogenic coupling zone was estimated to be at 20 km. It has been recognized by Byrne et al. (1988) that most subduction zones do not show shallow events along the plate interface updip to the trench area. This is likely due to the existence of an aseismic zone formed by unconsolidated sediments with stable slip properties. This behavior changes at greater depths provided that the sediments become more consolidated and dewatered, and are in contact with harder rocks of the overriding plate. However, the subduction zone in north Chile has been characterized as erosional type, where the sediment cover in the trench area is very thin. Husen et al. (1999) propose therefore, that the detachment zone suggested by von Huene et al. (1999) at middle-lower continental slope levels is responsible for the lack of strong events at shallow depths. This detachment zone represents the border between the extensional regime observed at the surface of the continental slope of the overriding plate and the compressional regime along the plate interface.

On the other hand, surface heat-flow density measurements along a profile parallel to 21°S were used to construct quantitative models to investigate effects on the thermal field (Springer, 1999). From the final model it can be concluded that temperatures on the order of 250 to 300°C are reached at the maximum depth of seismic coupling between the plates, while at the maximum depth of plate contact (60 km approximately) temperatures are on the order of 300 to 350 °C.

Springer and Foerster (1998) observed changes in the heat-flow density in W-E direction which correlate with the N-S striking morphologic units and which are related to different thermal regimes. In the forearc region three different trends can be distinguished:

- In the trench area heat-flow density values of about 30-40 mW/m² were estimated within the Nazca plate. These values are lower compared to similar studies that relate the cooling of the oceanic lithosphere with the increasing age. According to these studies, the Nazca plate with an age of about 50 Ma in the trench area at 20°S (Mueller et al. 1993), the heat-flow density should be about 70 mW/m². This difference is attributed to faster cooling as a result of heat convection.
- The subduction of oceanic lithosphere yields the minimum value of about 20 mW/m² observed in the area under the Coastal Cordillera.
- In the transition zone from Coastal Cordillera to Precordillera the heat-flow density value increases up to 40-60 mW/m², as a response of greater distance from the trench. In this region, temperatures in the continental crust are less affected by the cooling of the subducting oceanic plate.

A combination of the wide-angle prestack migration section at 21°S, hypocentral location (Farías et al. 2005) and thermal studies results (Springer, 1999) for the outer forearc area is shown in Fig. 9.4.

It is clear that the imaged structures in the vicinity of the plate interface occur in the region below the upper limit of the seismogenic coupling zone. The isotherms indicate that most of the upper and lower crustal reflectivity is located between 100°-200°C while the heat-flow density curves suggest values ranging between 20-50 mW/m². In the region of Antofagasta thermal modeling studies carried out by Springer (1997) suggest a temperature range of 120°-150°C for the upper limit of the seismogenic zone. Although the sediment cover in the trench area does not exceed 300 m thickness (Hinz et al. 1995), these temperatures may correspond to the range of dehydration of frictionally stable clays to illite and chlorite as proposed by Dixon and Moore (2007) and references therein.

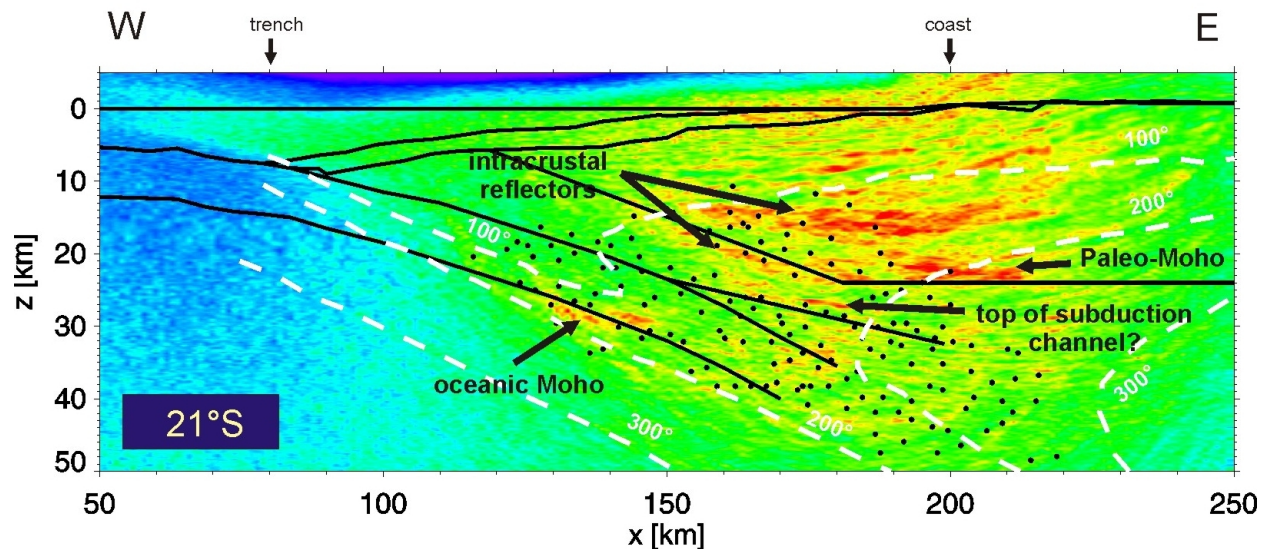


Figure 9.4: Overlay of CINCA wide-angle KPSDM results at 21° with isotherms (Springer, 1999) and hypocentre locations at ~19°30' S (Farias et al. 2005).

Tomography and Vp/Vs ratios

Results of simultaneous inversion of Vp, Vp/Vs ratios and hypocentral parameters using the aftershock series of the great Antofagasta event were presented by Husen et al. (2000). The results were presented along five vertical depth sections between 23°-24.75°S.

For interpretation purposes the tomographic and Vp/Vs sections are overlaid with the wide-angle migration results at 23.25°S (Fig. 9.5). In the Vp and Vp/Vs sections, areas of good resolution are shown in full color while areas with fair resolution are displayed in faded colors. The Vp model shows the subducting Nazca plate as an east dipping feature with high Vp (>7.25 km/s) and Vp/Vs (>1.8) values, typical of cold and dense mafic rocks. The width of the oceanic crust is defined by the narrow velocity zone between 7-8 km/s while its top is marked by the upper envelope of the seismicity. This geometry derived for the subducting slab coincides with the CINCA velocity models and wide-angle migration results. The high Vp/Vs values can be also associated with high fluid content in the oceanic crust. Because the subduction zone in northern Chile has been defined as erosive (von Huene et al. 1999), small amount of sediments are expected to be subducted. Therefore, the high Vp/Vs ratios seen at the plate interface and within the downgoing plate are associated with the presence of fine sediment layers that cover and fill the horst-graben structures and related fractures of the oceanic crust before descend beneath the continental crust. As the slab bends into the trench, these fractures are reactivated, leading to the increase of porosity and permeability within the oceanic crust.

Beneath the coast, at approximately 15-30 km depth and below the subducting slab, the Vp sections show low velocity values (~6.2 km/s) interpreted as underplated material carried down from the trench along the plate interface. The underplating of sediments along this section may be associated to the vertical uplift of the Mejillones Peninsula since Pliocene times as suggested by von Huene et al. (1999).

Due to the lack of crustal seismicity, fair Vp and Vp/Vs values were obtained down to 15 km depth in the continental crust. In areas with good resolution, high Vp values fit well with the occurrence of outcrops of basic and intermediate rocks (like the Caleta-El Cobre batholith between 23.75°-24°S) formed in the magmatic Jurassic arc. These rocks conform 70% of the volume of the present Coastal Cordillera (Husen et al. 2000). The upper crust is characterized by low Vp/Vs ratios. The boundary between the upper and lower crust estimated by the tomographic section at 23.25° coincides with those proposed by the CINCA velocity model at the same latitude (Fig. 7.15).

North of 23.5°S the lower continental crust exhibits average Vp (6.8-6.9 km/s) and Vp/Vs (1.72) values indicating the presence of normal metamorphic rocks. South of this latitude high velocity anomalies (7.0 km/s) are correlated to plutonic rocks outcropping at the surface, suggesting that these velocity anomalies may represent residual intrusion material.

The average values of Vp and Vp/Vs ratio do not indicate the presence of hydrated and serpentized asthenospheric mantle as observed Graeber and Asch (1999) in the region between 69.75°-68°S at depths of about 50 km. The mantle wedge in this area is characterized by lower than average Vp values (7.5 km/s) and higher than average Vp/Vs ratios (>1.8).

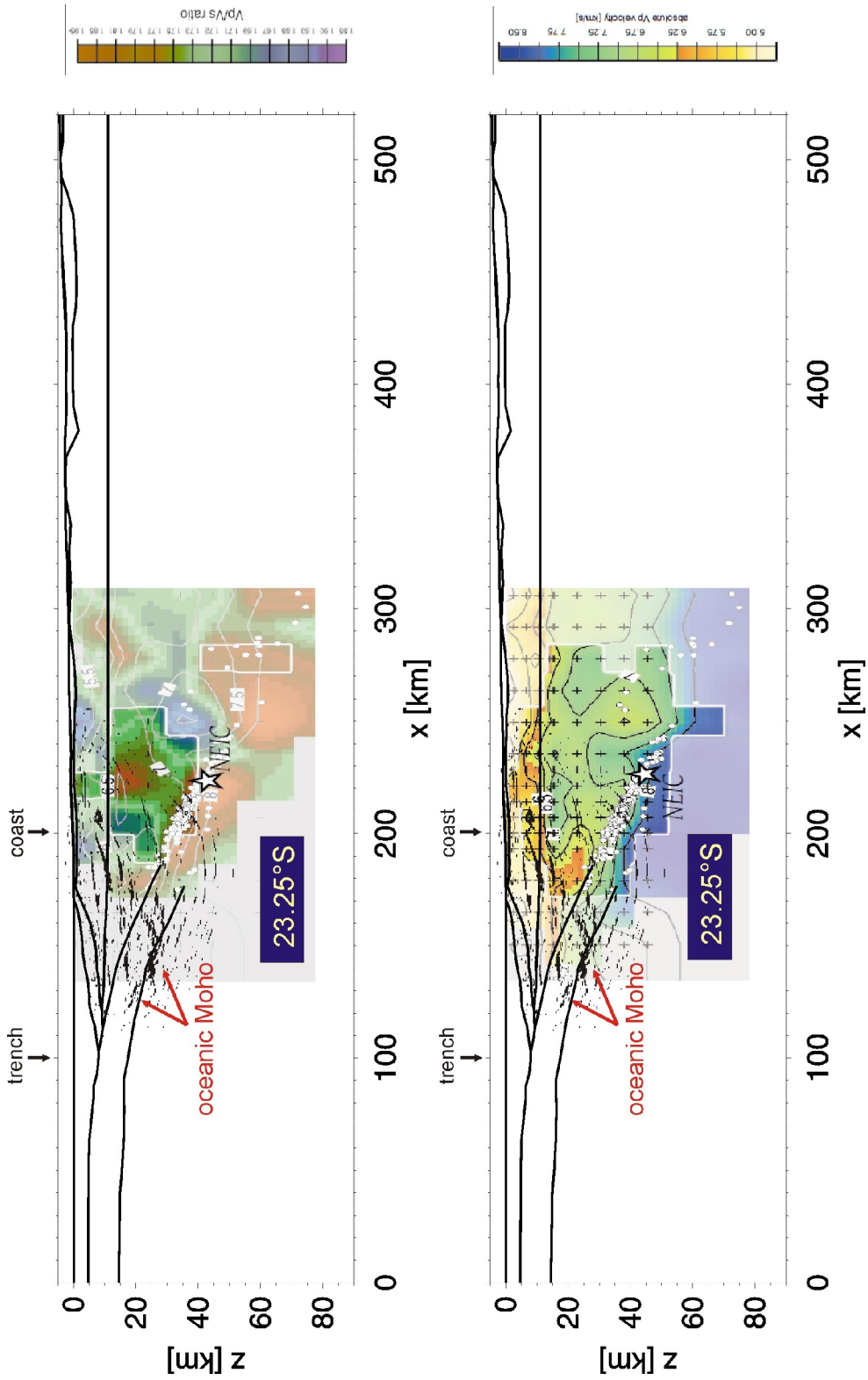


Figure 9.5: Overlay of wide-angle KPSDM image at 23.25°S with Vp/Vs section (top) and seismic tomography (bottom) from Husen et al. (1999). Full color areas denote good resolution while fair resolution is shown in faded colors. The white star marks the hypocentre determination of the Antofagasta earthquake by NEIC.

9.2 Accretive margin in southern Chile

The trench area and the subducting Nazca plate

The structures imaged by KPSDM of the amphibious and onshore wide-angle data aimed to confirm geological features interpreted by previous studies and to provide further information producing a continuous image across the convergent margin, from shallow oceanic crust levels west of the trench to 50 km below the Longitudinal Valley.

Migration of offshore reflection seismic data (pre/post stack) produced high resolution images of the accretionary margin, with the goal to image the outer trench area and its sedimentary infill, the shelf slope and the shallow water area (Rauch, 2004); Contreras-Reyes et al. 2008). Seaward from the trench area, Rauch (2004) described the Nazca plate along the SPOC-NVR profile at 38°S as presenting horst-graben structures yielded by bending-related faulting. These structures are filled with turbidites and pelagic sediments whose thickness increase trenchwards. The oceanic Moho is imaged at 6-6.5 km below the sea. For this part of the margin, typical velocities (4.5-7.2 km/s) for a mature oceanic crust far away from the spreading center were reported by Contreras-Reyes et al. (2008). Therefore, an oceanic crustal thickness of about 6-7 km can be suggested, which is in agreement with the SPOC velocity model (Fig. 7.16) and with the migration of the OBS/OBH data, where the oceanic Moho is imaged up to 25 km west of the trench area (Fig. 8.16).

Images of the trench area show a periodic sequence of deformed terrigenous sediments accreted to the oceanic plate and affected by normal and thrust faulting (Rauch, 2004). Bending-related normal faults extended from the top of the subducting plate cut part or the entire trench infill, whereas thrust faults occurring east of the deformation front mark the onset of the lowermost slope, a compression zone dominated by synclinal, anticlinal and folded structures. Since the ocean bottom is dipping northward, the trench sediments are dragged through the canyons and deposited by turbidites in south-north direction. Also, no relative shifts were found between the oceanic crust and sediments, indicating high friction capable to transmit the convergence rate of the Nazca plate to the trench sediments (Rauch, 2004). Unfortunately, the migration of the wide-angle data did not image structures within the trench area.

The Mocha fault zone (MFZ) trending N55°E is striking the trench axis in the study area and plays an important role in the seismic structure of the Nazca plate. Furthermore, the MFZ is thought to be partly responsible for the uplift of the Arauco Peninsula (Kaizuka et al. 1973) and linked to the main Valdivia event in 1960 (Cifuentes, 1989). Under the trench area, oceanic plate thinning (<7 km) was considered for the forward modeling carried out by Contreras-Reyes et al. (2008) due to the intersection of the MFZ with the trench axis. Such a oceanic crust thinning was also taken into account in the SPOC velocity model (Fig. 7.16). However, Contreras-Reyes et al. (2008) argued that part of this difference may be attributed to velocity and depth uncertainties in the modeling of the oceanic Moho. On the other hand,

the inclusion of the amphibious data in the SPOC velocity model, provide a good control of the structures in the trench area and further inland.

The migration of the SPOC wide-angle data supports the position and thickness of the subducting Nazca plate under the trench area as proposed in the above mentioned velocity models.

The OBS/OBH migrated section shows strong segmented reflectors on the bottom of the oceanic plate following its bending between 75-145 km along the profile. The top of the incoming plate is also clearly visualized from a sharp reflector occurring at 13-14 km depth between 135-140 km distance (Fig. 8.16). Additionally, the migration of amphibious data also shows sharp reflectors along the bottom of the subducting plate under the trench area between 125-150 km distance (Fig. 8.15). On the same section the top of the downgoing plate is imaged at 15 km depth between 150-160 km distance.

Hence, the migration of the SPOC wide-angle data constrained the thickness of the subducting Nazca plate down to 6-8 km depth which agrees not only with the modeled geometry by ray tracing methods but also results of other seismic experiments carried out in the study area.

The offshore-onshore forearc region

The amphibious migrated section shows sharp reflectors at upper-mid crustal levels between 7-12 km depth west of the coast, indicating layering within the Permo-Triassic accretionary complex (Fig. 8.15). The reflectors imaged at upper crustal levels on the onshore section may be also associated to layering in the accretionary complex. The metasediments comprising the Eastern Series were deposited on Proterozoic continental crust in the frame of a continuous passive margin environment during the Early Carboniferous and before the Pennsylvanian subduction. The Eastern Series underwent metamorphism and folding as a result of the beginning of subduction processes. Additionally, folding and inversion in the Eastern Series may be associated to the development of the Western Series. On the other hand, the Western Series form an extinct forearc accretionary prism developed by basal accretion in the Late Paleozoic-Triassic. South of 38°S the Western Series extend from the coast to the Longitudinal Valley while further north the complex is not exposed but has been recognized in boreholes under the coastal platform and offshore forearc (Glodny et al. 2006).

Thus the reflectors observed on the migrated section may be associated to changes in the acoustic impedance caused by the occurrence of the basally accreted and uplifted metabasites and metapelites rocks of the Western series, characterizing the upper continental plate as strongly segmented as seen also by Krawczyk et al. (2006) and Gross et al. (2007) through the imaging of the onshore SPOC-NVR and TIPTEQ-NVR data respectively.

In the prestack depth migrated section of the onshore data, the continental Moho is visualized at 39-42 km depth in the vicinity of the region where the mantle wedge corner encounters the subducting slab (Fig. 8.17). A clear reflector defining the interface between continental crust

and uppermost mantle east of the coast was not identified in the TIPTEQ-NVR migrated sections (pre/post-stack) (Gross et al. 2007; Micksch, 2008). These authors argue that the dehydration of the subducting oceanic plate might produce serpentinization of the rocks within the mantle wedge, leading to a reduction of the velocity contrast which hinders the formation of Moho reflectivity in the seismic section. Nevertheless, three possible positions were suggested for the continental Moho: a) the horizontal Moho at 38 km depth as seen in the SPOC velocity model which constrained the relocation of the 1960 Valdivia event hypocentre (Krawczyk & SPOC Team, 2003), b) a shallower location at 32 km depth and c) at 25 km depth based on receiver function results at 39°S (Yuan et al. 2006). The migration of the wide-angle data supports the first possible location since the SPOC velocity model was derived by modeling the wide-angle data.

Concerning the intracrustal reflectors observed at 9-32 km depth on the same section, they represent the basally accreted and uplifted rocks comprising the segmented Permo-Triassic accretionary wedge of the forearc.

In the TIPTEQ pre/post-stack migrated sections (Gross et al. 2007) a 2-5 km thick reflectivity band occurring above the plate interface below the coast at 25-35 km depth has been interpreted as the subduction channel. The subduction channel narrows downdip, suggesting movement of material upwards leading to increase of crustal thickness due to basal accretion. The subduction channel reaches its maximum below the Coastal Cordillera, here Glodny et al. (2006) indicate uplift due to the basal accretion of material carried down along the subduction channel. This basal accreted material forms at the present the metabasites and metasediments of the Permo-Triassic accretionary wedge as also seen in the wide-angle migrated sections. It has been suggested that the subduction channel exists from the deformation front and the 1960 Valdivia hypocenter along a distance of 130 km approximately (Krawczyk et al. 2006).

9.2.1 Integration with other geophysical methods

Gravimetry

The combined free-air (offshore) and Bouguer (onshore) anomaly map of south-central Chile (Krawczyk et al. 2006 and references therein) shows evident variations of the gravity field along the margin (Fig. 9.6) associated to changes in depth of the subducting plate under the forearc region. Three main forearc segments have been identified (Tašárová, 2007): the northern Arauco-Lonquimay segment (36°-39°S), the middle Valdivia-Liquiñe segment (39°-40°S) and the southern Bahía Mansa-Osorno segment (40°-42°S). Since the SPOC data was collected within the northern segment, the description of the gravity anomalies will be concentrated only in this region.

In the Arauco-Lonquimay segment an offshore minimum (~ -120 mGal) in the free-air anomaly which increases southward is observed along the trench. The coast is characterized by a gravity high of 60-90 mGal while landward the volcanic arc and the backarc region show gravity lows of about -180 mGal. Near the coast there are two areas associated with high free-air anomaly values. The area around the Arauco peninsula ($\sim 37^\circ$ S) the anomaly values reach 50-70 mGal, whereas southward in the area around Mocha island, the average value is about of 60 mGal. The high anomaly values along the coast are produced by the shallow subducting oceanic plate and features in the continental plate i.e. accretionary wedge, high density structures at the wedge base and crustal thinning under the Longitudinal Valley. On the other hand, gravity lows landwards decrease due to the crustal thickening, the basin fill in the Longitudinal Valley and a decreased mantle density under the arc region.

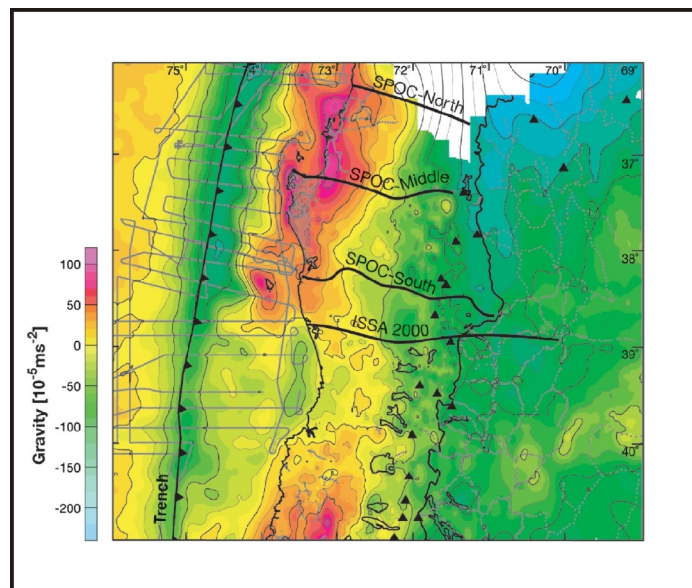


Figure 9.6: Free-air and Bouguer anomaly map of southern Chile (after Krawczyk et al. 2006).

An integrated 3-D density model was derived for the area from 36-42°S using onshore data collected within the framework of several research projects carried out in the central-south Andes together with marine data acquired along the offshore seismic profiles of the SPOC project (Tašárová, 2004, Tašárová, 2007). The ~1400x300 km model consists of 40 bodies approximately representing the oceanic crust and lithospheric mantle, the subducting slab, the continental crust and the asthenospheric mantle. In order to integrate the migration of wide-angle data and gravity data, only the area of the model comprising the forearc region down to 80 km depth is considered (Fig. 9.7).

The intracrustal reflectors observed between 170-190 km distance and 7-12 km depth in the wide-angle migrated section are located inside the body with density value of 2.87 Mg/m³ (Fig. 9.7a). This body represents the rocks of the Western and Eastern Series whose density value was assigned from direct density measurements carried out on rock samples collected in the study area (Tašárová, 2004). Although the rocks of the Western Series present high P/T metamorphism and those belonging to the Eastern Series are low P/T rocks the accretionary wedge is represented by only one body for simplicity purposes. Additionally, the assigned density value of 2.87 Mg/m³ corresponds to an average P-wave velocity of 6.5 km/s at 20 km depth which agrees the SPOC velocity models constructed from wide-angle measurements between 36-39°S.

In the same way, intracrustal reflectors imaged by the onshore data at 8,10 and 20 km depth under the Coastal Cordillera are also located inside the body representing the accretionary wedge (Fig. 9.7b). On the other hand, the reflectors located at 32 and 42 km depth occur inside the unidentified body which has been associated with crustal material (3.15 Mg/m³) in the upper part and serpentized mantle (3.2 Mg/m³) in the lower part (Krawczyk et al. 2006). The reflector at 42 km depth is located below the lower limit of the upper part of the unidentified body, meaning that it may represent the transition from the crustal upper part and the lower mantle serpentized part.

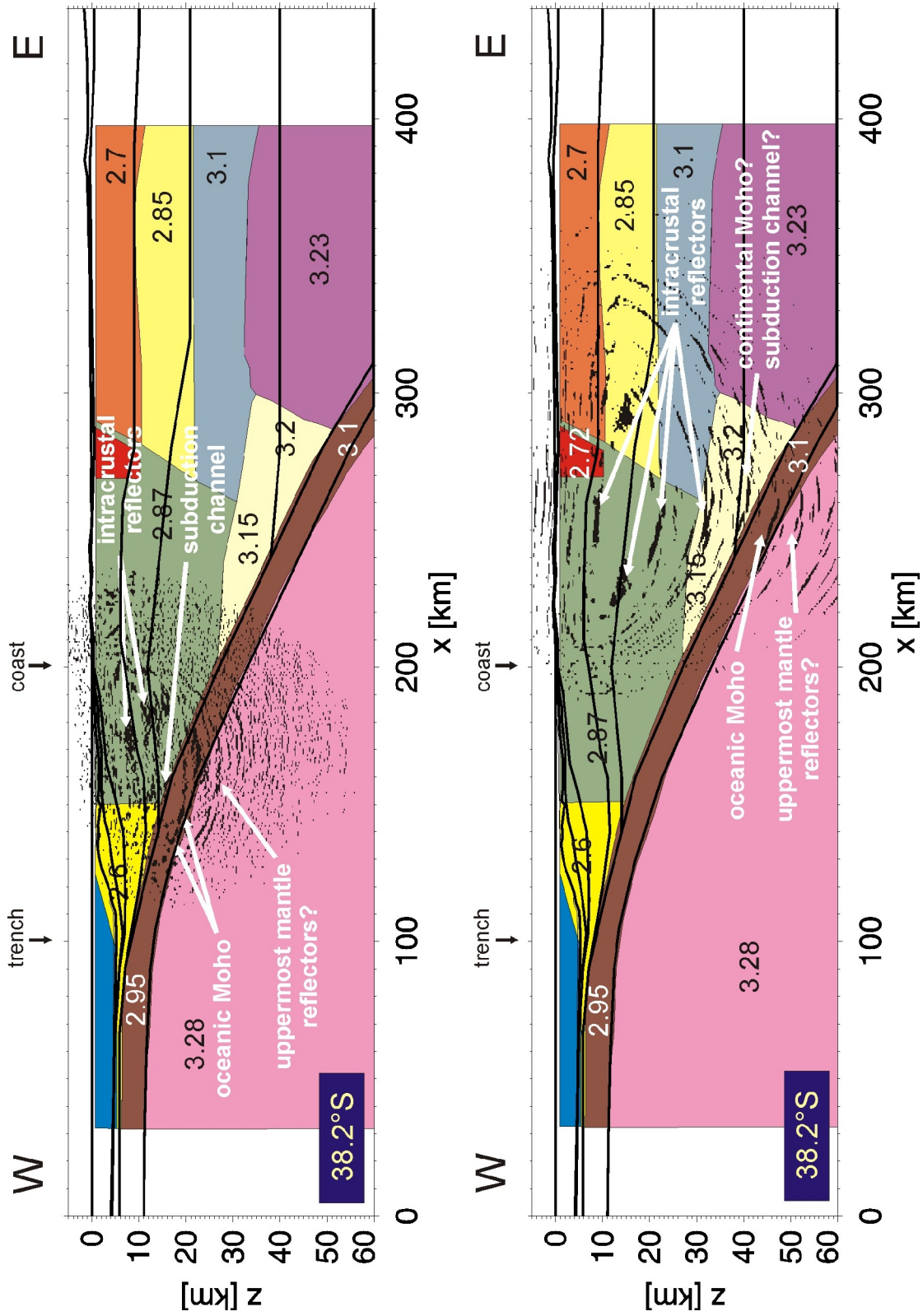


Figure 9.7: Overlay of SPOC wide-angle KPDM images at 38.2°S with gravity results of Tašarová (2007). Top: KPDM of amphibious data; bottom: KPDM of onshore data. Density values are in Mg/m³ indicated.

Magnetotelluric methods

A combined offshore-onshore magnetotelluric (MT) sounding data were collected as a component of project TIPTEQ in order to image resistivity/conductivity structures of the subduction zone. 30 stations were deployed along a profile from the trench area until the Chile/Argentina border. A 2-D model was obtained by applying smooth-inversion techniques (Kapinos, 2009 pers. comm.). The subducting Nazca plate was included in the starting modeling as a highly resistive body but inversion without the slab imaged similar structures. Fig. 9.8 shows a comparison of the final model and the migration of wide-angle data.

The most prominent MT anomaly in the area under the Coastal Cordillera (labeled with A in the MT model) occurs at 10 km depth and 200 km distance. The intracrustal reflector imaged by migration of wide-angle data occurring at 12 km depth is located 10 km west of the center of the anomaly. The origin of this good conductor remains unknown but it has been interpreted as fluid accumulation ascending through faults originated at the downgoing slab (Brasse et al. 2009). This anomaly coincides with a strong reflective structure imaged in the pre-stack section of the TIPTEQ NVR data derived by Gross et al. (2007) and from seismic tomography data it could be related to the existence of a low velocity zone (Brasse et al. 2009).

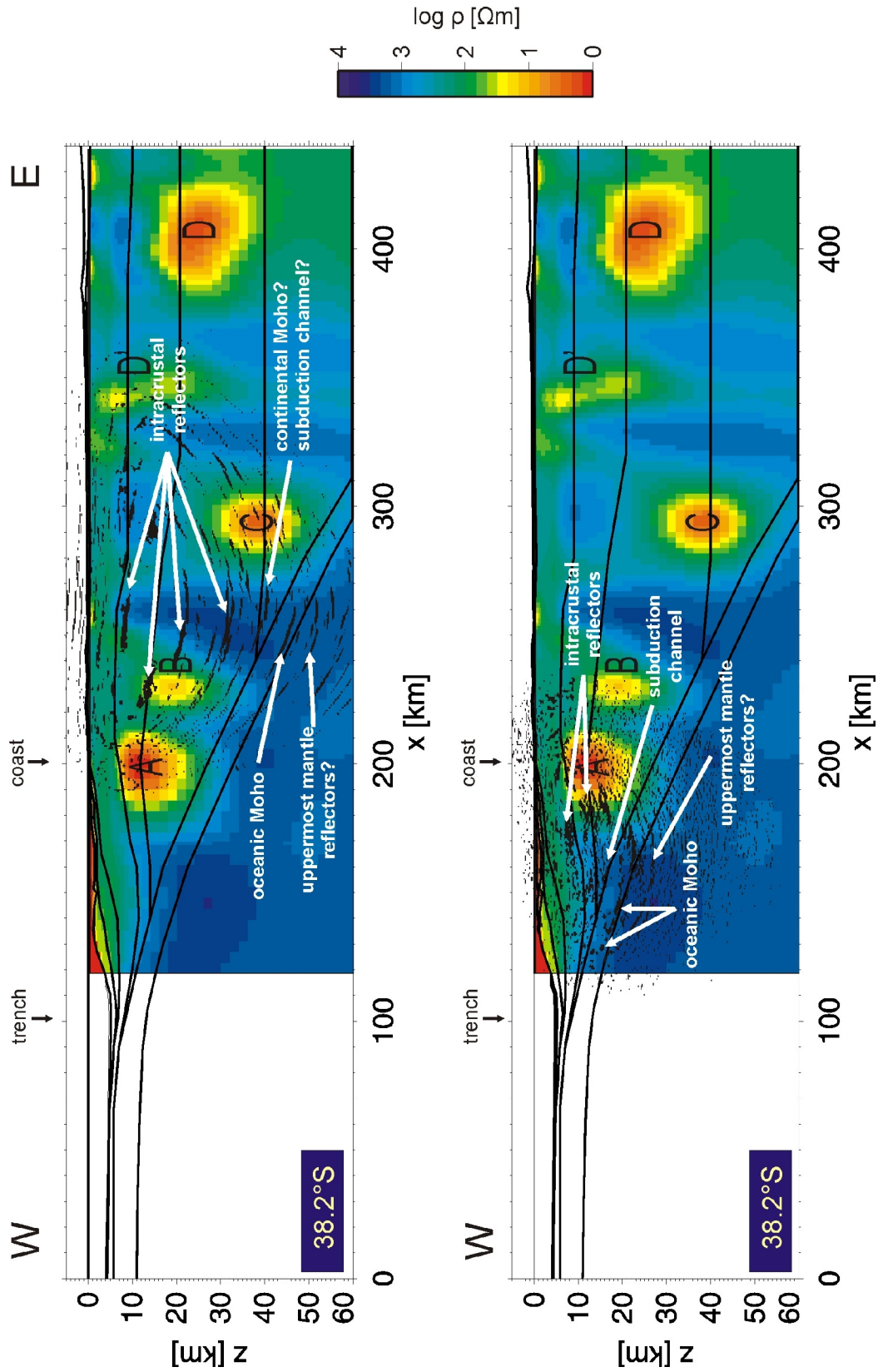


Figure 9.8: Overlay of SPOC wide-angle KPDM images with magnetotelluric results at 38.2°S from (Kapinos pers. comm., 2009). Top: KPDSM of onshore data; bottom: KPDSM of amphibious data.

Tomography and Vp/Vs ratios

Fig. 9.9 and 9.10 show the overlay of the 2-D tomographic velocity model and Vp/Vs sections with the SPOC wide-angle migrated sections.

In the region where migration of wide-angle data images the oceanic Moho, the tomographic model shows a P-wave velocity around 7 km/s. Although the tomographic model does not resolve the slab thickness and the exact position of the oceanic Moho, the migrated sections corroborates the 5-8 km thick oceanic plate occurring at 20 km depth approximately in the marine forearc and at 42 km depth below the Coastal Cordillera. The subducting oceanic plate (labeled C) is characterized by high Vp/Vs ratio around 1.8 which can be associated to: a) the presence of metamorphosed mid-ocean ridge basalt or gabbro under typical temperature and pressure regimes in the region or b) to hydrated and altered crustal and mantle material as a product of bending-related faulting and related hydration of the downgoing slab. Above this region a lower Vp/Vs region occurs, interpreted as underplated crustal material free of fluids expelled from the downgoing plate due to the compaction or phase transformation within the slab. Therefore the zone between the high and low Vp/Vs anomalies may represents an impermeable seal that could be prolonged down to 50 km depth (Haberland et al. 2009).

The intracrustal reflectors imaged by the amphibious data occur within a region (labeled F) characterized by low P-wave velocities and a very high Vp/Vs ratio. The low P-wave velocity values are associated with fluid-saturated material in the Permo-triassic accretionary complex while the high Vp/Vs values indicate partial overpressure. The fluids contained in the rocks of the marine forearc were released by dehydration processes from the downgoing plate and expelled from the subduction channel migrating throughout fractures in the base of the upper plate to shallower depth ranges.

On the other hand, the intracrustal reflectors imaged by the onshore data coincide with the wedge-shaped prism of the onshore forearc (labeled B). Here, the P-wave velocities range between 6 km/s at 10 km depth to 7 km/s at 45 km depth approximately, representing the metasediments of the Western/Eastern Series and the intruded granite rocks of Nahuelbuta. The P-wave values lower than 7 km/s are prolonged in a wedge like shape down to 45 km depth approximately indicating an eastward thickness increase of the continental crust. The reflectors interpreted as the continental Moho or subduction channel on the onshore section coincide with the eastern deepest corner of the anomaly.

Another important feature shown in the tomographic model is the so interpreted by Haberland et al. (2009) as a low velocity channel (labeled I) represented by the eastward dipping layer in the lower continental forearc. The origin of this layer may be linked to the presence of upper plate offscraped material or subducted sediments dragged downward by the subduction process.

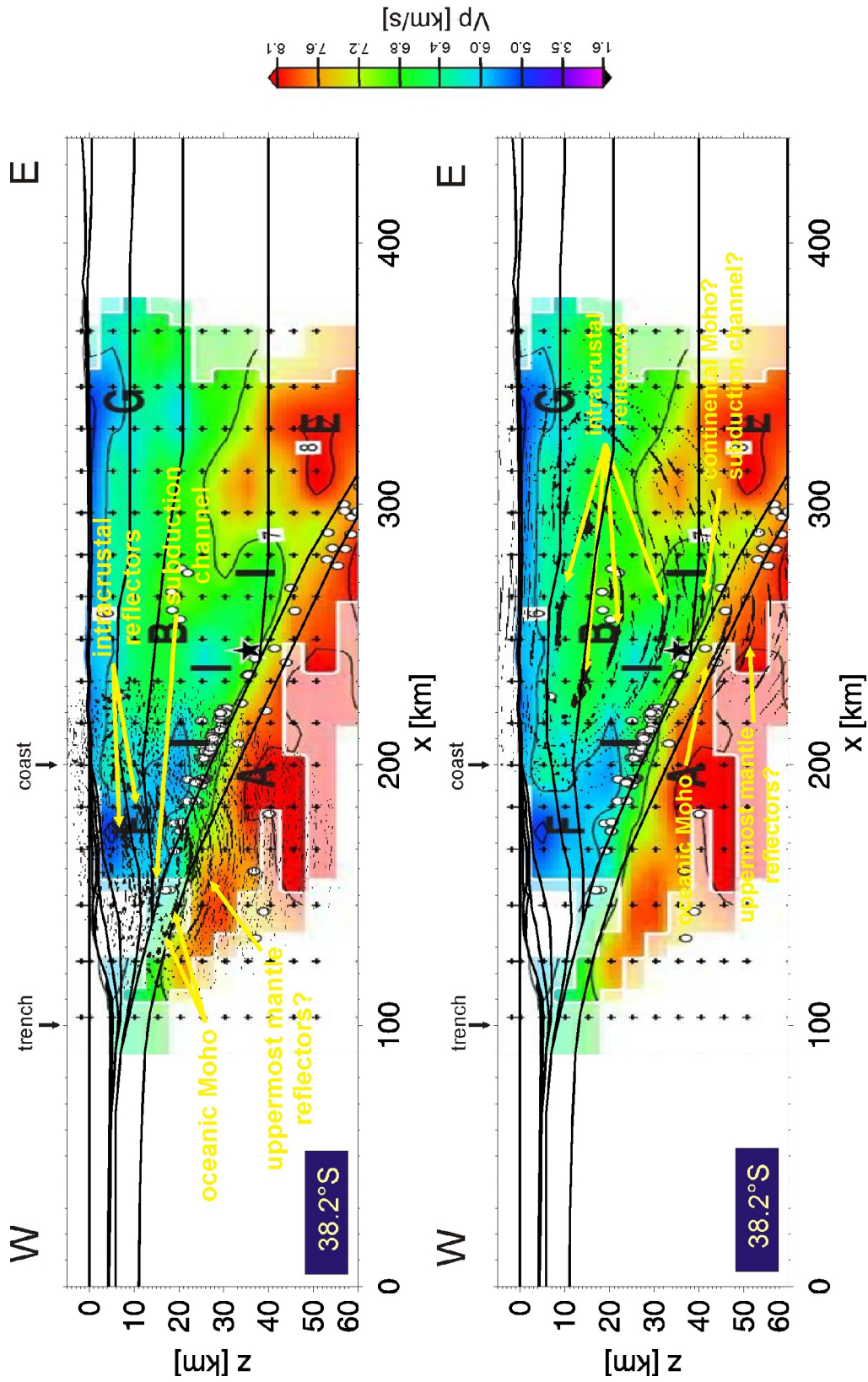


Figure 9.9: Overlay of SPOC wide-angle KPDM images with hypocentre location and tomographic velocity model of (Haberland et al., 2009). Top: KPDM of the amphibious data; bottom: KPDM of the onshore data. Black star indicates the hypocentre of the 1960 earthquake (Engdahl and Villaseñor, 2002).

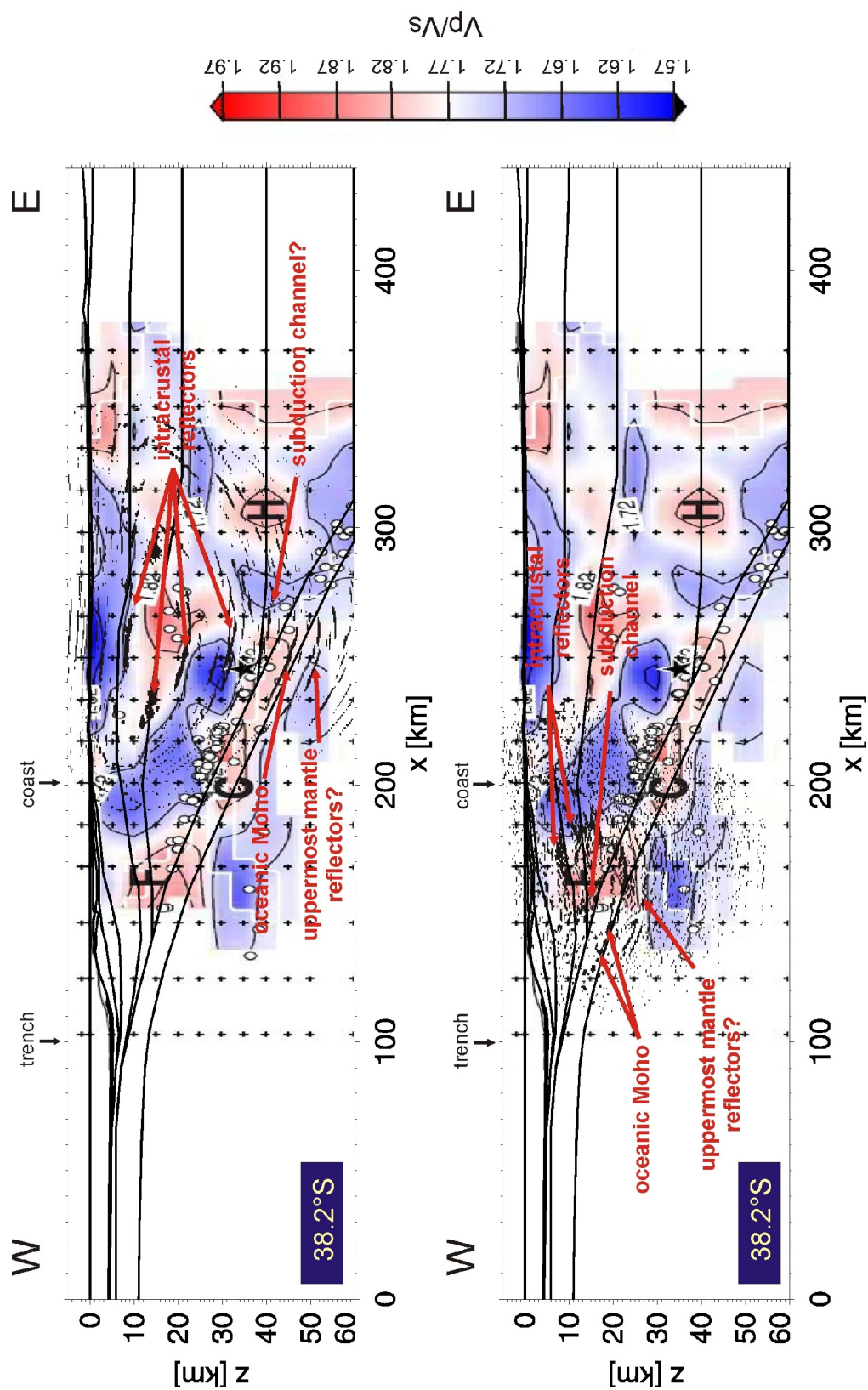


Figure 9.10: Overlay of SPOC wide-angle KPSDM images and V_p/V_s section of (Haberland et al., 2006). Top: KPSDM of the onshore data; bottom: KPSDM of the amphibious data. Black star indicates location of the 1960 earthquake (Engdahl and Villaseñor, 2002).

Hypocentre locations, heat-flow density and temperature distribution

Passive seismic data was recorded between November 2004 and October 2005 by a dense amphibious array consisting of 140 stations installed onshore and 30 deployed offshore covering an area of 250 x 250 km between 37° and 39°S (Rietbrock et al. 2005). The station array was designed to locate local events originating from the coupling zone, to increase the spatial resolution in the construction of tomographic models and to study the crustal seismicity originated along the strike-slip fault systems such as the Lanalhue Fault Zone.

Local seismicity recorded by the amphibious array is shown in Fig. 9.11. It forms an east-dipping cloud between 20 and 40 km depth from the coastal area, which is interpreted as background seismicity occurring at the plate interface during the interseismic cycle (Haberland et al. 2009). As seen in Fig. 9.10 the hypocentres separate the oceanic crust and uppermost mantle region characterized by high V_p/V_s ratio and a lower V_p/V_s region interpreted as the base of the continental crust. This feature confirm the hypothesis that the seismicity occurs along the plate interface.

Oleskevich et al. (1999) used finite element numerical modeling to construct 2D thermal cross sections for four continental subduction zones, including the Chilean margin, in order to study the updip and downdip limits of the seismogenic coupling zone. More recently, Kellner (2007) generated a thermal model with the aim of estimating the width of the coupling zone in southern Chile. The main difference between both thermal modeling is the inclusion by Kellner (2007) of corner flow in the continental mantle. This is based on the fact that mantle flow is produced during the descending of the oceanic slab which moves hot mantle material into the junction point slab-continental crust-mantle wedge. The resulting section shows depressed isotherms along the plate interface different to the Oleskevich et al. (1999) models in which the temperatures above the plate interface are lower and not as depressed.

Considering the updip and downdip limits of the coupling zone as being controlled by temperature ranges of 100°-150°C and 350°-450°C respectively (Oleskevich et al. 1999), the thermal cross section produced by Kellner (2007) suggest that the updip limit of the coupling zone in southern Chile occurs at <10 km depth whereas the downdip limit is estimated at 36-45 km depth. The coupling zone width was estimated to extend from the trench area to 165-220 km landward. Fig. 9.11 shows a comparison between the wide-angle migrated section, hypocentres location (Haberland et al. 2009) and thermal model for southern Chile (Kellner, 2007). It is clear that the top and bottom reflectors of the oceanic slab imaged by the migration of amphibious experiment and the OBS/OBH data occur at intermediate levels of the seismogenic zone suggested by Kellner (2007). The oceanic Moho visualized in the migrated section of the onshore data occurs a few kilometers deeper than the suggested downdip limit of the seismogenic coupling zone.

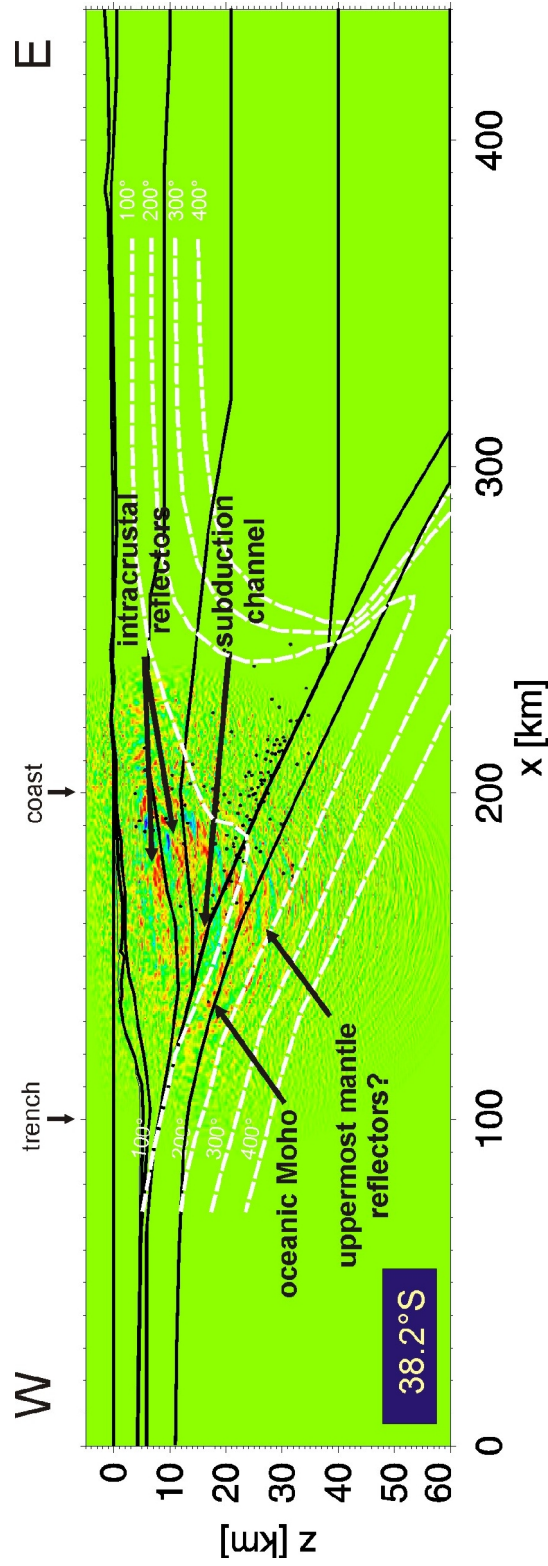


Figure 9.11: Overlay of SPOC wide-angle KPSDM results at 38.2° with isotherms (Kellner, 2007) and hypocentre locations (Haberland et al., 2009).

9.3 Summary: filling the gap

As described in Chapter 3, the Chilean subduction zone has been imaged using different geophysical methods, in particular seismic reflection/refraction data. High quality images of the erosive and accretive margin have been delivered by applying the KPSSDM approach, a valuable tool for the imaging of the complex geometry of the seismogenic coupling zone, revealing important stratigraphic and structural details not imaged by other approach. Furthermore, the evolution of the entire Chilean margin and its internal processes like the migration of fluids from the incoming plate, have been better understood throughout the application of KPSSDM.

The combination of previous migration results from off-onshore NVR data and those obtained in the present study from wide-angle data, produced a high quality and reliable image of the seismogenic zone. Now, the structure of the subduction zone in the forearc region is better constrained. The subducting Nazca plate can be traced along more than 250 km from the vicinity of the trench down to 60-80 km depth.

Fig. 9.12 and 9.13 display the compilation of KPSSDM results of the different datasets collected in northern Chile at 21°S and southern central Chile at 38.2°S respectively.

In north Chile, KPSSDM was applied to the CINCA offshore NVR data (Sick, 2005), the ANCORP onshore NVR data (Yoon, 2005) and the CINCA wide-angle data. The ocean bottom exhibits seamounts and a fine pelagic cover. The top of the oceanic crust is characterized by horst-and-graben structures whose frequency increase towards the trench. In the frontal prism a series of parallel to the slab reflectors connected to escarpments observed on the bathymetry mark the upper part of the subduction channel. These images also show the top and bottom of the downgoing plate subducting at angles of about 10-11°.

The migration of the CINCA wide-angle data provides successful results about the geometry of the slab that correspond to the migration of the offshore NVR data and the adjacent ANCORP NVR data. The oceanic Moho is visualized as a strong reflector at 25-32 km depth, thus constraining the subduction angle of about 17° at this depth. A series of horizontal intracrustal reflectors are observed below the coast, indicating the existence of a layered continental upper crust. Additionally, a strong east-dipping reflector establish the transition to a high velocity zone associated to the lower crust of the ancient Jurassic magmatic arc. At 25 km depth an horizontal sharp reflector suggest the existence of an ancient crust-mantle boundary. Above the LVZ, a strong east-dipping reflector likely marks the top of the subduction channel.

The migration of the ANCORP NVR data yielded outstanding results relevant not only to the geometry of the subducted slab but also linked to the migration of fluids from the oceanic crust towards upper continental levels. The top and bottom of the oceanic slab are observed as two parallel east dipping reflectors at 40-50 km depth. The top reflector is visible down to depths greater than 80 km where it becomes blurred as a consequence of the influence of

Interpretation

heterogeneous overburden on the reflector image, in particular those caused by the Quebrada Blanca Bright Spot occurring above 30 km depth. Immediately above the top of the oceanic plate, the continental Moho is visualized as an east dipping reflector at 35 km depth.

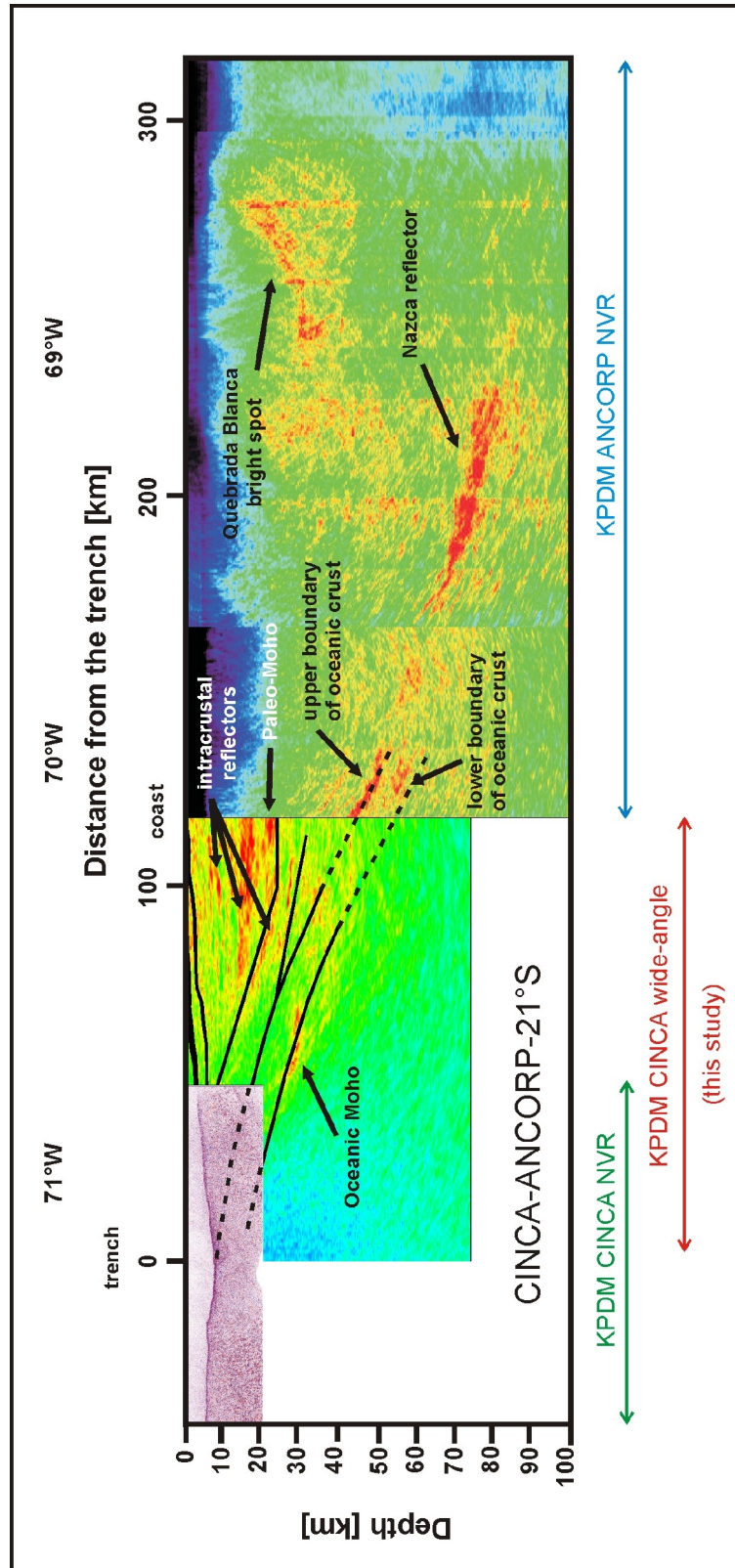


Figure 9.12: Combination of KPDSM results at 21°S (modified after Buske et al. 2002 and Sick et al. 2006).

Similarly the KPSDM approach has been applied to the dataset collected in the accretive margin in South-Central Chile. Fig. 9.13 illustrates from west to east, depth migrated sections corresponding to the SPOC NVR data (Rauch, 2005), SPOC wide-angle data and TIPTEQ NVR data (Gross et al. 2007). A common input for KPSDM of the above mentioned dataset is the interval velocity model constructed by Lüth et al. (2004) from which the Green's functions were calculated.

The offshore portion exhibits 2-3 km thick trench sediments, representing the source for the transported material through the subduction channel to greater depths and responsible for crustal growth by basal accretion. The faulted oceanic plate is covered by a ~150 m thick pelagic layer. The oceanic Moho occurs at 10 km depth below the pelagic cover.

The wide-angle migrated section shows the oceanic Moho between 16-20 km depth dipping with angle around 8° as indicated by Krawczyk et al. (2006). The top of the subducting slab is indicated by a small and sharp reflector at 15-16 km depth. Thus the migration of wide-angle data confirms the 6-8 km thick of the oceanic crust derived from ray tracing modeling (Lüth et al. 2003). Also, some uppermost mantle reflectors can be recognized at roughly 25 km depth. The upper part of the Permo-Triassic accretionary wedge has been imaged west of the coast by a series of intracrustal reflectors between 8-14 km depth.

KPSDM of the OBS/OBH data (Fig. 8.16) also contributes to the imaging of the Nazca plate at 38.2°S . A strong reflective band trace the oceanic Moho at 10-11 km depth west of the trench axis and up to 20 km depth at 50 km from the coast line. The top of the oceanic crust is also visible at 13-14 km depth and 35 km from the trench.

The prestack depth migrated section of the TIPTEQ data (Gross et al. 2007) displays an east dipping reflector with a thickness about 2-5 km at 25 km depth beneath the coast area that can be followed down to 50 km depth below the Longitudinal Valley. The lower boundary of this reflectivity, which coincides with plate interface modeled with ray tracing, is interpreted as the top of the subducted material dragged down to greater depths, whereas the top indicates the existence of a subduction channel. The reflectivity of the sharp reflector parallel to the plate interface between 42-55 km depth is associated to dehydration and embrittlement of the sediments that continue going down through the subduction channel.

Farther east, several horizontal structures are visible up to the limit with a transparent area interpreted as a granitic body covered by sediments of the Eastern Series. These horizontal structures are suggested to represent possible continental Moho positions given the lack of a clear reflection associated to it.

It can be concluded that the migration of wide-angle data represents a valuable contribution to the imaging of the Chilean continental margin since results that contribute to understand the geometry and inner processes of the seismogenic coupling zone were obtained.

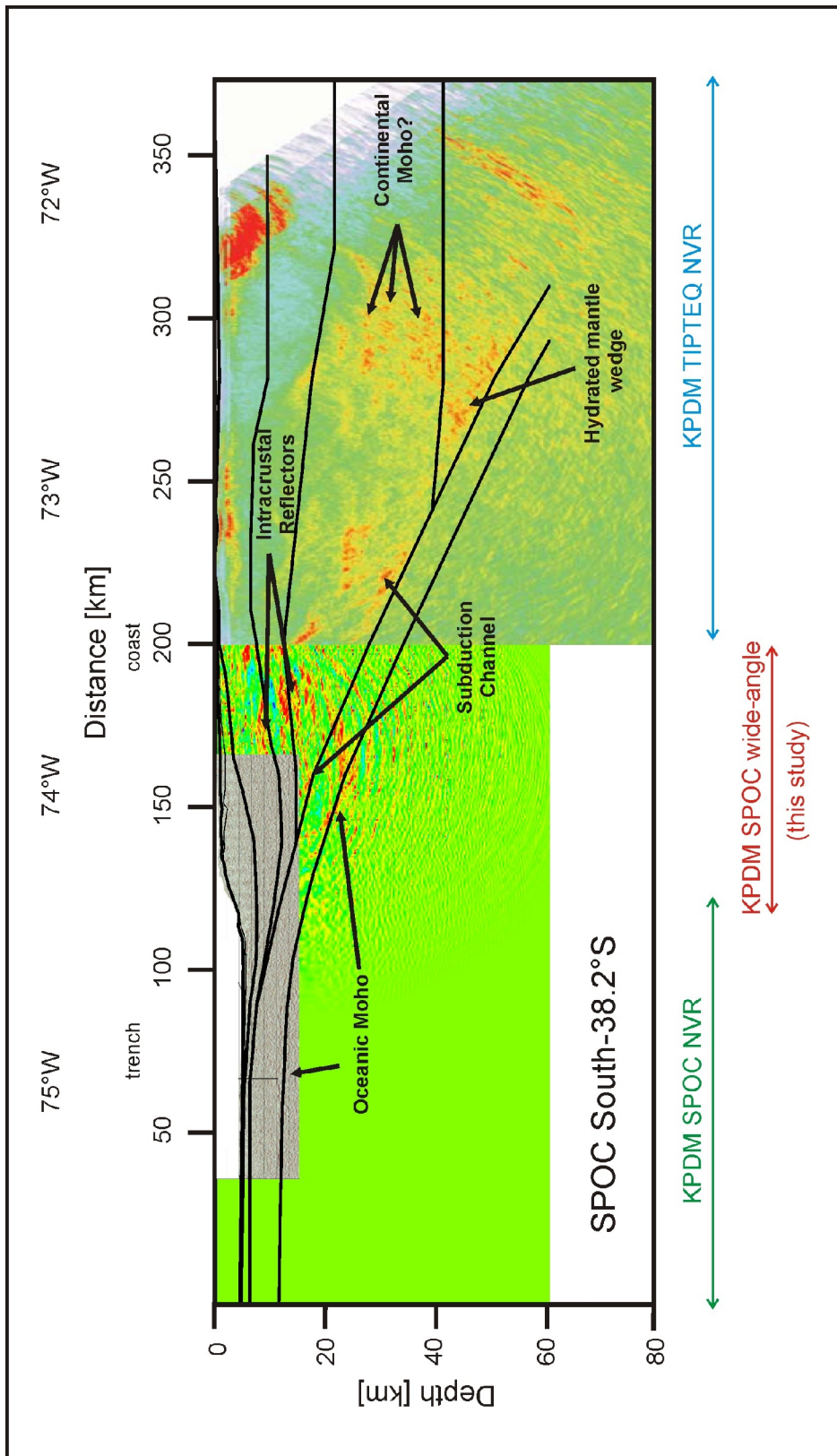


Figure 9.13: Combination of KPDSM results at 38.2°S (modified after Krawczyk et al. 2006).

10 Summary and overview

Wide-angle experiments represent one of the most common methods to study deep structures of the lithosphere in different tectonic settings. The principal benefit of this methods is the recording of strong amplitude signals reflected at larger incidence angles, originating not only from first order discontinuities, but also from higher discontinuities located in zones with small velocity contrast. Prominent phases interpreted in the record sections are the input data for forward modeling and ray tracing methods, which are the most popular approach for the construction of velocity models.

The CINCA-95 and SPOC-2001 are multidisciplinary research programs with the aim to determine the geometry and composition of the northern and southern Chilean continental margin by using different geophysical methods including the recording of wide-angle data. NVR data were collected offshore and onshore in order to study the structure of the oceanic crust and trench region and to explore the deep structure of the continental crust respectively. However, due to the experiments configuration, the data coverage on the edge of the profiles is very low compared to the center where full coverage is reached. That means that in the area below the coast and the offshore forearc, the NVR experiments were not able to image major structures efficiently. The acquisition of wide-angle data under amphibious configuration led to visualize the oceanic Moho and the most prominent features of the continental crust in the area below the coast. Thus, the data gap left by the NVR profiles was filled by the inclusion of the wide-angle data. In addition, onshore wide-angle data was recorded as well with the goal to determine the thickness of the continental crust and major structures.

The first important contribution derived from the wide-angle data was the construction of a macro velocity model (Patzwahl, 1999; Lüth et al. 2004). The most prominent interpreted seismic phases on recording sections were modeled using ray tracing and forward modeling techniques.

High quality images from the oceanic and continental crust were obtained from the prestack migration of the NVR data by using the velocity models derived from wide-angle data. In this thesis a step forward is made by the migration of the wide-angle data of the CINCA and SPOC projects using Kirchhoff prestack depth migration. The successful migration results exhibit either the oceanic Moho and intracrustal structures within the offshore-onshore forearc transition zone, showing the potential of the wide-angle data for the application of imaging techniques.

A summary of the most important results is given in the following, including the presentation of two geological interpretation models of the forearc region in the northern and southern Chilean subduction zone.

10.1 Erosive margin in northern Chile

Prestack depth migration of the CINCA wide-angle data imaged major features below the forearc region of the erosive continental margin in northern Chile. These results are supported by the application of FVM, which produced well focused images of the forearc at 21°S by means the restriction of the migration operator around the region of the actual reflection point using the concept of Fresnel volumes. Likewise, the application of the offset analysis and RIS led to the define the offset and frequency ranges that actually contribute to the imaging process.

The crystalline upper crust is imaged by a series of horizontal reflectors visualized in the amphibious and onshore data between 10-20 km depth, which reveals layering in a region composed mainly by remnants of the Paleozoic continental crust and the volcanic and granitoid rocks of the ancient Jurassic magmatic arc.

The lower crust conforms a high velocity zone imaged by east dipping reflectors occurring 20 km west of the coast at 15-24 km depth. According to previous investigations, the origin of these structures may be linked to: a) the formation of horst-and-graben structures due to the extensional tectonic regime dominating in the Jurassic, b) underplating of oceanic crust material and c) the existence of an ancient crust-mantle boundary called Paleo-Moho.

Strong horizontal reflectivity at about 25 km depth observed in the full frequency image and those derived in the RIS analysis support the existence of the Paleo-Moho. The migration of the onshore data allows the prolongation of the Paleo-Moho from the area below the coast to 100 km inland.

The top of the LVZ is also imaged by weak east dipping reflectors parallel to the subducting slab. The LVZ has been interpreted as an extension of the subduction channel that begins beneath an active thrust fault system observed at 10 km depth in the migrated section of the offshore NVR data. It broads to the east as response to underplating of material flowing through the subduction channel. The underplating could be the cause of thickening of the continental crust and related uplift and extensional structures in the outer forearc.

A possible location of the continental Moho or continuation of the subduction channel below the Coastal Cordillera is indicated by a east dipping sharp reflector observed at 47-55 km depth in the migrated section of the onshore data.

The oceanic Moho is imaged west of the coast as a east dipping strong reflector at 25-32 km depth. Its occurrence supports the slab geometry and the subduction angle about 17° modeled with forward methods in previous investigations.

10.2 The accretive margin in southern Chile

Despite of the smaller number of record section with high signal-to-noise ratio, the prestack migrated section of the SPOC amphibious wide-angle data the most prominent structural features below the outer forearc have been imaged.

The migration of the OBS/OBH data significantly contributes to the imaging of the oceanic Moho west and east of the trench axis. A strong reflective band trace the oceanic Moho at 10-11 km depth west of the trench axis and up to 20 km depth beneath the trench sediments. The top of the oceanic plate is also observed as a sharp reflector at 13-14 km depth. These results support the 6-8 km thickness of the oceanic crust and the subduction angle of 8° as derived from forward modeling in earlier works.

The migration of the amphibious data images structures in the upper continental crust beneath the offshore forearc. The reflectors observed on the migrated section may be associated to changes in the acoustic impedance caused by the intercalation of the basally accreted and uplifted metabasites and metapelites rocks of the Western series, characterizing the upper continental plate as strongly segmented.

The migrated section of the amphibious data also shows the oceanic Moho at depths of 16-20 km beneath the accretionary wedge. The subduction channel is also visible as a small reflector located 50 km westward from the coast at 15-16 km depth.

The onshore data was also prestack depth migrated. The results show a strongly segmented upper crust as observed in the migration of the amphibious data. The lower crust presents sharp reflectors between 19-32 km depth, likely associated to accreted and underplated material flowing along the subduction channel. The oceanic Moho is imaged by the onshore data as well. It is observed as a strong east dipping reflector at 30 km from the coast between 42-49 km depth. Its appearance supports the subduction angle of 15° as derived by ray tracing/forward modeling. In addition, the continental Moho is visualized at 39-42 km depth in the vicinity of the region where the mantle wedge corner encounters the subducting slab, but this reflectivity may be also linked to the subduction channel.

A clear reflector defining the interface between continental crust and uppermost mantle east of the coast was not identified in the TIPTEQ-NVR migrated sections. Earlier investigations argued that the dehydration of the subducting oceanic plate might produce serpentinization of the rocks within the mantle wedge, leading to a reduction of the velocity contrast which hinders the formation of Moho reflectivity in the seismic section. Nevertheless, three possible positions were suggested for the continental Moho: a) the horizontal Moho at 38 km depth as seen in the SPOC velocity model which constrained the relocation of the 1960 Valdivia event hypocentre, b) a shallower location at 32 km depth and c) at about 25 km depth based on receiver function analysis at 39°S . The migration of the wide-angle data supports the first possible location since the SPOC velocity model was derived by modeling traveltimes picked on the wide-angle record sections.

10.3 Geological cross sections of the forearc

The wide-angle imaging has provided valuable information that completes the knowledge about the geometry and composition of the offshore-onshore forearc of the Chilean subduction zone. Merging the results obtained in this thesis with earlier investigations in the study area, two geological cross sections are proposed. These sections describe the major structural and geological features of the erosive margin at 21°S and the accretive margin at 38.2°S. The bodies conforming the models are identified with numbers and their tectonic and geological interpretation are explained in the following.

Forearc in northern Chile

Fig. 10.1 (modified after Pelz, 2000) illustrates the forearc region at 21°S as derived from migration of seismic data. It is conformed by several bodies, representing the segmented continental crust, the subducting Nazca plate and the lithosphere mantle.

1. The continental slope. Four seismic units were recognized in the CINCA NVR time migrated sections (Hinz et al. 1998). The uppermost seismic unit is characterized by P-wave velocities of 2.05 km/s and composed by semi-consolidated siltstones and sandstones of Neogene age. Normal faults that can be traced to the sea bottom are observed, indicating recent tectonic extension. The second unit consists of sedimentary rocks, volcanic rocks associated to the La Negra Formation and metamorphic remnants of the Paleozoic crust. The top of the unit is segmented by listric faults dipping trenchwards that reach the unit below. The P-wave velocities assigned to this unit range from 4.35 km/s to 5 km/s. The third unit presents P-wave velocities between 5-6 km/s and it is characterized by large blocks that are downthrown along deeply penetrating west dipping faults. The origin of this fault group is linked to subduction and tectonic erosion processes. The fourth unit forms the frontal wedge which limits with the trench axis. This unit comprises sedimentary rocks slumped from the middle and upper slope.

East of the trench, the prestack depth migrated section of the CINCA NVR data shows a series of reflectors parallel to the subducting slab that represent active thrust operating at low strain rates (Sick et al. 2006). These fault system marks the upper part of the subduction channel where material slumped trenchwards from the middle slope and upper continental plate is then underthrust.

2. The deeper upper continental crust. This region can be seen as the deeper extension of the second and third unit of the continental slope. Layering above 15 km depth is suggested by the horizontal intracrustal reflectors observed in the wide-angle prestack depth migrated section at 21°S. This part of the upper crust is conformed by relict of the Paleozoic continental crust and the volcanic and granitoid rocks of the ancient Jurassic magmatic arc, intruded as a consequence of strong changes in the kinematic of the plate convergence that led to subduction of the oceanic crust (Pichowiak, 1994).

3. The high velocity block. The sharp east dipping reflectors imaged west of the coast in the wide-angle migrated section define the transition to a high velocity zone whose origin is not clear and might be explained by: a) extensional structures formed during the Jurassic arc, b) underplating of oceanic crust and c) the crust-mantle boundary of the Jurassic magmatic arc or Paleo-Moho. Strong wide-angle reflectors mark the occurrence of the Paleo-Moho at about 25 km depth.

4. The subduction channel. Seismic data collected in northern Chile do not reveal directly the existence of subduction channel. Weak reflectors parallel to the subducting slab imaged in the wide-angle data are linked to the top of the LVZ associated recently by Lohrmann et al. (2006) to the subduction channel. The thickness of the subduction channel up to 25 km depth is derived from the 3 km wide zone defined by the hypocentres located by Patzig (2002) where material movement between the continental and oceanic plate could take place. Below 25 km depth the subduction channel broadens as a consequence of oceanic plate bending forming a wedge-like structure overlying the top of the Nazca plate where material transported through the subduction channel is finally underplated. The underplating leads to thickening of the continental crust and may be the origin of uplift and extensional structures in the outer forearc. On the other hand, Wigger et al. (1994) proposed partial serpentinization caused by dewatering of the subducting oceanic crust as the process that originates the low velocities values observed in this region.

5. The mantle wedge. The occurrence of the mantle wedge is derived from the position of reflectors imaged in the wide-angle and NVR data that define the continental Moho. The mantle wedge in the forearc has been interpreted to be heterogeneously hydrated according to the high V_p/V_s ratio between 1.75-1.83 derived from passive seismic studies (ANCORP Working Group, 2003).

6. The subducting Nazca plate. The top of the oceanic crust is characterized by horst-and-graben-like structures whose frequency increase towards the trench. In the migrated sections of the CINCA NVR data the subduction of some of these horst-and-graben-like structures are clearly visible. These images also show the top and bottom of the downgoing plate subducting at angles of about 10-11°. Further down, between 25-32 km depth and beneath the offshore forearc, the wide-angle migrated section shows the oceanic Moho as strong reflectors dipping at approximately 17°. Farther inland, the top and bottom of the oceanic slab are observed in the ANCORP migrated section as two parallel east dipping reflectors at 40-50 km depth. Additionally, results of analysis of receiver function image the oceanic Moho below 50 km depth. In summary, the combination of the different depth migrated sections allows the tracing of the Nazca plate from the trench area up to 80 km depth. Also, these results support the 6-8 km thick oceanic crust as derived by the forward modeling of traveltimes arrivals.

7. Lithospheric mantle. The uppermost mantle below the oceanic crust is characterized by P-wave velocities over 8.1 km/s, typical values of mafic and ultramafic rocks. Some reflectivity has been identified in the wide-angle migrated section but its origin is not clear yet.

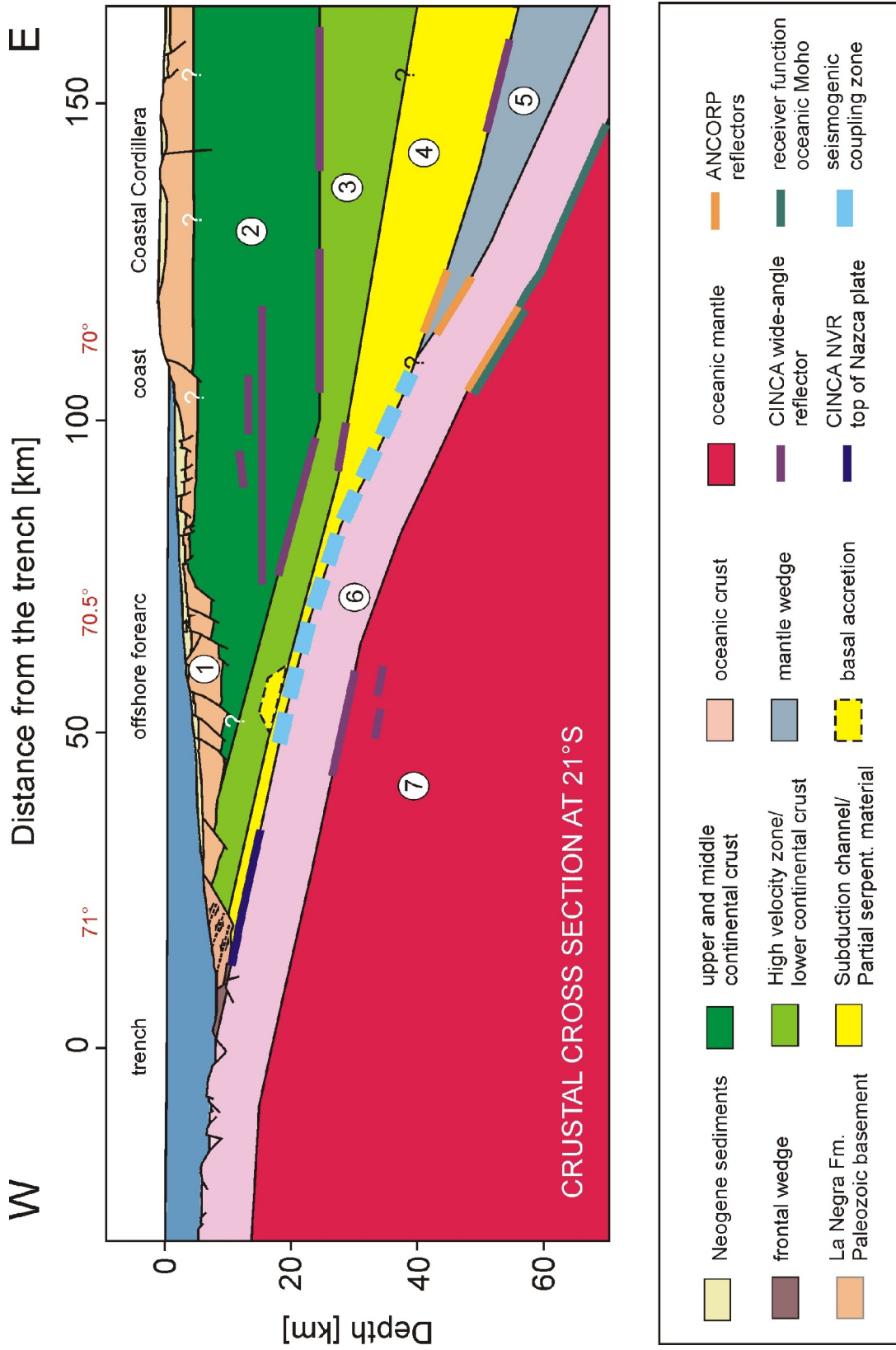


Figure 10.1: Geological cross section of the forearc region in northern Chile as derived from migration of seismic data. Modified after Peiz (2000).

Forearc in southern Chile

The geological cross section for the forearc region of the southern accretive margin is illustrated in Fig. 10.2.

1. Trench sediments. A 2-3 km thick terrigenous sediments wedge fill the trench area, representing the source for the transported material through the subduction channel to greater depths and responsible for crustal growth by basal accretion. The terrigenous sequence comprise turbidites and hemipelagic/pelagic sediments deposited during the Quaternary.
2. The accretionary wedge. This region revealing compressional folding limits with the trench fill and mark the onset of the lowermost slope.
3. Permo-Triassic accretionary complex. It is formed by a complex of metasediments of the Eastern Series which were deposited on Proterozoic continental crust during the existing passive margin before the Pennsylvanian subduction. Metabasites and metapelites rocks of the Western series which form an extinct forearc accretionary prism developed by basal accretion in the Late Paleozoic-Triassic also integrate the Permo-Triassic accretionary complex. The Western Series were basally accreted leading to extensional tectonic and uplift of the Coastal Cordillera. The reflectors observed on the migrated sections may be associated to changes in the acoustic impedance caused by the intercalation of the basally accreted and uplifted metasedimentary rocks of the Western series, characterizing the upper continental plate as strongly segmented.
4. Western Series. This region is constrained by the first-break tomography of the project TIPTEQ (Micksch, 2008) and was interpreted to comprise rocks of the Western Series outcropping in the coast area. This region is separated from the bodies 5-6 by the LFZ.
- 5-6. The granitoid Coastal Batholith. This region occurring east of the LFZ is also constrained by the NVR migrated section and first-break tomography of the TIPTEQ project (Micksch, 2008). It has been visualized as a transparent zone conformed by the granitic rocks of the Coastal Cordillera covered by Quaternary sediments. In the seismic section the transparent zone extends up to 23 km depth where coincides with high reflectivity material that is interpreted as trapped fluids below the granite body.
7. The Lower crust. The continental lower crust is characterized by layering as revealed from wide-angle imaging results and NVR data of the TIPTEQ project (Gross et al. 2007). The continental Moho is not clearly imaged in the NVR depth sections. However, migration of the SPOC onshore data images a sharp reflector in the region where the oceanic plate, the continental plate and the mantle wedge meet. This feature can be associated to the existence of continental crust-mantle boundary at this depth.

8. The subduction channel. A 2-5 km thick reflectivity band occurring above the plate interface below the coast at 25-35 km depth has been interpreted as the upper bound of the subduction channel (Gross et al. 2007). The subduction channel narrows downdip, suggesting movement of material upwards leading to increase of crustal thickness due to basal accretion. The subduction channel reaches its maximum below the Coastal Cordillera, here Glodny et al. (2005) indicate uplift due to the basal accretion of material carried down along the subduction channel. It has been suggested that the subduction channel exists from the deformation front and the 1960 Valdivia hypocentre along a distance of 130 km approximately.

9. The mantle wedge. Its location is constrained by the occurrence of the continental Moho. In the migrated section of the TIPTEQ NVR data are no clear reflectors indicating the existence of the continental Moho. Nevertheless, the wide-angle migrated section of the onshore data images a sharp reflector at 39-42 km depth interpreted as the continental Moho.

10. The subducting Nazca plate. Wide-angle and NVR migration results support the geometry of the subducting oceanic plate. Below the trench axis the Nazca plate subducts at angles of about 8° , while at greater depths the subduction angle increases up to 15° . Top and bottom of the oceanic plate are clearly imaged west of the coast in the SPOC wide-angle migrated sections, supporting the 6-8 km oceanic crust thickness as derived from ray tracing/forward modeling techniques.

11. The lithospheric mantle. The uppermost mantle below the oceanic crust is characterized by P-wave velocities over 8.0-8.1 km/s, typical values of mafic and ultramafic rocks. Some reflectivity has been identified in the wide-angle migrated section but its origin is unclear.

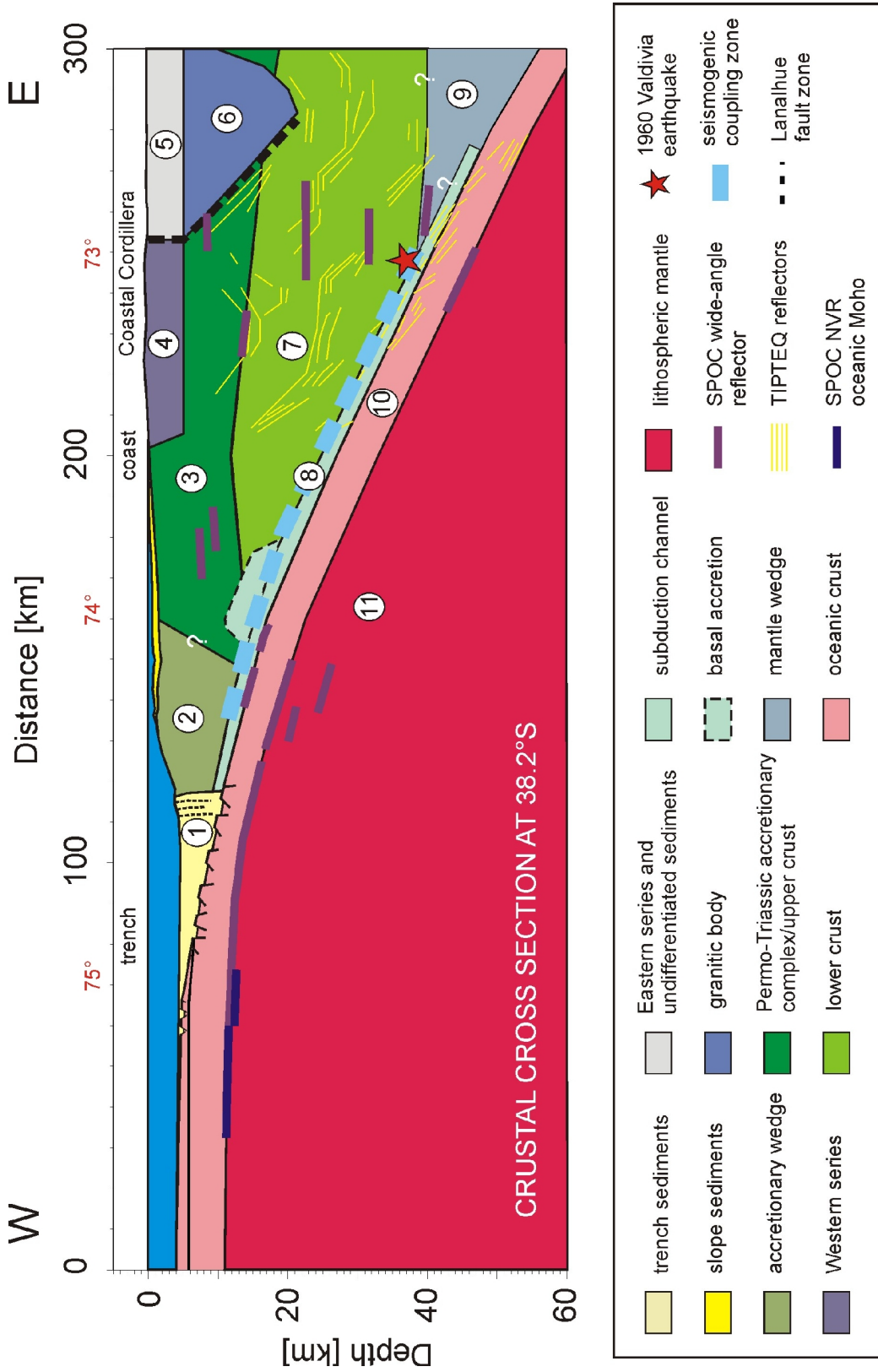


Figure 10.2: Geological cross section of the forearc in southern Chile as derived from migration of seismic data.

References

- Audebert, F., Nichols, D., Rekdal, T., Biondi, B., Lumley, D., Urdaneta, H., 1997, Imaging complex geological structure with single-arrival Kirchhoff prestack depth migration: *Geophysics*, 62, 1533-1543.
- Aki, K., and Richards, P., 2002, *Quantitative seismology*. University Science Books, pp 704.
- ANCORP Working Group, 2003, Seismic imaging of a convergent continental margin and plateau in the central Andes (Andean Continental Research Project 1996 (ANCORP'96)): *J. Geophys. Res.*, 108 (B7), 2328, doi:10.1029/2002JB001771.
- Biondi, B., 2007, Concepts and applications in 3D seismic imaging. Distinguished instructor series, No.10, sponsored by the Society of Exploration Geophysicists, European Association of Geoscientists and Engineers, pp 243.
- Bleibinhaus, F., Stich, D., Simon, M. and Gebrande, H., 2003, New Results from amplitude preserving prestack depth migration of the Münchberg/Vogtland segment of the MVE deep seismic survey: *Journal of Geodynamics*, 35, 33-43.
- Brasse, H., Kapinos, G., Li, Y., Muetschard, L., Soyer, W., Eydan, D., 2009, Structural electrical anisotropy in the crust at the South-Central Chilean continental margin as inferred from geomagnetic transfer functions: *Physics of the Earth and Planetary Interiors*, 173, 7-16.
- Brown, A, 1991, Interpretation of three-dimensional seismic data: *AAPG Memoir* 42, pp 341.
- Buske, S., 1999, Three dimensional pre-stack Kirchhoff migration of deep seismic reflection data: *Geophys. J. Int.*, 173, 243-260.
- Buske, S., Lüth, S., Meyer, H., Patzig, R., Reichert, C., Shapiro, S., Wigger, P., Yoon, M., 2002, Broad depth range seismic imaging of the subducted Nazca slab, North Chile: *Tectonophysics*, 350(4), 273-282.
- Buske, S., Heigel, M., and Lüth, S., 2005, Fresnel-Volume-Migration of single component seismic data: *Annual WIT report* 2005.
- Buske, S., Gutjahr, S., and Sick, C., 2009, Fresnel volume migration of single-component seismic data: *Geophysics*, 74, WCA47–WCA55
- Byrne, D.E., Davis, D., Sykes, L., 1988, Loci and maximum size of thrust earthquakes and the mechanics of the shallow region of subduction zones: *Tectonics*, 7, 833-857.
- Červený, V., and Pšenčík, P., 1983, Gaussian beam and paraxial ray approximation in three dimensional inhomogeneous media: *Bulletin of Seismological Society of America*, 70, 47-77.

Červený, V., and Soares, P., 1992, Fresnel volume ray tracing: *Geophysics*, 57, 902-915.

Cifuentes, I.L., 1989, The 1960 Chilean earthquakes: *J. Geophys. Res.*, 94, 665-680

Christensen, N., and Salisbury, M., 1979, Structure and constitution of the lower oceanic crust: *Rev. Geophys.*, 29, 279-316.

Colombo, D., 2005, Benefits of wide-offset seismic for commercial exploration targets and implications for data analysis: *The Leading Edge*, 352-363.

Contreras-Reyes, E., Grevemeyer, I., Flueh, E.R., and Reichert, C., 2008, Upper lithospheric structure of the subduction zone offshore of southern Arauco peninsula, Chile, at ~38°S: *J. Geophys. Res.*, 113, B07303, doi:10.1029/2007JB005569.

Claerbout, J., and Doherty, S., 1972, Downward continuation of moveout-corrected seismograms: *Geophysics*, 37, 741-768.

Cloos, M., and Shreve, R., 1988, Subduction-channel model of prism accretion, melange formation, sediment subduction, and subduction erosion at convergent plate margins: 1. Background and description: *Pageoph*, 128, 455-500.

Dixon, T., and Moore, C., 2007, *The seismogenic zone of subduction thrust faults*. Columbia University Press, pp 692.

Delouis, B., Cisternas, A., Dorbath, L., Rivera, L., and Kausel, E., 1996, The Andean subduction zone between 22 and 25°S (northern Chile): precise geometry and state of stress: *Tectonophysics*, 256, 81-100.

Farías, M., Charrier, R., Comte, D., Martinod, J., Hérail, G., 2005, Late Cenozoic deformation and uplift of the western flank of the Altiplano: Evidence from the depositional, tectonic, and geomorphologic evolution and shallow seismic activity (northern Chile at 19°30'): *Tectonics*, 24, TC4001, doi:10.1029/2004TC001667.

Fliedner, M., and White, R., 2003, Depth imaging of basalts flows in the Faroe-Shetland Basin: *Geophys. J. Int*, 152, 353-371.

Fujie, G., Ito, A., Kodaira, S., Takahashi, N., and Kaneda, Y., 2006, Confirming sharp bending of the Pacific plate in the northern Japan trench subduction zone by applying a travelttime mapping method: *Physics of the Earth and Planetary Interiors*, 157, 72-85.

Gazdag, J., 1978, Wave equation migration by phase-shift: *Geophysics*, 43, 1342-1351.

Giese, P., Prodehl, C., Stein, A., 1976, *Explosion Seismology in Central Europe*. Springer Verlag Berlin Heidelberg New York, pp 429.

Giese, P., Scheuber, E., Schilling, F., Schmitz, M. and Wigger, P., 1999, Crustal thickening processes in the Central Andes and the different natures of the Moho discontinuity: *Journal of South American Earth Sciences*, 12, 201-220.

Glodny, J., Echtler, H., Figueroa, O., Franz, G., Graefe, K., Kemnitz, H., Kramer, W., Krawczyk, C., Lohrmann, J., Lucassen, F., Melnick, D., Rosenau, M., Seifert, W., 2006, Long-term geological evolution and mass-flow balance of the South-Central Andes. In: Oncken, O., Chong, G., Franz, G., Giese, P., Goetze, H-J., Ramos, V., Strecker, M. and Wigger, P. (eds) *The Andes-active subduction orogeny. Frontiers in Earth Sciences Series*, vol 1. Springer-Verlag, Berlin, Heidelberg, New York, pp 401-428.

Goetze, H-J., and Kirchner, A., 1997, Interpretation of gravity and geoid in the Central Andes between 20° and 29°S: *Journal of South American Sciences*, 10, 179-188.

Gohl, K., and Smithson, S., 1993, Structure of Archean crust and passive margin of southwest Greenland from seismic wide-angle data: *J. Geophys. Res.*, 98, B4, 6623-6637.

Graeber, F., and Asch, G., 1999, Three dimensional models of P-wave velocity and P-to-S velocity ratio in the southern Central Andes by simultaneous inversion of local earthquake data: *J. Geophys. Res.*, 104, 20237-20256.

Gross, K., Micksch, U., and TIPTEQ Research Group, Seismic Team, 2007, The reflection seismic survey of project TIPTEQ-the inventory of the Chilean subduction zone at 38.2°S: *Geophys. J. Int.*, doi: 10.1111/j.1365-246X.2007.03680.x

Haberland, C., Rietbrock, A., Lange, D., Bataille, K., and Dahm, T., 2009, Structure of the seismogenic zone of the southcentral Chilean margin revealed by local earthquake traveltome tomography: *J. Geophys. Res.*, 114, B01317, doi:10.1029/2008JB005802.

Hackney, R., Echtler, H., Franz, G., Goetze, H-J., Lucassen, F., Marchenco, D., Melnick, D., Meyer, U., Schmidt, S., Tasarova, Z, Tassara, A. and Wienecke, S, 2006 The segmented overrinding plate and coupling at the South-Central Chilean margin (36°-42°S). In: Oncken, O., Chong, G., Franz, G., Giese, P., Goetze, H-J., Ramos, V., Strecker, M. and Wigger, P. (eds) *The Andes-active subduction orogeny. Frontiers in Earth Sciences Series*, vol 1. Springer-Verlag, Berlin, Heidelberg, New York, pp 355-374.

Haslinger, F., 1994, Ein Verfahren zur automatisierten Bestimmung von Scheingeschwindigkeiten aus Mehrspurseismogrammen. Master's thesis, Ludwig-Maximilian-Universität Munchen, 80p.

Herve, F., 1994, The southern Andes between 39°-44°S latitude: the geological signature of a transpressive tectonic regime related to a magmatic arc. In *Tectonics of the Southern Central Andes*. Reutter, K-J., Scheuber, E., Wigger, P., editors. Springer Verlag, Berlin, Heidelberg, New York, pp 243-248.

- Hinz, K., Reichert, C.J., Flueh, E.R., Kudrass, H-R, 1995, Final Report: Crustal Investigations off and onshore Nazca/Central Andes (CINCA). Bundesanstalt fuer Geowissenschaften und Rohstoffe, pp 217.
- Holbrook, S., Reiter, E., Purdy, G., and Tokzoez, M., 1992, Image of the Moho across the continent-ocean transition, U.S. East coast, *Geology*, 20, 203-206.
- Hong, T., and Kennett, B., 2003, Scattering attenuation of 2D elastic waves: theory and numerical modeling using a wavelet-based method: *Bull. Seismol. Soc. Am.*, 93, 922-938.
- Husen, S., Kissling, E., Flueh, E., and Asch, G., 1999, Accurate hypocentre determination in the seismogenic zone of the subducting Nazca plate in northern Chile using a combined on-/offshore network: *Geophys. J. Int.*, 138, 687-701.
- Husen, S., Kissling, E., and Flueh, E., 2000, Local earthquake tomography of shallow subduction in north Chile: a combined onshore and offshore study: *J. Geophys. Res.*, 105, 28183-28198.
- Jenkins, F., and White, H., 1957, *Fundamental of optics*, McGraw-Hill, New York.
- Kaizuka, S., Matsuda, T., Nogami, M., Yonekura, M., 1973, Quaternary tectonic and recent seismic crustal movements in the Arauco Peninsula and its environs, Central Chile, *Geogr. Rep.* 8, 1-49.
- Kellner, A., 2007, Different styles of deformation of the fore-arc wedge along the Chilean convergent margin: Insights from 3D numerical experiments, Ph.D thesis, 175pp., University of Potsdam.
- Kirchner, A., 1997, 3D-Dichtemodellierung zur Anpassung des Schwere-und des Schwerepotentialfeldes der zentralen Anden, Ph.D thesis, 98 pp., Freie Universitaet Berlin.
- Kopp, C., Fruehn, J., Flueh, E.R., Reichert, C., Kukowski, N., Bialas, J., and Klaeschen, D., Structure of the Makran subduction zone from wide-angle and reflection seismic data: *Tectonophysics*, 329, 171-191.
- Kosminskaya, I., 1971, Deep seismic sounding of the Earth's crust and upper mantle: c/b Consultants Bureau, New York-London, pp 184.
- Krawczyk, C. & the SPOC Team, 2003, Amphibious seismic survey images plate interface at 1960 Chile earthquake: *EOS Trans. Am.Geophys. Union*, 84(32), 301, 304-305.

Krawczyk, C., Mechie, M., Lueth, S., Tasarova, S., Wigger, P., Stiller, M., Brasse, H., Echtler, H., Araneda, M., and Bataille, K., 2006, Geophysical signatures and active tectonics at the South-Central Chilean margin. In: Oncken, O., Chong, G., Franz, G., Giese, P., Goetze, H-J., Ramos, V., Strecker, M., and Wigger, P (eds) The Andes-active subduction orogeny. *Frontiers in Earth Science Series*, Vol 1. Springer-Verlag, Berlin Heidelberg New York, pp 171-192.

Lafond, C., and Levander, A., 1995, Migration of wide-aperture onshore-offshore seismic data, central California-seismic images of the late stage subduction: *J. Geophys. Res.*, 100, 22231-22243.

Lay, T., and Wallace, T., 1995, *Modern global seismology*. Academic Press, pp 519.

Lessel, K., 1997, Die krustenstruktur der Zentralen Anden in NordChile (21-24°S), abgeleitet aus 3D-Modellierungen refraktionsseismischer Daten: *Berliner Geowiss. Abh., Reihe B, Band 31*.

Levander, A., Zelt, C., Symes, W., 2007, Crust and lithospheric structure-active source studies of crust and lithospheric structure. In: Romanowicz, B., Dziewonski, A (eds) *Treatise on Geophysics*, vol 1, Seismology and the structure of the Earth, Elsevier B.V., 247-283.

Lindsey, J.P., 1989, The Fresnel zone and its interpretative significance: *The Leading Edge*, 8, 33-39.

Lizarralde, D., and Holbrook, S., 1997, U.S. Mid-Atlantic margin structure and early thermal evolution: *J. Geophys. Res.*, 102, B10, 22855-22875.

Lohrmann, J., Kukowski, N., Krawczyk, C.M., Oncken, O., Sick, C., Sobiesiak, M., Rietbrock, A., 2006, Subduction channel evolution in brittle fore-arc wedges- a combined study with scale sandbox experiments, seismological and reflection seismic data and geological field evidence. In: Oncken, O., Chong, G., Franz, G., Giese, P., Goetze, H-J., Ramos, V., Strecker, M., and Wigger, P (eds) *The Andes-active subduction orogeny*. *Frontiers in Earth Science Series*, Vol 1. Springer-Verlag, Berlin Heidelberg New York, pp 237-262.

Luccassen, F., Trumbull, R., Franz, G., Creixell, C., Vásquez, P., Romer, R., Figueroa, O., 2004, Distinguishing crustal recycling and juvenile addition at active continental margins: the Paleozoic to recent compositional evolution of the Chilean Pacific margin (36-41°S): *Journal of South American Sciences*, 17, 103-119.

Ludwig, J., Nafe, J., and Drake, C., 1970, Seismic refraction. In A. Maxwell, editor, *The Sea*, volume 4, 53-84. Wiley, New York.

Lüth, S., Wigger, P., and ISSA Research Group, 2003, A crustal model along 39° from a seismic refraction profile ISSA2000: *Rev Geol Chile*, 30(1), 83-101.

Lüth, S., Wigger, P., Mechie, J., Stiller, M., Krawczyk, C., Bataille, K., Reichert, C., Flueh, E., and SPOC Research Group, 2004, Crustal structure of the Chilean forearc between 36° and 40° from combined offshore and onshore seismic wide-angle measurements-SPOC 2001: *Geosur* 2004.

Lüth, S., Buske, S., Giese, R., and Goertz, A., 2005, Fresnel volume migration of multicomponent data: *Geophysics*, 70, 121-129.

Meissner, R., 1967, Exploring deep interfaces by seismic wide-angle measurements: 29th meeting of the European Association of Exploration Geophysicists, Stockholm.

Melnick, D., and Echtler, H., 2006, Morphotectonic and geologic digital map compilations of the South-Central Andes (36°-42°S). In: Oncken, O., Chong, G., Franz, G., Giese, P., Goetze, H-J., Ramos, V., Strecker, M., and Wigger, P (eds) *The Andes-active subduction orogeny. Frontiers in Earth Science Series, Vol 1.* Springer-Verlag, Berlin Heidelberg New York, pp 565-568.

Micksh, U., 2008, The Chilean subduction zone at 38.2°S: New geophysical images derived from reflection data of project TIPTEQ. Ph.D thesis, Freie Universitaet Berlin, pp 279.

Milkereit, B., 1987, Migration of noisy crustal seismic data: *J. Geophys. Res.*, 92, 7916-7930.

Mueller, R.D., Roest, W., Royer, J., Gahagan, L., Sclater, J., 1993, A digital age map of the ocean floor. *SIO Reference Series No 93-30.*

Mueller, C., Friedrich, T., and Milkereit, B., 2001, Combined vertical-incidence and wide-angle seismic study of deepwater bright-spot reflections: *The Leading Edge*, 854-857.

Mutter, C. and Mutter, J., 1993. Variations in thickness of layer 3 dominate oceanic crust structure: *Earth and Planetary Science Letters*, 117, 295-317.

Nelson, E., Forsythe, R-H. and Arit, I, 1994, Ridge collision tectonics in terrane development: *Journal of South American Earth Sciences*, 7, 271-278.

Niemeyer, H., 1996, Evolucion tectonica cenozoica del margen continental activo de Antofagasta, norte de Chile: *Rev. Geol. Chile*, 23, 165-186.

Okoye, P. and Uren, N., 2000, Fresnel zones and spatial resolution for P- and SH- waves in transversely isotropic media: *Geophysics*, 65, 1168,1178.

- Oleskevich, D., Hyndman, R., and Wang, K., 1999, The updip and downdip limits to great subduction earthquakes: Thermal and structural model of Cascadia, south Alaska, SW Japan and Chile: *J. Geophys. Res.*, 104, 14965-14991.
- Ortlieb, L., Barrientos, S., and Guzman, N., 1996, Coseismic coastal uplift and coralline algae record in northern Chile-The 1995 Antofagasta earthquake case: *Quat. Sci. Rev.*, 15, 949-960.
- Patzig, R., 2000, Lokalbeben-Tomographie der Umbiegung von Antofagasta (Nordchile), Ph.D. thesis, 219 pp., Freie Universitaet Berlin.
- Patzig, R., Shapiro, S., Asch, G., Giese, P. and Wigger, P., 2002. Seismogenic plane of the northern Andean Subduction Zone from aftershocks of the Antofagasta (Chile) 1995 earthquake: *Geophys Res Letters*, 29, 10.1029/2001GL013244
- Patzwahl, R., 1998, Plattengeometrie und Krustenstruktur am Kontinentalrand Nord-Chiles aus Weitwinkelseismischen Messungen. *Berliner Geowiss. Abh.*, Reihe B, Band 3.
- Patzwahl, R., Mechie, J., Schulze, A., and Giese, P., 1999, 2D velocity models of the Nazca plate subduction zone between 19.5°S and 25°S from wide-angle seismic measurements during the CINCA'95 project: *J. Geophys Res*, 104 (B4), 7293-7317.
- Pelz, K., 2000, Tektonische Erosion am zentralandinen Forearc (20°-24°). Scientific Technical Report STR/00/20, GFZ Potsdam, pp 118.
- Pichowiak, S., 1994, Early Jurassic to early Cretaceous magmatism in the Coastal Cordillera and the Central Depression of North Chile. In: K.J. Reutter, E. Scheuber, and P.J. Wigger (eds), *Tectonics of the Southern Central Andes: Structure and Evolution of an Active Continental Margin*, Springer-Verlag, Berlin Heidelberg New York, pp. 203-218.
- Prezzi, C., Goetze, H-J., and Schmidt, S., 2005, Density structure of the Central Andes from 3D integrated gravity modelling: 6th International Symposium on Andean Geodynamics (ISAG 2005, Barcelona), Extended Abstracts: 574-577
- Prezzi, C., Goetze, H-J., and Schmidt, S., 2009, 3D density model of the Central Andes: *Physics of the Earth and Planetary interiors*, 177, 217-234.
- Podvin, P., and Lecomte, I., 1991, Finite difference computation of traveltimes in very constricted velocity models: a massively parallel approach and its association tools: *Geophys. J. Int.*, 105, 271-284.
- Rauch, K., 2004, Zyklische reflexionen terrigener sedimente in Peru-Chile Graben. PhD thesis, Freie Universitaet Berlin, 97 pp.

Ranero, C., von Huene, R., Weinrebe, W., Reichert, C., 2006, Tectonic processes along the Chile convergent margin. In: Oncken, O., Chong, G., Franz, G., Giese, P., Goetze, H-J., Ramos, V., Strecker, R., Wigger, P, (eds) The Andes-active subduction orogeny. *Frontiers in Earth Science Series*, vol 1. Springer-Verlag, Berlin Heidelberg New York, pp 91-122.

Reutter, K., Giese, P., Goetze, H.-J., Scheuber, E., Schwaab, K., Schwarz, G., and Wigger, P., 1988. Structures and Crustal Development of the Central Andes between 21°S and 25°S. In Bahlburg, H., Breitzkreuz, C., and Giese, P., editors, *The Southern Central Andes*, Volume 17 of *Lecture notes on Earth Sciences*, pp. 231-261. Springer Verlag.

Roessling, R., 1989, Petrologie im einem tiefen Krustenstockwerk des jurassischen magmatischen Bogens in der nordchilenischen Küstenkordillere südlich von Antofagasta. *Berl Geowiss Abh (A)* 112, pp 73.

Rosenau, M., 2004, Tectonics of the Southern Andean intra-arc zone (38°-42°S), PhD thesis, Freie Universitaet Berlin.

Ruff, L., and Tichelaar, B., 1996, What controls the seismogenic plate interface in subduction zones?. In: *Subduction: Top to Bottom*, Geophys. Monogr. Ser., vol. 96, edited by G.E. Bebout, D. Scholl, S. Kirby, Platt, J., AGU, Washington, 105-111.

Scheuber, E. And Reutter, K., 1992, Magmatic arc tectonics in the Central Andes between 21° and 25°S: *Tectonophysics*, 205, 127-140.

Scheuber, E., and Giese, P., 1999, Architecture of the Central Andes-a compilation of geoscientific data along a transect at 21°S: *Journal of South American Earth Sciences*, 12, 103-107.

Scheuber, E., Bogdanic, T., Jensen, A. and Reutter, K., 1994, Tectonic development of the North Chilean Andes in relation to plate convergence and magmatism since the Jurassic. In: K.J. Reutter, E. Scheuber, and P.J. Wigger (eds), *Tectonics of the Southern Central Andes: Structure and Evolution of an Active Continental Margin*, Springer-Verlag, Berlin Heidelberg New York, pp. 121-139.

Schilling, F., Trumbull, R., Brasse, H., Haberland, C., Asch, G., Bruhm, D., Mai, K., Haak, V., Giese, P., Munoz, M., Ramelow, J., Rietbrock, A., Ricaldi, E., and Vietor, T., 2006, Partial melting in the Central Andean Crust: a review of geophysical, petrophysical, and petrological evidence. In: Oncken, O., Chong, G., Franz, G., Giese, P., Goetze, H-J., Ramos, V., Strecker, R., Wigger, P, (eds) The Andes-active subduction orogeny. *Frontiers in Earth Science Series*, vol 1. Springer-Verlag, Berlin Heidelberg New York, pp 459-474.

Schmitz, M., Lessel, K., Giese, P., Wigger, P., Araneda, M., Bribach, J., Graeber, F., Grunewald, S., Haberland, C., Lueth, S., Roewer, P., Ryberg, T., and Schulze, A., 1999, The crustal structure beneath the Central Andean forearc and magmatic arc as derived from seismic studies-the PISCO 94 experiment in northern Chile (21°-23°), *Journal of South American Sciences*, 12, 237-260.

Schneider, W., 1978, Integral formulation for migration in two and three dimensions: *Geophysics*, 43, 49-79.

Schleicher, J., Tygel, M., and Hubral, P., 1993, 3-D true-amplitude finite-offset migration: *Geophysics*, 58, 1112-1126.

Schmidt, S., and Goetze, H-J., 2006, Bouguer and isostatic maps of the Central Andes. In: Oncken, O., Chong, G., Franz, G., Giese, P., Goetze, H-J., Ramos, V., Strecker, R., Wigger, P, (eds) *The Andes-active subduction orogeny. Frontiers in Earth Science Series*, vol 1. Springer-Verlag, Berlin Heidelberg New York, pp 559-562.

Shearer, P., 2006, *Introduction to Seismology*: Cambridge University Press, pp 260.

Sheriff, R.E., and Geldart, L.P., 1995, *Exploration Seismology*, Cambridge University Press, pp 592.

Sick, C., 2005, *Structural investigations off Chile: Kirchhoff prestack depth migration versus Fresnel volume migration*. PhD thesis, Freie Universitaet Berlin, pp 122.

Sick, C., Yoon, M., Rauch, C., Buske, S., Lüth, S., Araneda, M., Bataille, K., Chong, G., Giese, P., Krawczyk, C., Mechie, J., Meyer, H., Oncken, O., Reichert, C., Schmitz, M., Shapiro, S., Stiller, M., Wigger, P., 2006, Seismic images of accretive and erosive subduction zones from the Chilean margin. In: Oncken, O., Chong, G., Franz, G., Giese, P., Goetze, H-J., Ramos, V., Strecker, R., Wigger, P, (eds) *The Andes-active subduction orogeny. Frontiers in Earth Science Series*, vol 1. Springer-Verlag, Berlin Heidelberg New York, pp 147-169.

Simon, M., 1993, *Entwicklung eines 3D-Migrationsverfahrens mit Anwendungen auf seismische Daten aus dem Umfeld der Kontinentalen Tiefbohrung Oberplatz*. Dissertation d. Fak. f. Geowissenschaften, LMU München, pp 168.

Simon, M., Gebrande, H., and Bopp, M., 1996, Pre-stack migration and true-amplitude processing of DEKORP near-normal incidence and wide-angle reflection measurements: *Tectonophysics*, 264, 381-392.

Sobolev, S.V., and Babeyko, A.Y., 1994, Modeling of mineralogical composition, density and elastic wave velocities in anhydrous magmatic rocks: *Surveys in Geophysics*, 15, 515-544.

Springer, M., and Foester, A., 1998, Heat-flow density across the Central Andean subduction zone: *Tectonophysics*, 291, 123-139.

Springer, M., 1999, Interpretation of heat-flow density in the Central Andes: *Tectonophysics*, 306, 377-395.

- Stern, R., 2002, Subduction zones: *Rev. Geophys.*, 40(4), 1012, doi:10.1029/2001RG000108.
- Stolt, R.H., 1978, Migration by Fourier Transform: *Geophysics*, 43, 23-48.
- Tatel, H., and Tuve, M., 1958, Seismic studies in the Andes: *Am. Geophys. Union Trans*, 39, 580-582.
- Tašárová, Z., 2004, Gravity data analysis and interdisciplinary 3-D modeling of a convergent plate margin (Chile, 36-42°S), PhD thesis, Freie Universitaet Berlin, pp 169.
- Tašárová, Z., 2007, Towards understanding the lithospheric structure of the southern Chilean subduction zone (36°S-42°S) and its role in the gravity field: *Geophys. J. Int.*, 170, 995-1014.
- Thornton, M. and Zhou, H., 2008, Crustal-scale prestack depth imaging of the 1994 and 1999 LARSE surveys: *Geophysical Prospecting*, 56, 577-585.
- van Avendonk, H., 2004, Slowness-weighted diffraction stack for migrating wide-angle seismic data in laterally varying media: *Geophysics*, 69, 1046-1052.
- Vidale, J., 1990, Finite difference calculation of traveltimes in three dimensions: *Geophysics*, 55, 521-526.
- von Huene, R., and Ranero, C.R., 2003, Subduction erosion and basal friction along the sediment-starved convergent margin off Antofagasta, Chile: *J. Geophys. Res.*, 108(B2), 2079, doi:10.1029/2001JB001569.
- von Huene, R., Weinrebe, W. and Heeren, F., 1999, Subduction erosion along the North Chile margin: *Geodynamics*, 27, 345-358.
- Widess, M. B., 1973, How thin is a thin bed?: *Geophysics*, 38, 1176-1180.
- Wigger, P., 1986, *Krustenseismische Untersuchungen in Nord-Chile un Süd-Bolivien*: *Berl Geowiss Abh (A)*, 66, 31-48.
- Wigger, P., 1988, Seismicity and crustal structure of the Central Andes. In: Bahlburg, H., Breitzkreuz, C., Giese, P. (eds), *The southern Central Andes. Lecture Notes in Earth Sciences 17*. Springer, Berlin, Heidelberg, New York, pp 209-229.
- Wigger, P., Baldzuhn, S., Giese, P., Heinsohn, W., Schmitz, M., Araneda, M., Martínez, E., Ricaldi, E., Viramonte, A., 1994, Variations of the crustal structure of the Southern Central Andes deduced from seismic refraction investigations. In: K.J. Reutter, E. Scheuber, and P.J. Wigger (eds), *Tectonics of the Southern Central Andes: Structure and Evolution of an Active Continental Margin*, Springer-Verlag, Berlin Heidelberg New York, pp. 23-48.

Yilmaz, O., 2001, Seismic data analysis: processing, inversion and interpretation of seismic data: Society of Exploration Geophysicists.

Yoon, M., 2005, Deep seismic imaging in the presence of a heterogeneous overburden: Numerical modeling and case studies from the Central Andes and Southern Andes. PhD Thesis, Freie Universitaet Berlin.

Yoon, M., Buske, S., Shapiro, S.A., and Wigger, P., 2009, Reflection Image Spectroscopy across the Andean subduction zone: Tectonophysics, 472, 51-61.

Yuan, X. et al., 2006, Deep seismic images of the southern Andes, in Evolution of an Andean margin: a tectonic and magmatic view from the Andes to the Neuquen Basin (36-39°S), vol 407, pp 61-72, eds Kay, S. & Ramos, V., Geological Society of America special paper.

Zelt, C., 1992, Seismic travelttime inversion for 2-D crustal velocity structure: Geophys. J. Int, 108, 16-34.

Acknowledgments

I am grateful to the DAAD-Fundayacucho Cooperation Program for giving me the opportunity to participate in such an interesting and challenging P.h.D. work in one of the elite universities in Germany and for providing the financial support.

I would like to thank Prof. Dr. Serge Shapiro for his guidance, advices and support given every time I needed since the beginning of this project. Likewise, I would like to thank Dr. Stefan Buske for his patience, support and for having always an answer to my questions and for finding a solution to the technical problems.

Many thanks to Dr. Stefan Lüth for providing me his expertise and knowledge at the beginning of my stage at the FU.

I wish to thank Dr. Peter Wigger for the useful discussions about the data interpretation and for providing me all the necessary bibliography for the development of this work.

I would like to acknowledge the support given by Dr. James Mechie (GFZ-Potsdam) and the valuable discussions about the CINCA wide-angle data. Likewise, I would like to thank Dr. Manfred Stiller (GFZ-Potsdam) for providing the SPOC raw data and discussions about seismic data processing.

Special thanks to Ingeborg Siddike and Malgorzata Grünenberg for helping me with the academic and bureaucratic formalities of the university.

I am also thankful to Dr. Jörn Kümmerow and Dr. Makky Jaya for their help and advices given all these years.

Very special thanks to Pablo Salazar and Liey-si Wong for their friendship, support and the delicious meals we prepared together.

I would like to thank my colleagues Jannis Tzavaras, Carsten Dinske, Nicolas Hummel, Karsten Stürmer, Stine Gutjhar, Oliver Krüger and Kolja Gross for their friendship, support and the good times at the Institute. Many thanks to Gerhard Kapinos for his help in the construction of the location maps with GMT and for the useful discussions about the magnetotelluric results in southern Chile.

I also want to thank Dr. Michael Schmitz for his support all these years from Venezuela and for encouraging me to study in Germany.

Special thanks to members of our majestic football team *The Phasers* for having enjoyed together every Friday afternoons during the summer time.

Many thanks to my family in Venezuela, specially to my Father, for the wonderful words of encouragement, all the support and for being there every time I needed them despite the distance.

Last but not least, I want to thank my wife Lis, my love, for her infinite patience, understanding, support and mainly for being at my side in good and bad times. I could not have been done it without you!